Optical polarimetry studies of Seyfert galaxies

Felton, Michelle Ann

Optical polarimetry studies of Seyfert galaxies

Michelle Ann Felton
B.Sc. (Theoretical Physics)
M.Sc. (Radio Astronomy)

A thesis submitted to the University of Durham
for the degree of Doctor of Philosophy

Department of Physics
University of Durham
Durham
September 1999

Abstract

Optical imaging polarimetry has been performed on seven nearby Seyfert galaxies, three with face-on and four with edge-on host galaxies of various morphological classifications. Observations in V, R, B and H_α wavebands are presented as maps of total intensity and of polarized intensity, overlaid with polarization vectors. Independent determinations of the interstellar polarization (ISP) contribution from our own galaxy are made where possible, and are used to produce ISP corrected maps.

The polarization patterns seen in the maps show evidence of either dichroic extinction, which indicates the presence of non-spherical dust grains in large-scale galactic magnetic fields, or scattering, which is due to the illumination of regions of dust grains or electrons. The polarization features, which are observed at the different wavebands, are then compared to recent models of polarization in external galaxies. Estimates of the intrinsic Seyfert nuclear polarization are made where possible by correcting for ISP and for an approximation of the dilution due to the host galaxy flux by using values from previous studies. Both the measured and the corrected nuclear polarizations are compared with previously published values, and are discussed in the context of the standard models of Seyfert galaxies.

Most of the observed galaxies show evidence of polarization, both from the host galaxy and from the intrinsic Seyfert nucleus. In particular, distinct polarization features: bands of polarization consistent with extended dusty disks aligned with the dusty tori proposed in Seyferts, and regions of polarization corresponding to scattering of the nuclear continuum along the biconical extended Seyfert emission-line regions, have been identified in several of the observed galaxies.

Contents

List of Figures

Declaration and copyright

None of the material contained within this thesis has previously been submitted for a degree at Durham University or any other university.

The data in this thesis were taken on telescope allocations made to Dr. S.M. Scarrott and his permission must be obtained by anyone wishing to publish or use the results beyond this thesis.

The Digitized Sky Survey was produced at the Space Telescope Science Institute under U.S. Government grant NAG W-2166. The images of these surveys are based on photographic data obtained using the Oschin Schmidt Telescope on Palomar Mountain and the UK Schmidt Telescope. The plates were processed into the present compressed digital form with the permission of these institutions.

Chapter 1

An introduction to Seyfert galaxies

Deep in the nuclei of a significant number of galaxies, some highly energetic phenomena are taking place. These processes are not due merely to high concentrations of stars or enhanced rates of star formation, but to something intrinsically different, fundamentally more powerful and extreme. This chapter presents the background to the discovery of these highly active nuclei in galaxies, and gives an introduction to the properties of Seyfert and other active nuclei, their classification, links between the different classes, and the basis of the theoretical models proposed for the processes occurring in these active nuclei.

1.1 Classification of galaxies

Galaxies can be classified into four main categories by their appearance[1]: elliptical, lenticulars and spirals (both disk galaxies), and irregular galaxies. Elliptical galaxies are designated by their degree of ellipticity, E0 (spherical) to E7 (most elongated). Disk galaxies are either unbarred and denoted SA, or barred and denoted SB. Lenticulars (which have no spiral arms) denoted by SA0 (unbarred) or SB0 (barred). Spirals are further classified according to the degree of spirality, **a**-type meaning tightly wrapped, **b**-type more open, **c**-type clearly open spiral structure[2]. De Vaucouleurs added an extra subdivision to each of these, labelled either **d** meaning the spiral structure is well-defined, or **m** to indicate that although of spiral nature it is somewhat chaotic in detail. The sizes of the central bulge of the galaxy, the amount of gas, and the angular momentum per unit mass all

[1]Based on Hubble classification as modified by De Vaucouleurs.

[2]At one time the Hubble sequence was thought to indicate a simple evolutionary scheme and accordingly c-type are also known as early-type spirals and a-type as late-type spirals.

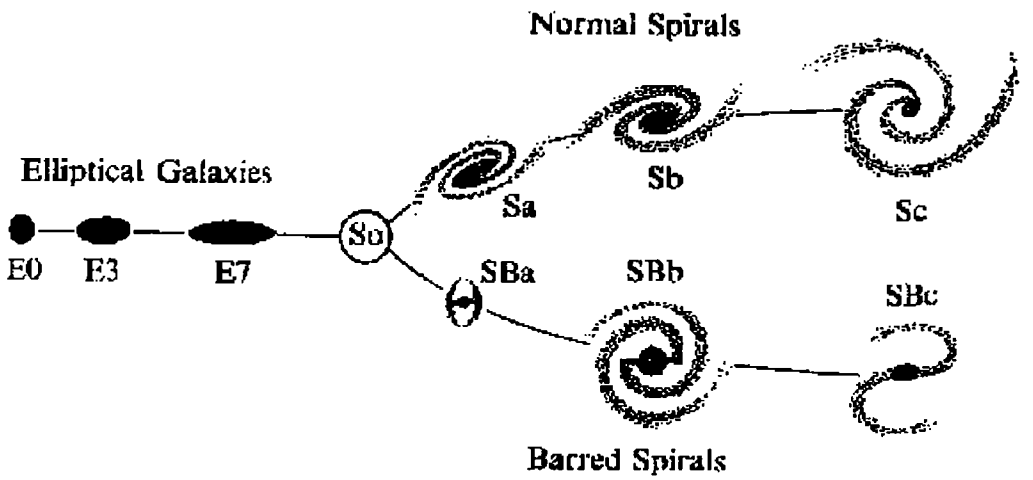

Figure 1.1: The Hubble classification of galaxies (taken from Birney 1974 [32])

correlate with the degree of spirality, a-type with the largest bulges, least gas and angular momentum to c-type with the smallest bulges with the most gas and angular momentum. Irregular galaxies show no spiral structure, and are divided in to type I which can be resolved into groups of highly luminous O and B stars, and type II which cannot. Peculiar galaxies are regarded as perturbations to the main categories, usually suggestive of some interaction or merging activity (Barthel 1989 [21]) and are denoted by appending **pec** to their closest Hubble classification. A schematic diagram of the Hubble and De Vaucouleurs classification is given in figure 1.1.

Elliptical galaxies constitute about 60% of known galaxies, spirals less than 30% and irregulars less than 15%, although locally the figures are dependent on density of galaxy clustering and redshift. A fundamental difference between elliptical and spiral galaxies is that ellipticals lack the large amounts of cool gas and dust that are found in spirals (which often have a clear dust lane across their centre). This means that the spirals have extensive star forming regions and many young stars, whereas ellipticals usually have very limited amounts of either. The significant amounts of interstellar gas in spirals lead to the existence of H_{II} (ionized hydrogen gas) regions in the spiral arms and central regions, which are regions of gas clouds illuminated by suitable ultra-violet light (*e.g.* from bright O and B class stars), giving rise to weak emission lines of hydrogen, oxygen and nitrogen. The spiral pattern is believed to be due to spiral density waves in the galaxy (a theory based on wave dispersion relations developed by Lin & Shu in the 1960s [137]). These waves cause compression regions in gas clouds as they pass through the waves, increasing the density sufficiently to cause a burst of star formation activity, producing local high luminosity due to the larger concentration of young bright stars in these spiral regions.

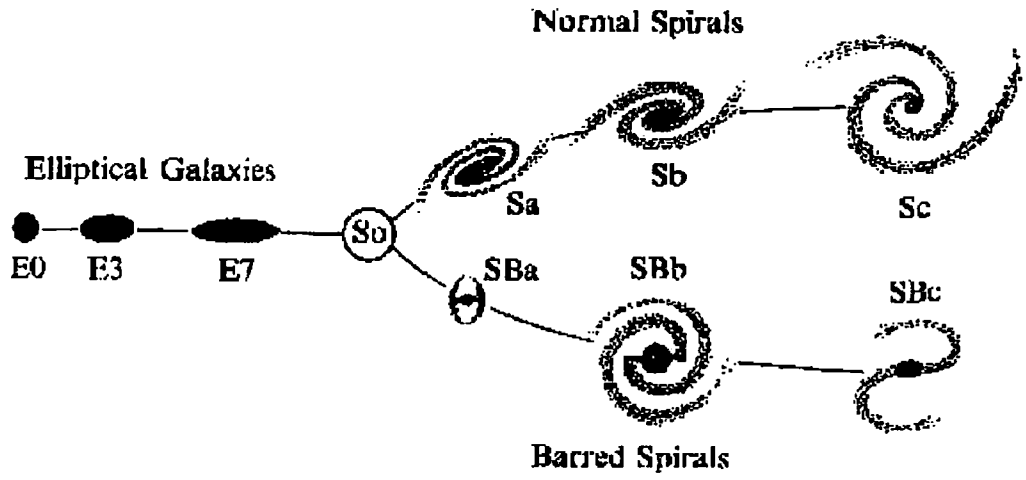

Figure 1.1: The Hubble classification of galaxies (taken from Birney 1974 [32])

correlate with the degree of spirality, a-type with the largest bulges, least gas and angular momentum to c-type with the smallest bulges with the most gas and angular momentum. Irregular galaxies show no spiral structure, and are divided in to type I which can be resolved into groups of highly luminous O and B stars, and type II which cannot. Peculiar galaxies are regarded as perturbations to the main categories, usually suggestive of some interaction or merging activity (Barthel 1989 [21]) and are denoted by appending **pec** to their closest Hubble classification. A schematic diagram of the Hubble and De Vaucouleurs classification is given in figure 1.1.

Elliptical galaxies constitute about 60% of known galaxies, spirals less than 30% and irregulars less than 15%, although locally the figures are dependent on density of galaxy clustering and redshift. A fundamental difference between elliptical and spiral galaxies is that ellipticals lack the large amounts of cool gas and dust that are found in spirals (which often have a clear dust lane across their centre). This means that the spirals have extensive star forming regions and many young stars, whereas ellipticals usually have very limited amounts of either. The significant amounts of interstellar gas in spirals lead to the existence of H_{II} (ionized hydrogen gas) regions in the spiral arms and central regions, which are regions of gas clouds illuminated by suitable ultra-violet light (*e.g.* from bright O and B class stars), giving rise to weak emission lines of hydrogen, oxygen and nitrogen. The spiral pattern is believed to be due to spiral density waves in the galaxy (a theory based on wave dispersion relations developed by Lin & Shu in the 1960s [137]). These waves cause compression regions in gas clouds as they pass through the waves, increasing the density sufficiently to cause a burst of star formation activity, producing local high luminosity due to the larger concentration of young bright stars in these spiral regions.

1.1.1 Active galactic nuclei

A number of otherwise normal-looking galaxies have extremely bright, very small often point-like nuclei. Some of these are starburst galaxies, with high rates of star formation occurring in the centre[3] giving rise to a bright nucleus due to larger numbers of bright young O and B class stars, but when the spectra of the rest of these bright nuclei is examined, it is found that most have a spectrum distinctly different from that of most normal galaxies. The powerful nuclear radiation spectrum cannot be modelled purely as that from the rest of the galaxy, *i.e.* primarily blackbody radiation peaking in the optical region of the spectrum from a collection of stars with regions of gas and dust producing absorption lines and weak emission lines. Instead, in addition to weak normal galaxy spectral features, the nuclear spectrum shows excesses in X-ray, ultra-violet and infra-red regions, variability in various wavebands and strong characteristic line spectra of very broad emission lines associated with a range of ionization states with velocity dispersions up to 10^4 km s^{-1}. The emission lines are much broader than those found in H_{II} regions and starburst galaxies, which indicates that the gaseous emission region is in motion with a spread of velocities of at least 700 km s^{-1} and a minimum velocity of at least 200 km s^{-1}. These nuclei are termed AGN, active galactic nuclei[4].

AGN have been classified at several levels according to spectroscopic and luminosity differences. The main division is on the basis of radio power, into radio-quiet AGN and radio-loud AGN[5]. Radio-quiet AGN are subdivided primarily on the basis of luminosity into lower luminosity Seyferts and high luminosity quasars (or QSOs, quasi-stellar objects[6]). Radio-loud AGN are subdivided into the lower luminosity narrow-line FR I[7] and broad-line radio galaxies and the higher luminosity narrow-line FR II radio galaxies, quasars and Blazars (a collective name for BL Lacs and Optically Violent Variables - OVVs, characterised by large fast flux variations and high polarization). There is another class of galaxy classed as active, but not necessarily as of AGN origin. LINERS (Low-Ionization Nuclear Emission-line Regions) are active galaxies characterised by spectra similar to Seyfert 2s (a subclass of Seyferts), except that their low-ionization lines are relatively strong and they have very low nuclear luminosities compared with other AGN.

[3]Starburst galaxies do not necessarily have to have their increased rate of star formation concentrated in or limited to their nucleus.

[4]Strictly, the original acronym AGN means Active Galactic Nucleus, but in this thesis AGN is taken also to mean the plural Active Galactic Nuclei, where appropriate.

[5]This distinction is loosely based on radio-loud objects having a ratio of radio flux (at 5 GHz) to optical (4400 Å) flux of greater than and equal to ten, and radio-quiet objects having this ratio less than ten, Kellerman 1989 [120].

[6]Originally the term quasar referred to only radio-loud quasars first found in radio surveys, but now quasar encompasses radio-quiet optically selected QSOs as well.

[7]Fanaroff-Riley type I (FR I) objects are the lower power radio galaxies typically having twin radio jets, FR II objects are the higher power radio galaxies which generally have an asymmetric jet structure and limb-brightening.

They are very common in spiral galaxies, however their spectral origins are ambiguous, and could be produced by several different processes, including normal H_{II} regions, normal galaxies with starburst-driven winds or some sort of shock-heated gas, as well as very low luminosity Seyfert 2 nuclei.

Implications of general size and mass constraints

Observations have shown that AGN display appreciable continuum variations over most of their spectrum from IR to X-rays over time scales of less than a year, with shorter wavelength emission often varying over shorter time scales of less than one day, and in some AGN, at the shortest X-ray wavelengths, variations on time scales of an hour have been measured. This variability can be used to place constraints on the size of the nuclear emission region.

If the nucleus is considered to be made up simply of spherical shells, then a physical signal emitted from the centre of the sphere (travelling at a speed no more than c) will reach all parts of each shell layer at the same time causing the brightness of the shell to change simultaneously. An outside observer however, will see a time delay in brightening of different parts of the shell because of the difference in time it takes the light to travel from the nearest part of the shell compared with the furthest part. The brightening will take a time of duration $t = 2R/c$ where R is the radius of the nucleus. Therefore, if there is a significant change in brightness observed in a time t, then the size of the source can be no larger than $2R = ct$. The time scale of a year corresponds to a distance $2R \approx 0.3$ pc and a day gives a distance $2R \approx 8.4 \times 10^{-4}$ pc, *i.e.* roughly comparable to the size of the Solar System. An hour corresponds to a distance $2R \approx 3.5 \times 10^{-5}$pc.

To generate the implied huge amounts of radiation from this relatively tiny nuclear volume (of the order 1 pc in diameter to include most of the spectrum variations) requires an immensely powerful engine. If the nuclei are gravitationally bound, then by a simple virial argument the nuclear masses are very high. For a nuclear mass M, with matter bound to radius r, moving with velocity v, and gravitational constant G, then equating the gravitational and centripetal forces implies that:

$$M \approx \frac{v^2 r}{G} \tag{1.1}$$

The velocity dispersions can be calculated from the widths of the broad emission lines, which are of the order 10^3 km s^{-1}, and taking r to be 1 pc for the region of the broad-line emission. Hence, using the virial equation, the masses of nuclei are of the order of $10^8 M_\odot$ ($M_\odot$ = solar mass). Recent reverberation mapping data (time-delays) by Peterson *et*

al. (1998) [182] of the optical broad emission lines and continuum fluxes of nine Seyfert nuclei, lead to mass estimates in the range 10^7 to $10^8 M_\odot$.

These large implied masses in such small regions, together with the discoveries of solar mass black holes in this galaxy, have led to the general acceptance of a black hole and accretion disk system as being the central engine producing these immense quantities of radiation, in the absence of any better models. Nearby matter in the galaxy is being gravitationally pulled towards the black hole forming an accretion disk, which becomes heated by the extreme conditions, and emits radiation over the whole spectrum from radio, through infra-red, optical, ultra-violet to soft X-ray emission. Surrounding this disk there may be clouds or other structures of dust and gas obscuring and/or reprocessing the radiation from the accretion disk.

1.2 Seyfert nuclei

Seyfert galaxies are one of the lower luminosity classes of active galaxies and were first classified as a group by Carl Seyfert in 1943 [209]. He took spectra of a set of spiral galaxies selected because of their high point-like central surface brightness, and found that six of these spirals unexpectedly had strong high-excitation broad nuclear emission lines in addition to the normal continuum. He grouped them together and contrasted them to H_{II} regions in irregular galaxies and in the arms of spiral galaxies. This original, primarily morphological definition has now been replaced by a spectroscopic definition of AGN primarily on the basis of strong high-ionization emission lines. In Seyferts, the AGN continuum with the characteristic AGN features of IR, ultraviolet and X-ray excesses is relatively weak compared to other AGN, and hence it is more difficult to distinguish from the host galaxy continuum.

Almost all Seyfert nuclei hosted in galaxies close enough to be classified, are in spiral galaxies and their spectra also show weak absorption lines from the late giant stars present in the host galaxy. Conversely, approximately 1% of spiral galaxies have an active (Seyfert) nucleus. Sizes of the non-thermal (UV) continuum region have been measured to be of the order of a light day *e.g.* NGC 4151 (Ulrich & Horne 1996 [239]), with the broad-line emission surrounding this to within 4 light days, and the narrow-line region much larger, about of the order of 100 pc. The absolute magnitudes of Seyfert nuclei are designated $M_B > -21.5 + 5\log h_0$ (where $h_0 = H_0$ in units of 100 km s^{-1} Mpc) to distinguish them from the lowest luminosity quasars (Schmidt & Green 1983 [204]). Seyferts and quasars are the two largest subclasses of active galaxy, with nuclear energies of $\sim 10^{11} L_\odot$ and

$\sim 10^{13} L_{\odot}$ respectively. For comparison, the total energy emitted by all the stars in a typical spiral galaxy is of the order $10^{11} L_{\odot}$.

Seyferts can be distinguished from the H_{II} regions found in normal galaxies by the much wider range in ionization level found in Seyferts and by their $[O_{III}]$ to H_{β} emission ratio being greater than 3. The low luminosity active galaxy class of LINERS have much more prominent low ionization lines and a much lower $[O_{III}]$ to H_{β} ratio, and although it is possible that some LINERS may be just extremely low luminosity Seyfert 2s, most are due to other non-AGN processes (*e.g.* illumination by ultra-violet light from bright stars). About half of spiral galaxies show LINER characteristics.

Another subclass of AGN that has been identified is narrow-line X-ray galaxies, which have the same high excitation lines as Seyferts, but a lower luminosity, and are Seyferts whose optical spectra has been heavily reddened and extinguished by dust in the galaxy. Some Seyferts *e.g.* NGC 4945 (Moorwood & Olivia 1994 [161]) have nuclear starbursts going on in addition to the nuclear emission of the central AGN engine, further complicating the nuclear spectrum. These might be cases of galaxies in the process of changing from starburst to Seyfert, in an evolutionary scenario, *e.g.* Norman & Scoville (1988) [168].

1.2.1 Seyfert types

Khachikian and Weedman (1974) [121] classify Seyferts into two spectroscopic groups, named type 1 and type 2. Seyfert 1s are defined as those having very broad permitted emission lines (*e.g.* $H_I, He_I, He_{II}, Fe_{II}$) with FWHMs (full width at half maximum) broader than 1000 km s^{-1} and forbidden lines somewhat narrower than this, with FWHMs typically of several hundred km s^{-1} (*e.g.* $[O_{II}]$, $[O_{III}]$, $[Ne_V]$, $[N_{II}]$, $[S_{II}]$, $[Fe_{VII}]$)[8]. Seyfert 2s have permitted lines narrower than 1000 km s^{-1} (but broader than 200 km s^{-1}) with the forbidden lines of comparable narrow or intermediate widths. Although the narrow emission-line spectra of Seyfert 1 and 2 galaxies are similar, there do exist subtle differences. Seyfert 1s often have higher ionization, stronger emission from Fe_{II} and, if not highly reddened, show a 'blue bump' (excess flux at wavelengths shorter than 4000 Å). Seyfert 2 galaxies have a very high $[O_{III}] : H_{\beta}$ ratio.

There are intermediates between the two Seyfert definitions which have composite Balmer line profiles, *i.e.* a narrow profile similar to that of the forbidden lines superposed on a broad Seyfert 1 type profile. Cohen (1983) [45] showed the intermediate spectrum can be obtained by adding the typical spectrums of a Seyfert 1 and 2; and that all Seyfert 1s

[8]Forbidden lines are usually written enclosed in square brackets to differentiate them from the allowed lines.

have composite H_I line profiles to some extent. This can be explained by stratification, the hydrogen and forbidden lines being emitted at the different distances from the centre of the nucleus, or a difference in spectral index of the ionizing continuum.

Osterbrock (1981) [174] further refined the classification by introducing the notation of Seyfert subclasses 1.5, 1.8, and 1.9. Seyfert 1.5s nuclei are those Seyfert 1s in which the composite H_I characteristic is more prominent, and also other intermediate properties are demonstrated such as the strength of their non-thermal radio emission, and that the H_α and H_β narrow and broad components have similar strengths. Seyfert 1.8s and 1.9s are more similar to Seyfert 2s. Seyferts 1.8 are distinguished as having strong narrow components of H_α and H_β and a weak but easily visible broad component of H_α, but only a very weak broad component of H_β. Seyfert 1.9s have strong narrow H_α and H_β and a weak but easily visible broad component of H_α, but almost no detectable broad H_β. Their broad band spectra are also more reddened, presumably by dust.

A subgroup of Seyfert 1s was proposed in 1985 by Osterbrock & Pogge [176], of 'narrow-lined Seyfert 1 galaxies' (NLS1 galaxies). These have normal Seyfert 1 luminosities but permitted line-widths significantly narrower than typical Seyfert 1s, on the order of 1000 km s^{-1} and certainly less than 2000 km s^{-1}, mostly weak forbidden lines, but otherwise have Seyfert 1 rather than Seyfert 2 characteristics. Stephens (1989) [221] estimates that about 10% of Seyfert 1s are NLS1s. They can also be distinguished by their very steep X-ray spectral index and high X-ray variability. Either a range in nuclear mass and accretion rate, or more plausibly, a difference in the circumnuclear gas of temperature, density, opacity or geometry could explain this division (Turner 1999 [238], Komossa 1999 [124]). There also appear to be analogues in QSOs, narrow-line QSOs *e.g.* I Zw 1, Oke & (Lauer 1979) [170].

Spectral variation has been observed in a few Seyfert galaxies, such that the broad H_I emission lines have disappeared, for example NGC 7603 appeared to change from Seyfert 1 to Seyfert 2 over a year (Tohline & Osterbrock 1976 [229]). The line profiles indicate high velocities (10^3 to 10^4)km s^{-1} of the gas, so spectral variation due to the movement of gas clouds within the nucleus (about 10^{13} km) could be expected. Conversely, Seyfert 2s have been observed to develop broad H_α lines characteristic of Seyfert 1s, *e.g.* NGC 7582 (Aretxaga *et al.* 1999) [14]. This could be accommodated in the unified scheme only if the dust in the torus is patchy, but Aretxaga *et al.* (1999) [14] favour the explanation being a supernova explosion in the circumnuclear starburst region causing the broad H_α emission by photo-ionization of the gas clouds by the gas clouds by the SN radiation.

Table 1.1: Number density estimate of active galaxies

Type of system	Number density estimate h_0^3 Gpc $^{-3}$ (Woltjer 1990 [267])
Seyfert 2	8×10^5
Seyfert 1	3×10^5
QSOs	800
FR I radio galaxies	2×10^4
BL Lacs	600
FR II radio galaxies	80
Quasars	20
Seyferts	$\approx$ 1% of spiral galaxies
LINERS	$\approx$ 30% of all galaxies*
Spiral galaxies	$<$ 30% of all galaxies

*with $B \leq 12.5$ mag, Ho 1996 [72]

1.2.2 Mechanism of line emission of Seyfert nuclei

The line emission of Seyferts can be well modelled by photo-ionization of the gas clouds that surround the engine by the ultra-violet or X-ray radiation from the black hole and accretion disk system. The gas will absorb and then emit the radiation as the characteristic lines of the gases that make up the clouds, as well as becoming heated. These clouds are mostly hydrogen, and accordingly, hydrogen lines appear strongly in the line emission. As in H_{II} regions, nitrogen and oxygen lines also are seen in the visible spectra. Photo-ionization accounts for the intensities of the strongest optical and UV lines, as well as the simultaneous presence of both strong high and low ionization states if the gas clouds are optically thick to the ionizing continuum.

The region of the AGN from where the broad-line (greater than 1000 km s^{-1}) emission emanates is termed the broad-line region, BLR, around the centre of the nucleus. Similarly, the narrow-line region (NLR), further out from the BLR, is where the narrow-line emission originates. Although termed the narrow-line region, the lines are still broad (about 700 km s^{-1}) compared to the hydrogen emission lines found in normal galaxies.

1.2.3 Broad-line region

Since it is the closest component to the central engine, the broad-line region is potentially an important probe of the engine, both because its bulk motion must be determined by

the central engine's strong gravitational force and radiation pressure. It is also important because the broad-line region reprocesses the ionizing ultra-violet radiation of the central engine that otherwise can not be observed directly. This is shown by the strong correlation between variations in the broad emission lines with the continuum fluxes, *i.e.* the central source drives these emission lines and the continuum, and that a large part of the recombinant radiation is emitted by clouds that are optically thick to the ionizing continuum. The broad line region is observed in Seyfert 1s, but not in Seyfert 2s, although a few have revealed a BLR in polarized light. The variability of the broad emission lines in a few cases, has shown a dramatic drop in intensity, implying changes in the structure of the BLR along the line-of-sight.

The electron densities in the BLR are high enough that virtually all the forbidden lines usually seen in highly ionized gas, are collisionally suppressed, *i.e.* the excited states are collisionally de-excited before emission can occur. In the high density limit, the emissivity j is proportional to the number density n, enabling limits to be determined. The absence of the [O_{III}] λ4363,4959,5007 lines implies a lower limit of 10^8 cm^{-3} (the critical density for this line). Conversely, the forbidden line [C_{III}] λ1909 is usually strong, and the critical de-excitation density for this to happen is 10^{10} cm^{-3}, suggesting this as an upper limit on the electron density in the BLR (Peterson 1997 [181]). Reverberation mapping however has shown that this [C_{III}] emission arises from a different part of the BLR meaning these limits are not necessarily spatially co-existent. Other studies also show evidence for geometrical or kinematic structure in the BLR by different ionization zones (*e.g.* Marziani 1996 [149]).

The similarity of the relative line intensities to those in other ionized gases suggests the temperature is about 10^4 K (Peterson 1997 [181]). The line-of-sight velocity dispersion, assuming thermodynamic equilibrium can be given by:

$$v = (\frac{3kT}{m_p})^{\frac{1}{2}} \tag{1.2}$$

where T is the temperature, k is Boltzmann's constant and m_p is the mass of a proton. At temperatures of around 10^4 K, velocity dispersions due to thermal broadening therefore are of the order of 10 to 20 km s^{-1}.

The widths of the broad emission lines measured in velocity units of the full width at half maximum (FWHM) range from a minimum of 500 km s^{-1}, up to 10^4 km s^{-1}, but typically about several thousand km s^{-1}. Since the thermal broadening is only of the order 10 km s^{-1} the main broadening is assumed to be due to Doppler broadening due to bulk motions of the line-emitting clouds, presumably due to the gravitational influence of the central engine. The profiles of the lines can be approximated as logarithmic to first order, but some lines are considerably more complicated and variable. The line profiles can vary for

different lines across the spectrum implying that the line of sight is important *i.e.* that the BLR has some internal structure. The widths of the allowed lines of hydrogen in Seyfert 1s are broader than the forbidden lines, implying that the denser regions of gas are in more violent motion then the less dense regions. If the denser regions are closer to the central engine, then it would follow that they would have acquired more kinetic energy by losing gravitational energy. The broad emission line profiles have a tendency to vary symmetrically, consistent with random or circular orbital motion, rather than radial outward or inward motion (Ulrich *et al.* 1984 [240]).

There are also a number of lines which are so broadened, that they are blended with other emission lines. The 'small blue bump' is a blend of Fe_{II} emission lines and Balmer continuum from 2000 Å to 4000 Å, but the precise mechanism for this feature is not clear; difficulties in photo-ionization models have led to suggestions that it may be associated with the accretion disk (Collin-Souffin 1980 [51]).

1.2.4 Narrow-line region

The narrow-line region is important for study, since it is the only AGN component (at least for nearby Seyferts) which can be spatially resolved, allowing some direct physical and kinematic mapping which shows non-isotropic illumination. It is the largest region over which the AGN contribution to the radiation dominates, shown by strong correlations between the narrow line $[O_{III}]$ luminosity and the core nuclear radio luminosity. It is present in both type 1 and 2 Seyferts.

Strong narrow lines at a range of ionization levels can be detected (the strongest unblended narrow emission lines are $[O_{III}]\lambda$ 4959, 5007). In Seyferts, the full widths at half maximum have a wide distribution of widths from 200 to 900 km s^{-1}, centred on about 350 - 400 km s^{-1} (Peterson 1997 [181]. The wide range of ionization states implies the ionizing radiation is hard and extends to high energies, with more higher energy photons than O-stars could produce. Photo-ionization models with a power-law dependence on frequency for the ionizing radiation give much better fits to the emission spectra than O-star thermal radiation.

The electron densities in the NLR are considerably lower than in the BLR, so most forbidden transitions are not collisionally suppressed. This means the intensity ratios of certain pairs of forbidden lines can be used to measure the electron densities and temperatures, although this method is complicated by the presence of significant amounts of dust. To determine the electron density, measurements are taken of the intensity of two lines from a single ion which are in closely spaced upper states decaying to a common lower

state. The $[S_{II}]\lambda\lambda$6716,6731 doublet can be used for this purpose, and in Seyfert NLRs this yields values from 10^2 cm^{-3} to 10^4 cm^{-3} (Peterson 1997 [181]. In a similar manner, the electron temperature can be measured from emission lines of the same ion. Lines are chosen which have very different excitation potentials χ so that the rate at which the different levels are populated by collisions is highly temperature dependent. $[O_{III}]\lambda$4363, 4959, 5007 is commonly used in AGN narrow-line region temperature determination given by Osterbrock 1989 [173]:

$$\frac{F(\lambda 4959 + \lambda 5007)}{F(\lambda 4363)} \approx \frac{7.33e^{(3.29\times 10^4/T_e)}}{1 + 4.5 \times 10^{-4} n_e T_e^{-1/2}} \tag{1.3}$$

The typical range of electron temperatures found in NLRs by this method range from about 10 000 to 25 000 K. This is only a rough indication since the electron density on which the temperature depends, is not constant throughout the NLR. This low temperature implies photo-ionization rather than thermal ionization.

The narrow-line profiles of Seyferts can be asymmetric, nearly always in that the profile has a longer tail extending to the short wavelength side than to the longer wavelength side. A purely rotational velocity field would not produce this effect, but a radial flow plus extinction by dust may produce this. If the flow is radially outwards, dust distributed through the AGN will on average cut down the emission lines from the far receding side more than the near side which would produced the observed profiles. Other features could also produce this asymmetry, such as an obscuring torus causing cylindrical symmetry. There are weak correlations of the narrow-line profiles with the morphological type of the host galaxy, and possibly with the luminosity of its bulge, showing that the gravitational effects of the galaxy also affect the velocity fields in the NLR.

Schmitt (1998) [205] compares the emission line ratios of the narrow-line regions of a sample of 52 Seyfert 1s compared to 68 Seyfert 2s. The distribution of emission-line ratios $[O_{II}]/[Ne_{III}]$ and $[O_{II}]/[Ne_V]$ shows that Seyfert 1s have smaller values than Seyfert 2s, indicating a higher excitation. A comparison of models with varying proportions of matter and ionization-bounded clouds suggests the most likely scenario to be that Seyfert 1s have a smaller NLR than Seyfert 2s, possibly due to preferential alignment of the torus axis close to the host galaxy plane axis in Seyfert 1 galaxies.

As an example, analysis of the Seyfert 1 galaxy, NGC 5548 by Kraemer 1998 [128], shows evidence of a high-ionization NLR very close to the nucleus, at about 1 pc, which is optically thin at the Lyman edge. A lower-ionization NLR is required at about 70 pc from the nucleus, and the majority of the narrow line emission must come from within 70 pc of the nucleus, much more compact than most Seyfert 2 galaxies.

1.2.5 Extended emission line regions

Spatially resolved narrow-line regions are referred to as extended narrow emission-line regions (ENLRs or EELRs) (Unger *et al.* 1987 [247]). These have a filamentary structure of high excitation gas, both in Seyfert 1 and 2 galaxies, and in Seyfert 2 galaxies, this is often in the shape of an axi-symmetric ionization cone. The emission lines are much narrower than in the nuclear NLR, with widths of the order 50 km s^{-1}. Some form of extended narrow-line emission is very common in both types of Seyfert; Mulchaey *et al.* (1996) [162] finds $\approx$ 80% of Seyferts in early-type hosts to show extension in $[O_{III}]$ images and $\approx$ 100% extension in H_α+$[N_{II}]$ images, but clearly defined cones are more rare. These extensions were first detected by long slit spectra taken parallel and perpendicular to the linear radio structure, which showed that there is ionized gas parallel to these radio structures, extending out as far as from $50h_o^{-1}$ pc to $15h_o^{-1}$ kpc, (where $h_0 = H_0$ in units of 50 km s^{-1} Mpc), but virtually none in the perpendicular direction. Unger *et al.* (1987) also show the velocity field of the ENLR is primarily the smooth rotation field of the host galaxy, *e.g.* Baldwin *et al.* (1987) [17] shows in NGC 1068 that beyond 15 arcseconds (750 pc) the ENLR has the velocity field of the host galaxy, but inside this radius, it shows a different rotational field, which could be consistent with the influence of a jet structure of the ionizing continuum radiation escaping from the nucleus.

Ionization cones have been detected in about 12 or so AGN, all radio quiet and mostly Seyfert 2 galaxies (Wilson & Tsvetanov 1994 [264]). They have opening angles of between 30° and 100°, and can be either conical, or biconical sharing the same axis, and are not correlated with the host galaxy symmetry. Presumably the single cones have a counterpart which is obscured by the geometry of the obscuring dust distribution. The edges of the ionization cone are sharp and well-defined as would be expected by collimation of the nuclear light source rather than defined by the actual gas distribution. They are most striking in maps of high excitation emission lines such as $[O_{III}]\lambda5007$. The ratio of $[O_{III}]$ $\lambda5007$ to H_α flux is greater than one, characteristic of gas ionized by an AGN continuum, whereas outside the cone this ratio drops, implying the ionization is primarily by starlight.

There is a strong correlation between the line fluxes of the unresolved nuclear core and the extended emission, evidence that the extended emission is ionized by the same source that ionizes the nuclear gas. In some sources, the radio emission shows evidence of shock fronts where the radio plasma hits the interstellar medium of the host galaxy, and strong narrow-line emission is observed from these post-shock cooling regions (Pogge 1993 [187]). It appears the radio plasma creates bowshocks where it meets the ambient NLR gas, so that collisional ionization is a partial energy source of the narrow-line emission in these regions, in addition to the AGN photo-ionization (*e.g.* Viegas-Aldrovandi & Contini 1989 [250]). The large narrow-line widths can be attributed to the radio plasma accelerating

the ambient gas (Pedlar, Dyson & Unger 1985 [178]), and if there is an obscuring medium in midplane then the near-side outflowing gas would give a relatively blue- shifted components and qualitatively explain the observed profile asymmetries.

These ionization cones are an important manifestation of radiation anisotropy on kiloparsec scales; the question is whether the radiation from the central engine is emitted anisotropically at very small radii so that a hole in the postulated dusty torus is caused by this strong radiation, or whether the nuclear radiation is isotropic at smaller radii, and is then collimated by the dusty torus itself. This question is still under debate.

1.3 Unified schemes

A recurring idea in astronomy is the theme of unification, to link apparently different objects simply as different manifestations of a single underlying continuous phenomena, and there are a number of unification schemes which have been proposed for AGN. The simplest of these is where the differences in the observed objects are due solely to orientational effects, *i.e.* the orientation to the line-of-sight. Strong anisotropies of the radiation and absorption geometries are further geometrical effects. Antonucci (1993) [9] reviews the evidence for the various unified schemes in AGN studies. He notes that if AGN are highly non-isotropic, but are spatially unresolved in observation, orientation will confuse the observations. An diagram showing a strong (linking across luminosity as well as orientation) unification scheme for radio-loud objects, and a similar one for radio-quiet objects is given in figure 1.2, adapted from Ogley (1995) [169]. The range in luminosities from Seyferts to QSOs is obviously intrinsic with respect to orientation, but the spectroscopic differences can be modelled very well by different viewing angles.

1.3.1 Unification of Seyfert types 1 and 2

A simple unification model was proposed by Osterbrook (1978) [172], who suggested that Seyfert 2s are really just Seyfert 1s that have their BLR obscured from the observer's view. Figure 1.3 shows the standard schematic model for Seyfert nuclei. The central nucleus is composed of a BLR (broad-line region) around the central engine (black hole and accretion disk system), then a fairly opaque torus of dust and gas around the BLR, perpendicular to the radio axis, and a NLR (narrow-line emission region) then surrounding this. Seyfert 1 characteristics will be observed if viewed close along the line to the radio

axis, and Seyfert 2 characteristics if viewed perpendicular to the radio axis. This would also explain why Seyfert 2s are on average observed to be less luminous than Seyfert 1s.

Another prediction of this model is that it should be possible to detect 'hidden' Seyfert 1 characteristics in Seyfert 2 nuclei by studying polarized emission. This is because some light from the BLR may be scattered and become polarized by scatterers in the torus (either dust or electrons), so when that viewed in polarized light emission, a 'hidden' Seyfert 1 nucleus would become apparent that would otherwise be swamped by the unpolarized component. This was first discovered observationally in NGC 1068 by Antonucci & Miller in 1985 [12]. Since then a number[9] of other Seyfert 2s have had polarized broad lines observed in their spectra, although there is no sign of such broad lines in polarized light in many others. Kay & Moran (1998) [118] note that such broad lines may be detected in even relatively weak classical Seyfert 2s, illustrating the need for well-defined H_α surveys of Seyfert 2s.

1.3.2 Unification of radio loud AGN

A similar orientation scheme for radio-loud AGN is also postulated. According to this, FR I and FR II radio galaxies are seen edge-on through the obscuring disc, whereas radio loud quasars are seen more pole-on and BL Lacs and blazars are seen almost exactly pole-on. The BL Lac spectrum is characterised by synchrotron radiation requiring magnetic fields and high energy relativistic electrons, and a lack of spectral lines which implies the radiation from the central engine is seen directly, without going through significant gas and dust clouds, and can be explained by relativistic beaming effects. Furthermore, the radio lobes observed in radio loud galaxies and radio loud quasars can be modelled by the central engine ejecting relativistic charged particles and magnetic fields along the poles which interact together and also with the ISM to produce large-scale radio emission.

These large-scale radio lobes however, are only associated with radio-loud AGN, so in radio-quiet AGN, either the central engine does not produce these relativistic particles and magnetic fields, or the radio emission are somehow obscured from sight. This difference may be due to the environment of the host galaxy, since the host galaxies of radio loud AGN with radio lobes are usually elliptical galaxies, which have very little gas or dust. Seyferts are found mostly in spiral galaxies containing large amounts of gas and dust, which might in some way 'damp' down the energetic electrons and magnetic fields that would produce strong radio emission or alternatively this morphological segregation may be an intrinsic luminosity effect.

[9]About sixteen have been detected as of August 1998.

1.3.3 Unification of Seyfert 1s and radio quiet quasars

Other unification schemes address the trends in luminosity. Originally Seyferts and radio quiet quasars were thought to be distinct classes of AGN, since there were three clear differences between them, but now with further observations these differences are not absolute, - there is significant overlap in properties. The first Seyfert 1s were detected as spiral galaxies with a bright nucleus and broad emission lines, whereas the first quasars were detected as quasi-stellar radio sources with broad emission lines and a high luminosity. There was originally a large gap in luminosity between the two classes, but now the most luminous Seyferts detected are of the same luminosity as the lower luminosity quasars. Quasars were found to demonstrate variability, whereas in Seyferts this was not detected in early studies, but now variability has been demonstrated in a number of Seyferts. The first Seyferts detected also had significantly stronger lines relative to the continuum than quasars, but since these quasars are at higher redshift, the difference is not striking. Seyfert 1s and quasars seem to form a progression along these properties rather than being completely separated populations, although of course at different values of luminosity or other properties, different processes may dominate.

1.3.4 Where are the high luminosity Seyfert 2 type nuclei?

A major problem in the unified scheme is a remarkable lack of high luminosity Seyfert 2 type nuclei, which would parallel the Seyfert 1 - QSO scheme. An X-ray source, 1E 0449.4-1823 was originally identified as a high luminosity Seyfert 2 'QSO', with a redshift of $z = 0.338$ and an absolute magnitude of -23.2 (assuming $H_0 = 50$ km s^{-1} Mpc^{-1}, with strong Seyfert 2 narrow lines but no detected broad lines. New spectra observed by Halpern, Eracleous & Forster (1998) [96] however, show broad emission lines of significant strength, and they attribute this to dynamic motion of the obscuring clouds around or in the BLR. The lack of observed Seyfert 2 type QSOs nuclei could mean either high luminosity sources nearly always produce an observable broad-line region, with the obscuring torus vanishing above a luminosity of about $M_B = -23$ (Miller & Goodrich 1990 [160]), or that there is a hidden population of type 2 QSOs.

The latter possibility is investigated by Wills & Hines (1999) [262]. Their broad-band and spectro-polarimetry work on 12 QSOs and 6 HIGs [10], selected by (orientation-independent) warm infra-red flux, shows that all six of the HIGs galaxies have strong Seyfert 2-like narrow lines and have broad-lines that are seen only in polarized flux, indicating the presence of buried QSOs, the high-luminosity analogues of Seyfert 2 nuclei.

[10]Hyperluminous Infra-red Galaxies

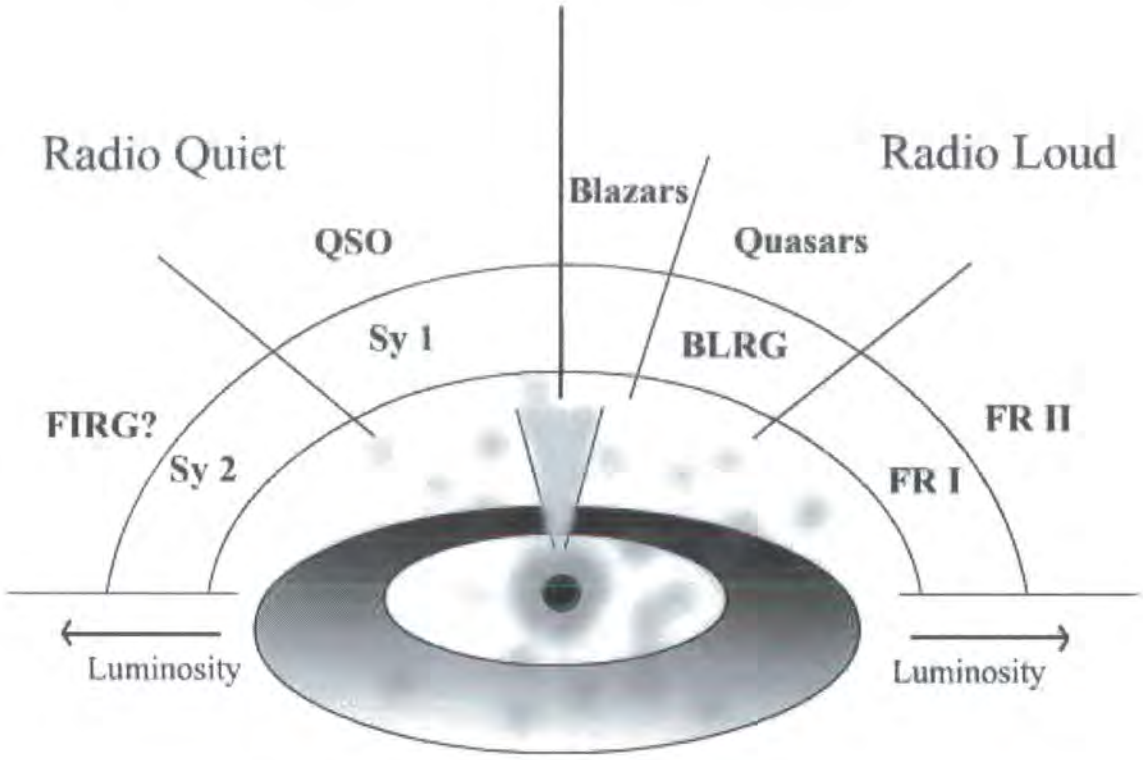

Figure 1.2: Diagram of a strong AGN unification scheme, adapted from Ogley (1995)

The 12 QSOs show less reddened spectra, and have broad lines visible in total light, *i.e.* they are QSOs, the high luminosity Seyfert 1 analogues. They note that in contrast, UV-optically selected samples would have only included 3-4 of the QSOs from the above sample, and none of the HIGs, hence missing all the type 2 QSOs. Larger surveys would be required to confirm this result.

1.4 Multi-wavelength continuum of Seyfert nuclei

Seyfert nuclei radiate with a characteristic broad-band spectral energy distribution (SED), strong in the infra-red, optical and often X-ray regions. At optical wavelengths, the AGN is about as luminous as the remainder of the rest of the galaxy (which radiates mainly at optical wavelengths), but the excess emission (relative to the spectra of normal galaxies) in the other wavebands, especially the infra-red, accounts for at least three times as much as the optical luminosity, so that Seyfert nuclei are at least 4 times as luminous as their host galaxy. Each region of the spectrum is examined in the following sections, finishing with a discussion of the mechanisms that are believed to be producing the broad-band continuum.

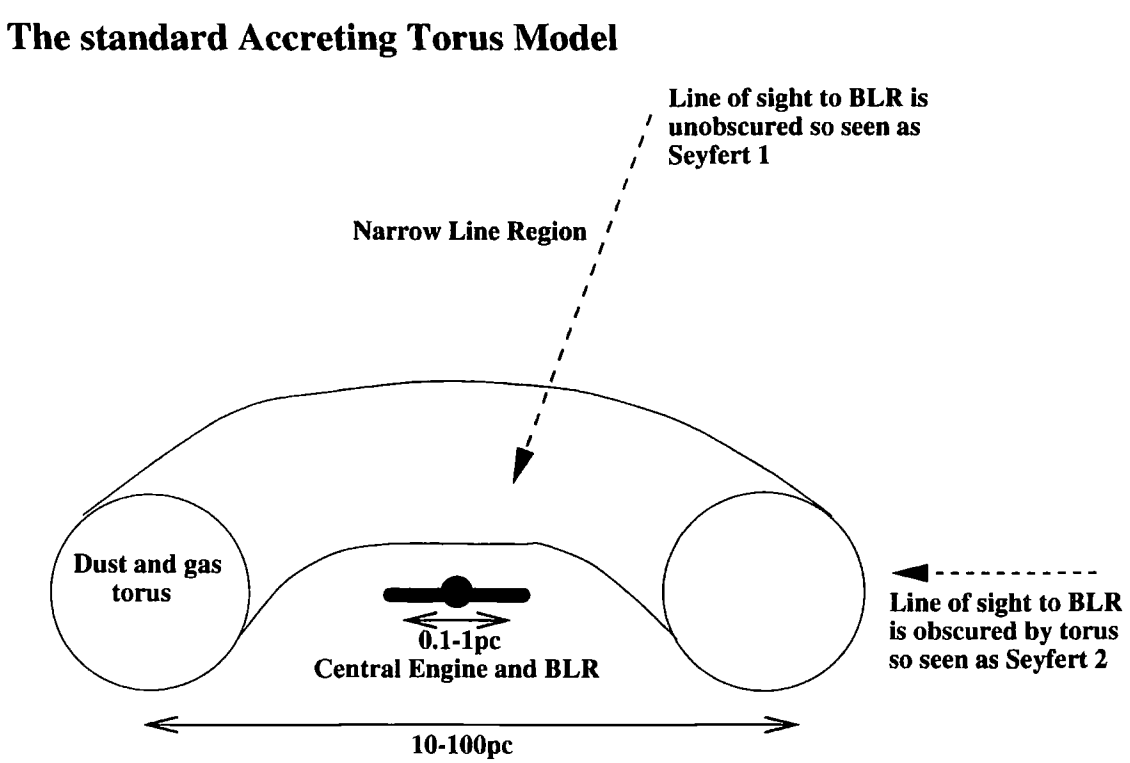

Figure 1.3: The standard model for Seyferts (taken from Malkan *et al.* 1998)

1.4.1 Broad-band spectral energy distributions of Seyferts

Multi-wavelength statistics of a large sample of Seyferts (330 type 1 and 357 type 2, redshift limit $z < 0.1$) were analysed by Dultzin-Hacyan & Ruano (1996) [63] to investigate their SEDs. They found that Seyfert 1s have higher luminosities on average than Seyferts 2s, excluding the far infra-red. The UV and X-ray emission in Seyfert 1s are significantly stronger than in Seyfert 2s, but only marginally stronger at optical wavelengths. Then, at longer infra-red and radio wavelengths, this difference disappears, suggesting intrinsic extinction (possibly by the postulated obscuring torus described in section 1.3.1). However using the standard extinction law on the mean spectral distribution, the extinction in the UV is predicted to be much greater than in soft X-rays, contradicting observations.

They performed principle component analysis and find that the spectral energy distribution of Seyfert 1s can be well accounted for by one underlying variable, whereas that of Seyfert 2s requires at least three. They interpreted this to mean that the main process in Seyfert 1s is the release of gravitational potential energy as mass accretes on to a supermassive black hole, whilst Seyfert 2s have two processes in addition to this, stellar and interstellar radiation (mostly emission from dust). This scenario fits well with previous findings that the circumnuclear regions of the host galaxy contribute more in Seyfert 2s. They found the variance in luminosity related to stellar/interstellar processes accounts for no more than 13% in Seyfert 1 SEDs, but can account for up to 46% in Seyfert 2 SEDs.

1.4.2 X-ray continuum properties of Seyferts

X-ray emission accounts for about 10% of the bolometric luminosity of most AGN. X-ray observations[11] show rapid variability, which makes them probes of the very innermost parts of the AGN engine. Most of the X-ray emission is from the unresolved nucleus, although some Seyfert galaxies also have extended soft X-ray emission. Variability of X-ray emission has been measured to be on time scales as small as 1 hour. Over longer time-scales of days, the X-ray variations are correlated with UV-optical variations, although it has not been determined whether they are simultaneous or not, *i.e.* originating from the same region.

The origin of the nuclear X-ray emission is still under much debate. Inverse-Compton scattering of lower energy photons by higher energy electrons is invoked in many models to produce the X-rays. In this process, UV-optical continuum from the central source is up-scattered in energy (Comptonized) by inverse-Compton scattering by hot, possibly relativistic electrons in a corona around the disk. The link between the channelling of the energy from accretion disk to the corona is not clear. One model that produces many of the features observed in X-ray spectra is a cold thick slab of gas illuminated from above with an X-ray power-law spectrum (Peterson 1997 [181]).

The average 1-500 keV spectrum of Seyfert 1s is given by Gondek *et al.* (1996) [82] and Zdziarski (1995) [273] as fitting to a power-law X-ray continuum with spectral index $\alpha \approx 0.9$, continuously absorbed by a partially ionized gas with a Compton reflection component and a cut-off in the power-law at a few hundred keV. They find this spectrum is consistent with emission from an optically thin relativistic thermal plasma in a disc corona, *i.e.* that is found above an accretion disk. Seyfert 2's however, show strong neutral absorption.

There are two distinct types of X-ray absorption/emission in Seyferts 2s, 'Compton-thick' where the direct emission is totally absorbed and so the X-ray luminosity is therefore at least one or two magnitudes larger than that inferred from the observed flux *e.g.* NGC 7674 (Malaguti *et al.* 1998 [143]) and 'Compton-thin', where some of the X-ray flux is observed directly.

Bassani *et al.* (1999) [23] represent X-ray and $[O_{III}]$ data for a large sample of Seyfert 2s on a diagram of K_α iron line equivalent width as a function of both the column density and the 2-10 keV flux. This shows that the hard X-ray properties of Seyfert 2s depend on a single parameter, the absorbing column density along the line of sight, and reveals

[11]The terminology used in X-ray studies usually classes soft X-ray as having energies of about 0.1-2 keV, hard X-rays 2-100 keV and over 100 keV are denoted γ rays, but these divisions are merely standard notation based on techniques of detection, and do not refer to the physical generation processes.

a large population of heavily obscured objects. The mean column density is $N_h = 10^{23.5}$ cm^{-2} with 23 - 30% of sources having $N_h > 10^{24}$ cm^{-2}.

Modelling of the iron K_α line by Weaver & Reynolds (1998) [255] in four Seyfert 1.9 and 2 galaxies is consistent with two viable models to produce the observed emission line profiles. The first is emission from a nearly face-on accretion disk (Turner *et al.* 1997 [237]) which is inconsistent with standard schemes, and the second model is superposition of emission from an accretion disk at intermediate inclination with a distinct unresolved feature some distance from the nucleus, *i.e.* the active nucleus is intersected and blocked by the outer edges of the obscuring torus. The latter is consistent with unified schemes and does not imply that Seyfert 2s are preferentially viewed with their inner regions face-on.

For Seyfert 1s and 2s which have been matched in FIR luminosity, the Seyfert 1s are on average 5 times more luminous in hard X-rays than Seyfert 2s (Dultzin-Hacyan & Ruano 1996 [63]. This could be due to some sort of beaming effect enhancing the hard-X-ray flux in Seyfert 1s, extra absorption of hard X-rays in Seyfert 2s, or an enhanced FIR luminosity in Seyfert 2s due to more starburst activity, or that Seyfert 1s are intrinsically more luminous at the highest energies.

A study by Alonso-Herrero *et al.* (1997) [6] compared the hard X-ray and IR properties of Seyfert 2 galaxies with those of Seyfert 1 galaxies. They assume that the hard-X-rays are good indicators of intrinsic nuclear luminosities and not dependent on orientation, and that part of the infra-red is produced by hot dust in the inner regions of a torus and as such is inclination dependent. They found that the correlations between $[O_{III}]$ and L-band, and between hard X-rays and L-band are lower in some Seyfert 2s than in Seyfert 1s, implying that part of the infra-red L-band emission is obscured. The correlation between L-band and hard X-ray emission for Seyfert 1s previously has been both found and disputed, but in this study is confirmed, implying a common (hot dust) origin for most of the L-band continuum. The lack of a similar correlation for Seyfert 2s can be explained if the near-IR emission comes from the inner walls of the postulated torus so is inclination dependent.

Smith & Done (1996) [216] analyse the hard X-ray spectra of 36 Seyfert 2 galaxies. They find that their mean intrinsic spectrum (with a power law of index $\alpha \sim 1$) and dispersion is similar to that of Seyfert 1s, supporting orientation unified schemes for Seyferts.

Colbert *et al.* (1997) [46] find soft X-ray nebulae in the kiloparsec-scale extending along the minor axis of three out of eight edge-on Seyfert galaxies. Since this X-ray emission is approximately co-spatial with the large-scale radio emission, it is likely they are both produced by large-scale galactic outflows.

The distribution of the galactic axial ratios of sample of soft X-ray selected low redshift Seyfert galaxies (Simcoe *et al.* 1995, 1997 [211] [212]) shows a clear bias against edge-on spirals, in spite of recovering some of the objects missed in UV and optical surveys, indicating the existence of a thick layer of obscuring matter in the host galaxy planes.

1.4.3 Optical and UV continuum properties of Seyferts

The main feature of the continuum UV-optical spectra is the 'big blue bump', apparently thermal emission in the range T = 10^4 to 10^6 K, depending on whether it is from an optically thin or optically thick region. The idea that this may be from an accretion disk surrounding the central black hole would fit in well with the standard model of AGN structure, but whether or not the shape of this bump can be consistent with this idea is still unclear. The mechanism of continuum radiation from an accretion disk is discussed in section 1.4.6.

The UV and optical continua vary in time together, and the spectral index tends to decrease as the emission brightens, *i.e.* the variations are larger at shorter wavelengths, even after accounting for dilution of the spectrum by starlight from the host galaxy. The UV region demonstrates additional small (*i.e.* a few percent) variations that are smoothed out at the optical wavelengths. The main optical-UV variations are irregular and seem to be small-scale of a maximum of a few percent on time scales of a day, and large-scale of tens of percent on longer time scales of several days though noise on the small-scale variations can make them difficult to determine. A recent study on optical microvariability (between 30 seconds and 6 minutes) with a precision of $< 1\%$ found no clear detection in any of the 22 Seyfert 1s observed (Petrucci 1999 [183]). This puts upper limits on the optical flux from the variable synchrotron component linked to the rapidly variable X-ray emission, showing that significant optical synchrotron emission must be very low, although such a component is not completely ruled out.

This observed simultaneity of the UV and optical continua requires that the different parts of the disk that provide the energy at these wavelengths must be causally coupled on a time scale such that information propagates though the disk at speeds greater than 0.1c. This is not reconcilable with viscous accretion disk models, which predict propagation at only the speed of sound, *e.g.* NGC 5548 Krolik *et al.* (1991) [130], and NGC 4151 Perola & Piro (1994) [180]. The viscous accretion disk model has radiation of specific wavelength coming from regions of different radius and specific temperature, therefore if there are changes in the local emitting conditions such as a change in accretion rate, then the different continuum bands would not be expected to vary simultaneously.

An alternative to the optically thick clouds source of the UV-optical spectrum is optically thin clouds *i.e.* free-free or bremsstrahlung radiation. However, Collin-Souffrin *et al.* (1995) [50] investigated this and found it fails to fit the spectral features; they find the best model for Seyfert optical to X-ray spectra is a geometrically thick distribution of optically moderately thick clouds around the accretion disk system.

The featureless continuum (FC) that is often detected in Seyfert 2s is attributed by Gonzalez *et al.* (1998) [85] to be from ultra-violet light from nuclear starbursts. The existence of the starburst is indicated by the signature of characteristic absorption lines of bright young O and B stars, and blueshifted interstellar absorption lines indicate outflowing gas presumably driven by the starburst. The UV absorption features in Seyferts always appear slightly blue-shifted relative to the broad emission lines, indicating that the absorbing gas is flowing outwards and may be from a nuclear starburst if present, and may be a counterpart to the broad absorption lines (BALs) seen in some quasars.

Storchi-Bergmann, Fernandes & Schmitt (1998) [222] look at 20 Seyfert 2 galaxies and find that the stellar populations are varied and in general are not well represented by and elliptical galaxy template. The central kiloparsec of most of these Seyfert 2s have significantly more 100 Myr stars than normal spirals of the same Hubble type or elliptical galaxies. Thus, a secondary featureless continuum component (FC2) is required. They also noted that if there is a causal link between star formation and nuclear activity, then the 100 Myr star-formation time scale should be comparable to the duration of the nuclear activity cycle. As 100 Myr is approximately 1% of the Hubble time, this implies 1% of galaxies should be active, consistent with evidence so far.

1.4.4 Infra-red continuum properties of Seyferts

Active galaxies emit a large part of their luminosity at infra-red wavelengths. The standard model of the central radiation-emitting engine surrounded by clouds or a torus of dust implies that the short wavelength ultra-violet and X-ray central radiation will heat the dust which will then re-radiate the energy at longer infra-red wavelengths. The dust structure is patchy, so the infra-red radiation observed may be a mixture of re-processed radiation and infra-red radiation coming directly from the central engine. Dust also surrounds the broad-line-emitting gas clouds of the nucleus so these dust structures are on at least the parsec scale. Further out, infra-red emission is also found to 1 kpc in all Seyfert 2s and many Seyfert 1s (Edelson 1987 [67]) and in NGC 4051, weak FIR emission is found to be even more extended (Smith *et al.* 1983 [217]), which is presumably due to dust heating from extended star-forming regions.

A study of the IRAS colours of samples of Seyfert 1 and 2 galaxies by Bonatto (1997) [34] shows no difference between the two classes, and that they have approximately the same number distribution for a given far infrared luminosity. Gu *et al.* (1997) [93] find that the far infra-red characteristics and H_α luminosities of infra-red selected Seyfert galaxies are similar to those of starburst galaxies, concluding that most of the FIR emission from Seyfert 2s is due to nuclear/circumnuclear starburst activity rather than non-thermal nuclear activity.

There is some controversy over the exact mechanism of the IR continuum. In lower luminosity objects, particularly Seyfert 2s, the IR emission is clearly of a thermal origin showing a blackbody spectrum, presumably from dust as detailed above. In other radio quiet galaxies Seyfert 1s and QSO however, the spectrum is not so clear. Previously, it was assumed to be primarily an extension of the power law nuclear spectrum, however more recently, evidence that it has a thermal origin is persuasive. The general AGN feature of the 1 μm minimum with the IR bump longwards of 1 μm implies the emission is thermal, since the required temperatures for this bump are in the range of < 2000 K for heated dust in the nucleus, and since dust would sublimate at temperatures ≈ 2000 K, this cut-off temperature would be a general feature of AGN spectra if dust is a general feature. Recent work by Garcia *et al.* (1998) [79] show that the far IR SEDs of the CfA Seyfert sample can be modelled by solely thermal emission from two or three different components, all due to dust at different temperatures: warm dust at T $\approx$ 150 K heated by AGN or circumnuclear starbursts, cold dust at T $\approx$ 40-50 K heated by star-forming regions in the galaxy disk and very cold dust at T $\approx$ 10-20 K in the general interstellar radiation field.

The IR continuum shows the similar variations as the UV-optical continuum but with a significant time delay, which is interpreted as a light travel time effect; the UV-optical emitting region must be from a smaller region much closer to the centre than the IR emitting region. The IR variations are due to variations in the UV-optical continuum that heats the dust clouds, and are consistent with the IR emission coming from dust some distance away from the centre.

A large fraction of the near IR continuum in Seyfert 1s however, also appears to be stellar but associated with very old starburst activity in the galaxy bulge (Oliva *et al.* 1995 [171]). IR observations by Oliva *et al.* in the same study show that the equivalent widths of the $Br(\gamma)$ and the IR H-band light-to-mass ratios in Seyfert 2s are consistent with the presence of starbursts which are older than those found in H_{II} galaxies. This lends support to evolutionary models where Seyfert activity is being fuelled by a black hole which itself was formed form the remnants of a previous starburst.

Hill *et al.* (1998) [105] use near-infrared spectroscopy to investigate galaxies whose optical

emission ratios are ambiguously placed between starburst and Seyfert. They find the infrared emission line ratios are also in-between, and that the CO absorption (from late-type stars) is weaker than typical starburst galaxies, and concluded this is due to dilution by the AGN flux, lending further evidence that these galaxies are composites.

A near-IR imaging study of 12 Seyferts by Alonso-Herrero *et al.* (1998) [5] shows the colours are consistent with a mixture of emissions from an old stellar population and unreddened hot dust, but can also be reproduced by unreddened starlight and hot reddened dust. If the hot dust is located in the inner part of the dusty torus as in the standard unification scheme, the dust emission should be substantially reddened. The circumnuclear colours are mostly similar to those of normal spiral galaxies, except some have extended emission at L'-band, presumably due to hot dust, probably heated by young stars.

1.4.5 Radio continuum properties of Seyferts

Seyferts generally have compact (sub-kiloparsec) radio continuum emission from a central radio core. The range of radio sizes (measured out to 10% of the central peak intensity at 20cm) of a distance-limited sample of 57 Seyferts was measured by Ulvestad & Wilson (1989) [245] to be point-like, or resolved from 100 to 3500 pc. Similar sizes from VLA measurements of narrow-lined Seyfert 1 galaxies were also found (Ulvestad 1995 [244]). Many Seyferts also have extended radio emission, either with a linear structure, or more diffuse and bubble-like with correlations with the far-IR emission, and this diffuse radio emission has been suggested to be a manifestation of a circumnuclear starburst by Baum *et al.* (1993) [24].

Giuricin, Fadda & Mezzetti (1996) [81] analysed relations between radio core emission and nuclear and host galaxy properties from high resolution (< 0.1") radio observations. They found that Seyfert nuclei in early-type galaxies are characterised by stronger radio core emission of approximately a factor two higher than normally found in Seyferts, perhaps reflecting the strong association of radio loud systems with early-type galaxies. They also found that Seyfert 2 types host more powerful (approximately 1.5 times greater) compact radio cores than types 1, and that the presence of a close companion appears to be associated with enhanced radio core-emission pointing to interaction activity. There was also a correlation between radio core emission and hard X-ray, mid-IR and narrow-line ($[O_{III}]\lambda 5007, H_\beta$) emission (which are signatures of AGN), implying that AGN are more likely to be powering Seyferts than radio supernovae.

Tsvetanov *et al.* (1998) [235] however, did not find that Seyfert 2s were significantly more

powerful than Seyfert 1s (from a sample of 50), but they did note that the most powerful Seyfert radio sources were Seyfert 2s, and that the radio sources on average had larger linear sizes in Seyfert 2s.

Sub-kpc resolution observations by Harrison *et al.* (1986) [98] and Kukula *et al.* (1993) [132] have revealed linear jet-like emission from the nuclei of a few Seyferts, outflows powered by the nucleus, in a lower power analogy to the much stronger jets from more powerful quasars and radio galaxies. Similarly high resolution images of two other Seyferts by Ulvestad *et al.* (1998) [243] with 0.1 pc resolution also reveal that in addition to the double-sided radio structures seen on scales of tens of parsecs, there seem to be one-sided jets of synchrotron radiation less than 1 parsec in length. Repeat observations suggest the jets are well below relativistic speeds, so they are not direct analogues of the relativistic one-sided beamed jets seen in some radio-loud AGN. The degree of collimation in these jets, particularly that of Markarian 3, is difficult to reconcile with the mechanism of supernova activity in a nuclear starburst region.

Larger, kpc-scale radio emission is found in starburst galaxies from the galactic outflow due to the starburst and supernovae generally with a diffuse spherical halo morphology (Colbert 1997 [46]). Since Seyferts can have strong starburst activity in the central regions of their host galaxy, then even if there is AGN-powered jet radio emission, it may be swamped by emission from the starburst galactic wind, hence difficult to determine whether extended radio emission along the minor axis of the galaxy is powered by the Seyfert nucleus or by the host galaxy's starburst superwind. Colbert *et al.* (1996) [48] found that 6 out of their sample of 10 Seyferts showed extended (> 1 kpc) radio structures. With a larger sample of 50 Seyferts, Tsvetanov *et al.* (1998) [235] found 30% to show an extended linear structure and a further 25% to be slightly resolved. Colbert*et al.* (1997) [46] note that the orientations of the linear radio emission are not confined to the galaxy's minor axis, as would be expected for nuclear starburst winds, implying that an AGN powers at least some of the radio structures observed. Many, but not all of the extended radio emission structures are associated with optical line-emission, which could be driven by shocks by either AGN or starburst powered outflows.

The relative orientation of the nuclear radio emission to the host galaxy major axis has been investigated, most recently by Nagar *et al.* (1999a) [165], who find that when account is taken of the deficiency of high inclination Seyfert galaxies in the sample, there is is a uniform distribution of relative angles, *i.e.* the radio jets are randomly orientated with respect to the galaxy disk. There is however, weak evidence that Seyfert nuclei in late-type galaxies may be more likely to have larger angles between the radio emission and host galaxy major axis.

1.4.6 Mechanism of continuum emission

To a first order approximation the broadband spectrum of most AGN, including Seyferts, can be modelled by a power law, $F_\nu = C\nu^\alpha$, where F_ν is the specific flux (per unit frequency interval, usually in units of ergs s^{-1} cm^{-2} Hz^{-1}), C is a constant and α the power-law index is between 0 and 1. In the high power AGN, apart from the infra-red region, the spectrum is assumed to be synchrotron on the basis of the similarity of the spectrum shape to known synchrotron sources such as SNR and the high energy relativistic conditions suitable for synchrotron emission. Given an initial power law distribution of energies, relativistic electrons in a magnetic field can produce a synchrotron power law over many decades of power, and all the way from radio up to X-rays via the synchrotron self Compton (SSC) mechanism (described in section 2.4).

The power law spectrum is only the first approximation; there are many broad bumps and depressions. The 'big blue bump' in the optical-UV region is significant, with a 'small blue bump' superposed on this, shortwards of 4000 Å, possibly all the way to soft X-rays. Its shape suggests a thermal origin, either optically thick blackbody radiation or less likely optically thin free-free emission. The infra-red bump is longwards of 1 μm, which is a minimum between the hot thermal blue bump, and the cool thermal spectrum from a population of warm ($T < 2000$ K) dust grains. There is also a sub-mm break, where the spectral energy distribution decreases rapidly at low energies.

The distinction between whether the primary radiation and secondary reradiated emission is thermal (*i.e.* due to particles which have attained a Maxwellian distribution by collisions) or non-thermal is important because thermal radiation is isotropically radiated, hence the observed flux and distance can be used to calculate the luminosity, whereas non-thermal synchrotron radiation can be highly directed in relativistic beaming and may swamp any underlying thermal radiation of a much larger energy. However in the optical regime, synchrotron emission occurs mainly in the higher power AGN rather than in Seyferts.

For the UV-optical spectrum, the big blue bump is assumed to be primarily from emission from the accretion disk. The first approximation for modelling an accretion disk spectrum is that locally it radiates like a blackbody:

$$B_\nu = \frac{2h\upsilon^3}{c^2} \frac{1}{e^{\frac{h\upsilon}{kT(r)}} - 1} \tag{1.4}$$

where B_ν is the monochromatic specific intensity at frequency ν, and $T(r)$ is the disk temperature at radius r from the centre. Assuming a geometrically thin and optically thick disk with radial symmetry and rewriting the specific luminosity of a ring, then integrating over the extent of the disk gives the disk luminosity. When there is a wide

range of temperatures in the disk, the luminosity can be approximated to be proportional to $\nu^{1/3}$. This model predicts that the UV radiation arises in significantly different parts of the disk than the optical radiation. When a mass of 10^8 $M_\odot$ is taken for the black hole accreting at the Eddington rate, the accretion disk equations show that the peak contribution to the 1500 Å radiation arises at r = $50R_s$, about 0.6 light days from the centre, and the peak contribution to the 5000 Å radiation is located at r = $240R_s$ about 2.8 light days.

Observations of the UV-optical continuum however do not seem to fit so well with the accretion disk characteristics. After correcting for the emission lines including the small blue bump, and starlight contributions, the resultant observed spectra give power-law fits of $F_\nu \propto \nu^{-0.3}$ *i.e.* the energy per unit frequency is decreasing with frequency rather than increasing like $\nu^{1/3}$ as predicted by the thin accretion-disk model. To get over this Malkan (1989) [144] showed that the combination of a cool thermal contribution peaking in the IR, plus an accretion disk spectrum can model the observed spectra over the IR and optical-UV regions. A strong prediction of the accretion disk in QSOs is that there is significant polarization due to electron scattering just longward of the Lyman edge, because of the wavelength dependence of the hydrogen absorption opacity. However, very few show a Lyman edge and none show an increase in polarization longwards of this edge, even in the recent search by Koratkar *et al.* (1998) [126], indicating that simple plane-parallel atmospheres with scattering-dominated opacity are not significant sources of UV flux in quasars.

More complex models of the accretion-disk radiation where rotational, relativistic and inclination effects are considered have been developed *e.g.* Sun & Malkan (1989) [224], Laor & Netzer (1989) [134], Laor, Netzer & Piran (1990) [135]. These make other significant predictions; the continuum should be polarized due to relativistic effects depending upon the inclination of the disk, there should be a Lyman edge in models with temperature gradients because the opacity changes drastically at the Lyman edge. Neither prediction has been well-demonstrated by current observations; blazars are the only AGN class that consistently have high polarization, and Lyman edges are evidently not a general feature although some mechanisms that might be masking this feature have been proposed.

1.5 Limitations of the orientational unified schemes: Host galaxy environments

A major question for AGN is how enough matter is funnelled by gravitational accretion into the active nucleus to provide the observed large amounts of radiation. To allow matter to fall into the nucleus requires significant angular momentum to be removed by breaking the azimuthal symmetry, and one obvious way of doing this is by some form of gravitational interaction with another system, hence a number of studies of the environment and neighbours of AGN have been carried out.

Some of these studies appear to have found small, but significant differences between the Seyfert types in terms of the environment of the host galaxy. If these systematic differences are real, then they pose problems for the unified scheme, because the scheme proposes that it is only differences in viewing the immediate nuclear region which determines what type Seyfert is observed, so such differences imply that the unified scheme is not the only factor governing the appearance of Seyferts.

1.5.1 Host galaxy morphology

Morphological surveys of Seyfert galaxies *e.g.* Adams (1977) [1] show that most Seyfert galaxies are spirals, mostly early-type *i.e.* Sa-Sb. Many studies have found that Seyferts and radio-quiet QSOs tend to reside in disk systems, whereas BL Lacs, radio galaxies and radio loud QSOs tend be in elliptical galaxies, with few exceptions of Seyferts in E/S0 galaxies. There is also a strong tendency for the more luminous host galaxies to harbour the more luminous AGNs, however this may be partially due to selection effects, as bright AGN in faint galaxies may prevent the faint surrounding galaxy emission from being detected, and faint nuclei in bright galaxies may also be difficult to detect.

A higher rate of morphological irregularities (attributed to tidal interactions) in well-resolved Seyfert galaxies compared to non-Seyfert galaxies was found by Simkin *et al.* (1980) [213], and has been confirmed by MacKenty (1990) [139] and Maiolino *et al.* (1997) [141]. Over half of Seyfert host galaxies are barred, but evidence that Seyfert nuclei reside preferentially in barred systems is marginal if at all.

The presence of stellar bars in Seyfert 2 galaxies are found (from hard X-ray measurements of Bassani *et al.* 1999 [22]) to be strongly correlated with the gaseous absorbing column density, Maiolino *et al.* (1998) [140]. They find the strongly barred Seyfert 2s to have an average column density two orders of magnitude higher than non-barred Seyfert 2s. As

the occurrence of bars in Seyferts is not higher than in normal galaxies, this implies that the bars are not important for the fuelling of the active nucleus, but there is evidence that bars do drive gas into the central regions of the galaxy, and this may be important for the obscuration of the active nucleus which underlies unification theories.

Enhanced star-formation in the circumnuclear region of Seyfert 2 galaxies compared to normal spiral galaxies suggested by Whittle (1992) [259], is confirmed by Gu (1999) [92] and evidence that Seyfert 2s have more circumnuclear star-formation than Seyfert 1s is provided by Gonzalez-Delgado & Perez (1993) [84] and Maiolino *et al.* (1997) [141]. This is supported by Storchi-Bergmann *et al.* (1998) [222], who conclude from spectral synthesis of a sample of Seyfert 2 galaxies compared with a study of early-type spiral galaxies by Bica (1988) [30] that the main difference between the nuclear stellar population of Seyfert 2s and of that of elliptical or early-type spiral galaxies is the larger contribution of stars of ages up to 100 Myrs in the Seyfert sample, *i.e.* evidence of star-formation. Maiolino *et al.* (1997) [141] investigated the amounts of CO molecular gas in Seyfert 1s, 2s and field galaxies and finds no significant difference after selection effects are taken into account between the classes, and concluded enhanced star formation in Seyferts is not due to increased amounts of molecular gas, but instead, they did find significantly higher rates of irregular morphologies in Seyfert 2s with respect to Seyfert 1s and field galaxies.

This excess star-formation in Seyfert 2s has lead to an alternative or at least complementary scheme to the obscuring torus unified scheme, proposed by Dultzin-Hacyan, (explained in Dultzin-Hacyan *et al.* 1999 [62]), whereby it is the relative contribution of Seyfert radiation from an accretion disk to the radiation from the circumnuclear starburst which determines the Seyfert type, Seyfert 2s having a larger contribution of circumnuclear stellar radiation than Seyfert 1s.

Malkan *et al.* (1998) [145] made a high resolution HST imaging survey of 91 Seyfert 1s, 114 Seyfert 2s and 51 H_{II} galaxies. About 10% of the galaxies showed tidal features, and rates of bars were the same in both Seyfert classes. The one morphological difference between the two Seyfert types was that, even after accounting for redshift, Seyfert 2 galaxies are significantly more likely to show nuclear dust absorption, especially in lanes or irregular patches. The galaxy classifications accordingly show Seyfert 1 nuclei are found preferentially in earlier morphological type galaxies than Seyfert 2s, in agreement with earlier findings. The intrinsic difference in the amount of dust obscuring the nuclear light suggests that, since it is not an orientational effect, it must be that a greater fraction of the sky as seen by a Seyfert 2 nucleus is blocked by obscuration, *i.e.* they have a larger 'dust covering fraction'. This would also explain some of the differences in the observed broadband properties as well as some difficulties with unified schemes. The statistical findings of this study are contrary to the simplest unified scheme for Seyferts. They

therefore postulate an alternative to the standard unification accreting torus model, and call it the Galactic Dust model. This is shown schematically in figure 1.4.

The key difference here is that it is the galactic dust outside the AGN that is producing the extinction to transform a Seyfert 1 to a Seyfert 2, rather than the nuclear dusty torus as proposed in the standard unified schemes. The Galactic dust model can only work if the galactic dust outside the nucleus could produce enough extinction to transform a Seyfert 1 to a Seyfert 2. Malkan *et al.* (1998) finds that the amount of extinction required is possible to achieve with typical values of column density that are measured in Seyferts. There are several important implications with this model, in particular that the orientation of the dust lane has no relation to the intrinsic orientation of the central engine, but in a Seyfert 2, it blocks the direct view of the central continuum, extinguishing scattered photons unless they escape out of the plane of the dust lane. This would explain why some Seyfert 2 nuclei have linear continuum polarizations which are modest - a few percent up to 15%, but always less than predicted by the simple torus plus conical scattering region, which predicts higher typical polarization.

If it is a good model for most Seyfert galaxies, then the obscuration has no relation to the hypothetical thick torus proposed by the unified scheme, and the orientation of the central engine with respect to the line of sight does not determine whether a Seyfert appears as a 1 or a 2. The central engines in Seyfert 1 and 2 nuclei may be intrinsically the same, but the inner regions of their host galaxies are not. If the nucleus is covered by a larger fraction of dust clouds, then they would more often be observed as Seyfert 2s rather than obscured Seyfert 1s. Also, more heavily reddened emission line ratios and different thermal dust emission in the infra red would be expected (*e.g.* Edelson *et al.* 1987 [67]). Galactic interactions might be a mechanism for temporarily increasing the dust covering fraction, which is consistent with there being a higher rate of galaxy interactions in Seyfert 2s than in Seyfert 1s. Malkan *et al.* (1998) also show that whereas Seyfert 1 galaxies tend to show a strong point source, in Seyfert 2 nuclei the non-stellar continuum is not viewed directly *i.e.* consistent with viewing Seyfert 2s through dust.

1.5.2 Evidence for close companions

Statistical studies by Dahari (1984) [53] on 103 Seyferts and MacKenty (1990) [139] on 51 nearby Seyferts have shown that there is an excess of close companions to Seyferts compared to field galaxies (15% of Seyferts compared with 3% of normal galaxies have companions). When broken down into Seyfert 1s and 2s, it is seen that Seyfert 2s are more likely than Seyfert 1s to have a companion. This was confirmed most recently by Dultzin-Hacyan *et al.* (1999) [62], who from studying Digitized Sky Survey (DSS) images

of 132 Seyferts found a significant excess of nearby large (diameter > 10 kpc) companion galaxies within 100 kpc for Seyfert 2s, but not around Seyfert 1s. Two previous studies by Fuentes-Williams and Stocke (1988) [78] and Rafanelli, Violato & Baruffolo (1995) [190] failed to find a clear significant excess of companions, but the most recent and comprehensive study by Dultzin-Hacyan *et al.* (1999) indicates their negative results are due to selection effects, and that the excess for Seyfert 2s is real.

MacKenty (1990) [139] also found non-Seyfert Markarian[12] galaxies to have a similarly elevated rate of close companions. This suggests that interactions are an important mechanism for the existence of gas in the nucleus of the galaxy, perhaps by gravitational perturbations modifying the flow of gas within them or perhaps capture of gas by one from the other, and that the same process of fuelling the nucleus by interstellar gas in starbursts is also important in AGN. Kollatschny and Fricke (1989) [123] found that the companion galaxies of AGN are themselves are more likely to show strong emission lines in their spectra compared to the companions of normal galaxies. However, the presence of a close companion or disrupted morphology is not sufficient or necessary for producing AGNs, and in fact very strongly interacting systems tend not to show AGN. Although radio-quiet AGN are more likely to have a companion, they are unlikely to be found in rich clusters, with only a few exceptions, and in loose clusters they tend to be absent towards the denser centre.

A CCD study of the environment of Seyfert galaxies by De Robertis and Vandalfsen (1998) [56] [57] made a comparison between the companion galaxies of a sample of 33 Seyfert galaxies and a control sample of 45 normal galaxies, concluding that the distributions of separations, angular distributions, magnitude difference and frequency of morphological differences were all found to be similar within the uncertainties. However, they found that the mean environment of Seyfert 1s was different to Seyfert 2s, in the sense that they had a larger covariance amplitude. This is not in accord with the unified model, which says there is no difference in the outer environments between Seyfert 1 and 2s. The triggering of the AGN may be caused by a number of mechanisms which may depend on the luminosity because the environments of radio-loud objects are different to those of Seyferts. They suggest Seyferts might be triggered by minor mergers *i.e.* a merger between a disk galaxy with a small bound satellite galaxy, since this would be consistent with the results. Taniguchi (1999) [225] goes as far as to propose that all AGN result from mergers, high luminosity quasars from major mergers, and lower luminosity Seyferts from minor mergers.

In conclusion, the difference in prevalence of close companions between Seyfert 1s and

[12]The Markarian survey selected UV-excess galaxies, *i.e.* mostly starburst and Seyfert galaxies.

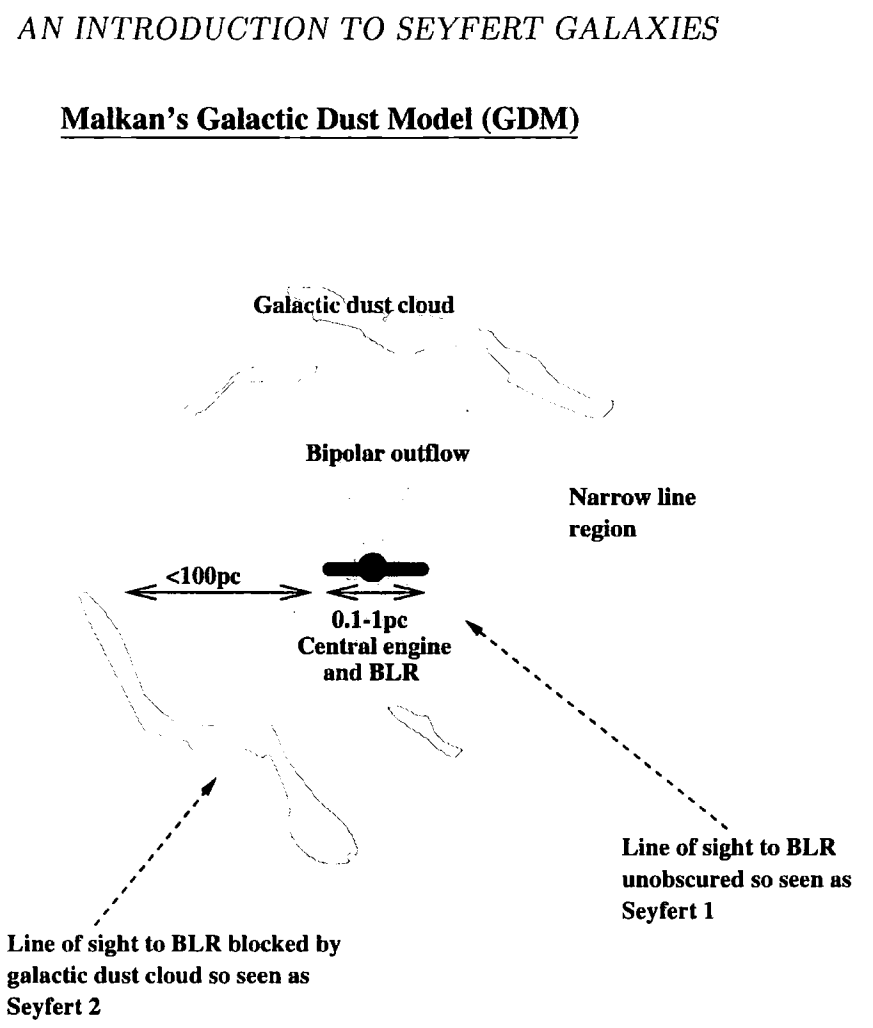

Figure 1.4: A schematic diagram of the galactic dust model of Malkan *et al.* (1998)

Seyfert 2s, and the morphological differences between Seyfert 1s to Seyfert are not something which can be explained purely by orientation effects in a unified scheme. An additional scheme is indicated whereby the interaction with a close companion drives an increase in circumnuclear star formation, which then obscures the AGN's broad-line region, thus increasing the contribution of the circumnuclear stellar radiation to the observed flux in relation to the AGN radiation from the accretion disk system, and creating a Seyfert 2 appearance.

1.5.3 Galactic outflows

The observed emission from ionized gas out of the plane up to tens of kiloparsecs can be explained by a galactic outflow from the nucleus of a starburst galaxy. A recent review of starburst galaxies is given by Heckman, Lehnert & Armus (1993) [102]. The connection between the high nuclear star formation rates in starburst galaxies and the formation of

a galactic super-wind was first investigated in detail by Chevalier & Clegg (1985) [44]. Supernovae heat up the gas in the starburst region, causing it to expand due to higher pressure, out into the ambient ISM. It expands along the steepest pressure gradient, which will be along the rotation axis (the minor axis), as a wind into the disk and halo. This hot wind sweeps up dense ambient interstellar gas in the halo causing shock heating to produce the observed optical line filaments. The material is swept up and accumulates behind the shock front of the wind, forming a large shell along the minor axis. Line emission from this may be from the front or the back surface, giving two different velocity components, so the profiles of the emission lines are double peaked along the minor axis. There may be synchrotron radio emission from relativistic electrons in the shocks and soft X-rays from the hot expanding gas and hard-X-rays from the internal shocks in the hot superwind fluid. Terlevich & Melnick (1987) [226] attributed the extended radio emission of Seyfert galaxies to this mechanism.

Colbert *et al.* (1996a) [49] has listed 12 edge-on Seyfert galaxies with evidence for minor-axis galactic outflows, consisting of double peaked emission lines and optical filaments. They calculate that approximately a quarter of Seyfert galaxies should have good evidence for such outflows. In radio emission, Colbert *et al.* (1996b) [48] out of 10 edge-on Seyfert and 4 starburst galaxies, six of the Seyferts showed radio structures consistent with large scale-outflows.

Pogge (1996) [186] searched in HST emission-line observations and radio maps of Seyferts for evidence of shock-like morphologies resembling bipolar out-flows and supernovae remnants. He found Mkn 3 to show a jet shock, and Mkn 573 to have an optical bowshock (where a nuclear outflow impinges on the surrounding ISM) and both of these Markarian galaxies have been subsequently imaged by the Durham polarimeter with the results presented here in chapters 5 and 6. Pogge concluded that there are shocks in at least some Seyferts, but how important their rôle is in determining the energetic properties of the Seyfert/host galaxy interaction requires further study. In the starburst spiral galaxy NGC 660, Alton (1996) [7] finds evidence of bipolar minor axis scattering in optical polarization maps, supporting the putative outflow. Similar evidence in polarized light is searched for in spiral galaxies with Seyfert nuclei in this thesis.

There are some observations of small scale extended dust in Seyferts, *e.g.* in NGC 1068. Rouan *et al.* (1998) [195] finds high resolution infra-red observations of NGC 1068 to imply warm dust within and around the torus, and also a compact spiral structure interpreted as originating from warm dust in the shaded part of the NLR or in stellar photospheres.

1.6 Summary

Seyferts have been introduced as a class of radio-quiet AGN, characterised as having strong high ionization narrow-line emission region, infra-red, UV and X-ray continuum excesses, and are powered by a central supermassive black hole and accretion disk system. They can be subdivided into type 1 Seyferts which also show an extremely broad-line emission region, and type 2 Seyferts which do not. In addition to this compact nuclear emission, extended radio and emission-line regions are detected in many Seyferts, and in some cases also extended X-ray emission. Where these extended regions are collimated forming an ionization cone, they may be due to either jet-like AGN activity, or a galactic superwind driven by starburst activity. Detailed reviews of active galactic nuclei are given by Osterbrock in 'Reports of Progress in Physics' (1991) [175], by Peterson in 'An introduction to active galactic nuclei' published in 1997 [181] and by Gregory Shields 'A brief history of AGN' (1999) [210].

The standard unified scheme that explains the two Seyfert types, proposes that there is an optically thick dusty torus around the nucleus, such that when viewed edge-on the BLR is obscured, resulting in Seyfert 2 characteristics, but viewed face-on the BLR is seen directly and results in Seyfert 1 characteristics. Although it has not been possible to observe a dusty torus directly, there are a good number of observations which support this scheme; for example, the greater amount of dust inferred for Seyfert 2s, the observation in some Seyfert 2s of a BLR seen in polarized light (due to scattered light from the nucleus through the torus), and emission-line ionization cones tracing out outflow from the nucleus.

Apparent differences in the environments of Seyfert 1s and 2s have also been found however, which are not consistent with the basic unified scheme. The main question seems to be exactly what rôles the dust in the host galaxy (circumnuclear dust as well as dust in the galaxy disk) and the emission from nuclear starbursts/circumnuclear star formation (which have been detected in a number of Seyferts), play in determining the Seyfert characteristics. Much investigation is therefore currently being carried out on the host galaxy - Seyfert connection, and one technique of study is polarimetry, which is the technique of observation investigated in this thesis. The theory and importance of polarization of light in Seyferts and other AGN is introduced in chapter 2, previous polarimetric observations of Seyfert galaxies are described in chapter 3, and the results of the polarimetry observations, discussion and conclusions are presented in the following chapters.

Chapter 2

Optical polarization

2.1 Introduction

This chapter briefly describes the theory of the polarization of light, introduces the description of polarization using Stokes parameters and discusses the mechanisms of the production of polarized light in astronomical sources. There are two main phenomena which have been proposed to produce the observed optical polarization in Seyfert nuclei and galaxies in general, these are: polarization from dust (scattering and extinction), and polarization from electrons (electron scattering, the inverse Compton effect and synchrotron radiation).

2.2 The theory of polarization of light

Light, as electromagnetic radiation, may be represented as mutually perpendicular electric and magnetic fields, oscillating perpendicular to the direction of propagation. For a plane monochromatic wave with angular frequency ω, wave number k, propagating in the z direction in a non-absorbing medium, the electric field E, at time t, can be represented by two orthogonal components:

$$E(z,t) = \hat{\mathbf{i}} E_x \cos(kz - \omega t + \epsilon_x) + \hat{\mathbf{j}} E_y \sin(kz - \omega t + \epsilon_y) \tag{2.1}$$

where E_x and E_y are the amplitudes of two (x, y) components, ϵ_x is the phase term of the x-component, and ϵ_y is the phase term of the y-component. The phase difference between the x and y components, ϵ, is given by the difference in their phase terms, $\epsilon = \epsilon_y - \epsilon_x$.

For 'natural' or 'unpolarized' light, over any appreciable length of time, the plane of the oscillations of the electric field will be random, *i.e.* continually randomly changing on time scales of the order of 10^{-8} seconds. If there is a preferred plane of oscillation for the electric field (or equivalently the magnetic field) then the light is said to be polarized. This preferred plane of oscillation is the plane of polarization. In the optical regime the electric vector (E-vector) is conventionally used to describe the direction of the polarization[1].

Three types of polarization of light are customarily distinguished by name, linear, circular and elliptical, although light of any polarization can be considered to be a manifestation of partially elliptically polarized radiation. Linear polarization of light is where the electric vector has a constant orientation, with a fixed amplitude of $\hat{\imath}E_x + \hat{\jmath}E_y$, this occurs when the phase difference $\epsilon = 0$. Circular polarization is where the electric vector is rotating with time at the frequency of the radiation[2] and the amplitudes of the E_x and E_y are equal, this occurs when the phase difference $\epsilon = -\frac{\pi}{2}$. Elliptical polarization is a combination of linear and circular polarization *i.e.* when the phase difference is not a multiple of $\frac{\pi}{2}$, so the electric vector traces out an ellipse in the wave plane, perpendicular to the direction of propagation z. The polarization may be total or partial, which is quantified by the degree of polarization, usually expressed as a percentage.

The polarization state of such a wave can be described completely by four time-averaged intensity parameters, known as the Stokes parameters, I, Q, U and V:

$$I = E_x^2 + E_y^2 \tag{2.2}$$

$$Q = E_x^2 - E_y^2 \tag{2.3}$$

$$U = 2E_xE_y \cos\epsilon \tag{2.4}$$

$$V = 2E_xE_y \sin\epsilon \tag{2.5}$$

where $\epsilon = \epsilon_y - \epsilon_x$, the phase difference between E_x and E_y. When multiplied by the constant $\frac{1}{2}c\epsilon_o$ (c = speed of light, ϵ_o = permittivity), these parameters have the dimensions of energy flow per unit area appropriate to the corresponding intensities (intensity = $\frac{1}{2}\epsilon_o cE^2$).

The Stokes parameter I corresponds to the total intensity of the light (*i.e.* $I = I_u + I_p$, the sum of the polarized intensity I_p and unpolarized intensity I_u), Q and U describe

[1] In radio studies however, it is conventional to use the magnetic vector (B-vector) to describe the direction of polarization

[2] If the E-vector rotates clockwise as seen as it travels towards the observer, it is termed right-handed circular polarization, anti-clockwise is left-handed.

the linear polarization giving the direction of polarization and V describes the sense of circular/elliptical polarization and the degree of ellipticity. In practice, U is usually taken to be the linearly polarized component at 45° to Q, and V to be the right-handed circularly polarized component. For fully polarized light, $I_u = 0$, so the total intensity $I = I_p = (Q^2 + U^2 + V^2)^{\frac{1}{2}}$. For partially polarized light, where $I = I_u + I_p$, the degree of polarization, P, is given by: $P = I_p/I = (Q^2 + U^2 + V^2)^{\frac{1}{2}}/I$.

For partially linearly polarized light (which is the subject of this thesis), the phase difference ϵ is 0, so therefore $V = 0$, hence the degree of (linear) polarization is given by $P_{linear} = (Q^2 + U^2)^{1/2}/I$. The key measurements which are normally quoted, are those of the polarized intensity (PI), the percentage polarization P(%), and the angle of polarization ϕ of the electric vector, which can be given by:

$$PI = \sqrt{Q^2 + U^2} \tag{2.6}$$

$$P(\%) = \frac{PI}{I} \times 100 \tag{2.7}$$

$$\phi = \frac{1}{2}\tan^{-1}\left(\frac{U}{Q}\right) \tag{2.8}$$

where the polarization angle is the orientation of the E-vector to a chosen frame of reference, usually taken to be north in astronomy studies.

The Stokes parameters can normalised (by dividing by the intensity), and when written as a column vector, are known as a Stokes vector, which is more convenient for mathematical manipulation. A more concise representation of polarized light is by Jones vectors, which are written in terms of the electric vector, and in terms of the addition of coherent beams, but these are only applicable to fully polarized light. Mueller matrices are a matrix method of representing the effects of optically active devices (*i.e.* polarizers, converters and depolarizers) for calculations with light beams which are represented by Stokes vectors. An introduction to Stokes vectors and Mueller and Jones matrices is given in Hecht (1987) [100], covered in more detail by Huard (1997) [109], and a rigorous mathematical treatment of polarized light using these methods is given by Bickell and Bailey (1985) [31].

2.3 Polarization by dust

Scattering (the absorption and re-emission of incident electromagnetic energy by a dust grain, gas atom, electron or other scattering centre) creates a polarization state in which

the E-vector of the scattered light is usually perpendicular to the scattering plane[3]. This means that a point source illuminating a nebula will result in a centro-symmetric pattern around the point source. This typically results in polarization levels of 10-20% if single scattering dominates, although levels of up to 70% may be obtained under certain geometries. In practice though, dilution by an unpolarized light source, can reduce the detected levels significantly. Scattering by dust grains is described by Mie scattering, although the special case where the scattering particle size is assumed to be much less than the wavelength of the incident radiation allows a simpler theoretical description, termed Rayleigh scattering.

2.3.1 Rayleigh scattering

The scattering of light by objects small in comparison to the wavelength is known as Rayleigh scattering. The dependence on wavelength of scattering in this case was first quantified by Lord Rayleigh, who showed that the scattered flux density is directly proportional to the fourth power of the frequency of the incident radiation ($I_s \propto \nu^4$). Quantitatively, the percentage polarization P(%) of the scattered radiation can be given as:

$$P(\%) = \frac{1 - \cos^2\theta}{1 + \cos^2\theta} \times 100 \tag{2.9}$$

where θ is the angle measured from the incident direction to the direction of the scattered radiation. Hence, forward scattering is the scattering at small values of θ, and back-scattering is when θ is greater than 90 degrees.

2.3.2 Mie scattering

This rigorous theory of scattering was developed by Mie in 1908 [157]. By solving Maxwell's equations for smooth homogeneous spheres, he developed a more realistic treatment of the scattering where the particle size can range from much less than to close to the wavelength of the radiation. There are two essential parameters, the dimensionless size parameter x, and the refractive index of the scattering medium. The size parameter is defined as:

$$x = \frac{2\pi a}{\lambda} \tag{2.10}$$

where a is the radius of the sphere, and λ is the wavelength of the incident radiation. Given these, Mie theory can be used to calculate the fraction of light scattered through as angle θ, and the polarization of the scattered radiation.

[3]It is possible, in a few cases, that the E-vector can be parallel to the scattering plane, then the polarization is called negative polarization

Monte-Carlo simulations and analytic studies have been performed for Mie scattering in AGN, as discussed by Martin (1985) [66]. Low polarizations ($\approx 1\%$) are produced from thin disc geometries with single scattering, and up to 15% from optically thick dust shells where multiple scattering occurs. More recent work by Wolf & Henning (1999) [265] includes Monte-Carlo simulations of combinations of electron and dust scattering, and multiple scattering in optically thin cone geometries, which are able to reproduce the observed wavelength dependence of linear polarization. Monte-Carlo models by Bianchi *et al.* (1996) [29] of scattering in spiral galaxies with various different inclinations predict polarization levels of no more than a few percent. This polarization is always perpendicular to the major axis, and increases slightly towards the I band, ascribed to a decrease in extinction towards red wavelengths.

2.3.3 Extinction and reddening

Light may be reduced in intensity by both scattering and absorption by gas and dust particles, the sum of these two processes being called extinction. For a given dust population, the extinction is dependent on the wavelength of the light. This selective extinction leads to an apparent reddening of the spectrum for all but the nearest objects, the exact effects depending on the amount and type of dust the light has travelled through. For standardised comparisons of the extinction of sources, the difference in magnitudes of the two sources, one known to be nearby and essentially unreddened, is measured at the mean wavelengths of the standard photometric bands, *i.e.* 4359 Å and 5550 Å for the B (blue) and V (visual) bands respectively. This difference gives a measure of the selective absorption and is termed the standard colour excess, E_{B-V}. Any non-sphericality of the grains does not seem to have much effect on the mean efficiency of extinction, unless there is some degree of alignment which then causes dichroic (preferential) extinction.

2.3.4 Dichroic (preferential) extinction

The polarization of light through dichroic extinction by magnetically aligned non-spherical dust grains is known as the Davis-Greenstein mechanism, (Davis & Greenstein 1951 [55]). This alignment is most widely considered to be by paramagnetic relaxation of thermally rotating grains, in which magnetic fields need only be as high as a few micro-gauss (*i.e.* about the level of the magnetic field in our galaxy) to produce alignment that has significant effects on the extinction of light.

In a region of interstellar space containing dust and gas, each with a Maxwellian distribution of velocities but with different temperatures, an initially stationary dust grain will be set spinning by random collisions from the gas atoms. Assuming elastic collisions, the rotational kinetic energy of the grain associated with the spin around the three principle axes of inertia will be the same and equal to:

$$\tfrac{1}{2}I_x\langle\omega_x^2\rangle \;=\; \tfrac{1}{2}I_y\langle\omega_y^2\rangle \;=\; \tfrac{1}{2}I_z\langle\omega_z^2\rangle \;=\; \tfrac{3}{2}kT \tag{2.11}$$

where I_x is the inertia and ω_x the angular velocity around the x-axis, k is Boltzmann's constant and T is the temperature of the gas. Therefore, if the grain is non-spherical, it will tend to rotate faster about its shortest axis, because the angular momentum will be greatest around the axis of maximum inertia. If a magnetic field B permeates that region of space, the spinning grains will experience a sinusoidally varying magnetic field, which induces an internal magnetisation in all paramagnetic grains. The internal field lags the external field and this slight misalignment causes a dissipative torque about the axis perpendicular to the magnetic field B, which tends to bring the angular momentum into alignment with B. Dust grains in a magnetic field therefore will tend to spin with their longer axis perpendicular to the field, and will scatter more effectively the component of light that is polarized parallel to the longest axis of the dust grains, *i.e.* transmitting more effectively the light polarized perpendicular to the long axis.

Incident light thus becomes polarized in a direction perpendicular to the long axis of the grains, and therefore parallel to the magnetic field in that region, so the polarization of light from a distant object traces out the transverse component of the magnetic foreground field. This is usually around the levels of 2% to 5 %, depending on the extinction in that region. In several spiral galaxies (*e.g.* M104, NGC 4565) polarizations of 2% to 4% have been found running along the dust lanes, parallel to their galactic planes, and attributed to large scale magnetic fields within the galaxies. The polarization in M104 has alternatively been attributed to scattered light by some authors (*e.g.* Jura 1982 [116], Matsumura & Seki 1989 [155]) but although these scattering models can account for the polarization, they predict a different wavelength dependence from that which is observed that fits well the Serkowski law for dichroic extinction as explained in section 2.3.5 following.

The necessary characteristics of dust grains for alignment by this mechanism are that they must be elongated, paramagnetic and dielectric. Interstellar grains are composites of smaller grains, and will show paramagnetic properties only if at least some of the grains contain iron or are superparamagnetic (which is more likely in larger grains). With such alignment of dust grains then, the amount of extinction will be different for the two directions of polarization, and will depend on the direction of the incident radiation. A number of authors have reinvestigated the Davis-Greenstein alignment mechanisms in

more detail, *e.g.* Roberge *et al.* (1993) [193], Lazarian & Draine 1997 [136] and Roberge (1997) [192], in particular for calculating the alignment efficiencies.

2.3.5 Galactic interstellar polarization

Early attempts to map magnetic fields in this Galaxy by linear polarization measurements were made by Hall (1949) [95] and Hiltner (1949) [107], who found evidence for a large scale magnetic field, confined to the plane of the Galaxy. Catalogues by Axon and Ellis (1976) [16] of over 5000 stars showed the polarization increases with distance as would be expected for a large scale uniform magnetic field in the Galaxy. This polarization is called interstellar polarization (ISP), and the degree of polarization is generally not more than about 2%. The highest ISP values are mostly along the galactic equator (l=-15 to l = 15). In many regions there is large scale alignment of the polarization angles, which can be seen in the map of the Galactic polarization given in figure 2.2, a plot of the interstellar polarization of starlight over the Galaxy, from Mathewson & Ford (1970) [150].

In 1975, Serkowski *et al.* [208] measured the linear polarization of 180 galactic stars with wavelengths from 0.45 to 0.8 μm. They found an empirical relationship to describe the linear polarization at a given wavelength, P(λ):

$$\frac{P(\lambda)}{P_{max}} = e^{-K(\ln \frac{\lambda_{max}}{\lambda})^2} \tag{2.12}$$

where λ_{max} is the wavelength at which the maximum linear polarization occurs is on average $\approx$ 5450 Å, but varies for different regions, which is evidence of differences in grain properties between interstellar clouds. and empirically $K = 1.15$. They found that the ratio (R) of total (A_V) to selective interstellar extinction, $R = A_V/E_{B-V}$, depends on λ_{max} and can be approximated as $R = 5.5\lambda_{max}/10,000$ Å where λ_{max} is measured in Ångstroms. Wilking (1982) [261] extended the wavelength range to include UV and infra-red and found that K is wavelength dependent. Whittet *et al.* (1992) [258] further empirically derived the value of K to:

$$K = (0.01 \pm 0.05) + (1.66 \pm 0.09)\lambda_{max} \tag{2.13}$$

where λ_{max} is in μm. This dependence can be interpreted physically as a decrease in the mean grain size. Serkowski found that generally the ISP value could be given as lying in the range between 2 and 9 times the E_{B-V} value. In the V waveband, in practice this interstellar polarization is usually at the level of about 1-3% per magnitude of extinction, with the orientation parallel to the projected field direction, which is along the plane of the Galaxy. Figure 2.3 shows a plot of the wavelength dependence according to Serkowski's equation (2.12).

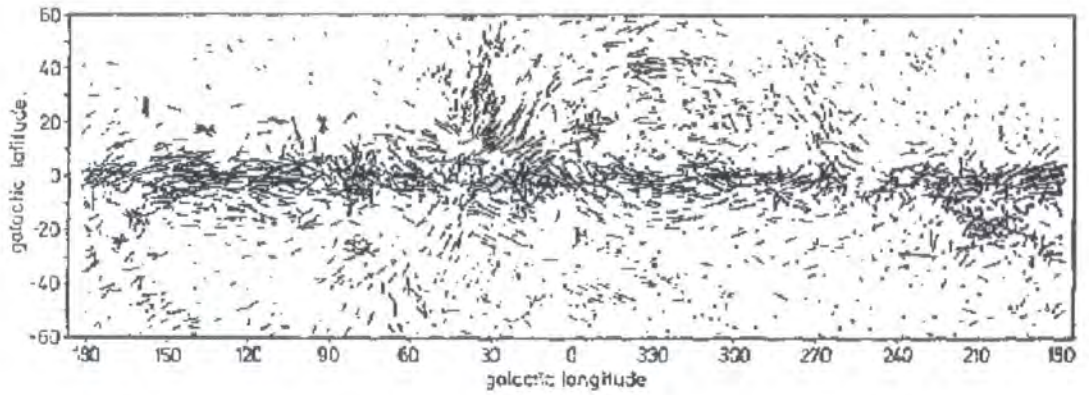

Figure 2.1: Measurements of Galactic interstellar polarization in galactic co-ordinates, from Mathewson & Ford (1970)

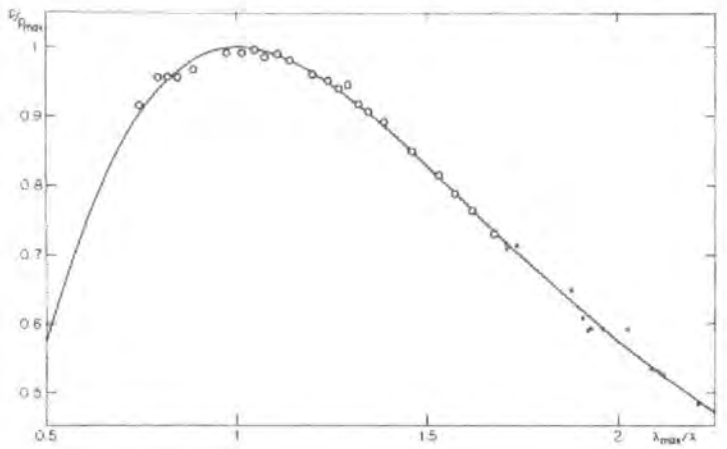

Figure 2.2: Wavelength dependence of the interstellar polarization of starlight, from Serkowski *et al.* (1975)

Interstellar dust

Interstellar dust dominates the heating and cooling of clouds through photoelectric emission and gas-grain collisions, and is dominant source of opacity over the shorter wavelength regions of the electromagnetic spectrum. Molecular hydrogen forms on the dust grain surfaces, and may lock up some elements; if metals are depleted from the gas phase in this manner then the ion-molecule chemistry and the cooling balance of the cloud is affected. Within our own galaxy, dust can be characterised by Galactic reddening, extinction and this depletion of elements from the gas phase.

There is no certain identification of interstellar grain composition, such are the ambiguities of present observations, but reviews of current theories and observations are given by Mathis (1993, 1990) [152] [151] and Draine (1997) [61] . There are two sources of dust; the first is stardust: silicates, graphite and amorphous carbon formed in high-density high-temperature regions in the outflow of late-type giants, planetary nebulae and possibly novae and supernovae. The second is dust formed in the interstellar medium itself; in the dense clouds, icy grain mantles are formed, and in diffuse clouds, complex organic refractory molecules are produced. The icy grain mantles are the accretion of gas-phase molecules (such as H_2O, NH_3, CH_3OH, and CO) on to the cores of stardust and are only found in dense clouds not diffuse ones.

The range of elements or compositions of elements that can successfully model the observations of galactic reddening, extinction and depletion is quite narrow; the best models consist mainly of carbon and astronomical silicate ([Fe,Mg] SiO_3, $[FeMg]_2$ SiO_4). Spectral and polarimetric evidence indicates a significant silicate component, and near-IR reddening suggests carbon is important.

At optical wavelengths, the extinction can be explained by the combined effects of scattering and absorption by grains with sizes from 0.1μm up to as large as 0.2μm, but the observed far-UV extinction also requires a population of smaller particles no more than 0.01μm in size. The wavelength dependence of the polarization suggests that the larger particles ($a > 0.1\mu$m) are non-spherical and fairly well aligned, whereas the smaller ones ($a < 0.05\mu$m) are either spherical or not aligned. There are various Galactic grain models giving good agreement with the reddening extinction law.

Grain models fitting the Galactic extinction curve

Mathis *et al.* (1977) [153] proposed a grain model which fits the extinction, the wavelength-dependence of dust albedo and opacity of dust in the far-IR well for wavelengths from

0.12μm to 1 μm. This consists of a mixture of uncoated silicate and graphite grains with a power law size distribution given by:

$$n(a) = a^{-3.5} \tag{2.14}$$

where a is the particle size and $n(a)$ is the number density of particles that have size a. In this model most of the volume is contributed by the larger particles but most of the surface area by small particles. The size limits on the grains of this model are: $a_{min} = 0.005\mu m$ and $a_{max} = 0.25\mu m$ for the graphite (which contributes 65% of the optical extinction), and $a_{min} = 0.025\mu m$ and $a_{max} = 0.25\mu m$ for the silicate (contributing 35% of the optical extinction).

An alternative model for a graphite-silicate mixture was proposed by Greenberg (1978) [90], which can reproduce the near-IR and as well as the optical Galactic extinction law within the abundance constraints. This model is characterised by the distribution:

$$n(a) \propto e^{-5(\frac{a-a_c}{a_i})^3} \tag{2.15}$$

where a_c is the core size, and a_i is a cut-off parameter beyond which the number of grain with size a falls rapidly.

Mathis & Whiffen (1989) [154] allowed for the possibility that the grains may not be well separated, but may exist in mixed aggregates, *i.e.* elongated grains as indicated by dichroic extinction. They derive a power law of:

$$n(a) \propto a^{-3.7} \tag{2.16}$$

which fits the Galactic extinction law and where $a_{min} = 0.03\mu$m and $a_{max} = 0.9\mu$m are the size limits on the grain aggregates.

In the absence of any other information, it is assumed that the galactic dust grain population can be taken as an approximation for the dust in external galaxies (although there are probably significant variations in the far-UV extinction from different extragalactic sources because different conditions for dust formation may dominate there).

2.4 Polarization from electrons

The main mechanism for optical polarization from electrons in Seyferts is Thomson scattering, where the highly ionized gas around the nucleus provides large numbers of electrons for scattering. Scattering of intrinsic nuclear emission from the accretion disk might be

expected from the electrons in the top layer in the upper layer of the disk, *i.e.* Thomson scattering. The inverse Compton effect is also scattering by electrons, but requires higher energy electrons and produces radiation at X-ray rather then optical wavelengths. Synchrotron radiation, also due to high-energy electrons, is produced by the relativistic motion of electrons in a magnetic field, and is intrinsically highly polarized, but it is not generally observed at optical wavelengths in Seyferts, except in the nuclear jets of a few special cases of radio loud Seyferts (*e.g.* 3C120).

2.4.1 Thomson scattering (lower-energy electron scattering)

The scattering of optical radiation by electrons can be described by Thomson scattering, see *e.g.* Lang (1980) [133]. An electromagnetic wave is incident on a (non-relativistic) electron which will cause the charge to oscillate and re-radiate the incident wave at the same frequency. For a cloud of N_e electrons at a distance r from an illuminating point source, the intensity of the scattered light is given by:

$$I_s = \frac{N_e \sigma_T}{4\pi r^2} I_0 \tag{2.17}$$

where σ_T is the Thomson scattering cross-section ($\sigma_T = \frac{8\pi}{3} r_e^2 = 6.7 \times 10^{-25}$ cm^2, r_e = electron radius), and I_0 is the intensity of the incident light source, and where the scattering is assumed to be isotropic. Assuming the scattered light is fully polarized (which is only strictly true for scattering in a geometry in the plane of the sky), then the polarized intensity (PI) can be estimated by the above equation, since it is the scattered light component, $PI = I_s$. For a resultant polarization to be observed, the geometry needs to be asymmetric (non-spherical) otherwise the polarization will cancel out.

Since values of PI and I_0 can be measured by the polarimeter, and r the distance of the scattering electrons from the central source may be estimated from current models of Seyfert nuclei, then the number of electrons N_e may be estimated using the above equation. Then, if it is assumed that the electrons are distributed along the line-of-sight with the same scale-length as their separation from the illuminating source, the electron density n_e may be estimated. Indeed, there is strong evidence of electron scattering in the narrow-line emission region of Seyfert nuclei, where there appear to be dense electron clouds within a few hundred parsecs of the central illuminating source.

2.4.2 Inverse Compton effect (high-energy electron scattering)

High-energy electrons can scatter synchrotron photons. A beam of relativistic electrons moving through a radiation field will interact with the photons. If the photons and electrons are in thermal equilibrium, the exchange of energy between them will have no net effect. If however, the photon temperature is less than the electron temperature, then there will be a net transfer of energy from the electrons to the photons; the photons then gaining energy. This process is known as the inverse Compton effect and is a major mechanism for the cooling of a relativistic plasma and for the production of high-energy photons, in particular the main source of X-rays in Seyfert nuclei.

2.4.3 Synchrotron radiation

Synchrotron emission, relativistic motion of electrons in a magnetic field, produces intrinsically linearly polarized radiation, and the emission region is highly directional - confined to a narrow cone about the instantaneous particle direction, so that light is seen only as this cone sweeps across the line-of-sight. So, for the radiation to be observed, the angle of the magnetic field to the line-of-sight must be approximately the same as the particle pitch angle. If the pitch angle is small then the power radiated will be small, so significant radiation emission will be observed only where there is a significant component of magnetic field in the plane of the sky. Since when viewed along the plane of the orbit of the electron the radiation is fully linearly polarized, therefore the observed emission must be highly polarized, $\approx$ 70% for an ensemble of electrons (Hughes & Miller 1991 [110]). With the typical luminosities and magnetic field strengths involved in AGN, this usually appears as radio emission.

Some optical synchrotron radiation has been observed, *e.g.* in the jets of M87 and 3C273 and the Crab nebula. This shows intrinsically high levels of polarization (observations often show around 70%), depending on the spectral index of the radiation and short timescale variability. The process of synchrotron radiation is treated in detail by textbooks on plasma physics, but it is not thought to be a significant contributor to the optical emission of Seyfert galaxies, apart from possibly NGC 4151, which may be an exception. In NGC 4151, the flat radio spectrum of the nuclear source is consistent with either synchrotron radiation or with free-free absorption from the inner ionized part of the accretion disk, Ulvestad (1998) *et al.* [241], and optical multi-band measurements of nuclear flare activity imply optical synchrotron radiation from a subparsecond nuclear jet according to Merkulova *et al.* (1999) [156].

Chapter 3

Polarization observations of spirals and Seyferts

3.1 Introduction

This chapter reviews polarization surveys and observations that have been performed on various spiral and Seyfert galaxies previous to this study, including radio and infra-red as well as optical polarimetry and comments on the difficulties in interpretation.

3.2 Polarization studies of spiral galaxies

Studies of the polarization of spiral and other galaxies, at both radio and optical wavelengths, have been used to determine their internal galactic magnetic field configuration and to obtain information and place constraints on the characteristics of the dust populations in different regions of these galaxies. Magnetic fields in galaxies can also be inferred by the presence of Zeeman splitting of the H_I 21 cm line, but in practice this is difficult to measure, so polarization observations are the main source of information. The strong observational evidence of magnetic fields in galaxies is summarised by Wielebinski & Krause in 1993 [260]; they present examples of galaxies where radio and optical polarization vectors indicate the magnetic fields in galaxies. A review of the configuration of the magnetic fields in face-on spiral galaxies is given by Kronberg (1994) [131].

3.2.1 Radio polarization

Radio observations of high polarization due to synchrotron radio emission have long established the presence of magnetic fields in spiral galaxies which are coherent on scale lengths of many kiloparsecs. Virtually every galaxy studied at radio frequencies has been observed to have a magnetic field, either indirectly through the existence of non-thermal radiation or directly from radio polarization measurements giving the field morphology. In face-on spiral galaxies, this radio polarization has been shown to follow the spiral arm pattern, the alignment of polarization vectors tracing out the magnetic field as is clearly shown in the map of NGC 1566, a face-on spiral (which is also observed for this thesis, see chapter 5, section 5.4), from Ehle *et al.* (1996) [71] in figure 3.1, where the polarization vectors are aligned with the magnetic field. In the edge-on spiral, NGC 3628 in figure 3.2 from Dumke *et al.* (1995) [64], the magnetic fields are seen to be generally parallel to the plane of the galaxy.

3.2.2 Optical polarization

In order to help determine which of these mechanisms is contributing to the polarization of an object, it is necessary to have results both over a large wavelength range (because the mechanisms have different wavelength dependencies) and over a large area, in order to show the pattern of polarization vectors clearly (because the mechanisms produce different polarization patterns). For small dust grains the polarized flux from scattering will be small in the infra-red, but for the wavelength-independent processes of electron scattering and synchrotron emission, more polarized flux might be seen in the ultraviolet and IR beyond 1.6 μm where there is less diluting flux from the host galaxy. Each mechanism is described in the following sections, and its relevance to the Seyfert galaxies is discussed.

In some cases the polarization pattern from scattering can be clearly distinguished from polarization pattern expected from dichroic alignment in magnetic fields, but in other cases the polarization patterns are ambiguous and the two main optical polarization mechanisms (scattering and dichroic extinction) may either compete with or complement each other.

Scattering models predict a polarization pattern perpendicular to the major axis in edge-on galaxies and a circular pattern in face-on galaxies. A circular polarization pattern is a clear indication of a scattering mechanism, such as that observed in detail around M82 (Scarrott *et al.* 1991 [198]), whereas a spiral polarization pattern would most likely be caused by dichroic extinction in the galaxy's magnetic field.

In edge-on galaxies with toroidal magnetic field, the two main optical polarization mechanisms produce polarizations perpendicular to each other, hence tending to cancel each another out. In the case of an additional magnetic field along the pole of the torus however, it is uncertain how these mechanisms compare. Radio measurements of M82 have indicated a vertical magnetic field in the galaxy halo, but no evidence of dichroic extinction is observed, as the polarization vectors are clearly seen to follow a circular pattern from scattering, dominating any possible polarization that might otherwise have been seen along the vertical field lines by dichroism in the halo.

3.2.3 Face-on spiral galaxies

Spiral galaxies that are nearly face-on (*i.e.* those with small inclinations) clearly display their spiral arm structure. In such galaxies, the first hint that the polarization pattern of light might be aligned in a spiral pattern following the spiral arm configuration of the galaxy was from optical polarization observations of M31 by Hiltner (1958) [106]. In spite of the problem of distinguishing between the tracing of a circular and a spiral pattern by polarization vectors, a number of galaxies have now been mapped which demonstrate alignment of the optical polarization vectors with the spiral pattern.

This phenomenon is due to dust grain alignment in the spiral magnetic fields of the galaxies causing dichroic extinction resulting in polarization of emerging light along the direction of the magnetic field. Previously published examples include M51 by Scarrott *et al.* (1987) (1991), [202] [200] which is reproduced here in figure 3.3. Scarrott (1996) [199] reviews optical polarization of spiral galaxies due to the internal magnetic fields and shows examples of these optical polarization patterns.

3.2.4 Edge-on spiral galaxies

The spiral structure of galaxies that are nearly edge-on (*i.e.* those with large inclinations) is difficult to discern. Instead, the edge of the disc is seen as a central dust lane bisecting the galaxy where extinction can be high. Scattering-dominated models (Bianchi *et al.* 1996 [29]) show that the polarization due to extinction by scattering would be perpendicular to the major axis in edge-on galaxies, but if there is a spiral magnetic field, then dichroic extinction will produce optical polarization parallel to the magnetic field, expected to be parallel to the dust lane. Models including both scattering and dichroism by Wood (1997) [268] and Wood & Jones (1997) [269] reproduce qualitatively the polarization features observed in edge-on galaxies with large scale toroidal magnetic fields: polarization parallel

Figure 3.1: Radio polarization vectors (at 6cm) overlaid on to an optical DSS intensity image of NGC 1566, a face-on spiral galaxy, by Ehle *et al.* (1996)

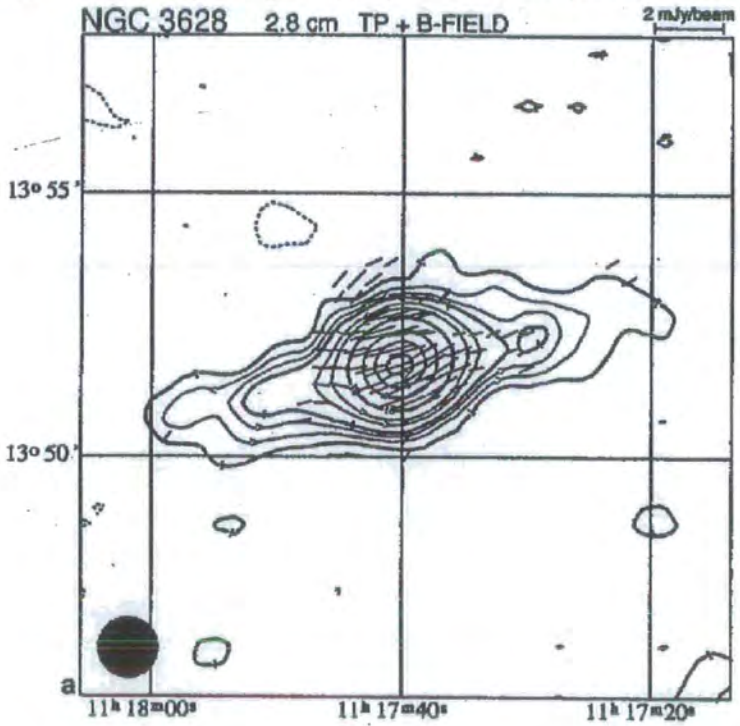

Figure 3.2: Radio polarized vectors overlaid onto a contour map of total intensity of NGC 3628, an edge-on spiral galaxy, by Dumke *et al.* (1995)

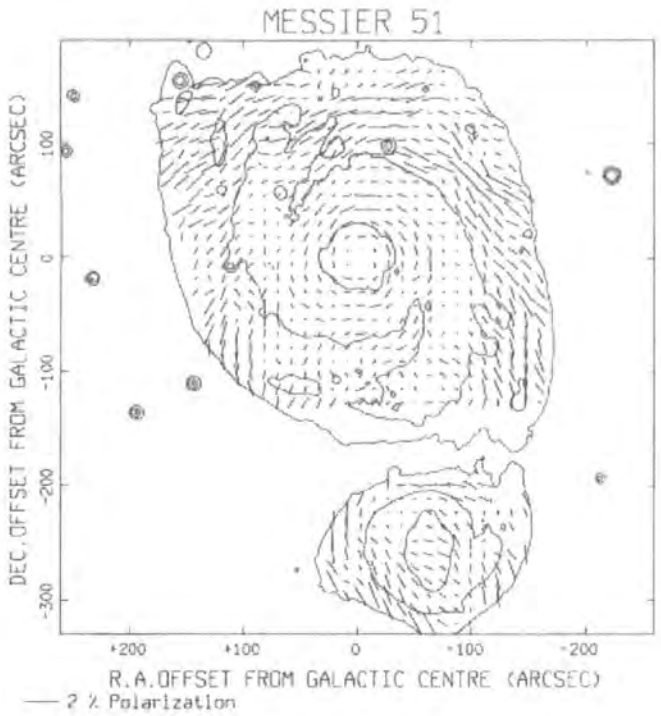

Figure 3.3: Optical polarization vectors in M51, a face-on spiral galaxy, by Scarrott (1987)

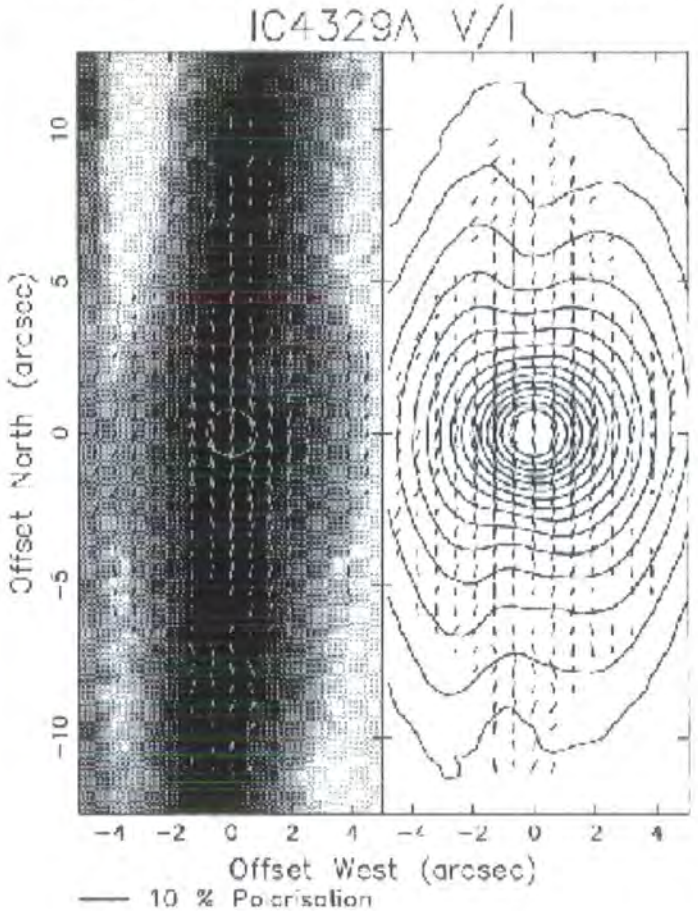

Figure 3.4: Optical polarization vectors IC 4329A, an an edge-on spiral galaxy, by Wolstencroft *et al.* (1995)

to the dust lane where dichroism dominates, polarization null points due to cancellation from scattering, and polarization perpendicular to the galactic plane where scattering dominates.

A well-studied example is M104, the Sombrero galaxy, which shows the optical polarization in the centre of the dust lane to reach levels of up to 4% orientated parallel to the lane. Measurements of this region at different wavebands show that the polarization can be accounted for by a Serkowski type law, with $\lambda_{max} \approx 0.42\mu$m. At the ends of the lane the polarization reaches up to 8% oriented perpendicular to the lane, which is consistent with the expected spiral magnetic field and is demonstrated in the map of IC 4329A, an edge-on spiral, by Wolstencroft *et al.* (1995) [266] shown in figure 3.4. The general trend in spiral galaxies with dust lanes is for the optical polarization to be orientated parallel to the dust lane in the central regions, with levels of $\approx$ 3-5% Scarrott (1996) [199].

3.2.5 Problems in polarization interpretation

The presence of dust and magnetic fields in other galaxies means that dichroic extinction is to be expected, but the question is how to determine the relative contributions of dichroic extinction and scattering to the measured optical polarization. The empirical Serkowski relationship (section 2.3.5) describing the wavelength dependence of polarization from dichroic extinction in this galaxy, provides a way of distinguishing dichroic polarization from polarization produced by scattering, which has a different wavelength dependence. This relationship can be applied similarly to other galaxies.

The polarizing effects of the magnetic field from our own galaxy need to be taken into account, since the light from the distant galaxies will also be polarized by the Galactic dust grains that lie in the line of sight, the interstellar polarization, as mentioned in section 2.3.5. This effect has been measured for different regions of the Galaxy by various authors using calibration stars and a calibration procedure. The measured ISP can then be removed from the polarization measurements of galaxies which lie close to the line-of-sight to the calibration stars of our Galaxy, to result in a measurement of the intrinsic polarization of that galaxy.

Some spiral galaxies host an AGN, so the very central nuclear emission of the galaxy, if determined with high enough resolution, will be predominantly from the AGN processes rather than from normal galaxy processes, and so polarization measurements will be affected by the AGN radiation which may be intrinsically polarized. Consideration of the polarization mechanisms thought to operate in Seyfert nuclei is given in the next section.

3.3 Polarization studies of Seyfert nuclei

A comparison of Seyfert galaxies to non-Seyfert starburst and interacting galaxies by Brindle *et al.* 1990 [35] found that the Seyfert nuclei had significantly higher polarization in the optical and near-IR. Initially this polarized emission found in Seyferts was assumed to be from synchrotron radiation, but in 1976, Angel *et al.* [8] showed the optical polarization from NGC 1068 was caused by dichroic extinction by dust. This finding subsequently prompted a number of large-scale optical polarization surveys of Seyferts.

The considerable evidence of dust (*e.g.* thermal infra-red emission, absorption features, reddening and opacity in the optical-UV bands) and evidence of magnetic fields (*i.e.* from radio synchrotron emission) in AGN have led to the proposal of the mechanism of polarization in Seyferts being: scattering by dust grains (Thompson 1980 [227]), scattering by electrons (Martin 1983 [148]), transmission through aligned grains (Martin *et al.* 1982 [147]) as well as synchrotron radiation (Miller & Antonucci 1983 [159]). Wavelength coverage of polarization measurements is a means of distinguishing between these polarizing mechanisms.

Spectro-polarimetric studies have detected a broad-line region in the polarized light of a number of Seyfert 2s (Miller & Goodrich 1990 [160], Kay & Moran 1998 [118]), as predicted by the unified scheme of AGN described in section 1.4. However, despite studies of a large number of Seyferts 2s, only 16 have had polarized broad lines detected in them, many others have failed to reveal broad lines even at high sensitivity.

3.3.1 Evidence of polarization from dust

The mechanisms of polarization by dust are described in chapter 2.3. Scattering from small dust grains can lead to a rise in polarized flux towards bluer wavelengths because in Rayleigh scattering, although the degree of polarization is wavelength independent, the scattering cross-section is proportional to λ^{-4} so the polarized flux increases with decreasing wavelength. This rise is demonstrated in a number of Seyferts, *e.g.* Brindle *et al.* (1990) [35] find several clear examples of rising polarization in the blue as well as a general trend of slightly increased polarizations in B-band. Dust is also implicated by Thompson (1988) [228] with evidence of a weak correlation between optical polarization and infra-red emission (characteristic of dust), in addition to higher polarization towards short wavelengths.

Evidence for dichroic absorption would be: orientation of the polarization vectors along the magnetic field *e.g.* parallel to the dust lane of an edge-on Seyfert, similar polarizations

of emission lines as for the adjacent continuum, and the wavelength dependence of polarization following a Serkowski type empirical law after correction for host galaxy dilution and other sources of polarization, *e.g.* ISP. This has also clearly demonstrated in Seyferts, 13 of the 71 objects observed by Brindle *et al.* (1990) [35] showed these polarization characteristics.

3.3.2 Evidence of polarization from electrons

The mechanisms of polarization from electrons are described in section 2.4, in chapter 2. The polarization from scattering by electrons (Thompson scattering) and of synchrotron radiation is wavelength independent, but because the diluting flux from the host galaxy diminishes in infra-red beyond 1.6 μm and in the ultra-violet, an increase in the degree of polarization would be expected in these regions. Brindle *et al.* (1990) [35] find an increase in polarized flux density with increasing wavelength with a significantly higher polarization in the red for several Seyfert 2s, implying either scattering from electrons rather than dust, or a significant non-thermal contribution to the polarization in the near-infrared.

It had originally been assumed that a substantial part of Seyfert 1 emission is synchrotron radiation, since this can explain the sometimes very high and significantly variable polarization (*e.g.* as found by Smith *et al.* 1997 [218]), but no evidence of this has been found in the surveys of Seyferts with the exception of NGC 4151. Polarization variability such as found in the Seyfert 1/QSO 1 Zw 1, cannot be due to synchrotron radiation because the broad lines are also polarized in a similar manner, so the variability has been attributed to the scattering dust clouds being very close to the nucleus and partially inside the BLR region, Smith (1997) [218].

Deshpande *et al.* (1993) [59] claimed detection of optical synchrotron radiation from Seyfert 2 nuclei. The polarization they detected however were levels of under 5%, so the other mechanisms suggested for the polarization, electron scattering, or scattering and transmission through aligned grains) can also account for this polarization, so there is no compelling evidence for optical synchrotron emission.

3.3.3 Infra-red polarization observations

Infra-red polarimetry studies of Seyfert 2s can probe more deeply into the scattering torus than optical studies, and can be used to investigate the properties of the warm dust

surrounding the AGN. If observations are extended from the optical into the infra-red, it can be possible to distinguish polarization by dust scattering from electron scattering or synchrotron radiation from the polarization properties across the spectra.

Brindle *et al.* (1990) [35] observed 27 Seyferts with multi-waveband optical to infra-red coverage (0.44μm to 2.2μm). Two of these showed an increase of polarization in the infra-red which together with a rise in polarization towards the blue, gives a U-shaped dependence of polarization on wavelength, and this suggests dilution by the host galaxy flux of wavelength-independent polarization - either electron scattering or non-thermal radiation.

Near-IR broad-band observations of several Seyferts by Young *et al.* (1996) [272] show a change in polarization angle from the optical to near-IR wavebands in some of the Seyferts, which might be indicative that an additional polarizing mechanism is required for the near-IR polarization. Heisler, Lumsden and Bailey (1997) [103] find a strong correlation between the warmth of the IRAS 60μm to 25μm ratio and the detection of scattered broad-line radiation in Seyfert 2s with a hidden BLR.

The necessity of an additional polarizing mechanism in the infra-red is also indicated by Lumsden *et al.* (1998) [138] from near- and mid-IR polarimetric observations of the well-studied Seyfert 2 NGC 1068. Pure scattering models fail to account for the polarization found in the infra-red wave bands measured, J, H, and K_n. Dichroic extinction by a warm dust screen over a background hot scattering dust source could explain this discrepancy. The hot dust should have a temperature $T > 1000$ K, and the warm dust $T > 350$ K, because the change in position angle when changing from emission to absorption occurs at $\approx 4 - 5\mu$m. Cooler dust is probably also present since the flip in position angle is not exactly 90°. The visual extinction provided by this hot dust (possibly the postulated dusty torus) may explain the absence of a near infra-red excess in NGC 1068 as typically seen in Seyfert 1s.

These results fit the type of polarization behaviour modelled by Efstathiou *et al.* (1997) [69]. They used radiative transfer relations to model the infra-red polarization properties from aligned grains in a dusty disc or torus, and this predicted the characteristic flip in position angle as the polarization changes from dichroic absorption to dichroic emission, dependent upon the optical thickness.

3.3.4 Optical-UV polarization observations

The first large survey of the optical polarizations of Seyfert galaxies was made in 1983 by Martin *et al.* [148], who observed 67 Seyfert 1 and 32 Seyfert 2 galaxies using a broad-band blue-green filter (3800 - 5600 Å). Most of the Seyferts had low polarizations of $< 1\%$, a result confirmed in the V band and at longer wavelengths by all other surveys of Seyferts (*e.g.* Brindle 1990 [36], Kay 1994 [119], Grupe 1998 [91]). Fourteen objects showed significantly higher polarization (above 3% polarized). The highest polarizations in the V-band reach 6% levels, and the highest level measured in the B-band is 10% (Brindle *et al.* 1990) but are only found in a couple of Seyferts. The peak in the distribution between 0 and 1% polarization can be attributed to the polarizing effects of foreground interstellar dust, much or all of the polarization of the low polarization Seyferts may be interstellar polarization rather than intrinsic polarization. Dilution of any intrinsic nuclear polarization by starlight of the host galaxy however, will underestimate the intrinsic polarization and was not accounted for.

There is a tendency for the optical polarization of Seyfert 2s to be perpendicular to the radio axis (Brindle *et al.* 1990 [36] and Tran 1995 [230]). In both types, there is a tendency for the electric polarization vector to be parallel to the galaxy optical or dust-lane axis, Thompson & Martin (1988) [228] and Brindle *et al.* (1990) [36] which is presumably a result of polarization through the dust lane of the host galaxy. Whether or not there is a significant difference between the levels of polarizations of Seyfert type 1s compared to type 2s is still not resolved. Martin *et al.* (1983) [148] found them to be the same, but Brindle *et al.* (1990) [36] considered that if allowance was made for polarization dilution by starlight, then Seyfert 2s would be more likely to have higher polarizations. If the polarization is due mainly to dust, then Seyfert 2s would be indeed be expected to be more highly polarized because as a group they have higher levels of reddening (extinction by dust).

For type 2 Seyferts, the lack of correlation of the nuclear polarization to reddening indicators indicates that the dominant mechanism in the narrow-line region is electron rather than dust scattering (Brindle 1990). In Seyfert 1s, there is evidence for decreasing obscuration with increasing luminosity, so the polarization of Seyfert 1s might be expected to depend on luminosity. This could be because the polarization is due to either non-thermal processes and would increase with luminosity, or due to dust, in which case it would decrease with luminosity.

The presence of a magnetised accretion disc in AGN should lead to the polarization of the radiation from the disc atmosphere. Theoretically, optically thick, pure electron scattering discs should linearly polarize optical and UV radiation up to levels of 11.7

percent, parallel to the plane of the disc (Chandrasekhar 1960 [42]), but this has not been observed in type 1 AGN where we have a direct view of the nucleus. The highest polarization levels in Seyferts tend to be about 5%-6% in V-band, but these are very few. High polarizations in Seyferts are generally only of the order of about 2-4%. One suggestion why this is not observed (Agol *et al.* 1998 [2]) invokes depolarization by Faraday rotation, but this is complicated since absorption opacity can interact with Faraday effects to either enhance the polarization or decrease it, and realistic modelling has yet to be done. Another mechanism to try to account for the lower-than-expected polarizations has been suggested by Beloborodov (1998) [27], where a fraction of radiation from the accretion disk is Thompson scattered by a wind flowing away from the disk. If the speed of the wind ($\beta = v/c$) is between 0.12 and 0.78, then polarization is produced parallel to the disc normal, *i.e.* perpendicular to Chandrasekhar's polarization, hence the lowering the expected polarization.

Simple Rayleigh scattering models by Goodrich & Miller (1994) [88] of the polarization expected from optically thin scattering of the continuum by dust or electrons surrounding the central regions also predict lower average values of the expected polarization. Using a uniform distribution of scatterers in an equatorial wedge, they calculate that the maximum polarization will be 7% and that this will be observed when the opening angle of the wedge is 25.° This upper bound is closer to the levels of polarization observed in higher-polarization Seyferts ($\approx 6\%$) than Chandrasekhar's maximum of 11.7%.

3.3.5 Seyfert 1 galaxies

Berriman (1989) [28] made a statistical analysis of 61 bright nearby ($z < 0.08$) Seyfert 1 galaxies which shows a correlation between the presence of optical polarization and narrow-line H_α/H_β nuclear 12 μm, and possibly a weak correlation with 25 μm luminosity. This implies that the optical polarization is predominantly from scattering and extinction by the dust that steepens the narrow-line Balmer decrements, and that radiates most of the luminosity at 12 and 25 μm. These correlations associate the scattering dust with the NLR, indicating that the scattering dust is either just outside or mixed in with narrow-line clouds. The optical depths implied by the mass contained in the NLR suggest electron scattering could not produce the observed polarization, unless there were also large amounts of hidden hot dust. The lack of correlation with indicators of the BLR reddening implies that the optical polarization does not originate from within the BLR.

Brindle *et al.* (1990) [36] [35] finds that Seyferts with a strong broad-line region (*i.e.* type 1) have correlations of the optical polarization with infra-red features suggesting the dominant polarization mechanisms are probably transmission through and scattering from

dust grains. This conclusion is supported by the results of Webb *et al.* (1993) [256], who measure UBVRI polarizations of Seyfert 1 galaxies and quasars. They find the position angle to be independent of wavelength and the percentage polarization tends to increase at blue wavelengths.

Goodrich & Miller (1994) [88] performed spectro-polarimetry on nine Seyfert 1 galaxies, four of which were essentially unpolarized after ISP correction. The other five all showed emission-line polarization and strong evidence for either dust scattering or electron scattering, including one Seyfert that shows evidence for both. The simple model of Seyfert 1 galaxies and quasars being polarized by scattering preferentially into the plane of a relatively thin disk is not sufficient to explain all these results. One Seyfert, Markarian 231, showed evidence for outflowing dust, with the polarization angle being perpendicular to the radio axis.

Imaging optical polarimetry by Wolstencroft *et al.* (1995) [266] of IC 4329A, an edge-on SO galaxy with a Seyfert 1 nucleus shows a high nuclear polarization due to both the host galaxy and the Seyfert nucleus. The optical polarization is parallel to the dust lane (tracing the magnetic field in the plane of the magnetic field), but the Seyfert 1 nucleus can be seen through the galaxy dust lane to have a slightly different polarization, *i.e.* showing an additional intrinsic nuclear polarization as the nuclear polarization cannot be realistically fitted to the Serkowski law for the dust-lane. Interactions with the neighbouring giant lenticular galaxy may have influenced the orientation of the AGN and host galaxy axes.

Grupe *et al.* (1998) [91] make an optical linear polarization survey of 43 bright soft X-ray selected AGN, all except one are Seyfert 1 nuclei, 50% of which are NL Seyferts. The vast majority show low polarization $\leq 1\%$ and no clear optical reddening, which, considered in conjunction with the rapid X-ray variability, disk-like spectral energy distributions and lack of cold X-ray absorption, indicates that a bare AGN disc is being viewed directly, and not observed through dusty gas. The two highly polarized Seyferts 1s show polarization increasing into the UV, evidence for scattering. They are narrow-line Seyfert 1s and show significant optical reddening, X-ray variability and low cold X-ray absorption. The reddening and variability imply dusty ionized gas along the line-of-sight very close to the nucleus, and hence observed scattering must be by dust rather than the polarization due directly from accretion disk. The lack of soft X-ray absorption could be because the gas around the nucleus is partially ionized and is more transparent to soft X-rays. The H_β line from the BLR and variability of the X-rays are similar in both low and high polarization Seyfert 1s, which supports a unified scheme where these properties are intrinsic and are not highly anisotropic. When the high polarization Seyfert 1 data of Grupe *et al.* (1998) [91] is amalgamated with that from Goodrich (1989) [86], the group of high polarization NL Seyfert 1 nuclei shows optical reddening values which underpredict

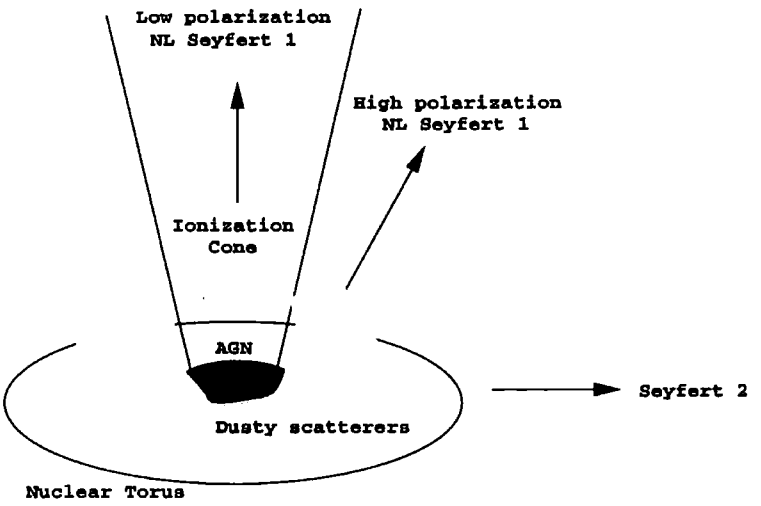

Figure 3.5: The unification model of Grupe *et al.* (1998)

the cold X-ray absorption, and most show warm X-ray absorption, implying warm dusty partially ionized gas in the highly polarized AGN.

This leads to the unified picture of Grupe *et al.* (1998), shown schematically in figure 3.5, where all narrow-line Seyfert 1s have obscuring dusty tori and scatterers, with some lines-of-sight unobscured (analogous to the unified scheme linking Seyfert 1s and 2s). The low polarization NL Seyfert 1s represent the unobscured views from within an ionization cone, but at higher inclination angles, the dusty ionized gas absorbs the direct UV, soft X-rays and 0.7 keV X-rays causing reddening and scatters radiation resulting in high polarization NL Seyfert 1s. At even greater inclinations all but the harder X-rays would be blocked by the thicker torus until giving the appearance of a Seyfert 2.

3.3.6 Seyfert 2 galaxies

Kay (1994) [119] performed blue spectro-polarimetry on 50 Seyfert 2 galaxies and, after correction for interstellar polarization and subtraction of a template galaxy to remove the flux due to starlight, found that the level of polarization is not related to the fraction of nuclear continuum flux. This argues against the idea that all Seyfert 2s have a highly polarized featureless continuum which may not be seen due to dilution by starlight. An average of 70% of the flux was attributed to galaxy starlight, however the 9 Seyferts with hidden BLR had much smaller starlight contributions of 30% of the total flux.

Brindle *et al.* (1990) [36] found a lack of correlation of the nuclear polarization to reddening indicators for type 2 Seyferts and argues this implies that the dominant mechanism in the narrow-line region is electron scattering. This is supported by Tran (1995) [230] [231]

[232], who performed spectro-polarimetry on 10 Seyfert 2 galaxies known to have obscured broad-line regions. After interstellar polarization was corrected for and a selected template galaxy spectrum was subtracted to correct for the starlight contribution from the host galaxy (the fraction of the total flux attributed to the different galaxies being between 0.15 to 0.88), this resulted in the corrected polarization levels being generally high ($\approx$ 5%). When combined with supporting evidence from X-ray observations, Tran concluded that electron scattering is the dominant polarization mechanism in 9 of the 10 galaxies, and dust scattering dominant in the remaining one, although significant contributions from dust scattering and/or transmission is likely in at least four others. The polarized broad lines are redshifted relative to the nucleus. If these results are to support the obscuring torus model with the general scattering geometry as proposed for NGC 1068, then an additional substantial unpolarized diluting nuclear component is also necessary otherwise the polarization levels are still too low. Tran suggested this component might be optically thin thermal radiation from the scattering region itself.

Young *et al.* (1996) [272] performed broadband optical and infra-red polarimetry and optical spectro-polarimetry on a number of Seyfert 2 galaxies to search for broad lines in the polarized flux. No corrections for ISP were attempted. The majority of type 2 objects observed did not show evidence for broad lines in the polarized flux, implying that either the scattered radiation is obscured from view, or that the lines are so thermally broadened that they are unobservable, or that there are problems with the unified scheme and its prediction of broad lines in the majority of type 2 objects. Hidden broad-line regions seem to be found mostly in multiple or interacting systems of galaxies, suggesting merging interactions may be important for the formation of these polarized BLRs in Seyfert 2s.

The polarizations of the Seyfert 2s in the sample of Young *et al.* (1996) showing broad lines, were used to model their optical and near-IR spectra, using a cone-based scattering geometry plus a dichroic view of the near-IR regions through the postulated torus surrounding the type 1 centre. Young *et al.* (1996) showed that most of the galaxies with polarized broad-lines had a U-shaped wavelength dependence, *i.e.* that rises towards the blue and infra-red, or at least rises towards the blue. A few of the objects showed a change in their angle of polarization with wavelength. For the low polarization objects this is probably due to ISP taking effect, but for the higher polarization objects this variation must be intrinsic, possibly delineating different polarization mechanisms.

3.3.7 Problems in polarization interpretation

When attempts are made to correct for host galaxy light dilution, the resulting polarization measurements are very sensitive to this flux subtraction, which has led to considerably

different results by different authors as they remove different amounts of host galaxy flux. The most common way of doing this is to subtract a selected galaxy template, usually an elliptical. However, work by Storchi-Bergmann *et al.* (1998) [222] suggests this in itself may be a misleading approximation in many cases. They observe long-slit spectra along the radio axis of four Seyfert 2 galaxies known to have polarized continua and investigate the rôle of the central stellar population, in particular the part that the young to intermediate age stars may play in contributing to the featureless continuum. They conclude that there is a significant young blue star population in many Seyfert 2s which is not subtracted when using a galaxy template, thus still significantly diluting the polarization measurements, particularly in the blue wavelength region.

Many Seyferts show evidence for more than one mechanism of polarization from different regions in the AGN, making it difficult to model the relative contributions. Complex polarization structure exists in the H_α and H_β data from the Seyfert 1 Mrk 486, which can be interpreted as at least some of the scattering material being inside the broad-line region. In some edge-on galaxies such as IC 4329 A, the scatterers are found in the disk of the host galaxy but in others they are within the AGN itself.

For the bulk of Seyferts which have low polarization, limitations of errors in the measurement of the polarization and the lack of accurate reliable interstellar polarization determinations valid for particular objects, make calculating any intrinsic polarization almost impossible in most cases.

3.4 Summary of polarization studies and their support for the unified scheme

The theory and technique of optical polarimetry have been established for investigating the dust and magnetic field structures of both the Seyfert nuclei and their host galaxies, and for comparing these observations with the results of analytic and Monte Carlo models of scattering and dichroism.

The polarization properties of spiral galaxies are strong indicators of galactic magnetic fields and dust populations. In face-on galaxies, the optical and radio polarization vectors clearly trace out the spiral magnetic field. In edge-on galaxies, polarization by both scattering and dichroism is demonstrated, and polarization values are of the order 3-5%.

Polarimetric measurements of Seyfert nuclei show generally low optical (V-band) polarizations of the order of 1%, although a small number show higher polarization up to about

6%. These figures however, are very sensitive to correction for dilution from the host galaxy stellar flux, estimates of which can imply much higher intrinsic nuclear polarizations of about 15% (levels predicted from accretion disc models). Evaluating the relative contributions of host galaxy flux and AGN flux, for example by choosing a suitable template galaxy, are difficult to estimate reliably. The situation is further complicated by the finding that many Seyfert 2 host galaxies seem to have an enhanced rate of star formation in their circumnuclear region. Therefore the validity of the derived intrinsic polarizations from different methods is arguable.

The wavelength dependence of nuclear polarization in both Seyfert types indicates scattering, either by dust or electrons or by both. Broad lines have been revealed in the polarized spectrum of some Seyfert 2 nuclei in support of the unified schemes, although the lack of even faint polarized broad-lines detected in most other Seyfert 2s raises questions as to the scope of the unified scheme which predicts all Seyfert 2s should have a hidden Seyfert 1 nucleus. Infra-red polarization (of the order of a few percent) has been shown to be from scattering plus an additional mechanism, probably dichroic extinction.

Imaging broadband and spectro-polarimetric measurements can place constraints on the models of the active nucleus in terms of the spatial extent and composition of dust in different regions, the BLR, the NLR, the postulated obscuring torus, magnetic fields and interactions with the surrounding nuclear region of the host galaxy. HST spectro-polarimetric studies of narrow-line emission regions in Seyferts have shown evidence of polarization originating from dense nuclear gas suggesting an obscuring nuclear torus or disk on the scale of a couple of parsecs in for example NGC 4258, Barth *et al.* (1999) [20], consistent with the unified scheme model.

Imaging polarimetry allows spatial correspondence between polarized regions and observations in different wavebands to be seen, and in particular, can show connections between the polarization properties of the host galaxy and the Seyfert dominated nucleus. In the case of polarization by scattering from a central source which may be obscured and hidden, imaging polarimetry of the the centro-symmetric polarization pattern allows an independent determination of the location of the hidden nuclear source, for example in HST UV observations of NGC 1068 examined by Kishimoto (1999) [122] and of Mkn 463E by Tremonti *et al.* (1996) [233].

Chapter 4

Optical polarimetry techniques

4.1 Introduction

This chapter describes the techniques of polarization measurements used in this study. It outlines the computational procedures used in the data reduction, discusses the error estimations and gives details of the observations presented in this thesis.

4.2 Measurement of polarization

A polarimeter resolves light into known polarization states and records the intensity at different states to determine the linear polarization. The first documented time a polarimeter was used to detect extra-terrestrial polarization was by Arago in Paris in 1811, from observations of moonlight (Dougherty & Dollfus 1989 [60]). This tube-like construction uses[1] a quartz plate to rotate the plane of polarization of the light through an angle highly dependent on the wavelength and then a Wollaston prism to split the light into two perpendicularly polarized images. If the light is polarized, the two images are of complementary colours, the shade of colour depending on the degree of polarization. In 1811, Arago (Arago 1856 [13]) observed the changes in polarization with the phases of the moon, and the difference in polarization between the lunar seas and highlands (higher in the seas) by using suitable lenses to convert the polarimeter into a telescope.

[1]Still in working order after restoration by Dougherty & Dollfus in 1986 [60].

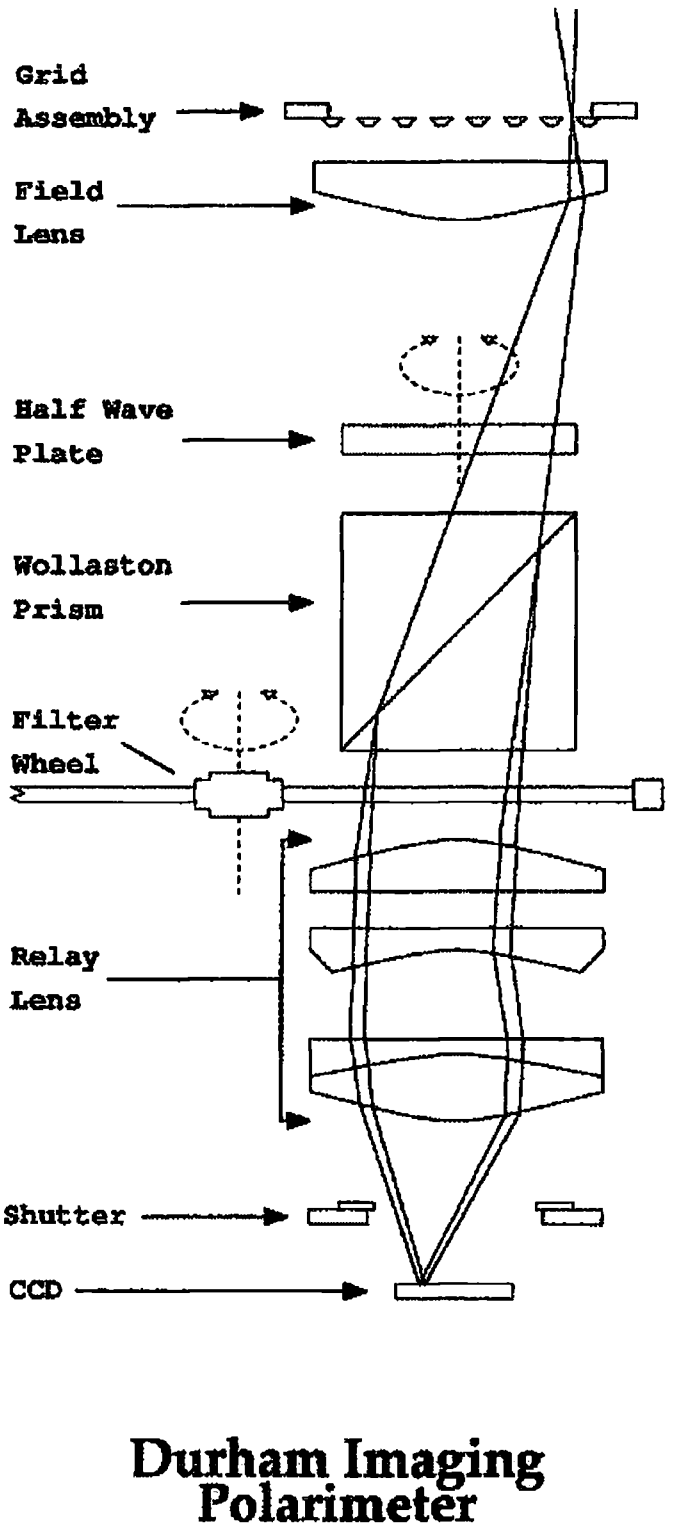

Figure 4.1: The optical imaging system of the Durham Polarimeter

The Durham optical polarimeter used for this study also uses a Wollaston prism, but employs a half-wave plate instead of a wavelength-dependent plate, and a different measuring system described in the next section, which compares the intensities of the polarized light rather than the colours. It measures the intensity of light polarized at two pairs of perpendicular position angles with 45° between them, (*i.e.* at 0° , and 90° , and at 45° and 135°), as this gives a direct measurement of the Stokes parameters as shown below, which are required in order to calculate the linear polarization.

$$\begin{aligned} I &= E_x^2 + E_y^2 &&= I_0 + I_{90} \\ Q &= E_x^2 - E_y^2 &&= I_0 - I_{90} \\ U &= 2E_xE_y &&= I_{45} - I_{135} \end{aligned} \tag{4.1}$$

where I_θ is the intensity of the component of light along the axis at position angle θ. If the x-axis is taken to define the angle $\theta = 0°$ then obviously $E_x^2 = I_0$ and $E_y^2 = I_{90}$, and for the pair of axes rotated by 45°, simple trigonometry shows that $2E_xE_y = I_{45} - I_{135}$. The angle of polarization ϕ of the electric vector ($\phi = \tan^{-1}(E_y/E_x)$) can be directly calculated from the Stokes vectors by the relation:

$$\tan 2\phi = \frac{U}{Q} \tag{4.2}$$

4.3 The Durham Polarimeter

The Durham polarimeter is a dual beam polarimeter which uses a Wollaston prism and a half-wave plate to measure I_θ, as shown schematically in figure 4.1. The incoming light beam is reduced in width by the field lens, and then goes through the super-achromatic half-wave plate which introduces a phase shift of π between the components polarized parallel and perpendicular to its optical axis. The plane of polarization of linearly polarized light therefore is rotated by 2θ where θ is the angle of incidence, and so a rotation of the half-wave plate by θ rotated the plane of polarization by 2θ. The Wollaston prism splits the beam into two mutually perpendicularly polarized beams, corresponding to I_0 and I_{90} (or I_{45} and I_{135}), which then diverge by approximately one degree. These two beams are focussed into two images through the relay lenses onto the CCD detector chip.

To prevent the overlapping of the images on the chip, a blocking mask is situated before the prism, which blocks outs alternate strips of the image from the telescope. A filter wheel allows the selection of an appropriate filter for observing. The polarimeter is fitted onto the telescope and has its own computerised control system. The current CCD detector is a thinned SiTe (Tektronix) chip (used from October 1997). Previous CCD chips also used in the observations in this thesis are an EEV blue coated P8603 chip (up to May

1994) and a GEC Astrochrome coated P86000 chip (from Jan 1995 to May 1997). The Durham polarimeter and its operation is described in detail by Scarrott *et al.* (1983) and (1991), [201], [198].

The intensities of I_θ beams are each measured twice when the polarimeter is used. This means that the position angles of the dual beam are exchanged to eliminate any variations due to possible small differences in the optical paths of the left and right hand beams. This therefore requires a total of four exposures, but since the mask blocks off half the object image, two further sets of (four) exposures are required after shifting the telescope enough to image all of the sky, plus enough overlap to align the images for reconstruction. Full coverage therefore requires considerable time, and time constraints mean that in most of the images in this thesis there are gaps in coverage. The technique of dual beam polarimetry avoids the problem of rapid changes in the night sky brightness and polarization due to atmospheric variations in between polarization observations of orthogonal states, because they are observed simultaneously. Total intensity images can also be obtained directly from the sum of the intensities of the two orthogonal states.

The technique of measurement by the polarimeter is described in detail by Scarrott *et al.* (1983) [201]. For most of the galaxies, exposures of approximately 10 minutes were taken at each of the 4 different half-wave plate orientations for each Seyfert to allow calculation of the linear polarization. Shorter exposures were taken in some cases to allow observation of the nucleus without saturation. Repeat observations were taken for the fainter images, particularly for the filters with a lower throughput in order to obtain a strong enough signal. These multiple observations were taken rather than increasing the exposure time because the longer exposures would be more likely to suffer telescope tracking errors and cosmic ray contamination. Appropriate flatfields for calibration purposes were obtained during the observing runs, and to enable an additional check on accuracy and reliability of the whole reduction procedure, either standard stars or other suitable calibration objects of known polarization were also observed.

4.3.1 Resolution of CCD detector

The resolution R of the detector of a telescope, in arcseconds per pixel, is given by:

$$R = \frac{648000MP}{\pi Df} \tag{4.3}$$

where D is the diameter of the primary telescope mirror in mm, f is the focal ratio, M is the demagnification factor introduced by the field and relay lens system (which is approximately 4 for the Durham polarimeter), P is the CCD detector pixel size in mm,

Table 4.1: Detector resolution

Telescope name	Diameter (metres)	Date	Focal ratio	CCD size no.pixels	Pixel size (μm)	Resolution arcsec per pixel
WHT	4.2	1/91	f/11	416 × 578	22	0.40
INT	2.5	8/91	f/15	416 × 578	22	0.49
JKT	1.0	5/90	f/15	416 × 578	22	1.2
JKT	1.0	11/92	f/15	416 × 578	22	1.2
JKT	1.0	1/95	f/15	416 × 578	22	1.2
JKT	1.0	7/96	f/15	416 × 578	22	1.2
AAT	3.9	3/94	f/15	416 × 578	22	0.31
WISE	1.0	4/86	f/13.5	416 × 578	22	1.35
SAAO	1.0	2/97	f/15	416 × 578	22	1.2
MAC	2.1	10/97	f/13.5	512 × 512	27	0.80

and the factor $648000/\pi$ is to convert from radians to arcseconds. Table 4.1 gives the resolutions of the detectors used in the observations for this thesis.

4.4 Data reduction

The data were reduced using the standard Durham polarimeter software suite, 'POLAR' written by R.F. Warren-Smith and T. Gledhill and updated by P.W. Draper, specifically for data collected with the Durham polarimeter. The suite comprises a number of calibration procedures detailed below, that are required in order to produce a total intensity image and to calculate and plot the polarization of the light.

4.4.1 CDPRELUDE

This performs the initial processing of CCD frames to make the signal positive and equal to number of electrons collected per pixel by converting from AD units (analogue-digital) into electrons, subtracting the ADC electronic zero (the bias level) and adjusting the data range. It also clips any saturated pixels and rotates the frames by -90 degrees.

4.4.2 FLATFIELD

Flatfields are required to correct for spatial variations in sensitivity over the detector, and to facilitate removal of the sky signal. These are frames taken of a photometrically flat source (the twilight sky) at the different half-wave plate positions.

The flatfield frames are merged and then through a combination of appropriate high-pass filters, normalisation, smoothing, subtraction, and using weighted medians with a cleaning algorithm, small blemishes are flagged and the large scale structure of the flatfield, depending on the analyser position, is calculated and stored for correction of the total intensity object images.

4.4.3 REDUCE

This procedure takes the object images and flatfield images as the input to produce a total intensity image and exposure factors corrections. The processing consists of: correction with flatfield, alignment to a common frame, sky background subtraction, and calculation of corrections for image exposure factors and instrument sensitivity (E and F factors).

The E factors (the relative sensitivities of each exposure - variable exposure time and atmospheric transmission) and F factor (relative sensitivity of the RH polarimeter channel to the LH channel) corrections and intensity information are output to a file, which can then be used to calculate the Stokes' parameters to determine the polarization of the light. A total intensity image is also produced.

4.4.4 POLCALC, POLPLOT

These procedures prompt for the parameters for the calculation, binning and plotting of polarization and intensity values from the file containing the E and F factor corrections. 'POLCALC' calculates and produces a list of corrected Stokes parameters, percentage polarization, polarized intensity and position angle and associated errors. 'POLPLOT' allows this list to be plotted in different formats together with the total intensity maps.

The errors in the Stokes parameters can be calculated by weighting the data according to an error model for the CCD detector, which includes read-out noise, photon noise, RMS flatfield calibration error and an estimate of the sky subtraction error. This however does not take into account the error cancellation that takes place in two channel polarimetry,

where errors that affect both channels equally are largely eliminated. The software therefore has an alternative, more sophisticated error model which makes some allowance for error cancellation which is discussed in the next section.

4.4.5 Measurement errors and ISP corrections

Since the levels of polarizations measured for most of the objects in this thesis are only of the order of a few percent, it is important to consider the possible sources of error to obtain a reliable estimate of the associated errors of the measurements.

The particular problems that arose during data reduction for the observations of this thesis occurred when there were insufficient stars in the field to allow accurate alignment between frames, when there was insufficient overlap of the image between the different positions of the telescope, and when the flatfields were poor. These problems and the steps taken to minimize their effects are discussed in chapters 5 to 8, in the observational details section of the object for which they occurred.

The error calculations for the Stokes parameters in dual channel polarimetry is complicated because of error cancellation. Errors common to both channels do not affect the resulting measurements of polarization. Therefore, the dispersion in the data values tends to give an overestimation of the actual error, although this is minimised by categorising the errors as common or differential, and treating accordingly. This more thorough error calculation option was used in the data reduction in this thesis. At high signal levels however, dispersion in the F factor values may lead to a higher error indicated than is true, so the calculated values give an upper limit on the 1σ errors, whereas for low signals the error estimation is more likely to be representative of the actual 1σ error levels. Finding suitable sensible signal-to-noise cut off levels for the maps can remove most disordered (spurious) polarization vectors.

For an internal check on consistency, wherever possible datasets of the same object were processed separately, then the measurements were compared before combining into a larger dataset. These proved to be reliably consistent unless otherwise noted in the results chapters. A further reliability check which is independent of the reduction procedures was also performed. Standard stars for polarimetric comparative measurements were observed during the observing runs. For example, HD 154445 has a known polarization of 3.7% $\pm$ 0.1% at a position angle of 90°$\pm$ 1°. This star was observed during the July 1996 observing run on the JKT with the broad V band filter. Following the standard reduction procedure, the polarization measurements were 3.7% $\pm$ 0.1% at 93°$\pm$ 5°, which demonstrates that the polarization levels are accurately determined within the calculated errors.

For some of the objects, interstellar polarization effects are significant, so where previously measured values are available these have been subtracted to remove this effect as far as possible. Where polarization levels are particularly low however, the resulting polarization is highly sensitive to the values of ISP subtracted, and the uncertainty in the ISP must also be taken into account. Table 4.2 lists the ISP values that have been adopted in this study. Polarization due to any moonlight in the image should in principle, be successfully removed as part of the sky subtraction.

4.5 Observations

Optical polarimetric observations were taken of nearby Seyfert galaxies which were selected on a practical basis of angular size, intensity, and positional availability during the allocated telescope time to ensure adequate signal-to-noise levels for reliable polarization calculation of the host galaxy emission as well as of the Seyfert nuclei. In total, 7 nearby bright Seyfert galaxies (Mkn 3, Mkn 348, Mkn 573, Mkn 1376, NGC 1566, NGC 2992 and NGC 3079) have been observed where some structure of the galaxy has been resolved, in some cases comprising multi-waveband measurements. A further 6 Seyferts were observed which were too small for much structure in the galaxy to be resolved, so these maps have not been included in this thesis for analysis.

These polarimetric observations of the selected Seyfert galaxies were taken with the Durham Imaging CCD Polarimeter [201], using the 1 m Jacobius Kapteyn telescope (JKT), the 2 m Issac Newton telescope (INT) and the 4 m William Herschel telescope (WHT) in La Palma, the Canary Isles, the 4 m Anglo Australian telescope (AAT) in Australia, the 1 m South African Astronomical Observatories telescope (SAAO) in South Africa, and the 2.1 m MacDonald Telescope in Texas (MAC), at various epochs from 1990 to 1997, and are listed in table 4.3. The observations were mostly done using a broad band V filter (FWHM 130 nm, mean wavelength 545 nm), since most scattering tends to take place in that wavelength range, and for some objects additional images were taken through an R and B filter. The characteristics of the filters used with the polarimeter are given in table 4.4.

Table 4.2: Adopted interstellar polarization values

Name	E(B-V)[1]	K	P_{max} (%)	Position angle (degrees)	λ_{max} (Ångstroms)	Reference
Mrk 3	0.45	1.15	1.20	132	5450	Schmidt & Miller (1985)
Mrk 348	0.24	0.69	1.14	114	4050	Tran (1995)
Mrk 573	0.03		0.31	125.3		Kay (1994)
Mrk 1376			0.48	84.1		Kay (1994)
Mrk 7674	0.10	0.84	0.505	86	5000	Kay (1994)

[1]Data taken from NASA/IPAC Extragalactic Database (NED), Epoch B1950.0

Table 4.3: Observation log (NF = no filter)

Name (Other name)	Telescope date	Filter	Frames taken at each position	Exposure (seconds)
Mrk 3	WHT 1/91	VV	4	200
Mrk 348 (NGC 262)	INT 8/91	VV	4	600
Mrk 509	INT 8/91	VV	8	400,150
Mrk 573	INT 8/91	VV	4,4	600,500
	MAC 11/97	R	4	300
	MAC 11/97	B	8	300
Mrk 1376	AAT 3/94	VV	8	600,30
(NGC 5506)	WISE 4/86	NF	8	500
NGC 1566	SAAO 2/97	VV	4,4,4	900
	SAAO 2/97	R	4,4	900,180
	SAAO 2/97	Ha	12	900
NGC 1672	SAAO 2/97	NF	4,4,4	600
NGC 2992	SAAO 2/97	VV	8	900
	JKT 1/95	VV	4,4,4	900
	JKT 1/95	I	4,4,4	900
NGC 3079	JKT 2/90	VV	4,4,4	600
NGC 5929	JKT 7/96	VV	4,4	600
NGC 6926	JKT 7/96	VV	4	600
NGC 7469	JKT 7/96	VV	4,4,4	300
NGC 7479	JKT 7/96	VV	4	900
NGC 7674 (Mrk 533)	INT 8/91	VV	4,4	600

Table 4.4: Characteristics of the Durham polarimeter filter

Filter	λ_{max} nm	λ_{mean} nm	FWHM nm
B	440	440	96
V(broad)	525	545	130
R	595	663	157
I	808	883	297
H_α	656	661	70

Table 4.5: Characteristics of other common filters

Filter	$\lambda_{central}$ nm	Bandwidth nm
R	700	220
I	900	240
J	1250	280
H	1640	280
K	2200	480
L	3400	700

Table 4.6: Basic data on observed galaxies

Name	Galaxy Type[2]	Seyfert Type[2]	Distance[1] Mpc	Rec. Vel.[2] km s^{-1}	Mag.[2]	Galactic Ext.[2] (B mag)
Mrk 3	S0	2	54	4050	14.0	0.45
Mrk 348	SA(s)0/a	2	61	4540	13.9	0.24
Mrk 573	(R)SAB(rs)0	2	69	5174	13.7	0.03
Mrk 1376	Sa pec sp	2	25	1853	13.4	0.12
NGC 1566	SAB(rs)bc	1	17.4	1496	10.3	?
NGC 1672	SB(r)bc	2	18	1350	10.3	-
NGC 2992	Sa pec	2	42	2308	13.1	0.25
NGC 2993	Sa pec	-	42	2420	13.1	0.25
NGC 3079	SB(S)c LINER	2	16	1125	11.5	-
NGC 6926	SB(s)bc pec	2	80	5970	13.2	0.53
NGC 7469	SAB(rs)a	1	65	4892	13.0	0.12
NGC 7479	SB(s)c	2	32	2381	11.6	0.16
NGC 7674	SA(r)bc	2	116	8713	13.9	0.10
NPM1G +31.0016	-	-			15.79	0.24

[1]calculated using H_0=75 km s^{-1} Mpc
[2]Data taken from NASA/IPAC Extragalactic Database (NED)

Table 4.7: Basic positional data on observed galaxies

Name	Right Ascension[1]	Declination[1]	Galactic Co-ords[2]	Diameters[1] (arcmin)	Inclination
Mrk 3	06h09m48.419s	+71d03m10.72s	143, 22	1.8 x 1.6	
Mrk 348	00h46m04.863s	+31d41m04.15s	122, -30	1.1 x 1.1	$< 20°$
Mrk 573	01h41m22.922s	+02d05m56.32s	148, -57	1.3 x 1.3	1/7
Mrk 1376	14h10m39.23s	-02d58m26.50s	339, 53	2.8 x 0.9	5/5
NGC 1566	04h18m53.30s	-55d03m23.0s	264, -43	8.3 x 6.6	$27° \pm$ 3 dg
NGC 1672	04h44m55.00s	-59d20m18.0s	269, 39	6.6 x 5.5	
NGC 2992	09h43m17.734s	-14d05m42.84s	250, 29	3.5 x 1.1	2/7
NGC 2993	09h43m24.01s	-14d08m12.6s	250, 29	1.3 x 0.9	?
NGC 3079	09h58m35.008s	+55d55m15.41s	158, 48	7.9 x 1.4	4/7
NGC 5929	15h24m18.935s	+41d50m40.82s	68, 55	1.0 x 0.9	1/7
NGC 6926	20h30m30.40s	-02d11m55.0s	43, -23	1.9 x 1.3	2/7
NGC 7469	23h00m44.427s	+08d36m16.12s	83, -45	1.5 x 1.1	3/7
NGC 7479	23h02m26.37s	+12d03m10.6s	86, -43	4.1 x 3.1	2/7
NGC 7674	23h25m24.430s	+08d30m12.91s	91, -48	1.1 x 1.0	0/5
NPM1G +31.0016	00h46m10.527s	+31d41m10.08s	122, -30	-	-

[1]Data taken from NASA/IPAC Extragalactic Database (NED), Epoch B1950.0
[2]Data taken from NASA/IPAC Extragalactic Database (NED), Epoch J2000.0

Chapter 5

Face-on Seyfert galaxies

5.1 Introduction

This chapter presents the results of polarimetric observations carried out on three nearly face-on Seyfert galaxies, together with a review of other observations that have been published about each galaxy and its Seyfert nucleus. Previous optical polarization measurements are compared to those found in this study and interstellar polarizations effects are taken into consideration. The results are discussed in relation to observations of other types, and theoretical predictions models, both of the host galaxies and of the Seyfert nuclei.

5.2 Markarian 348

5.2.1 Introduction

Markarian 348 is a nearly face-on early-type spiral galaxy, classified as SAa on the basis of faint spiral arms seen in H_α emission (Mulchaey *et al.* 1996 [162]). The digital sky survey (DSS) blue image reproduced in figure 5.1 shows Markarian 348 as the central galaxy, showing faint spiral arms in a field of 4 arcminutes by 3 arcminutes. The galaxy is tidally disturbed with the H_α spiral arms stretching towards its north eastern companion galaxy, NGC 266 (Pogge 1993 [185]), which is situated 23 arcminutes to the NNE (Gracia-Vargas

et al. 1989 [80]) and not shown in the field. A large atomic H_I envelope of extent 9.5 by 6 arcminutes ($\approx$ 170 kpc by 110 kpc[1]) was found surrounding the galaxy by Heckman *et al.* (1982) [101] which could have been produced during interaction with NGC 266, and their kinematic data suggests that the inclination of the disk is less than 20°. Simkin *et al.* (1987) [214] found a more complex H_I structure elongated along a position angle of around 170°.

Markarian 348 hosts a strong Seyfert 2 nucleus and has a faint ring of H_{II} regions at a distance of 10 arcseconds from the nucleus (Gonzalez *et al.* 1997 [83]). In polarized light however, very broad Seyfert 1 type emission lines (FWHM for H_α is 8400 km s^{-1}) have been detected in the nucleus by Miller & Goodrich (1990) [160], suggesting obscured Seyfert 1 characteristics. There is relatively strong hard X-ray continuum emission from the nucleus, with the photoelectric absorption corresponding to a column density of $N_H = 1.1 \times 10^{23}$ cm^{-2} (Awaki 1991 [15]), further supporting a dust obscuration of a Seyfert 1 nucleus. A compact variable nuclear radio source (about 300 mJy) with variability on a timescale of a few months and fairly strong amplitude changes for Seyfert nuclei was detected by Neff & de Bruyn (1983) [167], supporting an AGN rather than starburst origin for this nuclear radio emission.

Extended radio emission at 6 cm is imaged by Baum *et al.* (1993) [24] by subtracting out the central source. This shows an extended component reaching out to 18 arcseconds (about 5 kpc assuming $H_0 = 75$ km s^{-1} Mpc^{-1}) along the central source, at a position angle of 13°. A radio map at 20 cm by Nagar *et al.* (1999b) [166] shows a central source with faint extensions covering 28 arcseconds along a position angle of about 22°.

High resolution observations of the inner nuclear region have demonstrated striking correspondence between linear features in radio and optical images. Optical HST images (using a F606W filter[2]) of the central regions resolve a double nucleus, with a separation of about 90 milli-arcseconds at a position angle of 170°, Gorjian (1995) [89]. At a comparably high resolution, VLBI[3] 21 cm radio maps by Neff & de Bruyn (1983) [167] show a triple linear source with an extent of 180 milli-arcseconds at a position angle of 168°, also seen in the MERLIN[4] radio maps by Unger *et al.* (1984) [246] at 6 cm and 18 cm. Unger *et al.* [246] found the middle radio component to have an inverted spectrum whereas the two outer components have steep spectra, and their equipartition calculations indicate that the pressure of the relativistic plasma in the lobes is significantly higher than the thermal pressure in the forbidden line region. From this they concluded that the middle

[1]Assuming Mkn 348 to be at a distance of 61 Mpc as given by NED.
[2]Mean wavelength 594 nm, FWHM 150 nm.
[3]Very Long Baseline Interferometry
[4]Multi Element Radio Linked Interferometer Network

component is the core and that the two outer components are material ejected from the core.

When these high resolution radio and HST maps are superimposed with the middle radio source aligned with the brighter optical nucleus, as done by Neff & de Bruyn (1983) and Unger *et al.* (1984), neither of the other two radio components fit with the other optical component, although the north-west radio component is in the same direction from the core as the other optical nucleus. Gorjian (1995) suggests alternatively that the two outer radio components should correspond to the two optical components since the separation is almost the same. This would mean that the core is so heavily obscured by dust that it is not visible in the optical range. At even higher resolution, Ulvestad *et al.* (1998b) [243] found a compact nuclear jet-like synchrotron radio structure no longer than 1 parsec (3 milli-arcseconds) in length along the same position angle of 165°. These high resolution (sub-arcsecond) radio and optical studies investigate structures on a much smaller scale than the observations in this thesis which are order of an arcsecond (1 pixel corresponds to 0.49″).

The near infra-red properties of Mkn 348 were investigated by Simpson *et al.* (1996) [215]. After subtracting off a model for the surface brightness of the galactic bulge, they found a red linear structure in their J-K colour near-IR continuum map, which runs approximately 2 arcseconds (1 kpc) east-west (position angle 90°) and is unresolved in the north-south direction, and they interpret this as an edge-on disk or large-scale torus. Near infra-red (J,K and H band) isophotes on the maps of Alonso *et al.* (1998) [5] also show a slight elongation with a position angle of 90° on the scale of 5 arcseconds, consistent with the red linear feature found by Simpson *et al.* [215]. They conclude that these characteristics are best described by a combination of dust emission at ~750 K, and emission from late-type stars, and that it represents a large-scale dusty disk or torus viewed approximately edge-on. This scale length can just be resolved in the observations of this thesis.

An HST $[O_{III}]\lambda5007$ emission-line image by Capetti *et al.* (1996) [40] shows that the central line-emission is concentrated in a small linear structure 0.45 arcseconds in size, with position angle of 155°. Excitation images ($[O_{III}]\lambda5007/(H_\alpha + [N_{II}])$) by Simpson *et al.* (1996) [215] and Mulchaey, Wilson, & Tsvetanov (1996) [163] show two regions of high-excitation ionized gas to the north and south of the nucleus with a possible biconical morphology extending out over several arcseconds (≈1 kiloparsec) each side of the nucleus, aligned approximately north-south (around position angle 192/dg). Falcke *et al.* (1998) [74] confirms the existence of a north-south region of high-excitation gas, the most prominent excitation is at a distance of 1 arcsecond south of the nucleus, slightly offset to the west. This is along the nuclear radio axis and perpendicular to the position angle of the optical polarization and the near infra-red structure detailed above. Simpson *et*

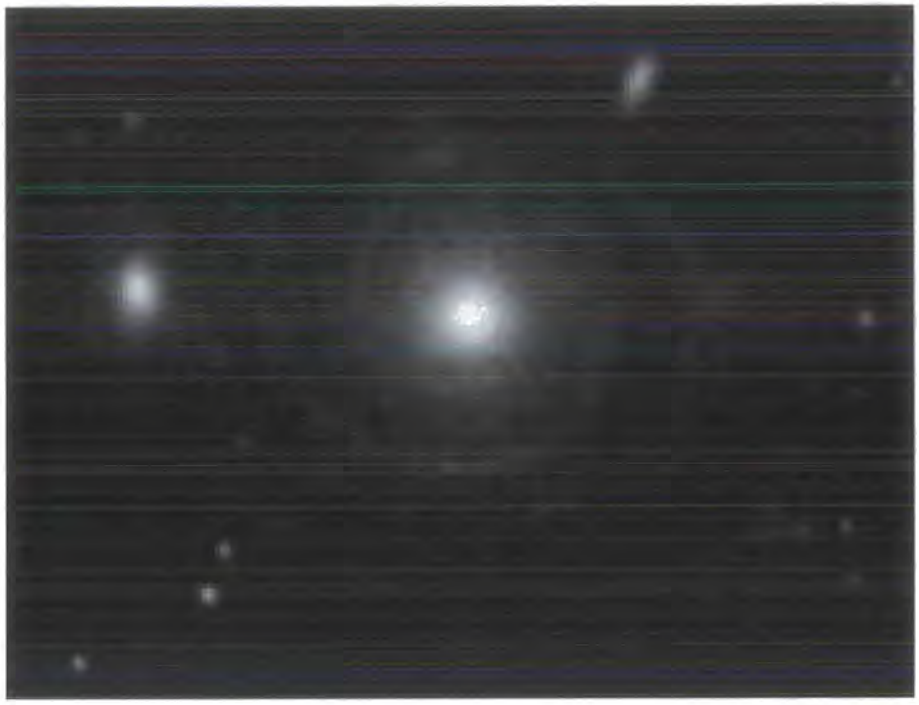

Figure 5.1: DSS intensity image of Mkn 348 and NPM1G +31.0016

al. (1996) suggest, in line with previous work and unification schemes, that these regions have an unobscured (or less obscured) view of the nucleus, and so are of higher ionization than elsewhere.

Colour maps by Mulchaey *et al.* (1996) [163] found a slight blue excess co-incident with the southern excitation peak, which could represent a scattered nuclear continuum. Kotilainen & Ward (1997) [127] found in their $B - I$ colour map of Mkn 348, a faint blue ring-like structure of diameter approximately 3 arcseconds, elongated along position angle 15° and also suggested this too may be due to scattered nuclear light. Figure 5.2 gives a diagram showing visually a scheme (not to scale) showing the regions and axes of the various observations for easier comparison. It also shows the angle of polarization of the nuclear optical polarization measured in this study.

5.2.2 Observational details

Mkn 348 was observed on the 8th of August 1991 with the 2.5 m Issac Newton Telescope (INT) in La Palma, the Canary Islands. The Cassegrain focus with focal ratio of 15 was used, and observations were taken using a broad band V filter. For this configuration, the scale of the sky on the CCD detector of the Durham Imaging Polarimeter was 0.49 arcseconds per CCD pixel, covering a total field of approximately 4.6 arcminutes by 3.4 arcminutes. At the estimated distance of 61 Mpc, assuming $H_0 = 75$ km s^{-1} Mpc^{-1}, 1

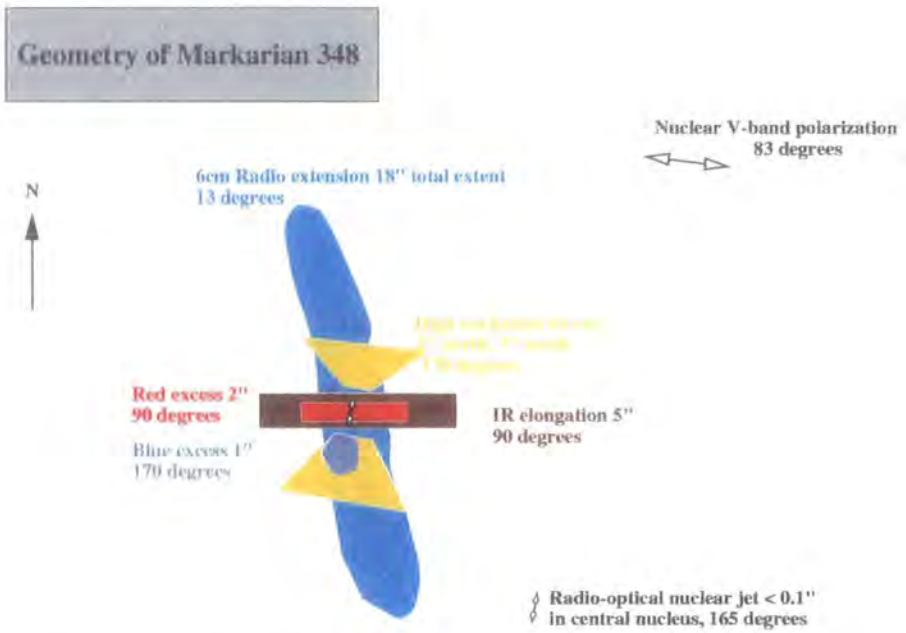

Figure 5.2: Diagram of the axes of observations of Mkn 348

arcsecond corresponds to approximately 300 pc. The seeing on this night was calculated to be approximately 1.5 arcseconds by using star images in the field as point sources.

Data were taken at one position only since most of the galaxy fitted onto one grid space on the detector. Four CCD frames of the object, each of 600 seconds, together with suitable flatfield frames were taken. Fortuitously, another galaxy just to the east of Mkn 348 was simultaneously centred on another of the grid spaces on the detector, so a polarization map of this galaxy was also made from these same CCD frames. A search in the extragalactic database (NED) around the measured co-ordinates of this galaxy reveals it to be the object NPM1G +31.0016. A digital sky survey (DSS) second generation blue image of the field (4 arcminutes by 3 arcminutes) mapped in these observations is given in figure 5.1, orientated with north to the top, east to the left, showing Mkn 348 as the central galaxy, with NPM1G +31.0016 located due east.

5.2.3 Image details

Figures 5.3 to 5.12 present broad V-band images of Mkn 348, and figures 5.13 to 5.15 give images of NPM1G +31.0016, all with north to the top and east to the left. The scale is in arcseconds, centred on the peak nuclear total intensity of the image. Unless otherwise stated, the greyscale and contour maps represent the total intensity images, with black representing the highest intensity. The contours of the maps are plotted logarithmically. The polarization vectors overlaid on the images were calculated by binning the polarization

data in square bins, and moving on by a set number of pixels for the next polarization vector to be calculated and plotted. The square sizes and step sizes are either 5 pixels moved on by 3 pixels, or 3 pixels moved on by 2 pixels. Since the shift (step size) is less than the size of the bins, this has the effect of smoothing the polarization data, because the bins overlap. To check on the continuity of the polarization therefore, figure 5.7 and 5.8 give maps where the 3 by 3 pixel bins are moved on by 3 pixels so they do not overlap. The polarization vectors are plotted with polarized intensity cuts and or total intensity cuts set appropriately to the noise levels in the maps.

Following convention, the orientation of polarization vectors represents the direction of the electric field and the percentage linear polarization is indicated by the length of the vector. Figures 5.9 and 5.10 give on the left-hand side a polarized intensity greyscale map overlaid with polarization vectors, where the darker shades represent higher polarized intensity. The right-hand sides of these figures show contour maps of total intensity overlaid with polarization vectors.

5.2.4 Interstellar polarization

The galactic co-ordinates ($l = 123°$, $b = -31°$) of Mkn 348 show that although it is not seen directly along the our galactic plane, it is seen close to the plane and therefore still seen through a considerable amount of the interstellar medium, so that some ISP correction might be expected. Also from the high E_{B-V} value of 0.24 in table 4.6, and using Serkowski's finding that the ISP level generally falls between 2 and 9 times the E_{B-V} value, Serkowski *et al.* (1975), then it is to be expected that the ISP correction would likely be about the level of 1%. Previous authors have made ISP estimates for Mkn 348 from measuring the polarization of nearby stars, assuming them to be intrinsically unpolarized, and therefore to be polarized due to ISP only. The general tendency of the polarization vectors to be oriented around 130° can be attributed to an ISP effect, in which case the angle of the ISP would be expected be in the region of 130°.

As the general (uncorrected) levels of polarization in the galaxy are quite low, around 1% to 1.5%, they will be very sensitive to the value of the ISP correction applied because this is of a similar level. It is, therefore, important to estimate the ISP as accurately as possible, and since there is considerable uncertainty in the ISP determination as is explained in the following section, maps corrected for different ISP values from different sources are presented for comparison and discussion.

Previous ISP estimates

Miller & Goodrich (1990) [160] note that the star HD 147550 is only 25 arcseconds away, and they use the polarization measurements by Mathewson & Ford (1970) [150] of 1.08% ± 0.03% at position angle 81.1°± 0.15° of this star to represent the ISP in their study of the nuclear polarization. A correction for this value of ISP was applied to the polarization map of Mkn 348, but on examination or the resulting map this did not seem to have significantly affected the polarization pattern. Most importantly the pattern still shows the same general alignment feature which was attributed to ISP in the original uncorrected maps, implying the correction was unsuccessful. Also it certainly did not make the distorted centro-symmetric scattering pattern become more clearly centro-symmetric as would be expected after correction. Hence, this value of ISP is not consistent with the results of the observations in this thesis.

Tran (1995) [230] observed the polarization of 4 foreground stars close to Mkn 348, located from 35 to 100 arcseconds away. Eliminating one on the grounds that it had a highly anomalous polarization compared to the others, he fitted the remaining three to a Serkowski style polarization law (section 2.3.5). The parameters he obtained for this law are given in table 4.2. Using these Serkowski parameters, the expected ISP at 5450Å (*i.e.* the mean wavelength of the V filter used in this study), can be calculated to give a value of 1.07% polarization at 114°. After correction for this value of ISP, the polarization patterns in the maps of both Mkn 348 and NPM1G +31.0016 (another galaxy in the field, detailed in section 5.2.7) become more plausible in terms of the centro-symmetric patterns expected from scattering, and removal of the large-scale general alignment feature attributed to ISP. Since Tran's estimate seems more plausible than Miller & Goodrich's estimate, Tran's figure of 1.07% at 114° has therefore been adopted as an ISP value (ISP_{Tran1}) in order to produce ISP corrected maps for Mkn 348 in this thesis.

Under closer investigation, it can be seen that the polarization of the three stars measured and averaged by Tran varied quite significantly (from 0.82% to 1.66%), with one star having a much higher polarization than the other two. Therefore, if this high polarization star is disregarded, an alternative ISP (ISP_{Tran2}) value of 0.87% at a position angle of 116° can be calculated using the average of the other two better matched stars (SAO 54135 and PPM 65618). This ISP_{Tran2} correction was applied to the map of NPM1G +31.0016 shown in figure 5.15. The justification for this ISP value is that the maps corrected for this value seem more plausible, as can be seen particularly in the map of NPM1G +31.0016 in figure 5.15 and explained in the next section. Since centro-symmetry is the most likely polarization pattern to be expected from a normal galaxy at low resolution (because of scattering from the bright central source), a more centro-symmetric pattern is likely to imply that this ISP correction, 0.87% at 116° is probably a better estimate. Therefore

this ISP correction (ISP_{Tran2}) has also been applied to a map of Mkn 348 for comparison in figure 5.12.

Determination of an ISP estimate

Although there exist ISP estimates from different observations, obviously it is important to try to calculate an ISP estimate from the actual observations of Mkn 348 made in this study, because then systematic errors will be minimised. Efforts therefore were made to calculate an ISP value from stars in the field around Mkn 348 in the observations taken for this thesis. However, because the field of the image is small, and there was only partial coverage, only two stars bright enough for polarization calculation were included in field. Unfortunately both of these were close located close to grid edges and were affected by light leaking round the grid edge, so the noise levels were too high for meaningful polarization to be measured. Two extended objects, the galaxy NPM1G +31.0016 and a much smaller galaxy were also in the image field. The very small galaxy was close to a grid edge, and the resulting low signal-to-noise levels did not allow meaningful polarization measurements.

The other galaxy in the field, NPM1G +31.0016 however, had a good signal-to-noise level in the nuclear region, and after a local sky subtraction, the polarization was measured over apertures from 2 to 6 arcseconds and found to be remarkably consistent, with reasonably small error estimates over the larger apertures. These polarization measurements are presented in table 5.1. Taking the average value over the 4, 5 and 6 arcsecond apertures because they have lower error estimates and are consistent with the other values, the average nuclear polarization is 0.61% at 116°. Assuming this galaxy nucleus to be intrinsically unpolarized, this can be taken as an alternative estimate of ISP. Since this value is calculated from the same data set as Mkn 348 data and is within an arcminute of the line of sight, it will be matched in terms of the instrument and observation conditions, so it is hoped this may be an accurate estimation. It is however, only one measurement rather than an average, and rests on the assumption that the nucleus of this galaxy is intrinsically unpolarized. This ISP (ISP_{Felton}) value has been applied to Mkn 348 in figure 5.11.

Table 5.1: V-band nuclear aperture polarimetry of NPM1G +31.0016 (ISP uncorrected)

Aperture (arcsec)	Aperture (pixels)	Polarization (percent)	Position angle (degrees)
2	4.1	0.53 ± 0.72	118°± 35°
2.5	5.1	0.60 ± 0.65	124°± 31°
3	6.1	0.61 ± 0.49	120°± 23°
4	8.2	0.61 ± 0.23	113°± 11°
5	10.2	0.61 ± 0.08	117°± 4°
6	12.2	0.62 ± 0.03	119°± 2°

5.2.5 Results: V-band

The pattern of the polarization vectors measured over Mkn 348 in figures 5.3, 5.5 and 5.7 show signs of the influence of three different polarization components: a general alignment effect, a localised nuclear polarization, and hints of centro-symmetry.

There is a general tendency for vectors to be orientated around an angle of about 130° to 140° over most of the map except the very central regions. The central few arcseconds show a polarization oriented at an angle of 90°, with an enhancement in polarization level compared to the surrounding region of the galaxy. There are faint signs of a centro-symmetric pattern of vectors appearing to centre around the nuclear region. This is seen more clearly in the higher resolution of polarization data in figure 5.5, as the vector orientations tend to curve around the centre.

The centro-symmetry in the pattern is seen more clearly in the north-east and south-west outer parts of the galaxy. The outermost polarization vectors which are plotted in the regions of lowest intensity, are strongly affected by noise in the data since the signal is lower, as can by seen by the loss of continuity in the polarization vectors, as they seem to become more randomized. Figure 5.7, where the polarization vectors are calculated in independent bins (*i.e.* not smoothed), gives a check on the reliability of the polarization patterns observed: the continuity of the orientations of the polarization vectors in this map, and the similarity in pattern between this map and the other smoothed maps shows that the smoothing procedure has not introduced artefacts in the polarization.

The centro-symmetric pattern of vectors suggests that nuclear light is being scattered by dust or electrons in circumnuclear region of the galaxy. The strong polarization around the nucleus as seen in the maps of polarized intensity indicates that a separate nuclear polarization mechanism is in operation, consistent with the presence of a strong Seyfert

nucleus, since Seyfert nuclei are predicted to be intrinsically polarized. The general tendency for alignment around 130° to 140°, which is distorting the other two patterns implies that this is polarization by dichroic extinction from a broad dust band where the dust grains are significantly aligned. Since this is a broad ranging effect, all over the galaxy, interstellar polarization (ISP) in this galaxy is a likely candidate mechanism and is discussed further in section 5.2.5.

Nuclear polarimetry

Aperture polarimetry centred on the peak nuclear intensity is given in table 5.2, with circular aperture diameters ranging from 2 to 6 arcseconds. Using an aperture of 3 arcseconds centred on the peak nuclear total intensity, the Seyfert nuclear polarization is 1.89% ± 0.21% at an angle 91.7°± 3.1°. It can be seen that the level of polarization in the nucleus is dependent on the aperture used for the measurement, decreasing as the aperture becomes larger. This suggests that the intrinsic Seyfert nuclear polarization is being diluted by the starlight from the galaxy.

Previously published measurements of nuclear polarizations are listed in table 5.2 for comparison with the values measured in this thesis (the hyphens indicate that the information was not available). These can not be compared directly, because most are from spectro-polarimetric observations averaged over a variety of wavelength ranges, slit widths, lengths and orientations, or they are made through a blue-green filter rather than the broad V-band filter that was used in this study. To try to partially compensate for the different sized apertures and slit dimensions, the polarizations in table 5.2 and table 5.3 should be compared to the corresponding closest aperture size. It can be seen that the corresponding polarization levels from this study are in good agreement with previously published values within the calculated errors, but the polarization angles in this study are consistently greater by about 6° to 10° than the average of the other values. This appears strange, because it is not obviously a systematic offset error in the telescope observing run, because other observations in the same run do not show this offset - for example those of Mkn 573 also presented in this thesis, and there were no obvious problems during these particular observations or calculation of the polarization values. This anomaly suggests that either the polarization angle measurement is very sensitive to the exact wavelength range/filter used or exact aperture so can't be compared equivalently, or perhaps because the polarization angle has intrinsically changed. Further observations with the same filter would help resolve this.

The polarization angle varies very little over all the other previous measurements in table 5.2; at around 84°, it is perpendicular to the nuclear radio axis which is at 170°

(Gorjian 1995 [89]). The measurement from this study gives a higher value of around 92°as discussed in the previous paragraph, but which is still approximately perpendicular to the nuclear radio axis. The large scale radio emission however, extends up to 18 arcseconds along position angle 13° (Baum 1993 [24]) or 22° (Nagar *et al.* 1999b [166]). In figure 5.9, it may be noted that the polarized intensity is slightly elongated along a position angle of about 25° in the south-west part of the galaxy.

Young *et al.* (1996) [272] made multi-wavelength spectro-polarimetric measurements of the nucleus of Mkn 348 in U, B, V, R, I, H and K bands, and these are shown in table 5.4. In the V-band, they measure 1.60% ± 0.06% at 88°± 1°which is in good agreement within the errors, to the measurements with a 5 arcsecond aperture in this thesis (1.60% ± 0.33% at 94°± 6°).

The polarization measurements by Young *et al.* (1996) show a strong U-shaped wavelength dependence, rising in the blue and infra-red regions. These values though are not corrected for interstellar polarization, of which the importance and level of are discussed in the following section. Since the ISP correction is both wavelength-dependent and of significant magnitude, it is necessary to examine the effect of that ISP would have across the whole wavelength region to be confident of a particular wavelength dependence. Using the ISP value calculated by Tran (1995) [230], and assuming it to follow the Serkowski law calculated for our galaxy (section 2.3.5), then in the infra-red regions the ISP correction will be very small (0.16% at 114° in K band), and would make very little difference to the high polarization in that band, so the observed polarization rise in the infra-red is real. In the blue/near-UV band, although the ISP correction is higher (1.12% at 114° in U band), the measured polarization is much higher still (3.42% at 82°), so that applying these ISP corrections will not change the U-shape of the variation of polarization with wavelength.

This type of wavelength dependence has been successfully modelled by electron scattering in a cone-based geometry by Young *et al.* (1996) [272]). Rayleigh scattering (in a cone geometry) was ruled out by these authors on the basis that it is unable to produce sufficient polarized optical flux in relation to the polarized infra-red flux that is seen through the torus, assuming that the central source gives a Seyfert 1 type spectrum obscured through a dusty torus. The rise in infra-red polarization may also require an additional polarizing mechanism, either dichroic absorption or that the grains that are emitting infra-red radiation are themselves aligned, and hence emit partially polarized light. Alternatively, the scattering geometry of the region producing radiation may be different at infra-red wavelengths *i.e.* scattering would be observed closer to the nucleus, which then could not be considered as a point source, thus affecting the polarization characteristics.

Table 5.2: V-band nuclear aperture polarimetry of Mkn 348 (Not corrected for ISP)

Aperture (arcsec)	Aperture (pixels)	Polarization (percent)	Position angle (degrees)
2	4.1	2.04 ± 0.10	90.3° ± 1.3°
2.5	5.1	1.99 ± 0.11	91.1° ± 1.5°
3	6.1	1.89 ± 0.21	91.7° ± 3.1°
4	8.2	1.73 ± 0.29	93.0° ± 4.8°
5	10.2	1.60 ± 0.33	94.2° ± 5.8°
6	12.2	1.51 ± 0.30	95.1° ± 6.7°

Table 5.3: Comparison of nuclear polarization measurements of Mkn 348 (Not corrected for ISP)

Range of wavelength Ångstroms	Aperture or slit width (arcsec)	Polarization level (percent)	Position angle (degrees)	Reference[1]
4600 - 7400[2]	2.4	1.74 ± 0.10	84.5 ± 2.7	T95
3300 - 4400[2]	2.4	2.96 ± 0.20	83.3 ± 2.5	T95
5100 - 6200[2]	2.4	1.78	83	T95
3200 - 6200[2]	2	1.93 ± 0.07	85.9 ± 1.1	K94
3200 - 6200[2]	2	2.32 ± 0.05	84.2 ± 0.6	K94
4189 - 6909[2]	-	1.48 ± 0.05	84.6 ± 0.8	MG90
4400 - 7200[2]	-	1.42 ± 0.04	84.1 ± 0.8	MG90
3250 - 6250[2]	-	2.09 ± 0.07	82.9 ± 1.0	MG90
3800 - 5600[3]	4	1.53 ± 0.32	86.4 ± 6.0	M83
3800 - 5600[3]	4	2.05 ± 0.31	83.6 ± 4.3	M83

[1]References: T95 = Tran (1995), MG90 = Miller & Goodrich (1990), K94 = Kay (1994), M83 = Martin (1983)
[2]Spectro-Polarimetry
[3]Survey using a blue-green Corning 4-96 filter (3800-5600 Å)

Table 5.4: Multi-wavelength nuclear polarization measurements by Young 1996 (Not corrected for ISP)

Band name	Nominal wavelength (Å)	Aperture (arcsec)	Polarization (percent)	Position angle (degrees)
U	3500	5	3.42±0.23	82±2
B	4400	5	2.04±0.10	81±2
V	5500	5	1.60±0.06	88±1
R	6600	5	1.32±0.06	85±1
I	8800	5	1.02±0.13	88±4
H	16000	5	0.69±0.14	85±6
K	22000	5	1.89±0.30	77±5

5.2.6 Results: V-band - after correction for ISP

These ISP-corrected polarization maps, figures 5.4, 5.6, 5.8, 5.10, 5.11 and 5.12, show some differences to the uncorrected ones because in general the levels of polarization are low (around 1%), and the ISP correction is of a similar level. Figure 5.6 has the polarization vectors binned into 1.5 arcsecond squares, which is at the limit of the seeing for that night so the fine structure should be interpreted cautiously. In figures 5.4, 5.6, 5.11 and 5.12 the vectors are binned into larger 2.4 arcsecond squares, which might smooth over any small-scale detail, but the average values will be more reliable.

Polarization in the host galaxy

Figures 5.4, 5.6 and 5.8 give maps corrected for Tran's ISP estimate of 1.07% at 114° (referred to hereafter as ISP_{Tran1}). The polarization levels in the south-west and north-east quarters of the galaxy are generally reduced after correction for ISP. Considering an imaginary line bisecting the galaxy diagonally from the north-east to south-west, the polarization are generally slightly higher over the south-east half of the galaxy. This can be seen most clearly in the polarization map in figure 5.4. The polarization vectors show a general centro-symmetric pattern around the nuclear region more clearly than before ISP correction, which more strongly indicates scattering of the central light source in the galaxy, and suggests that the ISP correction is at least partially successful. The polarization measurements in the circumnuclear area (within a radius of 4 arcseconds) show a different pattern, a broad alignment across the nucleus with a polarization position angle of approximately 75°.

Figure 5.11 gives a map corrected for the estimate of ISP derived in this study (0.61%

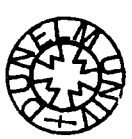

at 116°), and figure 5.12 is corrected for the second ISP value derived from Tran's measurements (ISP_{Tran2}, 0.87% at 116°). They are not strikingly different from the maps corrected for Tran's first ISP estimate.

Since in spiral galaxies the polarization tends to follow the spiral structure, and Mulchaey *et al.* (1996) [163] detect faint H_α spiral arms in this galaxy, their H_α image was compared to the polarization maps here to see whether any indication of the spiral arm or inter-arm pattern could be found. There does not seem to be any evidence of this in the polarization maps, but it is difficult to discern because the spiral arm structure is very faint and unclear, and the nuclear polarization resolution is not sufficiently high to be able to show a pattern in the central regions where the spiral arm structure is most apparent. Deeper H_α imaging and higher resolution polarization mapping including using an H_α filter would determine whether there is any spiral pattern.

As partially seen in the uncorrected maps, it may be noticed that the polarized intensity map in figure 5.10, with polarization vectors plotted reasonable signal-to-noise cuts, shows faint extensions of higher polarization along position angles of $\approx$ 22° (in the south west), 165° (in the north west) and 90° (in the west). Interestingly, there is large scale radio emission which extends along position angle 22° (Nagar *et al.* 1999b [166]), and the nuclear radio axis is 168° (Neff & de Bruyn 1983 [167]), which allows for the possibility that the polarization is being enhanced along these regions, because of some process linked to the ejection of material from the nucleus.

Polarization of the nucleus

Aperture polarimetry measurements of the nucleus over different aperture diameters with ISP correction are given in table 5.5. Over an aperture of 3 arcseconds, the ISP_{Tran1} corrected nuclear polarization is 1.40% ± 0.28% at 75°± 5°, or using the ISP derived in this thesis, the nuclear polarization is 1.55% ± 0.28% at 84°± 5°. This position angle is perpendicular to the orientation angle of the double optical nuclei and linear triple radio source ($\approx$ 170°). This could be used to lend some support to Gorjian's interpretation of these two optical nuclei both being ejecta from an obscured core, since this would fit in with the trend of Seyfert 2 nuclei having nuclear polarizations perpendicular to the axis of any ejected material. Figure 5.2 shows visually the axes of various previous observations of Mkn 348 together with the angle of polarization for easier comparison.

These ISP corrected measurements can be compared to the other published values given in table 5.6. However here comparison is of very limited use, because each author uses a different value of ISP: Tran uses 1.14% at 114° (for λ = 4050Å); Miller & Goodrich

used 1.08% at 81°; Kay does not specify the ISP value used; and Miller & Goodrich do not quote the ISP corrected nuclear polarization level (they only quote the polarization level after their corrections for both starlight dilution and ISP combined). In all measurements except for those of Miller & Goodrich, the angle of polarization decreases after ISP correction. Curiously the level of polarization is stated to increase after Kay's ISP correction, but for this study, the nuclear polarization levels were found to be lower after ISP correction. Since Kay does not quote the ISP levels used, this is presumably due to Kay either using a significantly different ISP correction, or differences in locations and sizes of the apertures of the different studies.

The map of ISP_{Tran1}-corrected polarized intensity plotted as greyscale is shown in figure 5.10 alongside a map of total intensity on the right-hand side. Very little nuclear structure can be resolved, but it is notable that the polarized intensity in the nuclear region (central few arcseconds) is elongated towards the south west, which is approximately similar to the emission-line excitation map of $[O_{III}/H_\alpha]$ by Falcke *et al.* (1998) [74], and to the location of the blue excess found by Mulchaey (1996) [162]. Higher resolution polarization maps would reveal whether there is an increase in polarized flux associated with these regions, which would be expected if the blue excess is due to scattered nuclear light. It appears similar to the case of NGC 1068, where the nuclear optical light is not visible directly as the absorbing column is too thick, but electron scatterers scatter some of the optical continuum into the line of sight and polarize it.

Spectro-polarimetric measurements of the nucleus of Mkn 348 made by Miller & Goodrich [160] and Tran [230], show broad lines in polarized light indicating a hidden Seyfert 1 type nucleus. They also observe a rise in polarization towards the shorter wavelengths, thought to be due to starlight dilution, and Tran suggests electrons are the major scatterers. The polarization is twice as great in the broad lines as in the adjacent continuum with a shift in polarization angle. After correction for interstellar polarization however, the position angle of the polarization of the continuum between H_α and H_β is approximately the same as in the polarized broad lines, and the value of 65° is close to the ISP corrected measurements made in this thesis in the V-band (using the same ISP values). Using an elliptical galaxy template to correct for the starlight dilution from the galaxy's nuclear regions, Tran estimates the contribution of the nuclear FC (featureless continuum) to be 27% at 5500Å, but only 5% out of this 27% is the expected polarized featureless continuum (FC1), thus requiring an additional unpolarized featureless continuum (FC2) to account for the remaining 22%.

Further investigation by Storchi-Bergmann *et al.* (1998) [222] using high signal-to-noise spectrometry of the circumnuclear region (at 4 arcseconds from the nucleus) found that the nuclear stellar population has a greater number of young blue stars than a standard

Table 5.5: V-band nuclear aperture polarimetry of Mkn 348 (ISP corrected)

Aperture (arcsec)	Aperture (pixels)	Polarization (percent)	Position angle (degrees)
ISP correction of 1.07% at 114°			
2	4.1	1.58% ± 0.29%	75°± 4°
2.5	5.1	1.49% ± 0.29%	75°± 4°
3	6.1	1.40% ± 0.28%	75°± 5°
4	8.2	1.20% ± 0.29%	75°± 5°
5	10.2	1.07% ± 0.29%	74°± 6°
6	12.2	0.96% ± 0.30%	73°± 6°
ISP correction of 0.61% at 116°			
2	4.1	1.72% ± 0.29%	82.5°± 4°
2.5	5.1	1.66% ± 0.29%	83°± 4°
3	6.1	1.55% ± 0.28%	84°± 5°
4	8.2	1.38% ± 0.29%	83°± 5°
5	10.2	1.24% ± 0.29%	85°± 6°
6	12.2	1.14% ± 0.30%	85°± 6°

elliptical template, so such a template is not adequate to subtract the starlight. A better representation of the nuclear stellar population would be the spectra of the immediate circumnuclear region. Using this method of correction for starlight, they estimated a starlight flux contribution of over 90% to the nuclear (the inner 2 arcsecond) spectrum plus a nuclear featureless continuum contribution of only 9% at 5176Å. There is then no need for a second unpolarized featureless continuum component (FC2 as required by Tran) in addition to the stellar and reflected nuclear contributions. If these relative contributions to the nuclear flux are correct, then the ISP-corrected polarization of 1.6-1.7% measured over the the inner 2 arcseconds in this thesis, implies a high intrinsic nuclear polarization of up to around 16%, which is even higher than necessary to be consistent with the levels found in models of emission from typical Seyfert accretion disk/black-hole systems. For electron scattering in the ionized atmosphere of an accretion disk, , Chandrasekhar (1960) [42] shows that for a disk with an inclination of 90°, the expected polarization is 11.7%, but only 7.5% at an inclination of 84°, with the angle of polarization being parallel to the projected surface of the disk.

Table 5.6: Comparison of nuclear polarization measurements of Mkn 348 (ISP corrected)

Range of wavelength (Ångstroms)	Aperture or slit width (arcsec)	Polarization level (percent)	Polarization angle (degrees)	Reference[1]
V-band (5450)[2]	2	1.45 ± 0.29	75 ± 6	F99
5200 - 6200[3]	2.4	≈ 1.5	≈ 65	T95
4150 - 4650[3]	2	3.15 ± 0.17	78.9 ± 1.1	K94
4500 - 6200[3]	-	-	84	MG90

[1]References: F99 = this thesis (1999), T95 = Tran (1995), K94 = Kay (1994)
[2]Imaging using a broad band V filter with a 3 arcsecond aperture
[3]Spectro-Polarimetry

Table 5.7: Polarization of the nuclear featureless continuum corrected for reddening, ISP and dilution

Wavelength range (Ångstroms)	Reddening E_{B-V}	Starlight flux (fraction)	Corrected polarization (percent)	Corrected angle of polarization (degrees)	Reference
4150 - 4650	0.06	0.65	9.09 ± 0.42	78.9 ± 1.3	K94
5100 - 6200	0.06	0.73	5.7	65	T95
5100 - 6100	0.24	0.53	2.5	84	MG90

5.2.7 NPM1G +31.0016

NPM1G +31.0016 is a galaxy to the east of Mkn 348. The extragalactic database, NED, does not include a type class or redshift, only that it has a magnitude of 15.79 and is listed in the Northern Proper Motion program catalogue. These are the first polarization measurements published for this galaxy.

NPM1G +31.0016, mapped with data from the same field as Mkn 348, is shown in figures 5.13 to 5.15. It shows a distinct polarization structure. The ISP uncorrected map in figure 5.13 shows a pattern which shows signs of centro-symmetry, hinting at a scattering mechanism, but somewhat distorted. It is possible to see a general preferred direction of an alignment all over the galaxy, suggesting foreground ISP effects. After correction for the ISP value (1.07% at 114°) calculated by Tran (1995), figure 5.14 shows that the polarization pattern is more centro-symmetric around most of the galaxy, implying polarization by scattering, although elongated somewhat along the galaxy's major axis. The levels of polarization are slightly higher in the north than around the south of the galaxy.

Aperture polarimetry of the nucleus is presented in table 5.1. This shows a very consistent value for all the aperture sizes, of 0.61% at 116° when averaged over the 4, 5, and 6 arcsecond aperture measurements, where the error estimates are reasonably small. If it is assumed that the nucleus of this galaxy is intrinsically unpolarized, then this polarization value can be taken as the value for interstellar polarization. After correcting the polarization map for this value, figure 5.15 shows that the polarization pattern has a clearer centro-symmetric pattern than the uncorrected map, characteristic of scattering, however it is not appreciably different to the map corrected for Tran's original ISP estimate of 1.07% at 114°.

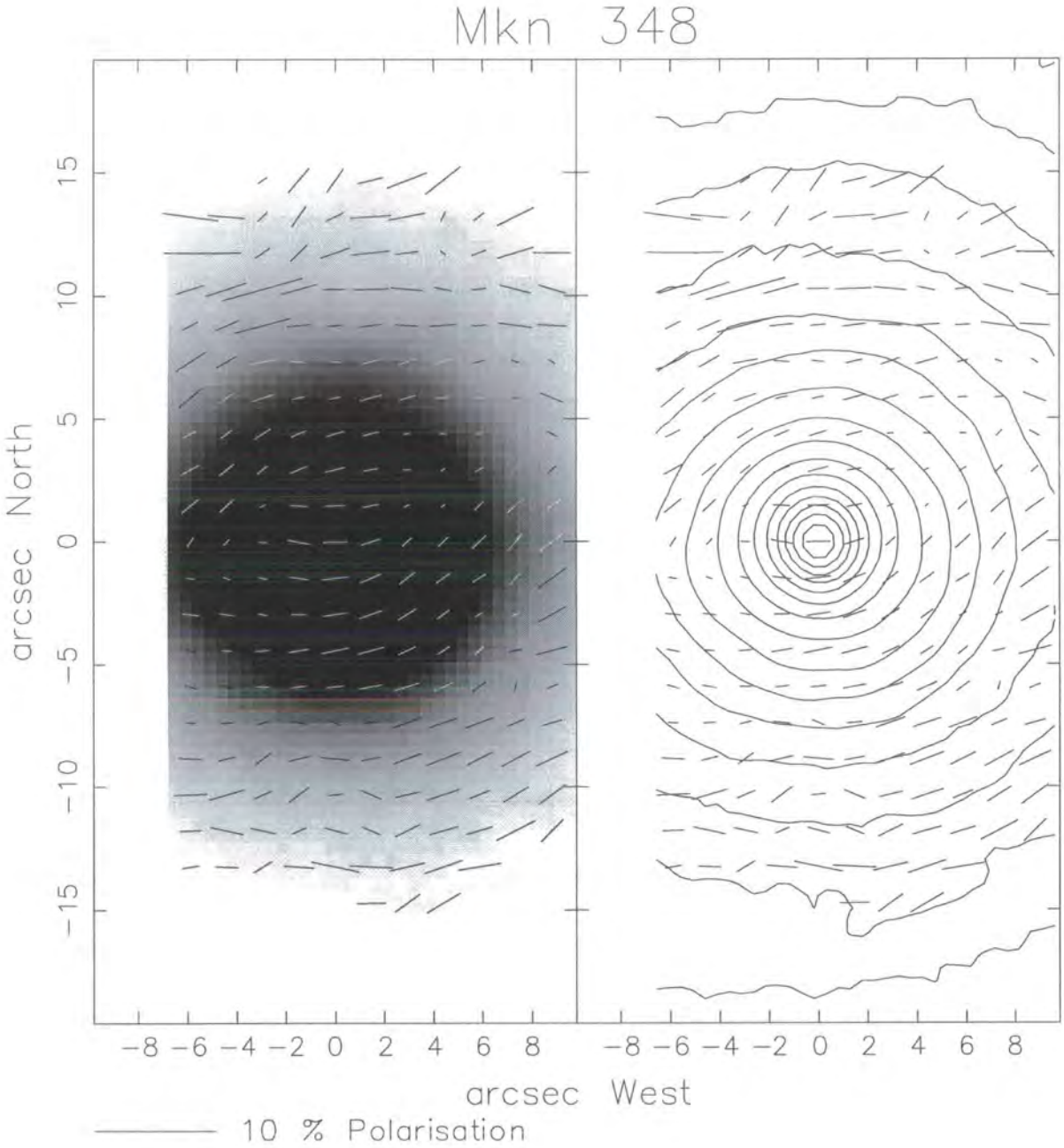

Figure 5.3: V-band total intensity images of Mkn 348, overlaid with polarization vectors binned with square size 5 and step size 3, uncorrected for ISP

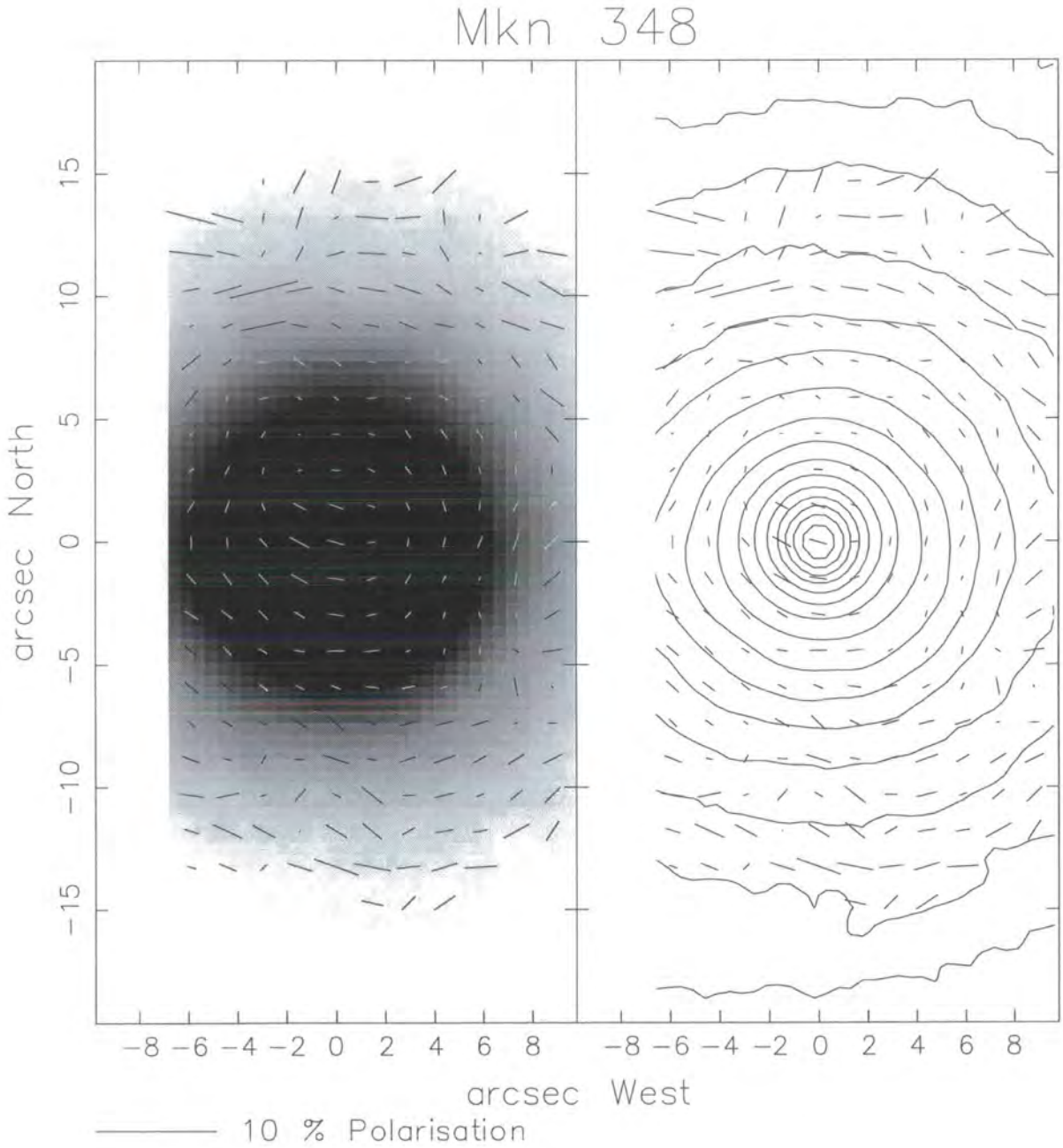

Figure 5.4: V-band total intensity images of Mkn 348, overlaid with polarization vectors binned with square size 5 and step size 3, corrected for ISP_{Tran1}

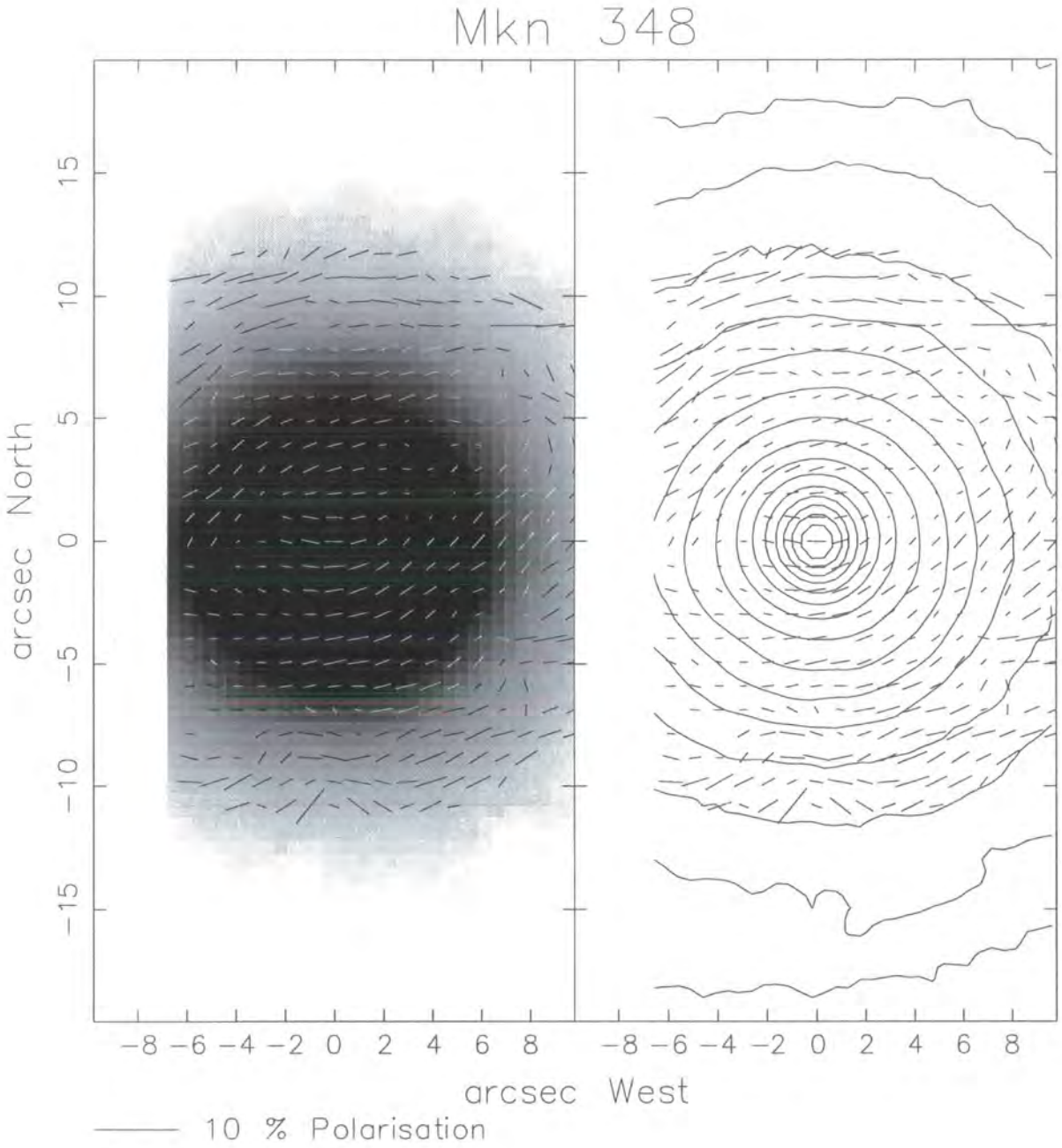

Figure 5.5: V-band total intensity images of Mkn 348, overlaid with polarization vectors binned with square size 3 and step size 2, uncorrected for ISP

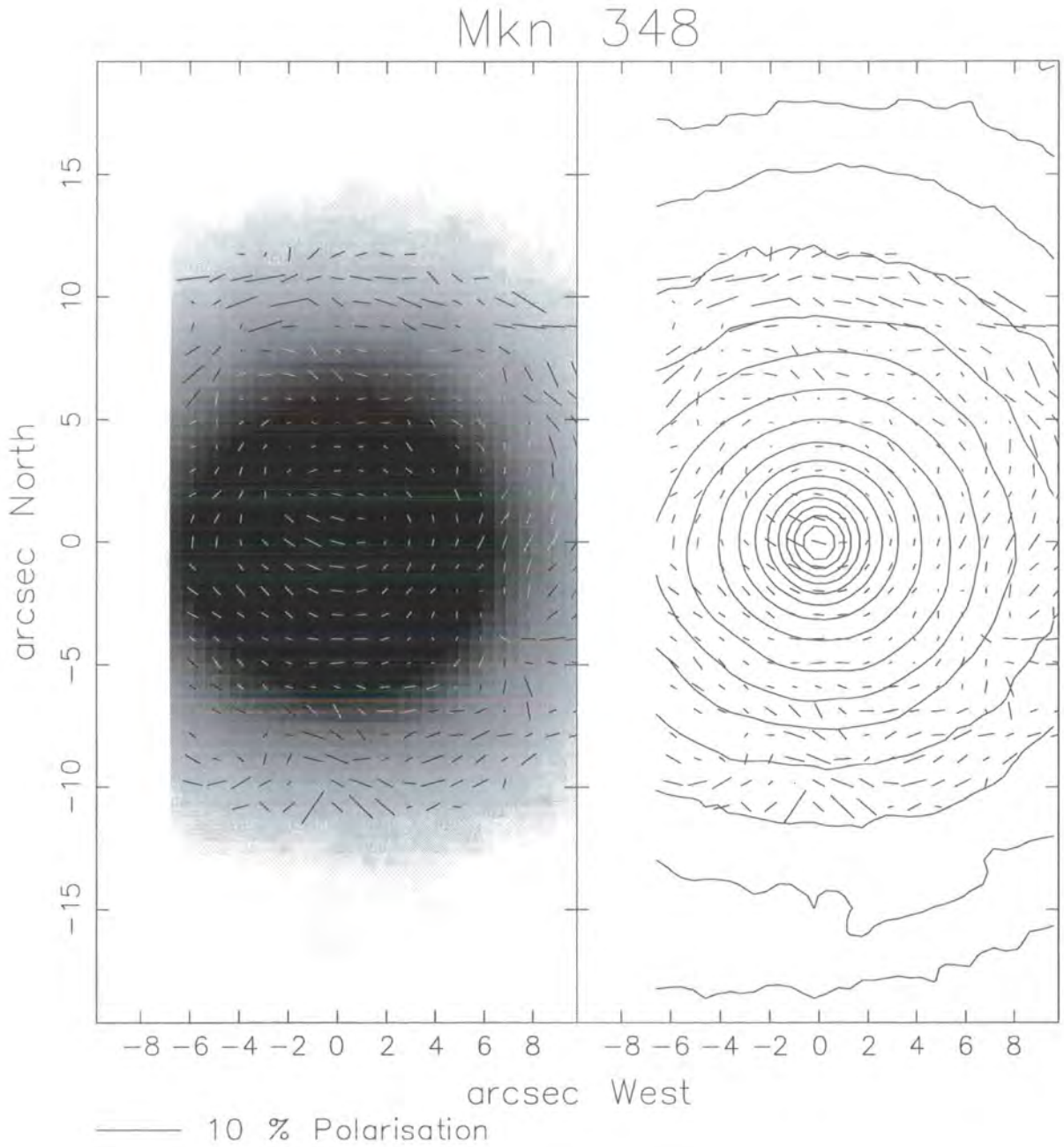

Figure 5.6: V-band total intensity images of Mkn 348, overlaid with polarization vectors binned with square size 3 and step size 2, corrected for ISP_{Tran1}

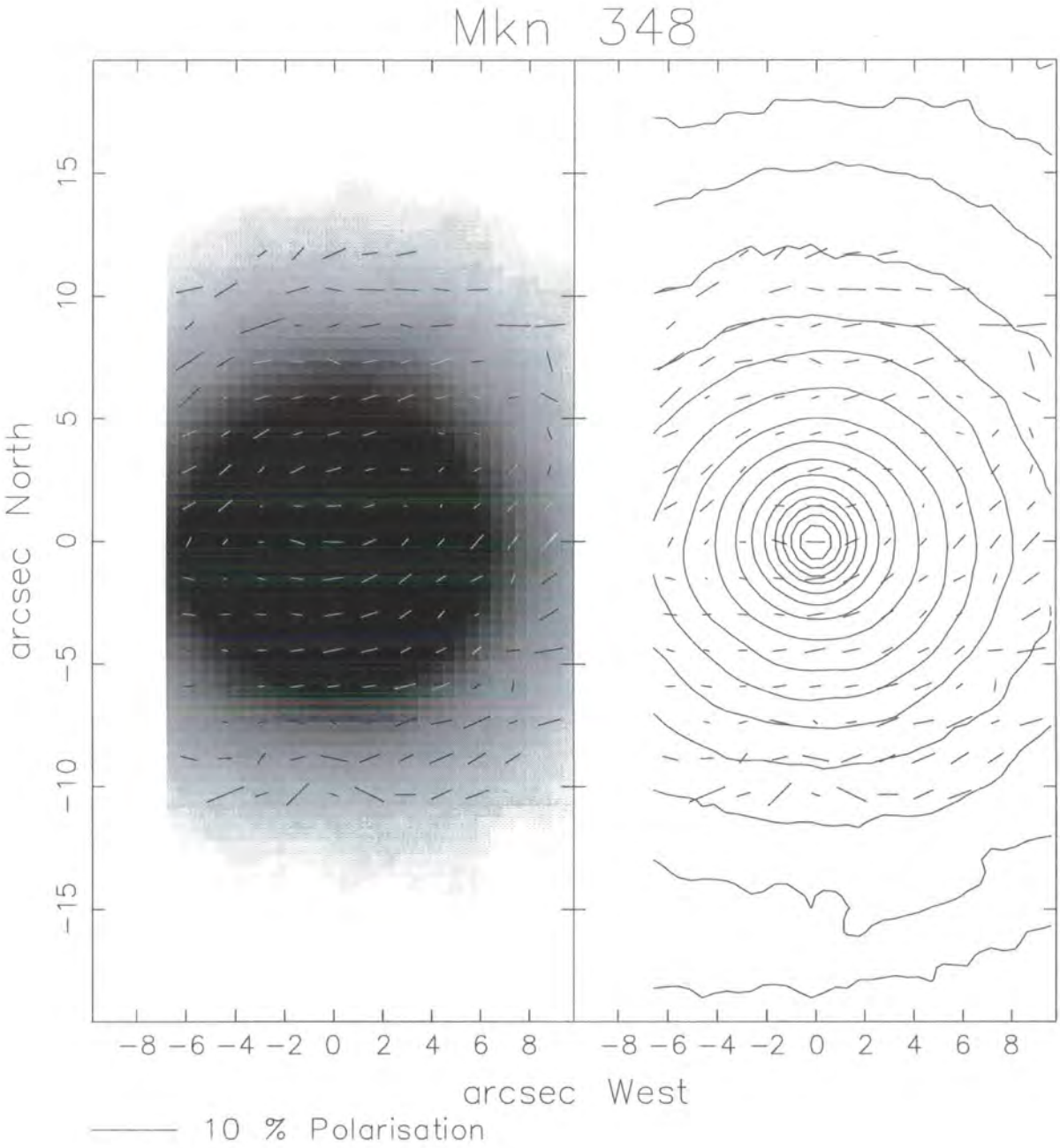

Figure 5.7: V-band total intensity images of Mkn 348, overlaid with polarization vectors binned with square size 3 and step size 3 (not smoothed), uncorrected for ISP

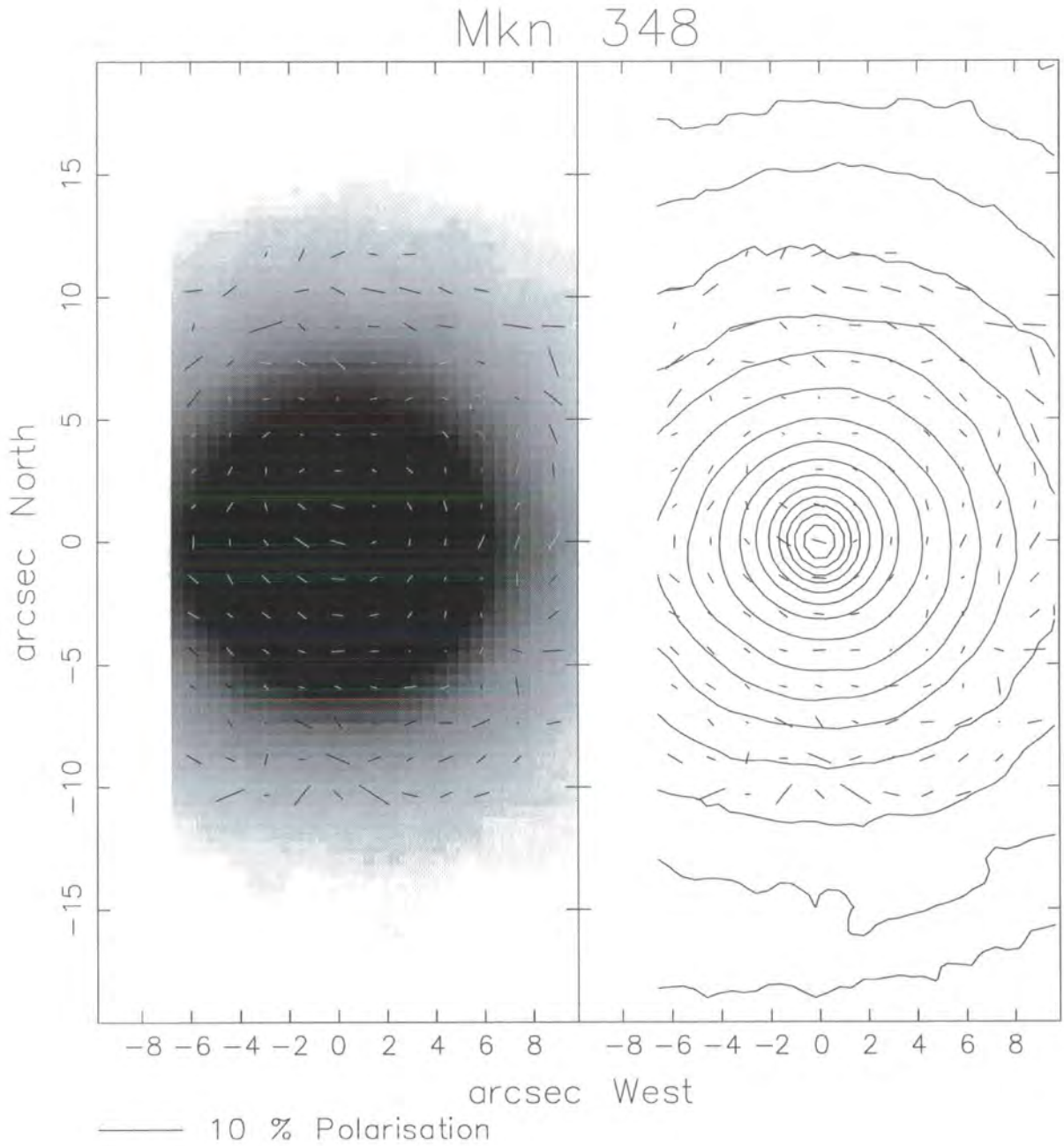

Figure 5.8: V-band total intensity images of Mkn 348, overlaid with polarization vectors binned with square size 3 and step size 3 (not smoothed), corrected for ISP_{Tran1}

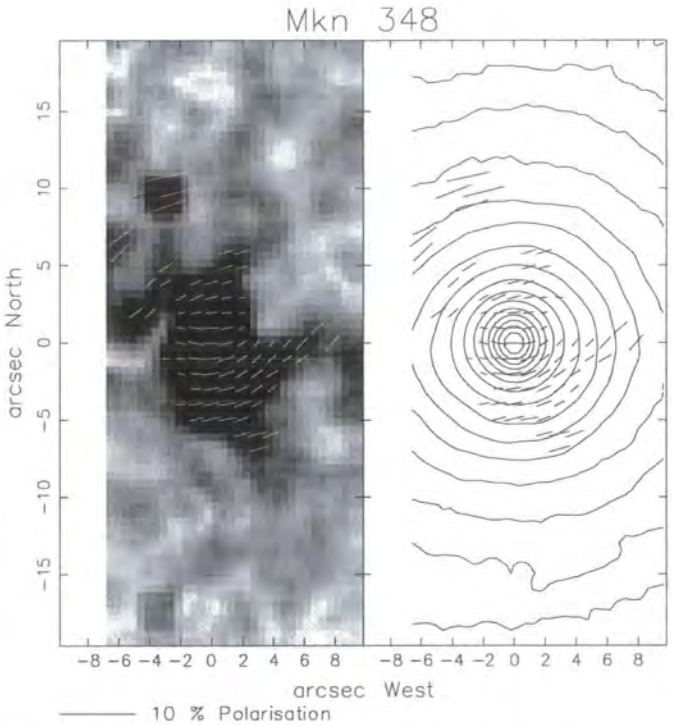

Figure 5.9: V-band polarized intensity greyscale and total contour images of Mkn 348, overlaid with polarization vectors binned with square size 3 and step size 2, uncorrected for ISP

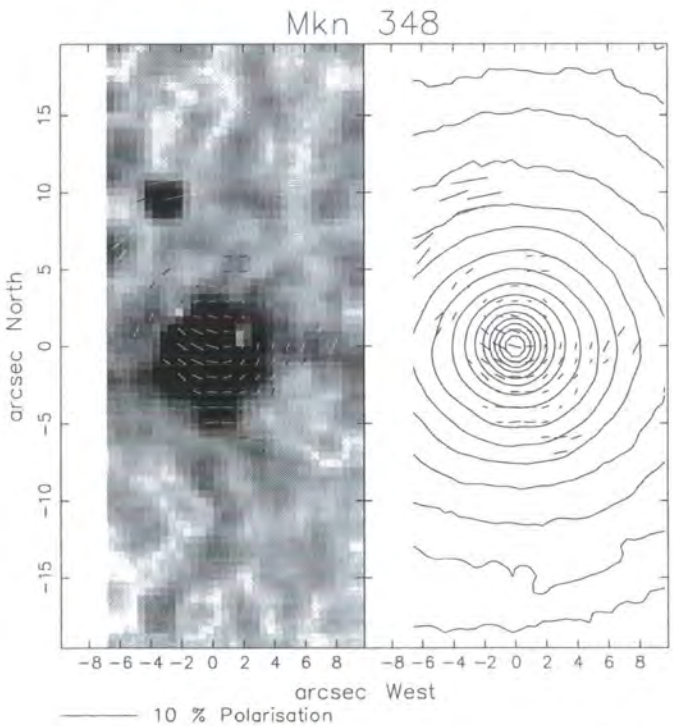

Figure 5.10: V-band polarized intensity greyscale and total contour images of Mkn 348, overlaid with polarization vectors binned with square size 3 and step size 2, corrected for ISP_{Tran1}

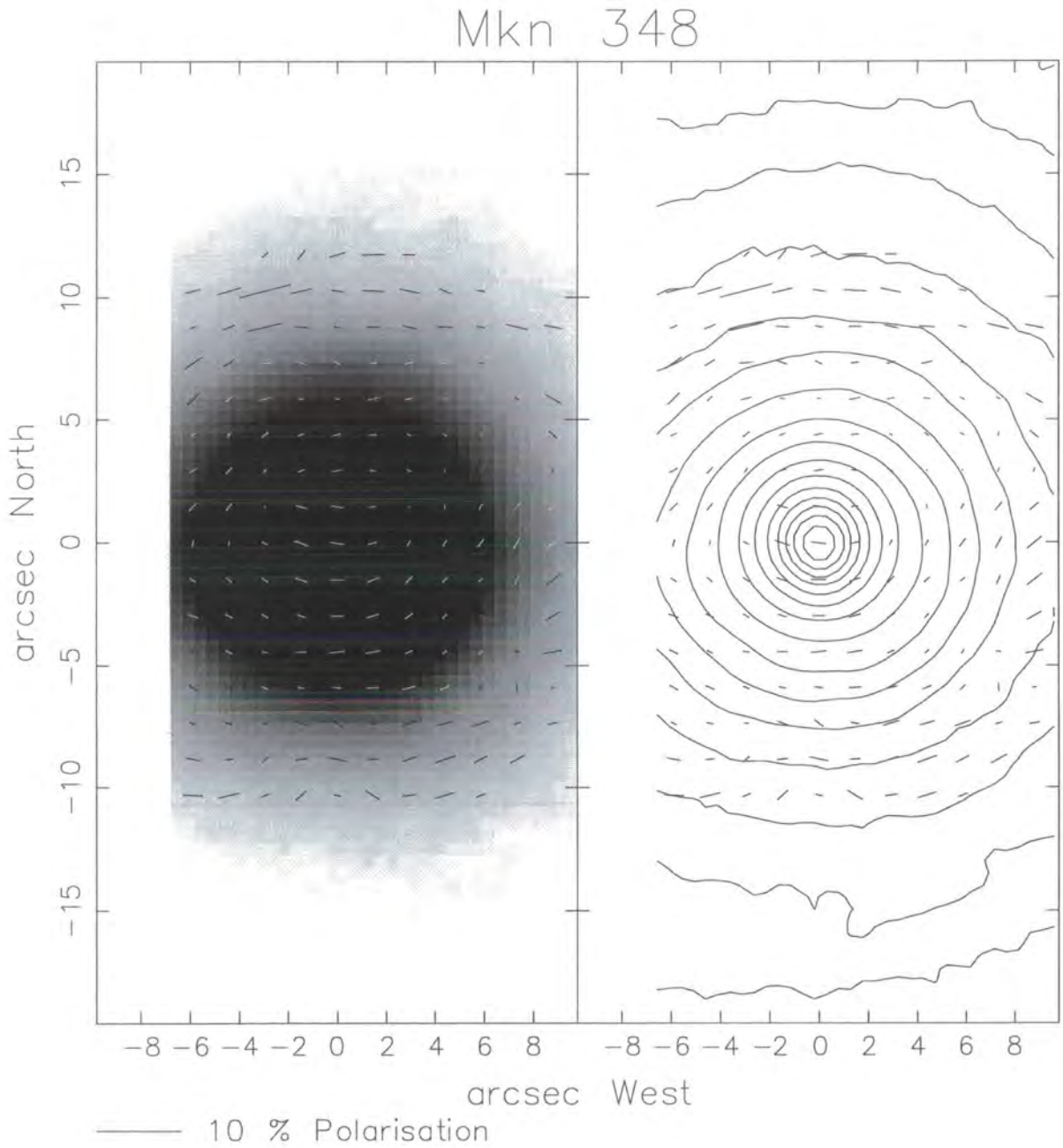

Figure 5.11: V-band total intensity images of Mkn 348, overlaid with polarization vectors binned with square size 5 and step size 3, corrected for ISP_{Felton} - the ISP calculated in this thesis

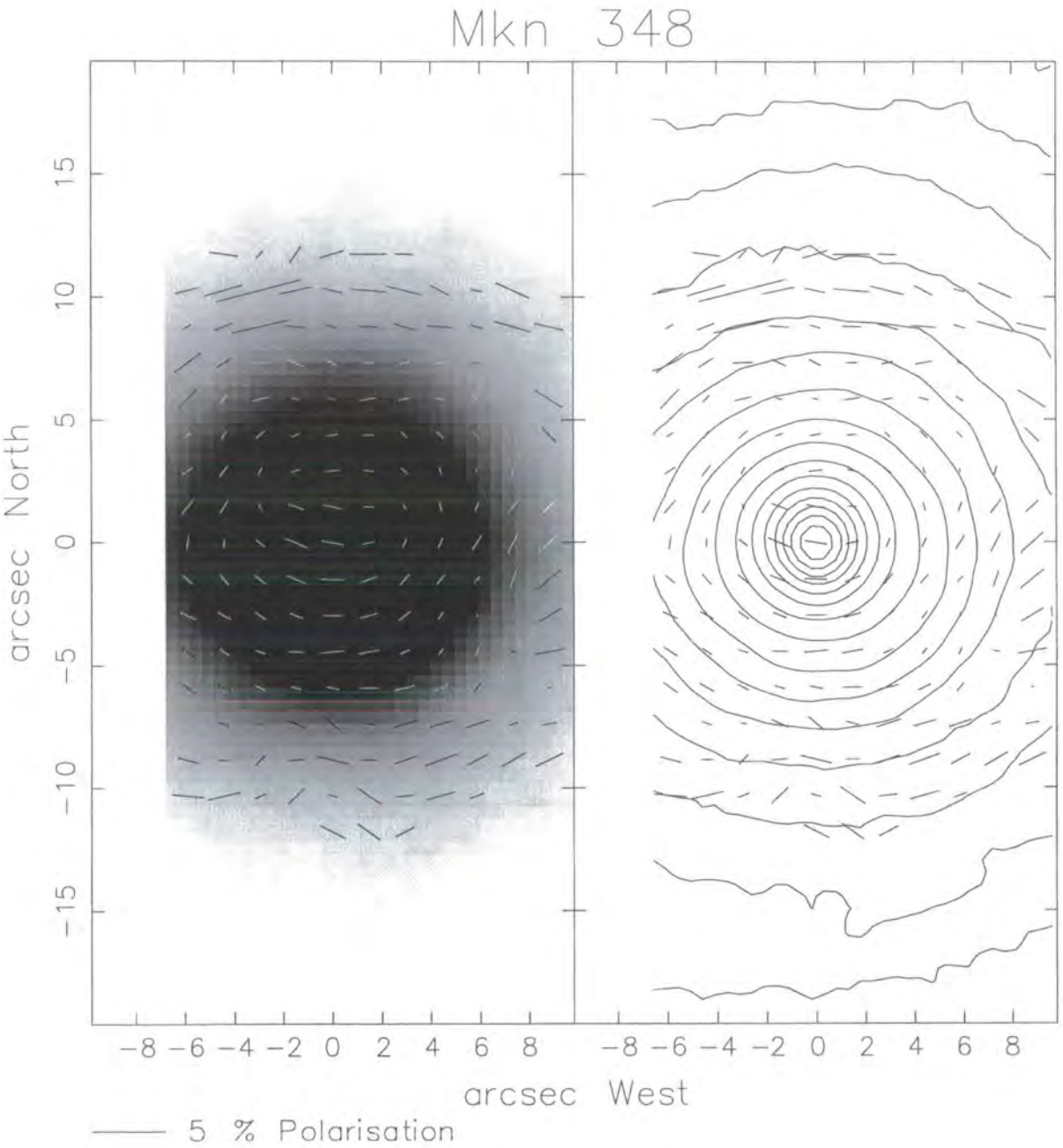

Figure 5.12: V-band total intensity images of Mkn 348, overlaid with polarization vectors binned with square size 5 and step size 3, corrected for ISP_{Tran2}, an alternative ISP estimated from Tran 1995

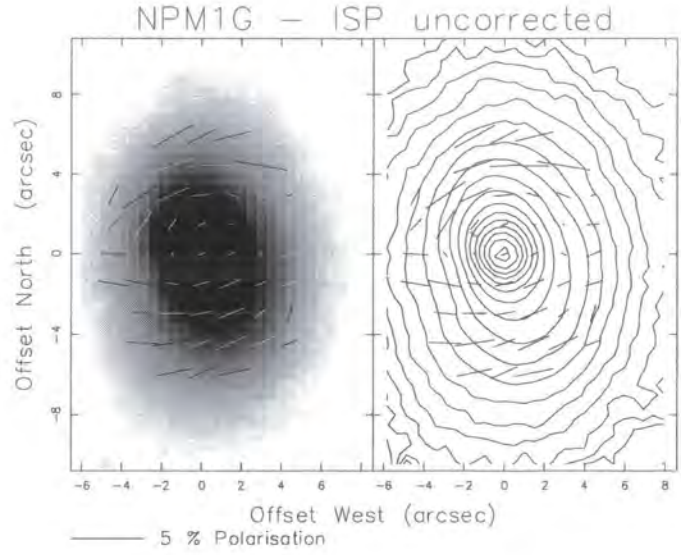

Figure 5.13: V-band intensity images of NPM1G +31.0016, overlaid with polarization vectors binned with square size 5 and step size 3, uncorrected for ISP

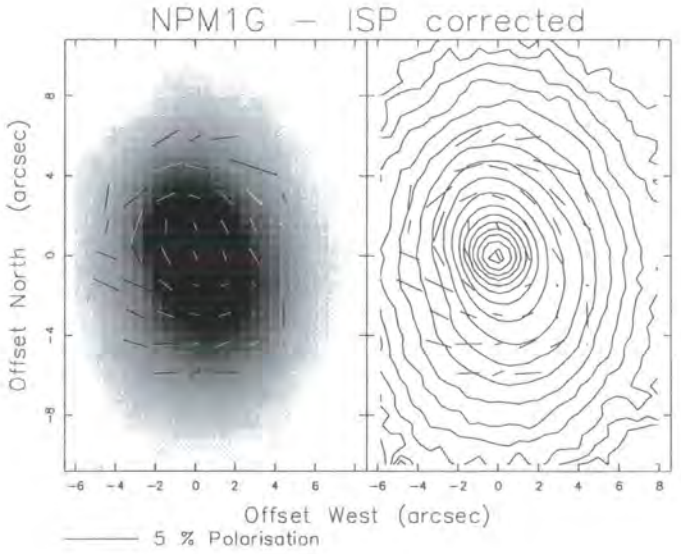

Figure 5.14: V-band intensity images of NPM1G +31.0016, overlaid with polarization vectors binned with square size 5 and step size 3, corrected for ISP_{Tran1}

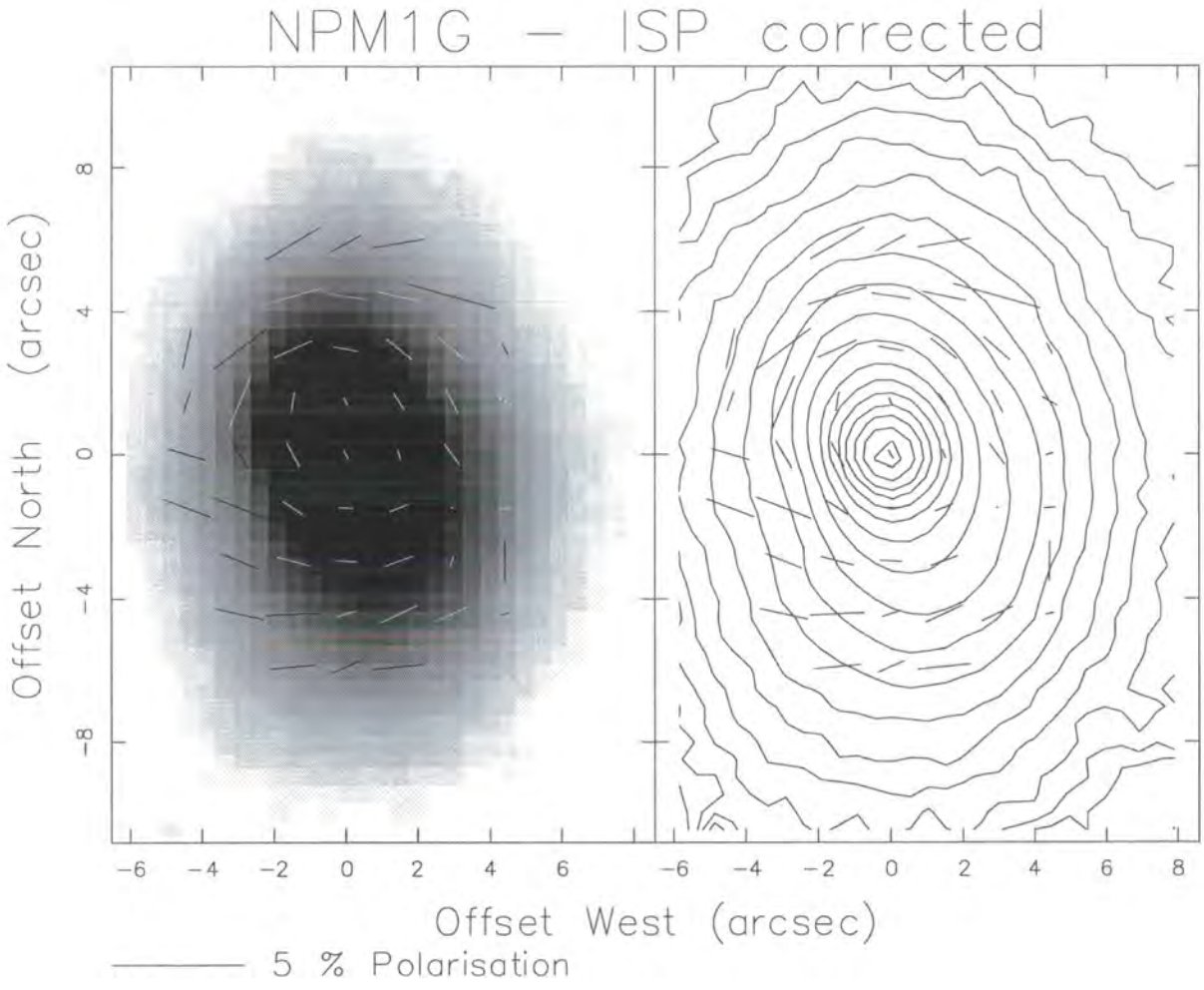

Figure 5.15: V-band intensity images of NPM1G +31.0016, overlaid with polarization vectors binned with square size 5 and step size 3, corrected for a lower ISP_{Tran2}

5.3 Markarian 573

5.3.1 Introduction

This early-type nearly face-on SAB galaxy shows strong Seyfert 2 characteristics in its nucleus. Its inclination is given as approximately 25° in the Morphological Catalog of Galaxies (Vorontsov-Velyaminov 1962-1974). It has bright extended emission-line regions, strong high-ionization lines and a linear radio structure. No nearby companions have been detected (Dahari 1985 [54]) and the nuclear optical and line emission does not dominate emission from the circumnuclear regions, which allows for the possibility of seeing some interaction between the nucleus and the host galaxy. The host galaxy is almost circular in the optical images, so a position angle cannot be assigned to it.

Radio measurements at 6 cm by Ulvestad & Wilson (1984) [242] detect a triple source, a nucleus (co-incident with the optical nucleus) with two lobes, each 1.5 arcseconds from the nucleus, symmetrically on either side along a position angle of 122° ± 3°. This position angle is confirmed by Nagar *et al.* (1999b) [166] in their maps at 3.6 cm and 20 cm, which show a double source, extending out to about 5 arcseconds at 20 cm. Falcke *et al.* (1998) [74] also find a linear triple source at 3.5 cm and 2 cm with a position angle of 125°, and with higher resolution find that the central radio component is extended along position angle 140°, a sub-parsec scale nuclear jet-like feature.

Infra-red measurements by Alonso-Herrero (1998) [5] show a twist in the J and K band elliptical isophotes occurring at a radial distance of 4.5 arcseconds, changing from position angle between 0°– 10° in the outer isophotes to between 80°– 90° in the inner isophotes. This is consistent with the existence of a bar within a bar; a large-scale stellar bar extending over about 20 arcseconds at position angle 0°, and a small-scale bar of 2 arcseconds along $\approx$ 100° as suggested by Pogge & De Robertis (1995) [188].

H_α images by Heisler & Vader (1995) [104] reveal a faint ring almost encircling the galaxy, also seen in the images by Pogge & De Robertis (1993) [187], which show it to be composed of two inner spiral arms. The H_α emission also shows a bar-like extension from the nucleus along P.A. $\approx$ 130°, *i.e.* elongated along the radio axis. Narrow band $[O_{III}]$ and $H_\alpha + [N_{II}]$ emissions show an extension out to 10 × 15 arcseconds along the radio axis, and two opposite cones of ionizing radiation, with the $[O_{III}]$ peak located 4 arcseconds from the continuum peak along the radio axis to the south-east (Tsvetanov & Walsh 1992 [236]).

Sub-arcsecond resolution narrow-band emission line and continuum HST images by Pogge & De Robertis (1995) [188] show complex biconical arc-like features within 2 arcseconds

of the nucleus in the emission regions (biconical narrow-line regions along the radio axis in the north-west and south-east), and also around and beyond the radio lobes. These arcs, also imaged by Schmitt & Kinney (1996) [206], show a rapid change in the ionization state of the gas and are interpreted as an interaction between the radio plasma from the nucleus and the interstellar medium (ISM), most probably a bowshock structure (Pogge 1996[186]). This is more clearly demonstrated on superposition of the HST $[O_{III}]$ emission-band image with the radio map of Ulvestad and Wilson (1984). Two other emission-line features are also apparent at 3 to 4 arcseconds either side of the nucleus, elongated almost perpendicularly to the symmetry axis of the radio and optical structures and beyond the radio emission, imaged at high resolution in the $[O_{III}]/H_\alpha$ excitation images of Falcke *et al.* (1998) [74] and also in the HST images of Ferruit *et al.* (1999) [77].

Pogge and De Robertis (1993) [187] found an extended biconical structure on a UV/Red map with position angle 124°, and also curved features 3.5″ south-east and 4.5″ north-west of the nucleus to about 4 arcseconds, which correspond to the $[O_{III}]$ peaks, but are beyond the radio lobes. They find an extended blue continuum in near UV light, probably due to scattered light along the ionization cones.

Optical $B-I$ colour maps by Kotilainen & Ward (1997) [127] show a blue double structure of total length about 8 arcseconds, where each blue maxima has width $\sim$ 2.5 arcseconds, and they are separated by 7 arcseconds along a position angle of approximately 135° (parallel to the radio axis). These two blue spots are divided by a red bridge crossing the nucleus, positioned perpendicularly to their position angle. A faint blue tightly wound spiral structure can also be discerned just outside these inner regions. Kotilainen & Ward attribute the blue maxima to scattered light from the nucleus tracing out a cone geometry, and the red bridge to be reprocessed emission from the obscuring torus across the nucleus. The blue light is unlikely to be from star formation because the continuum images show no signs of young stars, and the narrow emission-line ratios in this region indicate an ionizing spectrum from an AGN rather than star formation. The nucleus has an extinction of $E_{B-V} \sim 0.3$ which is most probably intrinsic to the galaxy, implying significant amounts of dust.

HST optical colour maps (F606W – F160W)[5] by Regan & Mulchaey (1999) [191] and Quillen (1999) [189] show both blue and red colour excesses. The blue regions, observed with higher resolution than Kotilainen & Ward (1997), show complex structure, but are bounded by a cone shape with the same position angle as the ionization cone ($\approx$ 124°) *i.e.* they are the same feature. The red absorption features are connected to the blue ones in a continuation of a spiral structure, and Regan & Mulchaey suggest this is evidence

[5]F606W is in the visual band, mean wavelength 594 nm and FWHM 150 nm. F160W is in the near infra-red, centred on 1.6μm

Figure 5.16: DSS intensity image of Mkn 573 centred in field 6x6 arcminutes

for Mkn 573 having symmetrical double spiral dust lanes, where the blue features are scattered emission from dust lanes illuminated from a central ionizing source, and the red features are due to absorption by the dust lanes.

Kay (1994) [119] tentatively identified a BLR in the polarized spectrum of the nucleus of Mkn 573, and calculated that 20% of the contribution at 4400 Å is due to the nuclear power-law featureless continuum, assuming that the nuclear stellar population was adequately represented by the spectrum of the elliptical galaxy used as a template. The work of Storchi-Bergmann (1998) [222] supports this assumption for the case of Mkn 573, verifying that the elliptical galaxy template gave a better match to the nuclear stellar population than the extra-nuclear spectrum of Mkn 573, although they calculated a lower figure of 15% for the contribution of the nuclear featureless continuum. Figure 5.17 gives a diagram showing visually the different emission regions and axes of the various observations for easier comparison. It also shows the angle of polarization of the nuclear optical polarization measured in this study.

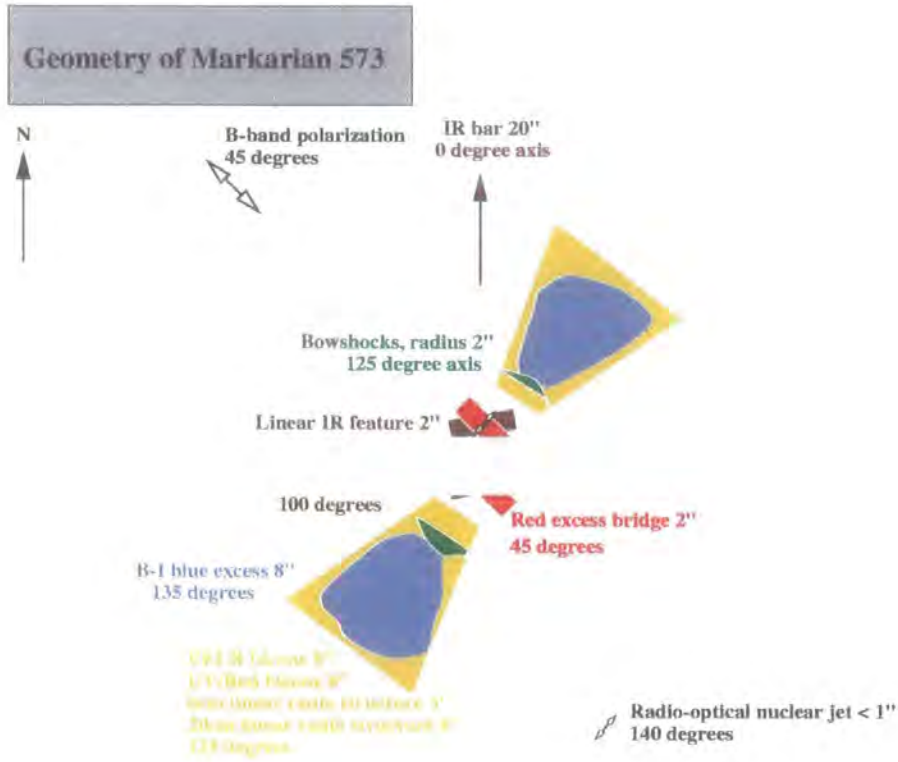

Figure 5.17: Diagram of the axes of observations of Mkn 573

5.3.2 Observational details

Two sets of data were taken for Mkn 573. The first set was taken on the 2.5 m Isaac Newton telescope, La Palma on the 7th August 1991 using a broad band V filter, with exposures of 600 and 500 seconds. The second dataset was from the 1 m MacDonald telescope, Texas on the 5th November 1997 using R and B filters with exposures of 300 seconds. The first set of B band images were very faint so a further set of four 300 second exposures was taken. Unfortunately the flatfields using the B filter were corrupted - the bias strips were lost. In order therefore to make some use of the B-band observations, the B-band images presented here have been reduced using V-band flatfield images taken on the same night. The efficiency response of the CCD over the V-band and most of the B-band is almost flat, with only a small linear decrease towards the blue. Therefore the V-band flatfield should be a fairly reasonable substitute for the missing B flatfield.

For the data set from the INT, the Cassegrain focus with focal ratio of 15 was used, and for this configuration the scale of the sky on the Durham polarimeter EEV CCD detector was 0.49 arcseconds per CCD pixel. Observations were taken at two positions to give just over two thirds sky coverage. For the more recent data sets from the MacDonald telescope using the new SiTe (Tektronix) CCD detector, the focal ratio was 13.5 and the scale of the sky was 0.8 arcseconds per pixel. Time limitations led to data being taken at only one position, resulting in a smaller sky coverage, so only the central regions of the galaxy were imaged. At the estimated distance of 69 Mpc, 1 arcsecond corresponds to

approximately 330 pc. The seeing for the observations was approximately 1.5 arcseconds (3 pixels) for the V-band, 2.9 arcseconds (3.5 pixels) for R-band, and 2.9 arcseconds (3.5 pixels) for B-band. These values were calculated using star images in the field on each night.

5.3.3 Image details

Figures 5.18 – 5.41 present broad V, R and B-band images of Mkn 573 with north to the top and east to the left. The scale is in arcseconds, centred on the peak nuclear total intensity of the image. Except where otherwise stated, the greyscale and contour maps represent the total intensity images, with black representing the highest intensity. The contours of the maps are plotted logarithmically. The polarization vectors overlaid on the images were calculated by binning the polarization data in square bins, and moving on by a set number of pixels for the next polarization vector to be calculated and plotted. The square sizes and step sizes are either 5 pixels moved on by 3 pixels, or 3 pixels moved on by 2 pixels. Since the bins overlap, this has the effect of smoothing the polarization data, maps are also plotted with independent bins of size 3 pixels, step size 3 pixels in order to check on the continuity of the polarization data. The polarization vectors are plotted with total intensity cuts and polarized intensity or signal-to-noise level cuts set appropriately to the noise levels in the maps.

The V-band data were taken at two telescope positions, and there were difficulties in accurate alignment between these two sets because there was only one common star and the nucleus in the overlap, both of which were very close to the grid edges on one data set. The two sets were aligned using these two positions, but for the galaxy nucleus it was difficult to know how accurately the true nucleus was located. Despite repeated efforts to minimise this error, and subsequent normalization of the data, the discontinuities visible in the maps of polarized intensity (figures 5.26 and 5.27) show that there is some residual misalignment, although it should be noted this is a distinct improvement on the initial data reduction procedure. The total intensity is also slightly affected, but at a level too small to be detected at the greyscale levels of the maps shown.

There were also some alignment difficulties with the R-band data, because although they were taken at only one telescope position, there were problems in aligning the left and right polarization channel accurately. By suitable re-adjustment and re-calculation of the alignment coefficients, this error has been minimised, but there is still some residual misalignment, which is clearly visible in the map of polarized intensity (figure 5.35), but was not possible to correct for.

5.3.4 Interstellar polarization

The galactic co-ordinates (l = 148°,b = −58°) show that Mkn 573 is seen out of the Galactic plane, suggesting that the ISP effect is probably very small. Furthermore, the galactic extinction value given in table 4.6 is very low, meaning that any ISP will be very low. Unlike in the maps of Mkn 348 in the previous section, there is not an obvious general tendency of the polarization vectors to be oriented in a particular direction around Mkn 573, which would have indicated a strong ISP influence.

Efforts were made to calculate an ISP value from the field around Mkn 573 in the V-band observations taken for this thesis. However, because the field of the image is small, and there was only partial coverage, there were only two stars bright enough for reliable polarization calculations. Unfortunately both of these were located close to grid edges and were adversely affected by light leaking round the grid edge, so that the polarization could not be reliably measured. Another, much fainter star was visible on the field, and its polarization was calculated to be 0.60% at 110° over apertures between 1.5 to 2 arcseconds. In spite of repeated attempts at careful local sky subtraction and alignment, the error estimates on these values were huge, larger than the measured levels themselves, so that this measured ISP estimate of 0.6% ± 3% at 110°± 45° is not very useful. At this level of uncertainty it was therefore not possible to determine from the data whether or not there is a significant ISP contribution. This derived value was applied to some of the maps to investigate the effect on the polarization pattern for interest only, but the huge uncertainties mean that these corrected results obviously must be viewed with caution.

Kay (1994) [119] calculated a figure of 0.31% ± 0.05% at 125°± 3.6° for ISP subtraction around Mkn 573, by making polarimetric observations of two nearby foreground stars (HD 9740 and HD 10441), assuming them to be intrinsically unpolarized and hence appropriate ISP probes. This figure was adopted for ISP corrections for the V-band observations in this study. For the R-band and B-band maps, an approximate ISP estimate was made assuming that the measured V-band ISP has λ_{max} of 5450Å and follows the Serkowski law given in section 2.3.5. This calculation gives the level of ISP to be 0.30% at 125° for both R and B bands.

5.3.5 Results: V-band

Figures 5.18 to 5.25 present total intensity V-band maps of Mkn 573 overlaid with polarization vectors. The polarization vectors in figure 5.19, and 5.23 to 5.29 are plotted with a minimum polarized intensity cut on the vectors to eliminate the less reliable vectors.

Figures 5.18 and 5.19 have the polarization data averaged over 5 pixel (2.5 arcsecond) bins, and figures 5.20 to 5.29 are averaged over 3 pixel (1.5 arcsecond) bins. This higher resolution is at the seeing limit, so small features should be interpreted with care, but there do not appear to be any problems with artefacts at this limit, because these maps show the same general features as the lower resolution maps.

Maps 5.18, 5.19, 5.22, and 5.23, which are not corrected for ISP, all show three main features in the polarization patterns: two separate regions of enhanced polarization, and signs of centro-symmetry. Signs of a centro-symmetric scattering pattern are clearly seen in the north half of the galaxy, but in the south this pattern does not continue because, apart from the south-east cone shaped feature, the region has a very low polarization. Curiously the centro-symmetric pattern seen in the north east quadrant of the galaxy does not fit very well with the scattering centre being located at the nucleus, the pattern is distorted, and if anything would indicate a scattering centre further south east than the peak nuclear intensity. This may be either a real pattern, indicating that the centre of the actual illuminating source is not indicated by the peak intensity on the map due to obscuring non-uniform dust cover, or a distorting effect (such as ISP) to the centro-symmetric pattern, or that it is an artefact of the map production due to misalignment effects. This third explanation is given more credence because the two arcsecond strip east of the nucleus is the area of overlap between the data sets, and it is known that there is some misalignment here, so the polarization data in this area is likely to be affected by this. Therefore the apparent inconsistency of the centre of the centro-symmetry with scattering from the optical nucleus is probably not a real feature.

There are two regions of enhanced polarization levels, the strongest one in the north-west quadrant of the map, and to a lesser degree in the south-east quadrant. These regions extend along a position angle of $\approx 125°$ out to ≈ 10 arcseconds in both directions from the nucleus. The angle of polarization in both these regions is around approximately 40°, perpendicular to the position angle of their extension. The degree of polarization is highest in the north-west, around 2.5%, reaching 3.3% at the peak values (as binned over 2.5 arcsecond squares). In the south-east, the values are mostly lower, between 1% to 1.5%.

Figure 5.23 (which has a cut on the minimum level of polarized intensity to try to avoid the vectors most affected by noise) shows more clearly that the north western region is polarized at an almost uniform position angle within a well-defined cone shape. The south eastern cone-shaped region of high polarization however, shows a lower degree of polarization, less well-aligned polarization angles and a less well-defined cone. Beyond a diameter of 8 arcseconds from the nucleus in the south-east, the alignment of the polarization vectors tends to be of a more centro-symmetric pattern. These cone-shaped

regions of higher percentage polarization are investigated further by looking at the polarized intensity levels to see whether it is an increase in polarized flux, or a decrease in unpolarized flux that leads to a higher polarization.

Figures 5.26 to 5.29 present maps of polarized intensity or polarization levels plotted as greyscale to further investigate this cone-shaped region of higher polarization levels. The contour maps alongside the greyscale images are contours of total intensity for comparison. The vertical discontinuity of the greyscale polarized intensity seen going through the nucleus is due to problems in alignment of the data sets as discussed in section 5.3.3. The polarized intensity maps show a region of high polarized flux elongated along a position angle of about 127°, and which extends further out to the west of the nucleus than the east, with a total length in the region of 10″(or out to 15″if the fainter levels are included) and width of the order 4″. The apparent spot of high polarized flux in the north-east corner of the polarized intensity maps is a spurious feature (not seen in the total intensity image or in either R or V-band data), possibly due to a cosmic ray. The polarization maps show two peaks of polarization, located 5 arcseconds north-west of the nucleus along a position angle of 135°, and 7 arcseconds south-east of the nucleus along 122°, *i.e.* corresponding to the cone-shaped region of higher polarization levels seen in the polarization vectors.

Figure 5.17 shows visually the axes of various previous observations of Mkn 573 together with the angle of polarization for easier comparison. The blue double peaked structure found by Kotilainen & Ward (1997) on their $B-I$ colour maps (described in section 5.3.1) extends out to 8 arcseconds along position angle 125°, with the two peaks separated by 7 arcseconds are attributed to scattered nuclear light. Since the two peaks in polarization in the V-band polarization map are along a very similar position angles, and the region of high polarized flux emission spans approximately 10″ along this position angle, it is seems plausible to conclude that the scattered light producing the blue feature, also produces the observed rise in polarization.

The position angle of this high polarization region is also along the same direction as the radio axis and the extended biconical narrow [O_{III}] emission-line region (Schmitt & Kinney 1996 [206] and Pogge & De Robertis 1993 [187]) and fainter extended narrow emission-line arcs (Falcke *et al.* 1999). The biconical features are found within 2″ of the nucleus, the radio emission extends out to about 5″, and the emission features extend to a maximum of only 3″ or 4″ either side of the nucleus. In contrast, the observed increase in polarized flux extends over 5″ to 6″, and the enhanced polarization levels extend as far out as 10″, on each side of the nucleus. Therefore the increased polarization levels are not due directly to the narrow-line emission, but the alignment of the axes of emission indicating nuclear outflow with the axis of increased polarization is consistent with a picture of the nuclear light escaping preferentially along the axis of outflow (dictated by

the obscuring torus model of Seyfert nuclei, section 1.3) and being scattered into the line of sight by dust in the central regions of the galaxy, hence causing in increase in polarization level.

ISP corrections

Figures 5.20, 5.24, 5.27 and 5.29 show maps corrected for Kay's ISP value of 0.33% at 125°, and figures 5.21 and 5.25 are corrected for the ISP value measured in this thesis, 0.61% at 110° (which, as explained previously is subject to huge errors, and therefore included for interest only). The maps corrected for Kay's value of ISP do not seem significantly different from the uncorrected ones, because it is a small level of correction. The maps corrected for the higher value of ISP measured in this thesis show an enhanced contrast in polarization levels of the polarization cones against the rest of the galaxy. The polarized intensity map corrected for this higher ISP value appears largely similar, with only a small reduction in polarized flux. From comparison of the maps and the ISP measurements from these V-band data, it is not possible to conclude whether either ISP value is a realistic estimate, or indeed whether in fact any ISP contamination is present at a significant value.

5.3.6 Results: R-band

The maps in the R waveband cover a smaller section of the nucleus than the V-band data, because only one section of the sky was observed due to time constraints. Some of the maps were replotted using Kay's ISP correction, but on inspection these corrected polarization patterns were not much different from the uncorrected ones. Additionally, since in the previous section it has been noted that the significance of ISP correction for the galaxy is highly uncertain, therefore only the uncorrected maps are presented here.

Figures 5.30 and 5.31 show R-band images of the central regions of Mkn 573 with vectors respectively averaged over 5 by 5 pixel bins, moved on by 3 pixels, plotted with no signal-to-noise cut and a 1σ signal-to-noise cut on the polarization respectively. The polarization pattern is broadly centro-symmetric except at the centre and in the southern middle regions, where the level of polarization drops to low levels, and the signal-to-noise levels are lower because the polarized flux drops drastically in the central region. In contrast, the corresponding region north of the nucleus is significantly polarized, $\geq 1.2\%$. There is no indication of the cone-shaped regions of enhanced polarization as seen in the V-band maps. The polarization at the nucleus is negligible.

At higher resolution, figures 5.32 and 5.33 give the polarization vectors averaged in 3 by 3 pixel bins, moved on by 2 pixels, plotted with no signal-to-noise cut and a 1σ signal-to-noise cut on the polarization vectors respectively. This shows the centro-symmetrical pattern more clearly, and there is slightly higher polarization shown in the areas corresponding to the cone-shaped regions seen in the V-band maps. The levels of polarization southwards of the nucleus are also shown to be lower than in the rest of the galaxy.

To check on the continuity of the data, figure 5.34 shows the polarization pattern from independent 3 by 3 pixel bins, moved on by 3 pixels (*i.e.* not smoothed). The polarization vectors are seen to be very similar to those in the smoothed 5 by 5 pixel binned map, showing that the smoothing has not hidden polarization discontinuities or introduced artefacts.

Figure 5.35 gives a map of polarized intensity as the greyscale image and the total intensity contour image plotted as greyscale (corrected for ISP). The structure seen around the nucleus in this image looks likely to be due to poor alignment of the data, bearing in mind the problems encountered with alignment between the two channels during data reduction. The high polarized flux around the nucleus and lack of polarized flux in the south of the galaxy are the only features that may reliably be extracted from this map.

Since there are probable errors in the alignment of the R-band data, any small structural features (*e.g.* those seen in the polarized intensity maps) should be interpreted with caution, as they are likely to be either caused by or affected by this problem. The general conclusions that may be made from the R-band data, are that there is evidence for centro-symmetric scattering around the centre of the galaxy, and that there seems to be a low polarization due to a lack of polarized flux in the southern half of the galaxy. This lack of polarization may be due to cancellation between competing polarization mechanisms rather than the lack of a polarizing mechanism.

5.3.7 Results: B-band

Like the R-band data, the B-band observations also cover only a single section of the nucleus due to time constraints, and after examination, applying Kay's ISP correction makes no significant differences to the polarization pattern in the maps, so only the maps without ISP correction maps are presented here.

Figures 5.36 and 5.37 show maps with vectors averaged over bins of 5 by 5 pixels, moved on by 3 pixels, plotted with a total intensity cut and a polarized intensity cut respectively. Figures 5.38 and 5.39 are similar, but at higher resolution with the polarization data

averaged over bins of 3 by 3 pixels, moved on by 2 pixels. The main features seen in these images are: two regions of enhanced polarization levels, a general tendency of the vectors to be aligned and signs of centro-symmetry in the outer regions

The two areas of enhanced polarization levels are situated in the north-west and the south east quadrants, and correspond spatially to the cone-shaped regions of enhanced polarized intensity seen in the V-band map. As discussed in the V-band results, the high polarization has been linked to the blue features detected by Kotilainen & Ward (1997). When the polarization is measured over a 3 arcsecond aperture at the positions of the two blue peaks found by Kotilainen & Ward (1997) [127], the level of polarization is high (2.8% at an angle of 49°) at the north-west peak, and 1.6% at 50°at the location of south-east blue peak. Since the blue maxima are thought to be due to scattered nuclear light, a higher level of polarization would be expected, and this would explain the polarization results. This explanation can be further supported by the cone morphology not being visible in the R-band maps, but clearly seen in the B and V-band maps, because scattering from dust in galaxies is usually more efficient at blue than red wavelengths.

There appears to be a slight general tendency, shown most clearly in figures 5.36 and 5.38, for the polarization vectors to be oriented approximately around 45°, particularly in the central region around the nucleus. This tendency is seen across most of the galaxy, particularly in the central regions. However in figure 5.40, where the polarization data is not smoothed, the trend is less strong, suggesting that part of this is due to the smoothing procedure. Such a general tendency might signal ISP contamination, but at 45° , it is almost perpendicular to the ISP estimate obtained by Kay (1994) of 0.3% at 125°, so is unlikely to be ISP.

Figure 5.41 shows a greyscale polarized intensity map of the central nuclear regions. The region of high polarized flux is clearly elongated about 15″along a position angle of 127°. It can be seen that the highest polarization levels (2%–3%) occur about 5″north-west and 6″south-east of the nucleus, over regions of approximately 4 in diameter, which is similar to the V-band data, and as explained in the previous section, this blue feature is probably the scattered blue light feature observed by Kotilainen & Ward (1997).

The continuity of the data was checked by plotting the polarization pattern from independent 3 by 3 pixel bins, moved on by 3 pixels (*i.e.* not smoothed) in figure 5.40. The polarization vectors are seen to be very similar to those in the smoothed 5 by 5 pixel binned map, showing that the smoothing has not hidden polarization discontinuities or introduced artefacts, but it should be noted that the centro-symmetry shows more clearly in the smoothed data.

5.3.8 Results: Wavelength dependence of polarization in the host galaxy

Strong dependence on wavelength of the polarization, from B-band to R-band, both in level and in angle, is observed in the polarization maps of Mkn 573 presented here.

Comparing the B-band and R-band maps, it can be seen that the polarization in the B-band is in contrast to the polarization in the R-band. After signal-to-noise cuts to the 95% confidence level, in some regions both the levels of polarization and the angle of polarization are very different, with no correspondence of regions of highest or lowest polarization, which strongly suggests different polarization mechanisms dominating over different regions of the galaxy. Largely the polarization in the B-band traces a biconical structure around the nuclear area most likely demonstrating dust grain alignment, whereas the R-band polarization is negligible in the central regions, but further out clearly shows centro-symmetry, *i.e.* polarization by scattering.

Variations in the angle and level of polarization with wavelength from extragalactic objects can sometimes be due to ISP effects because ISP itself is wavelength dependent. The ISP correction for Mkn 573 (discussed in section 5.3.4) however, is most likely to be a small correction, which does not significantly affect the polarization patterns. This leaves the possibilities that the shift in polarization signifies a change in dominant polarization mechanism, or more simply a characteristic change in the effectiveness of the polarization mechanism, or a difference in local unpolarized diluting flux. A change in dominant polarization mechanism could be either a transition between scattering and dichroic absorption, or, as has been suggested for near-IR wavelengths by Young *et al.* (1996) [272], a change from dichroic absorption to dichroic emission. The latter mechanism is where the grains emitting the IR flux are themselves aligned, so give partially polarized emission. This has a polarization perpendicular to that produced in dichroic absorption by grains oriented in the same manner, since emission and absorption probabilities rise for light polarized parallel to the grains.

For Mkn 573, the two regions of highest polarization are consistent with a dust scattering origin as the polarization is highest at B-band. As the centro-symmetric pattern centred on the nucleus is slightly clearer in the R-band and B-band than in the V-band, this may indicate dilution by the unpolarized visible light from the galaxy (which peaks in the V-band).

Table 5.8: Nuclear aperture polarimetry of Mkn 573 (uncorrected)

Aperture (arcsec)	Aperture (pixels)	Polarization (percent)	Position Angle (degrees)
B-band			
2	2.5	0.57 ± 0.32	49°± 16°
2.5	3.1	0.56 ± 0.29	50°± 15°
3	3.8	0.56 ± 0.26	51°± 13°
4	5.0	0.56 ± 0.24	53°± 12°
5	6.3	0.59 ± 0.22	53°± 11°
6	7.5	0.60 ± 0.22	52°± 10°
V-band			
2	4.1	0.50 ± 0.28	47°± 16°
2.5	5.1	0.45 ± 0.27	49°± 18°
3	6.1	0.41 ± 0.27	50°± 19°
4	8.2	0.34 ± 0.27	51°± 21°
5	10.2	0.32 ± 0.28	50°± 23°
6	12.2	0.32 ± 0.28	49°± 25°
R-band			
2	2.5	0.17 ± 0.29	52°± 32°
2.5	3.1	0.17 ± 0.28	57°± 30°
3	3.8	0.19 ± 0.28	56°± 33°
4	5.0	0.21 ± 0.28	56°± 35°
5	6.3	0.20 ± 0.28	55°± 33°
6	7.5	0.20 ± 0.28	55°± 33°

Table 5.9: Nuclear aperture polarimetry of Mkn 573 (ISP-corrected)

Aperture (arcsec)	Aperture (pixels)	Polarization (%)	Position Angle (degrees)
B-band			
2	2.5	0.86± 0.32	44°± 16°
2.5	3.1	0.86± 0.29	45°± 15°
3	3.8	0.85± 0.26	45°± 13°
4	5.0	0.85± 0.24	47°± 12°
5	6.3	0.88± 0.22	47°± 11°
6	7.5	0.88± 0.22	47°± 10°
V-band			
2	4.1	0.80± 0.28	42°± 16°
2.5	5.1	0.73± 0.27	45°± 18°
3	6.1	0.69± 0.27	45°± 19°
4	8.2	0.65± 0.27	45°± 21°
5	10.2	0.63± 0.28	44°± 23°
6	12.2	0.62± 0.28	42°± 25°

Table 5.10: Comparison of nuclear polarization measurements of Mkn 573

Range of wavelength (Ångstroms)	Aperture width (arcsecs)	Polarization (percent)	Polarization Angle (degrees)	Reference[1]
3200 - 6200[3]	2	0.44 ± 0.06	54.8 ± 4.0	K94
3200 - 6200[3]	2	0.83 ± 0.04	56.1 ± 1.3	K94
3200 - 6200[3]	2	0.52 ± 0.04	32.0 ± 2.3	K94
3800 - 5600[4]	4	0.58 ± 0.14	51.4 ± 7.1	M83
B-band[2]	2	0.56 ± 0.26	51 ± 14	F99
V-band[2]	2	0.41 ± 0.27	51 ± 16	F99
R-band[2]	2	0.19 ± 0.28	60 ± 32	F99
4150 - 4650[3]	2	1.33 ± 0.70	48.2 ± 1.6	K94 - ISP corrected
B-band[2]	2	0.86 ± 0.32	44 ± 16	F99 - ISP corrected
V-band[2]	2	0.80 ± 0.28	45 ± 16	F99 - ISP corrected

[1]References: F99 = this study (1999), MG90 = Miller & Goodrich (1990), K94 = Kay (1994), M83 = Martin (1983)
[2]Imaging using a broadband V filter, with a 2 arcsecond aperture
[3]Spectro-polarimetry with a slit width of 2 arcsecond orientated east-west
[4]Survey using a Corning 4-96 filter (3800-5600 Å), with a 4 arcsecond aperture

Table 5.11: Broad band nuclear polarization measurements of Mkn 573 by Young (1996) - uncorrected for ISP

Aperture (arcsecs)	Band	Polarization (percent)	Polarization (degrees)
5	U	2.36±0.32	47±4
5	B	0.89±0.16	38±5
5	V	0.06±0.09	35±45
5	R	0.25±0.08	42±9
5	I	0.44±0.19	36±12
5	K	0.66±0.19	20±9

Table 5.12: Polarization of the nuclear featureless continuum at 4150-4650 Å, Kay 1994

Correction:	Polarization (%)	Polarization angle (degrees)
Corrected[1]	1.33 ± 0.70	48.2 ± 1.6
Corrected[2]	5.56 ± 0.40	48.0 ± 2.0

[1]Corrected for ISP
[2]Corrected for ISP, Galactic reddening E_{B-V}=0.007, and galaxy dilution fraction of 0.80

5.3.9 Results: Polarization of the Seyfert nucleus

Aperture polarimetry of the nucleus with a range of aperture diameters was performed in all the observed bands, and is presented without ISP correction in table 5.8. For B and V bands, in table 5.9 values are also given after correction for Kay's value of ISP (0.3% at 125°). The V-band and R-band nuclear polarizations are all very low $\leq$ 0.5%, with B-band polarizations being greater. The correction for ISP increases the values in both B and V bands significantly, but is not attempted for R-band due to the measured polarizations being too small, with too great a probable error to give a meaningful answer.

The polarization in the B-band is greatest, the uncorrected level is 0.56% ± 0.26% at 51°± 13°, and after ISP correction this rises to 0.86% ± 0.26% at 45°± 13°. The uncorrected V-band nuclear polarization is low, about 0.41% ± 0.27% at an angle of 52°± 19°using a 3 arcsecond aperture. The ISP corrected nuclear polarization is greater at 0.69% ± 0.28% at 45°± 19°. This rise to blue wavelengths is indicative of scattering. In R-band the measured nuclear polarizations are not significantly above the noise levels, *i.e.* comparable to the error estimates. However, the series of polarization measurements across the nucleus are seen to be remarkably close in value if the error estimates are representative, although the measurements are not completely independent. From all the polarization measurements

in the table, it can be seen that the measurements are broadly similar, and that the error estimates therefore seem too large.

Table 5.10 gives other published values for the nuclear polarization of Mkn 573 for comparison. Bearing in mind the different sized apertures, aperture location and orientation, and wavelength range of the different observations, the measurements of this thesis are in good agreement with the previously published values.

Young *et al.* (1996) [272] made spectro-polarimetric measurements of Mkn 573 in U, B, V, R, I, and K bands which are given in table 5.11, and which are not corrected for ISP. The polarization increases towards the blue, which is confirmed in the measurements of this study. Within the errors (which are substantial for such small measured polarizations) both sets of measurements are in agreement.

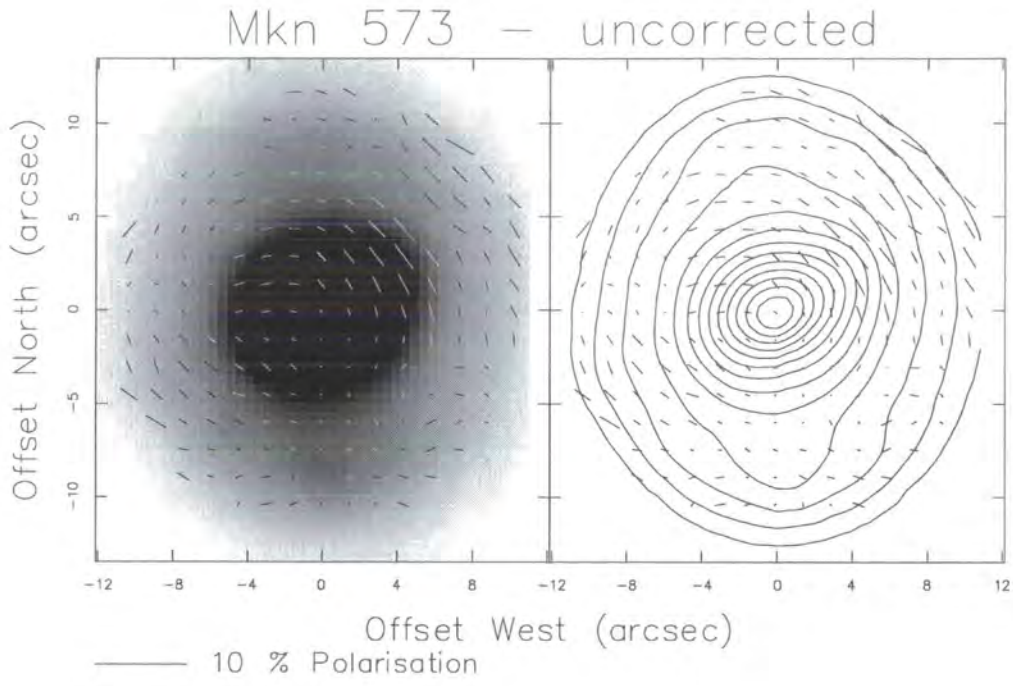

Figure 5.18: V-band total intensity image of Mkn 573, overlaid with polarization vectors binned with square size 5 and step size 3 pixels, uncorrected for ISP

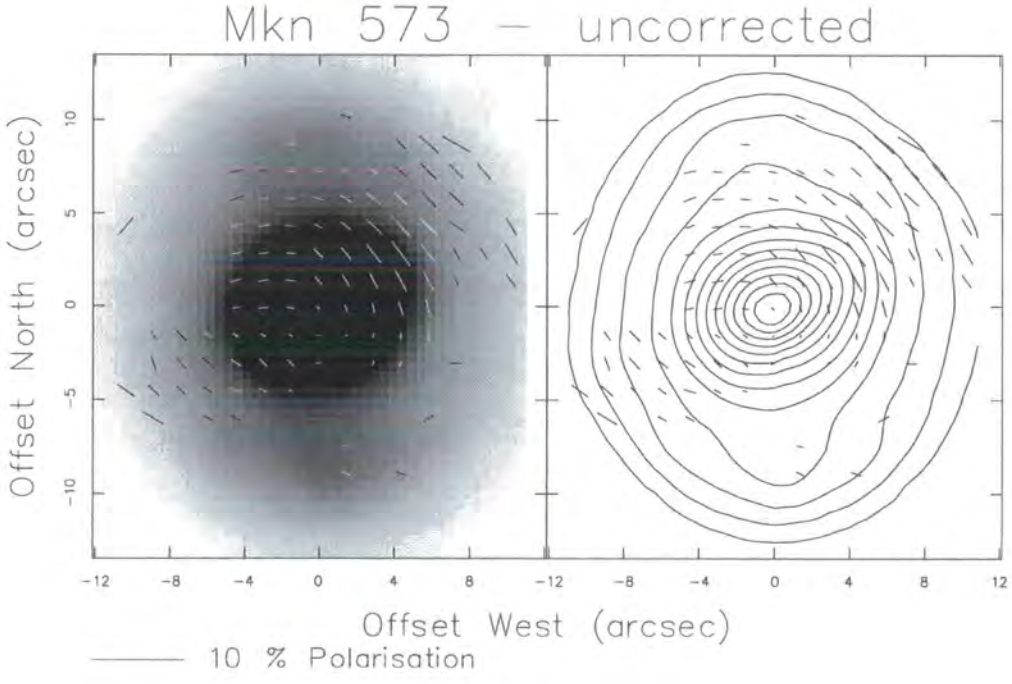

Figure 5.19: V-band total intensity image of Mkn 573, overlaid with polarization vectors binned with square size 5 and step size 3 pixels, with a polarized intensity cutoff, uncorrected for ISP

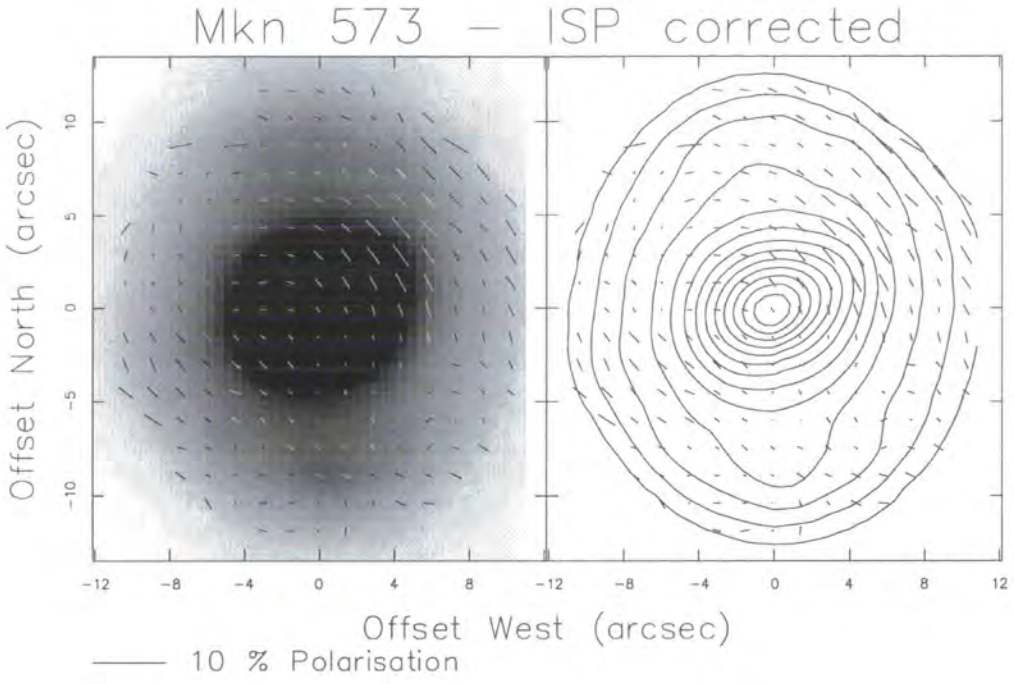

Figure 5.20: V-band total intensity image of Mkn 573, overlaid with polarization vectors binned with square size 5 and step size 3 pixels, with a polarized intensity cutoff, corrected for ISP of 0.33% at 125°

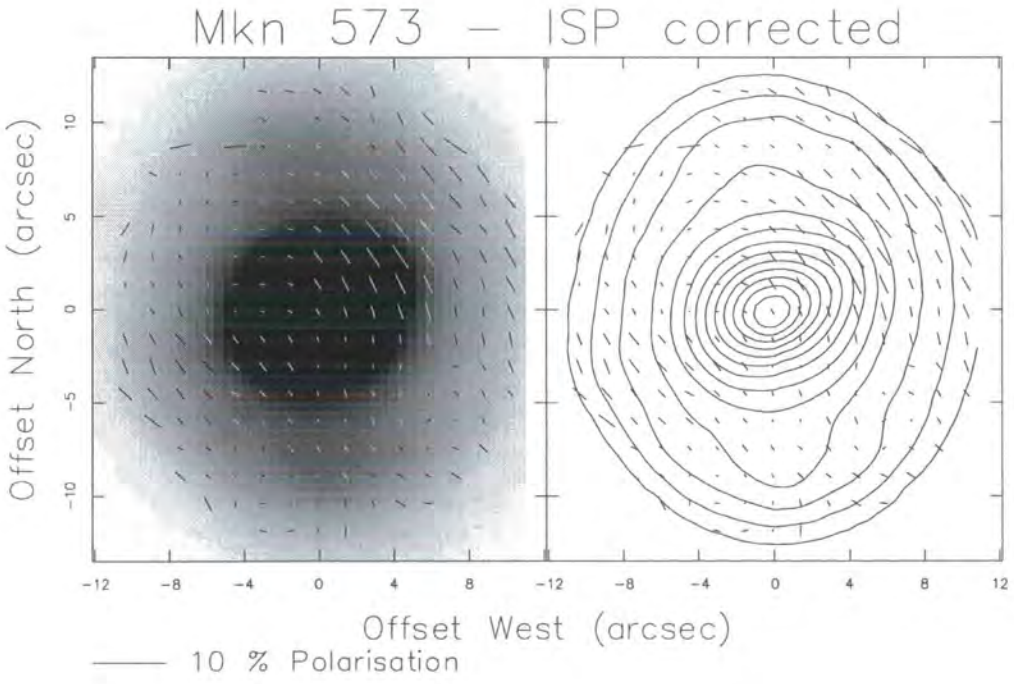

Figure 5.21: V-band total intensity image of Mkn 573, overlaid with polarization vectors binned with square size 5 and step size 3 pixels, with a polarized intensity cutoff, corrected for ISP of 0.60% at 110°

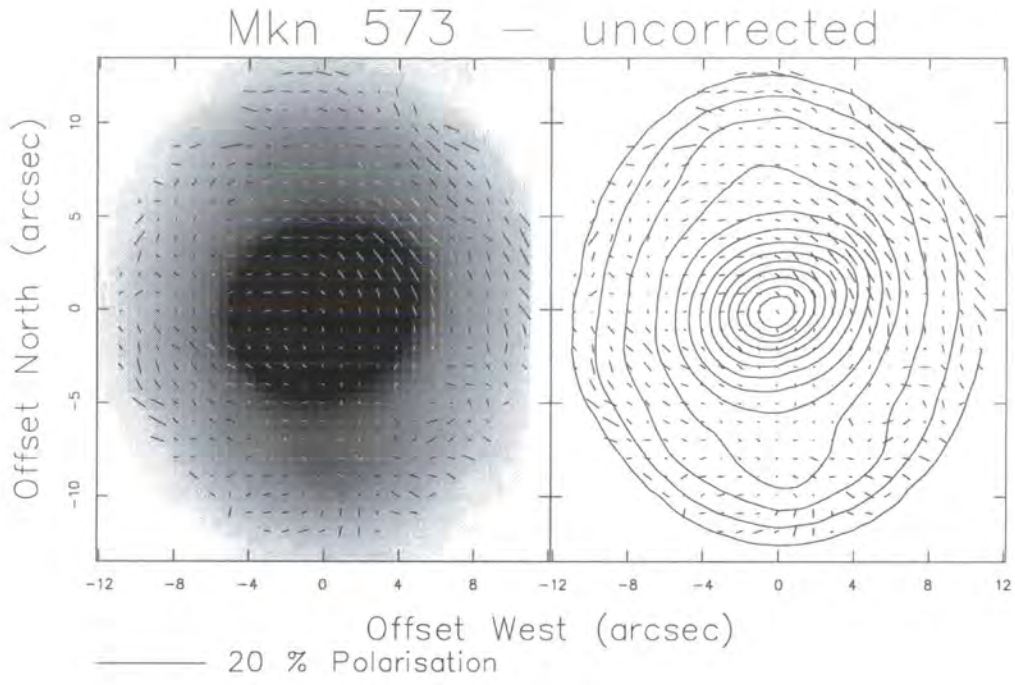

Figure 5.22: V-band total intensity image of Mkn 573, overlaid with polarization vectors binned with square size 3 and step size 2 pixels, uncorrected for ISP

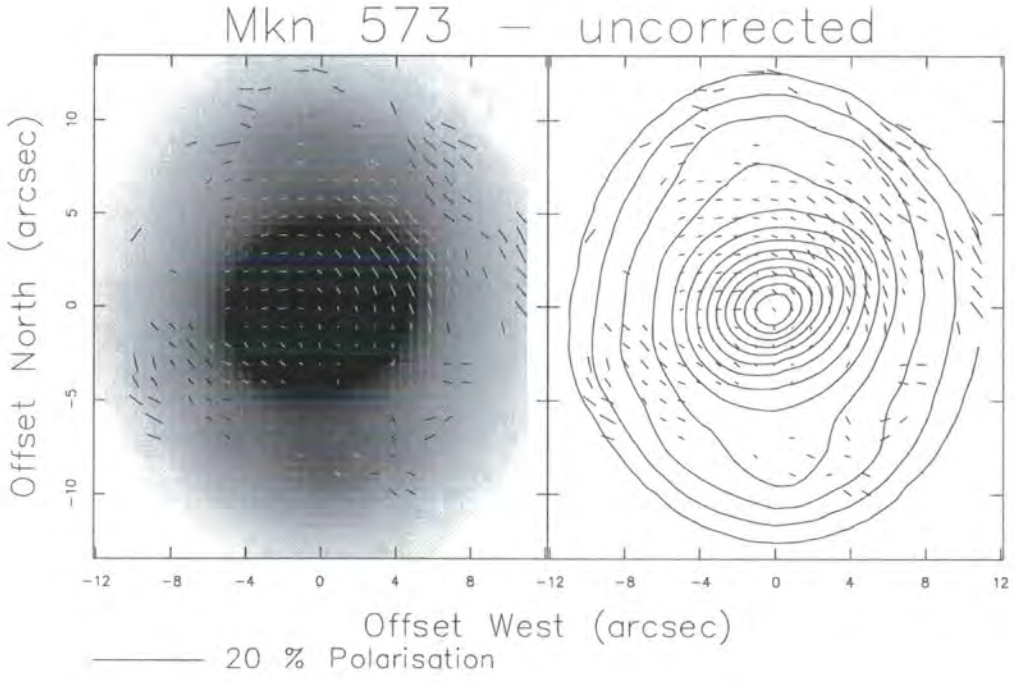

Figure 5.23: V-band total intensity image of Mkn 573, overlaid with polarization vectors binned with square size 3 and step size 2 pixels, with a polarized intensity cutoff, uncorrected for ISP

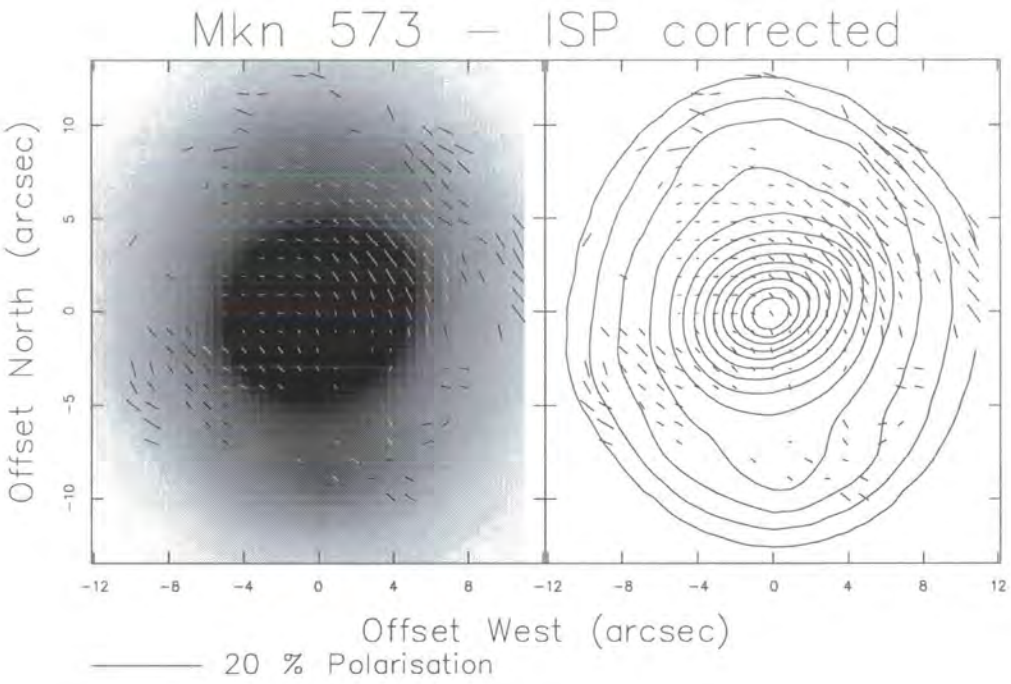

Figure 5.24: V-band total intensity and polarization image of Mkn 573, overlaid with polarization vectors binned with square size 3 and step size 2 pixels, with a polarized intensity cutoff, corrected for ISP of 0.33% at 125°

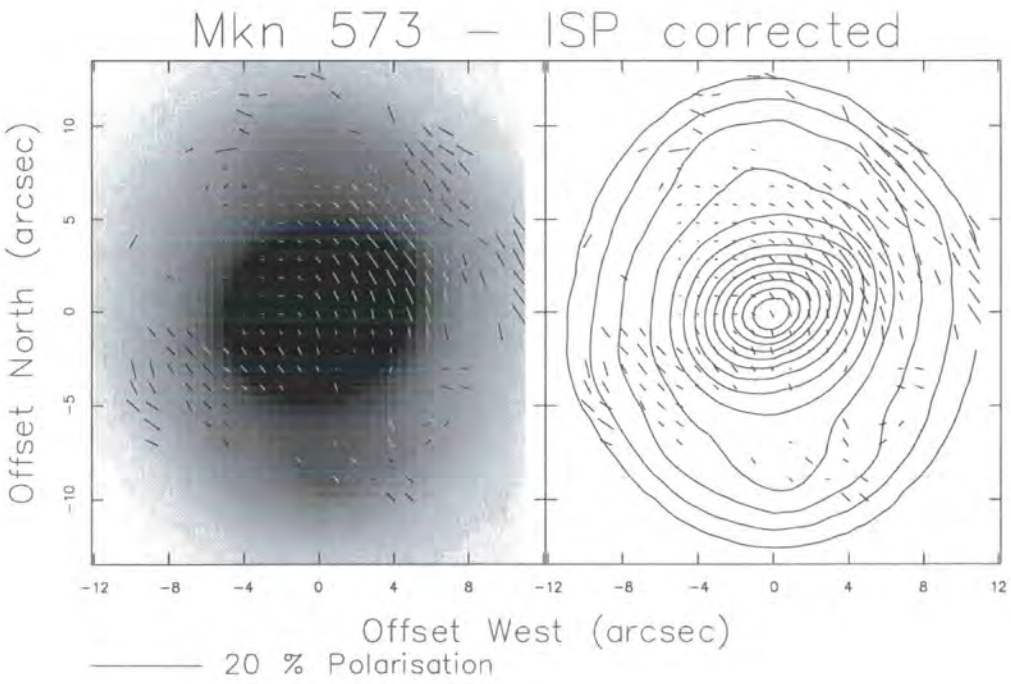

Figure 5.25: V-band total intensity and polarization image of Mkn 573, overlaid with polarization vectors binned with square size 3 and step size 2 pixels, with a polarized intensity cutoff, corrected for ISP of 0.6% at 110°

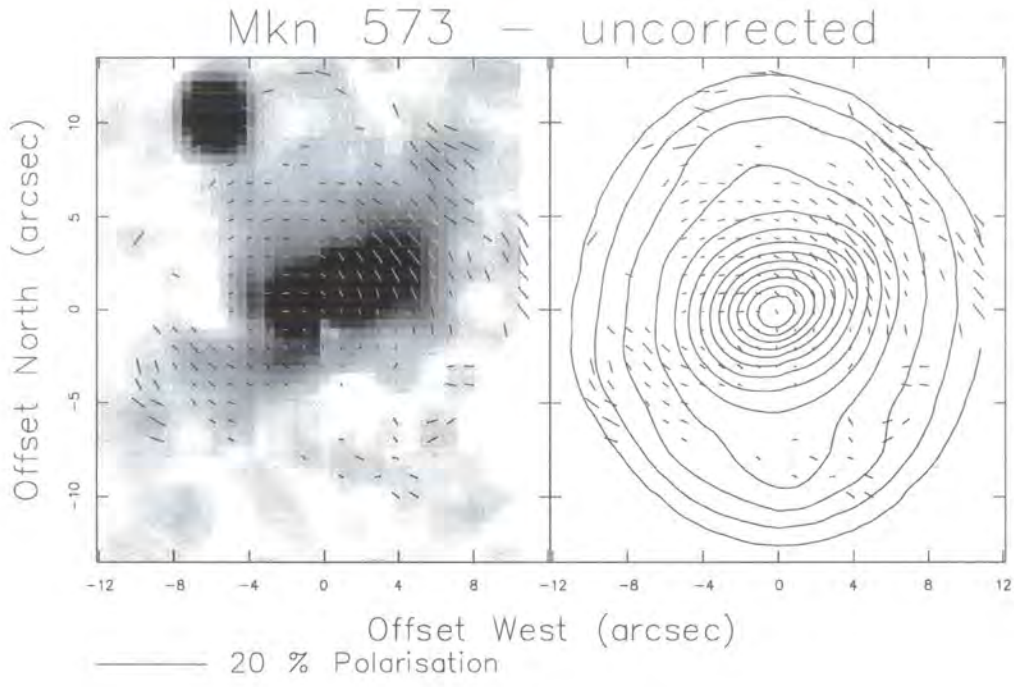

Figure 5.26: V-band polarized intensity greyscale image and total intensity contour image of Mkn 573, overlaid with polarization vectors binned with square size 3 and step size 2 pixels, with a polarized intensity cutoff, uncorrected for ISP

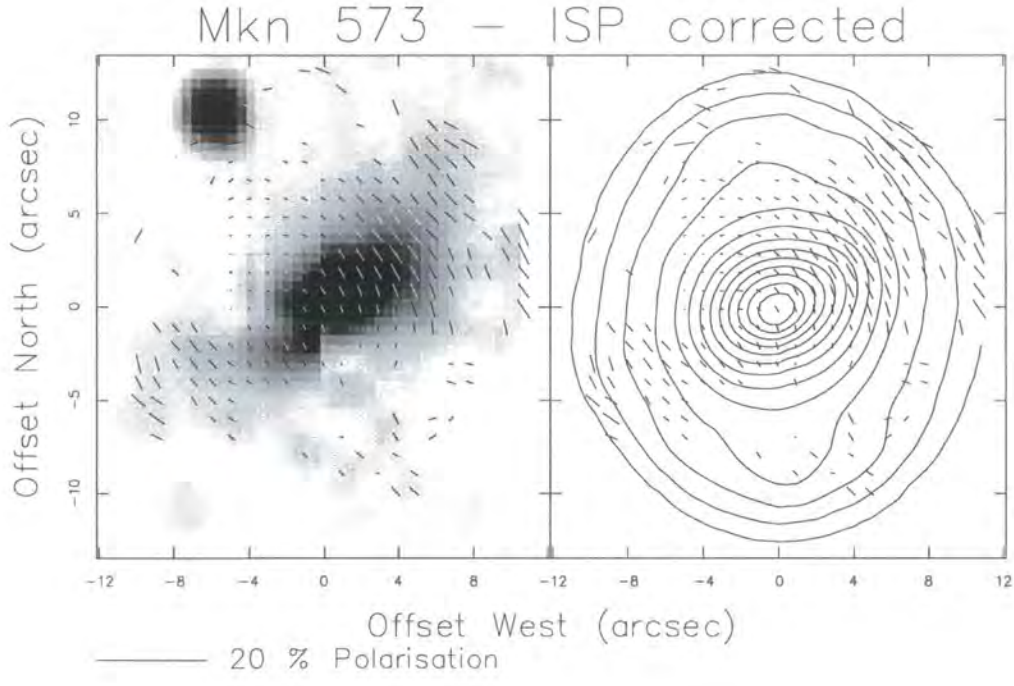

Figure 5.27: V-band greyscale polarized intensity image and total intensity contour image of Mkn 573, overlaid with polarization vectors binned with square size 3 and step size 2 pixels, with a polarized intensity cutoff, corrected for ISP of 0.6% at 110°

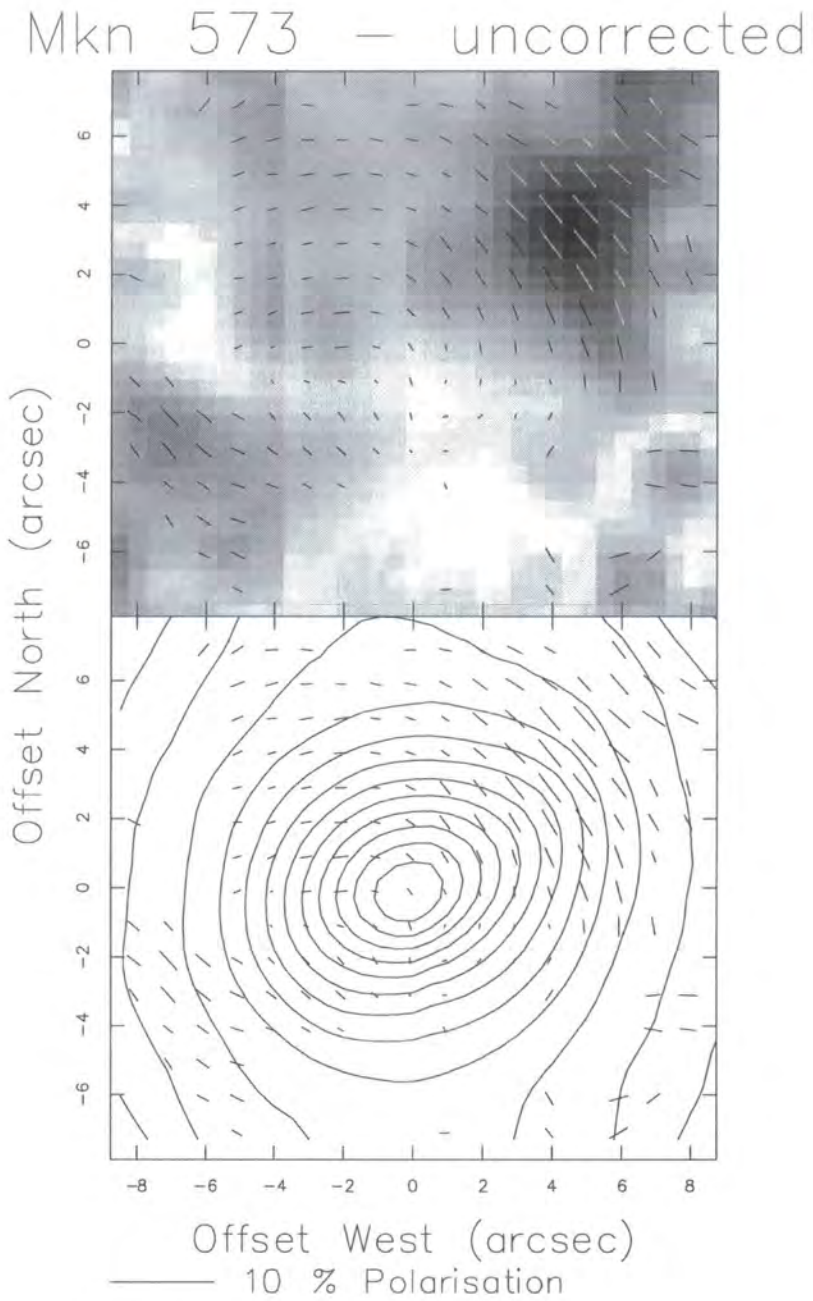

Figure 5.28: V-band degree of polarization greyscale image and total intensity contour image of Mkn 573, overlaid with polarization vectors binned with square size 3 and step size 2, with a polarized intensity cutoff, uncorrected for ISP

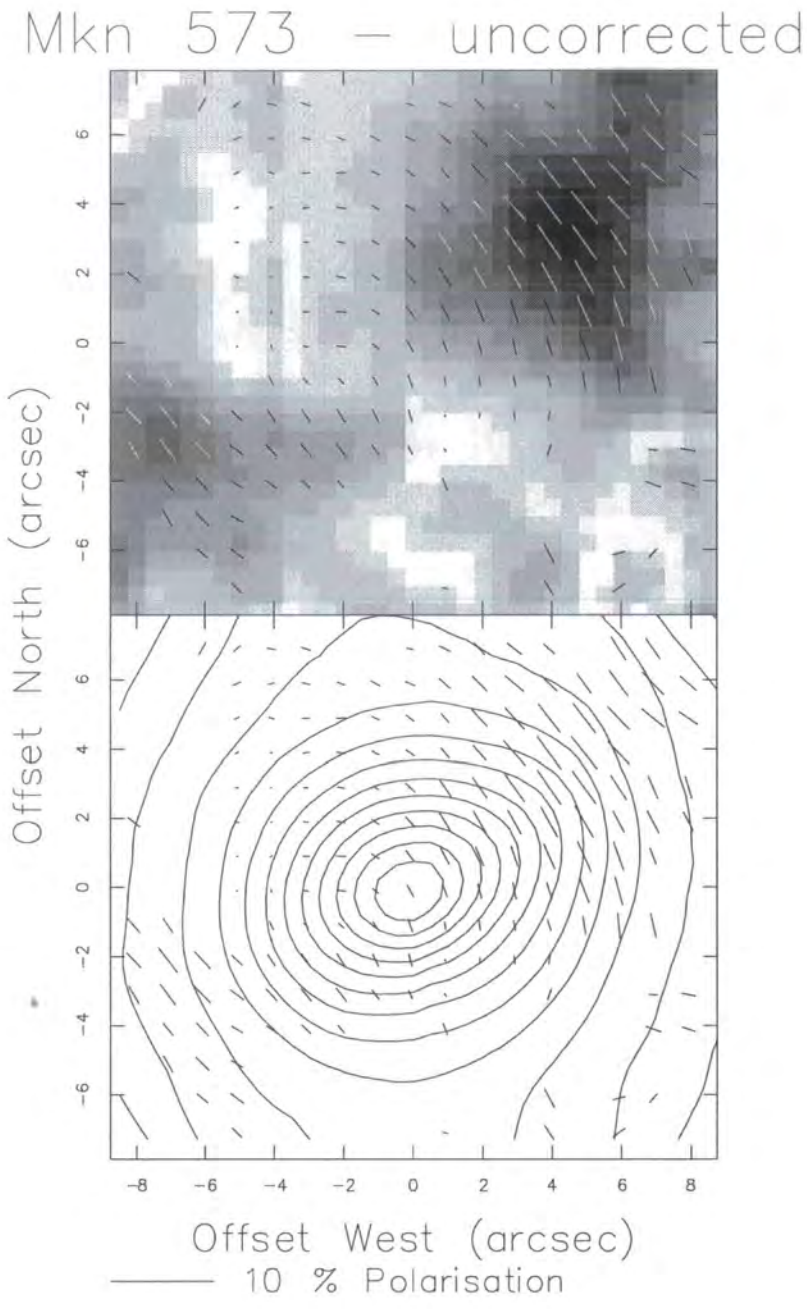

Figure 5.29: V-band polarization greyscale image of Mkn 573, overlaid with polarization vectors binned with square size 3 and step size 2, with a polarized intensity cutoff, corrected for ISP of 0.6% at 110°

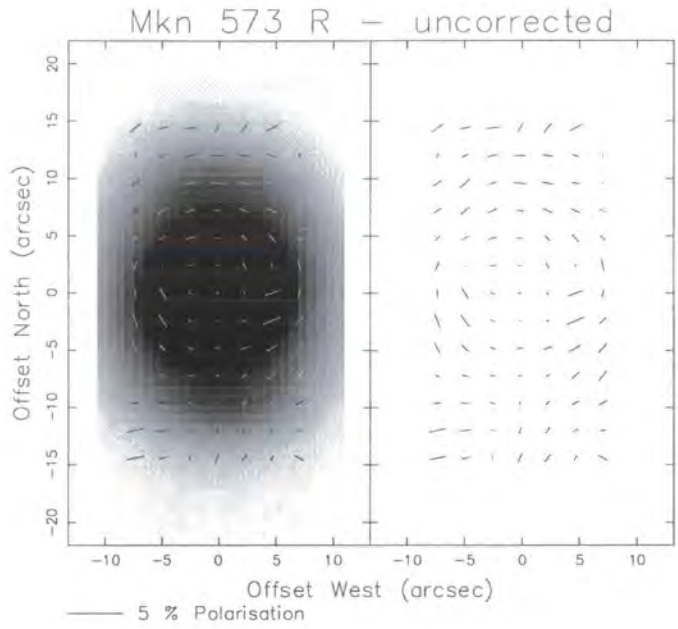

Figure 5.30: R-band total intensity image of Mkn 573, overlaid with polarization vectors binned with square size 5 and step size 3 pixels, uncorrected for ISP

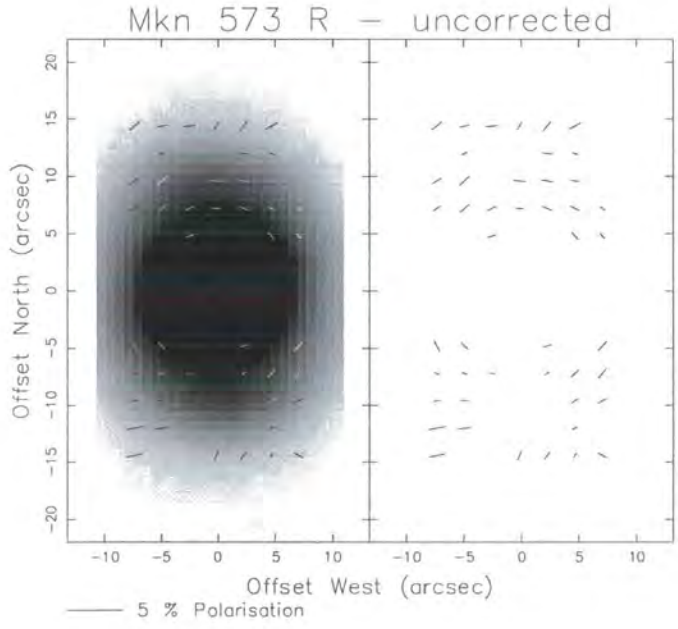

Figure 5.31: R-band total intensity image of Mkn 573, overlaid with polarization vectors binned with square size 5 and step size 3 pixels, uncorrected for ISP

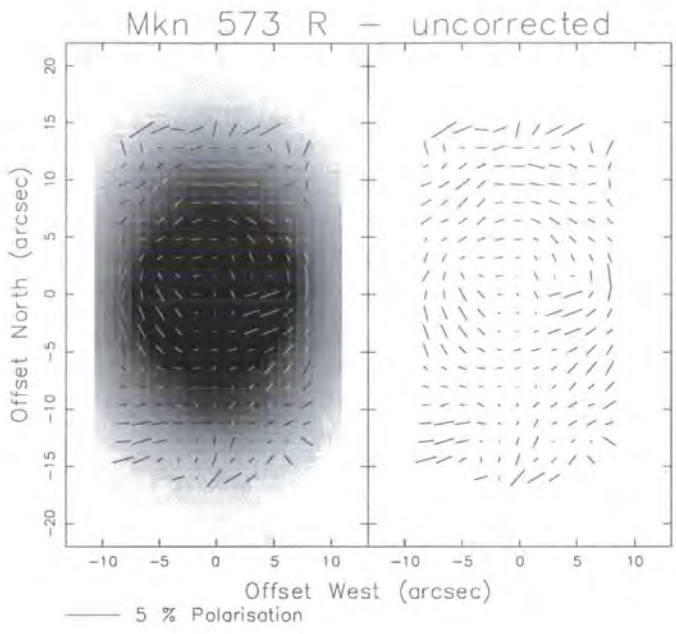

Figure 5.32: R-band total intensity image of Mkn 573, overlaid with polarization vectors binned with square size 3 and step size 2 pixels, uncorrected for ISP

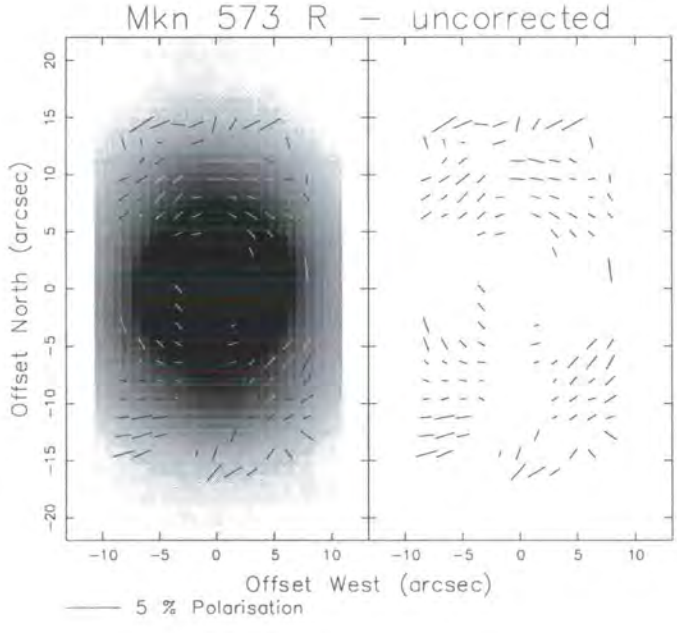

Figure 5.33: R-band total intensity image of Mkn 573, overlaid with polarization vectors binned with square size 3 and step size 2 pixels, uncorrected for ISP

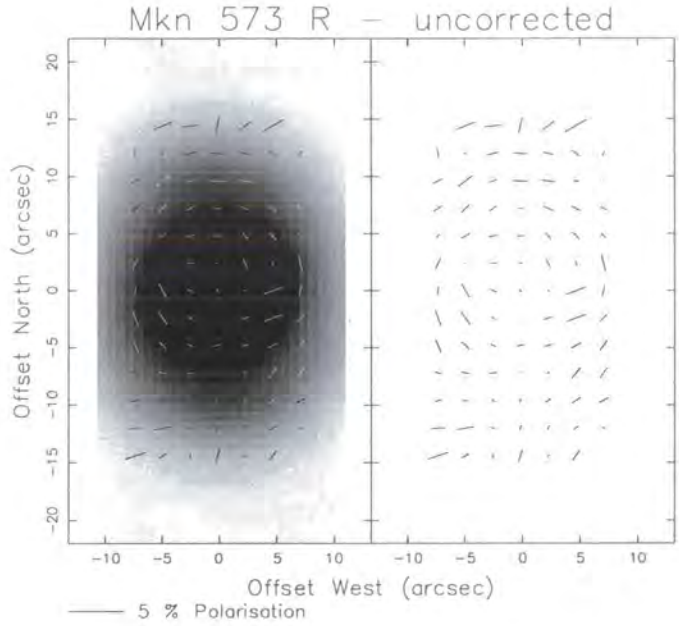

Figure 5.34: R-band total intensity image of Mkn 573, overlaid with polarization vectors binned with square size 3 and step size 3 pixels, uncorrected for ISP

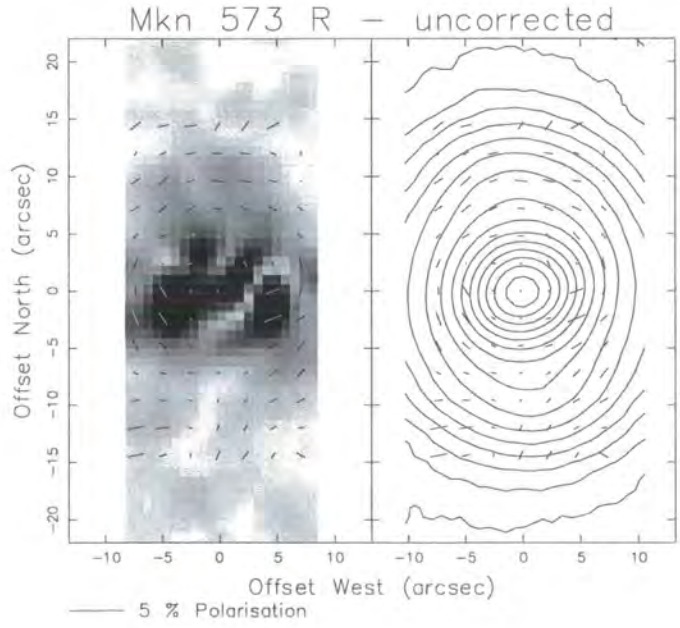

Figure 5.35: R-band polarized intensity image of Mkn 573, overlaid with polarization vectors binned with square size 5 and step size 3 pixels, uncorrected for ISP

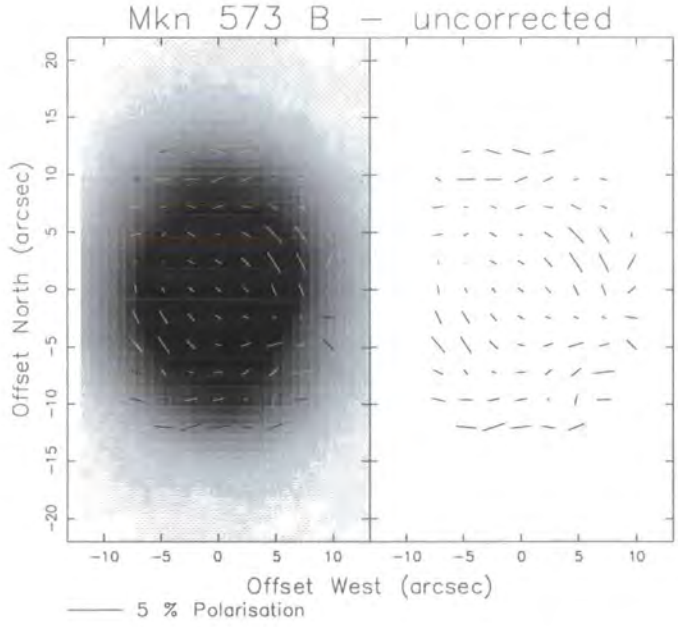

Figure 5.36: B-band total intensity image of Mkn 573, overlaid with polarization vectors binned with square size 5 and step size 3, uncorrected for ISP

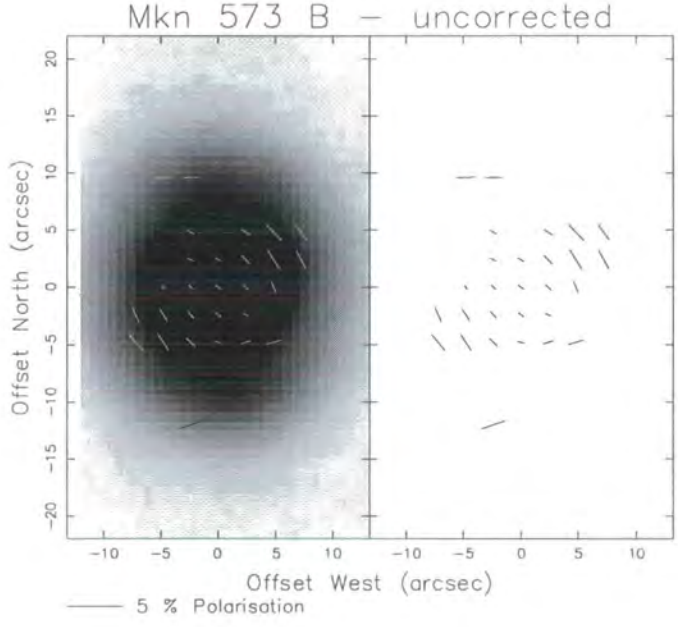

Figure 5.37: B-band total intensity image of Mkn 573, overlaid with polarization vectors binned with square size 5 and step size 3, uncorrected for ISP

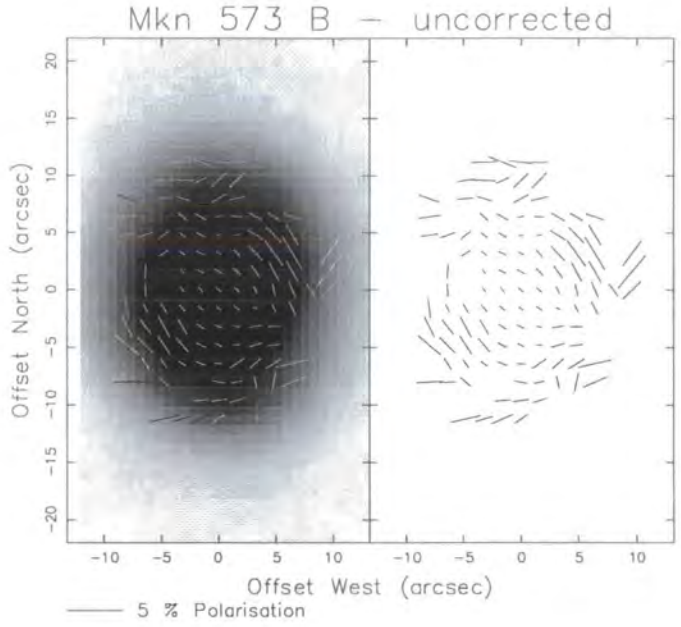

Figure 5.38: B-band total intensity image of Mkn 573, overlaid with polarization vectors binned with square size 3 and step size 2, uncorrected for ISP

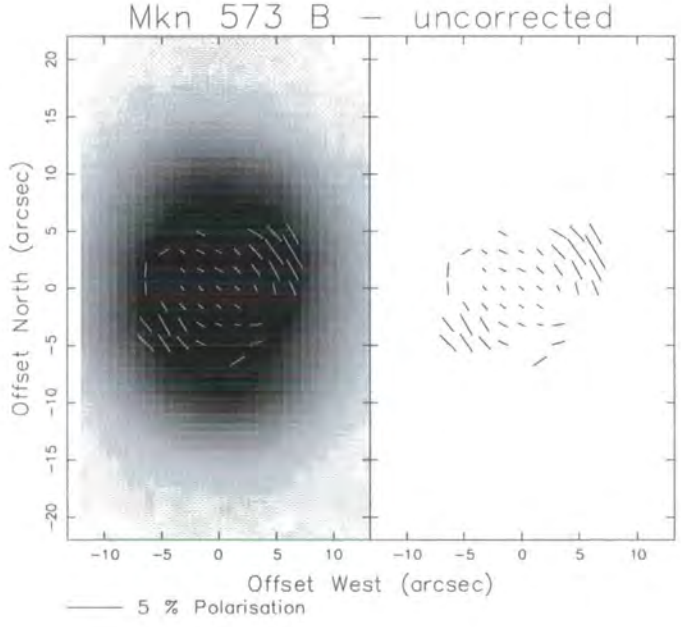

Figure 5.39: B-band total intensity image of Mkn 573, overlaid with polarization vectors binned with square size 3 and step size 2, uncorrected for ISP

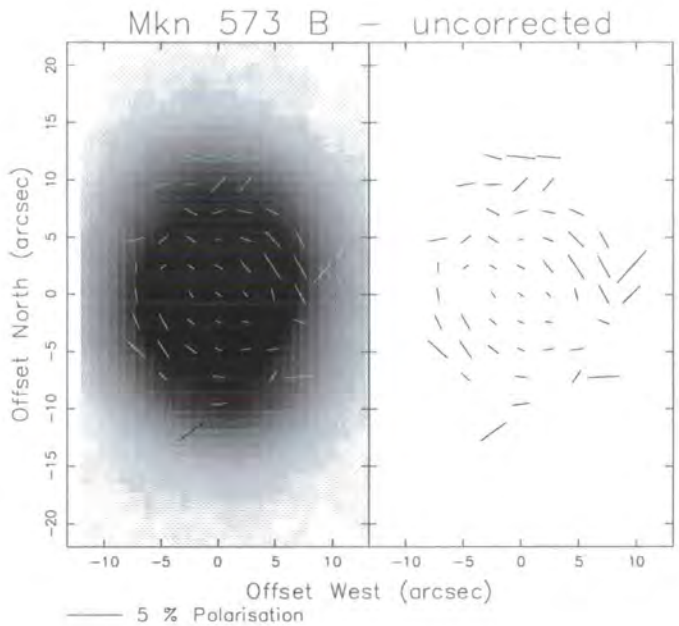

Figure 5.40: B-band total intensity image of Mkn 573, overlaid with polarization vectors binned with square size 3 and step size 3, uncorrected for ISP

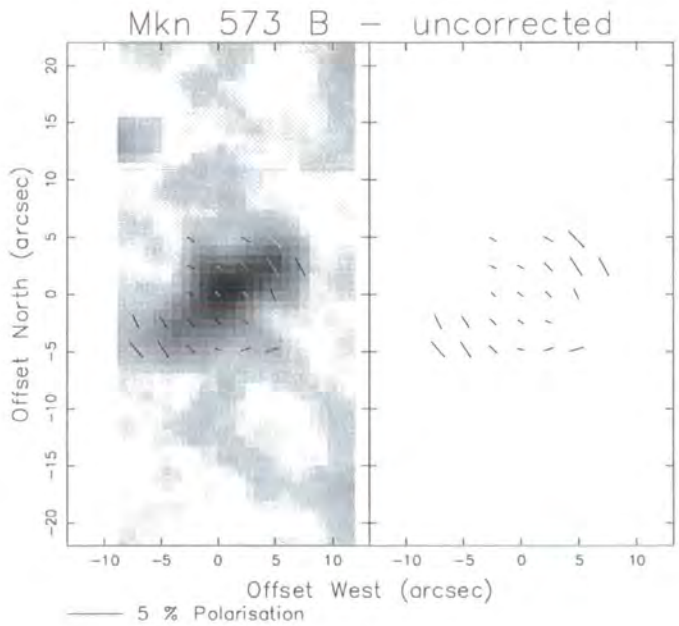

Figure 5.41: B-band polarized intensity image of Mkn 573, overlaid with polarization vectors binned with square size 5 and step size 3 pixels, uncorrected for ISP

5.4 NGC 1566

5.4.1 Introduction

NGC 1566, the brightest member of the southern Dorado Group, is classified as an SABbc galaxy (de Vaucouleurs 1973 [58]) with no nearby companions, and has an inclination of about 27°± 3° calculated from gas kinematic studies by Pence *et al.* (1990) [179]. A DSS image is of the galaxy reproduced in figure 5.42 with a field of 8 arcminutes by 6 arcminutes. From optical and infra-red photometry and ionized gas distribution data, it is seen to have a central 45″ by 30″ bar of major axis 15° and a highly symmetric double two-armed spiral structure. The two bright inner arms originate within 1 arcsecond of the nucleus from the ends of the bar, and extend over 5.5 by 3 arcminutes. The the outer arms are much fainter, extending out over 7 arcminutes continuing on from the inner arms (Pence *et al.* 1990).

The galaxy hosts a low luminosity AGN, which spends most of its time in a low activity state, so that it is difficult to measure the AGN emission against the star formation in the nucleus of the galaxy. Seyfert 1 characteristics were measured by Kriss *et al.* in 1991 [129] using HST data, demonstrating a BLR and a point-like narrow-line emission region (less than 0.7″ in diameter). It is now classified as a Seyfert 1, although published measurements in the 1980's tended towards a Seyfert type 2 classification *i.e.* broad lines were not detected, probably because of difficulties in measuring the lines in the low-luminosity states. The line ratios are close to those of a Seyfert 2 and the nuclear spectrum resembles a H_{II} region emission apart from the weak broad lines, Hawley & Phillips (1981) [99], so it is transitional in properties, and can be classified either as a Seyfert 1.9 or a 1.2 in the Seyfert scheme depending on the state of nuclear activity, Alloin *et al.* (1985) [4].

Radio continuum measurements by Harnett *et al.* (1984) [97] detect radio emission over both the nucleus and the disk. Multi-wavelength radio observations by Ehle *et al.* (1996) [71] show both a non-thermal and a thermal component to the radio emission, where the radio intensity peaks are mostly found to correspond to H_α intensity peaks, and at 3.3 cm generally follow the spiral arms, but at longer wavelengths the radio emission tends to extend over the whole disk. Linear polarization of about 30% in the inter-arm regions was detected at a wavelength of 6.2 cm, and some also at 12.7 cm, although 3 to 10 times weaker. No significant polarization was detected in 3.5 cm or 21.7 cm observations. The inferred magnetic field lines are very well aligned with the optical spiral structure, possibly due to magnetic field compression between the spiral arms.

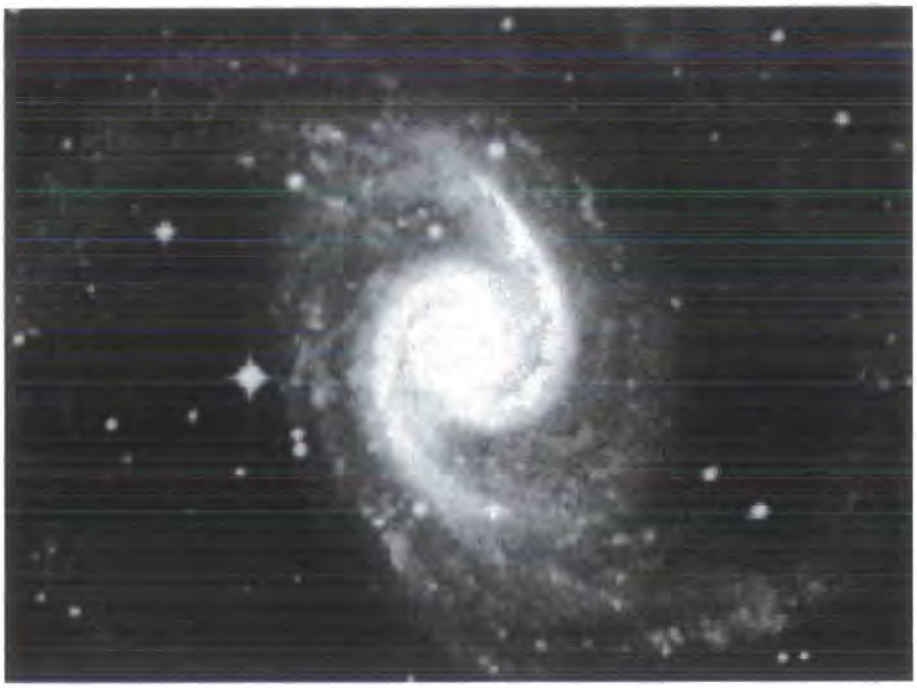

Figure 5.42: DSS intensity image of NGC 1566 in a field of 8 by 6 arcminutes

Infra-red H-band maps by Hackwell & Schweizer (1983) [94] show an unresolved nucleus, a central infra-red bar of $45'' \times 30''$ in extent, and the two inner spiral arms. High resolution measurements of the variable near-infrared component from the active nucleus by Baribaud *et al.* (1992) [18] indicate thermal emission by a sub-parsec scale nuclear graphite dust shell at about 1500 K, heated by the central nuclear UV source.

ROSAT X-ray measurements (Ehle *et al.* 1996 [71]) show hard and soft X-ray emission from the nucleus which can be fitted by a power-law spectral index of $\alpha = 2.3$, close to the mean for Seyfert 1 nuclei. The corresponding absorbing column density of 2.38×10^{20} cm^{-2}, fairly typical for Seyfert 1s. Strong X-ray emission is detected in the central regions out to 5 arcseconds around the nucleus, probably thermal emission from 10^6 - 10^7 K gas associated with a wind from the Seyfert nucleus. More diffuse extended X-ray emission is also detected over the galaxy, covering broadly similar regions to the extended radio emission, and suggesting a spatial link between the hot X-ray emitting gas and the magnetic field. Significant time variability of the nuclear continuum, in particular the soft X-ray flux was found by Baribaud *et al.* (1992) [18] with a timescale of less than a month, which is typical for Seyfert 1 nuclei.

5.4.2 Observational details

Observations of NGC 1566 were performed at the Cassegrain focus (focal ratio 15) of the SAAO 1-metre telescope in February 1997 using a broad band V filter (5450Å, FWHM 130Å), an R filter and an H_α (6613 Å, FWHM 70 Å) filter. The V band data were taken on the 5th - 6th of February, with exposures of 900 seconds for each half waveplate position; a further V-band set was also taken on the 7th February but the poor seeing conditions made the data of insufficient quality to include here. The R band data were taken on the 15th - 17th February, with exposures of 900 seconds and the H_α data also with 900 second exposures, on the 17th of February. Suitable flatfields were also observed for each dataset. The seeing for these observations was calculated from stars in the field to be approximately 2.5 to 3 pixels, (*i.e.* 3 to 3.6 arcseconds). There was significant moonlight present for the R and H_α band observations, although in principle the data reduction procedures should correct for this.

The scale of the sky on the CCD detector was approximately 1.2″per pixel, and at the estimated distance of 17.4 Mpc (Hackwell 1983 [94]), 1 arcminute corresponds[6] to approximately 5.1 kpc, 1 arcsecond to 84 pc. Data were taken in the V and R bands at three telescope positions, resulting in wide but not complete sky coverage. Time constraints limited observations to being taken at just one position for the H_α images, resulting in only a small part of the galaxy being mapped in this waveband, and unfortunately this region did not include the nucleus and central regions of the galaxy. The DSS image of NGC 1566 in figure 5.42 shows the field that was mapped by the polarimeter (approximately 8 arcminutes by 6 arcminutes).

There was a problem of saturation of the central pixels in several of the brighter stars, which has resulted in apparently very high polarization measurements for them, all similarly oriented at 45°. Fortunately such artefacts are easily identified, as most of the stars would be expected to be either unpolarized or polarized only due to interstellar polarization which is expected to be minimal for this line-of-sight.

5.4.3 Image details

Figures 5.43 to 5.60 present V, R, and H_α band images of NGC 1566, with north to the top and east to the left. The scale is in arcseconds, centred on the peak nuclear intensity in the image, with the exception of the H_α images in figures 5.47 to 5.50, which are aligned together by bright stars and centred on a rough estimate of where the nucleus would have

[6] Assuming $H_0 = 75$ km s^{-1} Mpc^{-1} and using the systemic velocity calculated by Hackwell & Schweizer 1983 [94]

been if it had have been imaged. The greyscale intensity is reversed, *i.e.* black represents the highest intensity. The plotting of the polarization vectors was achieved by binning the polarization data over squares of a set size (either 3, 5 or 7 pixels *i.e.* 3.6, 6.0 or 8.4 arcseconds) centred on the selected pixel, then moving the centre on by a set number of pixels (either 2, 3 or 4 pixels) to get the position of the next polarization vector to be calculated. For the maps showing vectors along a trace of the spiral arm and inter-arm regions, the polarization data were binned in circles 3.3 pixels (4″) in diameter located at various points along these regions.

5.4.4 Interstellar polarization

The galactic co-ordinates ($l = 264°$,$b = -43°$) show that this Seyfert is not viewed along the galactic plane, indicating that the ISP corrections are likely to be small. Examination of a map presenting the interstellar polarization of starlight by Mathewson & Ford (1970) [150], shows that the polarizations of the stars measured closest that region are negligible. Furthermore, the polarization patterns found in the uncorrected maps show no obvious sign of ISP contamination, so there has been no attempt to calculate or subtract an ISP contribution for these observations of NGC 1566.

5.4.5 Results: V-band

The V-band maps with polarization vectors presented in figure 5.43 and 5.44 (plotted at 65% and 95% confidence levels respectively) show that there is a distinct spiral pattern to the polarization outside of the very central nuclear regions. This polarization data, binned in 8.4″ squares, averages around 1.5% to 2% and is seen most distinctly in the west inter-arm region. There is a significant region of polarization just north of the nucleus, which seems to be associated with the beginning of the east inter-arm region rather than the spiral arm itself, with the highest polarization in the less bright areas. Unfortunately, most of the eastern inter-arm region falls into the gap in the map coverage, so it is not possible to see whether the high polarization extends along the rest of the inter-arm area.

The highest polarization levels (around 2.5%) are seen along the inner edge of the west inter-arm region (in the southern part), where the directions of the polarization vectors follow the spiral structure. There is significant polarization south of the beginning of the west arm in figure 5.44, on the outside edge of the arm which also appears to be following the spiral structure, with similar polarization levels to those in the inner west inter-arm region. The polarization in the spiral arms is not significantly above the signal-to-noise.

The spiral pattern is further investigated in figures 5.51 and 5.53, which give maps showing traces of the polarization along the spiral arms, and the inter-arm regions respectively, plotted without a signal-to-noise cut-off. The polarization vectors in the inter-arm regions are seen to clearly follow the spiral configuration in both the east and west interarm region. In the spiral arms, there is a trend in the west arm for the vector orientation is to follow the spiral pattern, but the vectors are less well aligned with the spiral patterns than the inter-arm vectors.

The polarization data of the central region of the galaxy is shown at in figure 5.45 where it is averaged in bins of 6″ square, and at higher resolution in figure 5.46 averaged in bins of 3.6″ square; in both cases the vectors are plotted at 65% confidence levels. The higher resolution data is near the seeing limit, so the reliability of fine detail should be interpreted with care. These maps reveal what appears to be a foreground star immediately to the east of the nucleus, which has an obviously different polarization orientation (45°) to the spiral pattern. As to why this star would be significantly polarized is unexpected as there is negligible ISP in the region. On closer inspection of the intensity levels however, it is seen that the intensity level is very high, saturating in one or more of the frames taken at different half-wave plate positions, thus causing the false appearance of polarization at 45°. The main result of these maps is the demonstration of clear and close alignment of the polarization vectors in the inter-arm regions with the spiral arm structure. In the south west corner of the map, there is an abrupt change of polarization orientation by approximately 90°at the outside of the western spiral arm, but the signal-to-noise in that region is quite low, so on a 95% confidence level plot, these vectors disappear.

The higher resolution map (figure 5.46) indicates that there is an intrinsic nuclear polarization, which appears as an increase in the centre-most polarization levels compared to the immediate surroundings. Aperture polarimetry of the nucleus over a range of simulated apertures is presented in table 5.13. This is compared to a previously published measurement of the polarization through a blue-green filter by Martin (1983) [148] in table 5.14. Over an aperture of 4 arcseconds in diameter, the level of polarization measured by Martin (1983) (0.6% at 53°) is seen to be smaller than that measured by this thesis (1.3% at 46°), but his measured angle of polarization agrees within the estimated errors to that measured in this study. There are two possible explanations, either this is an intrinsic difference in polarization level, or a systematic error in measurement due to differences in the observation techniques. The wavelength ranges over which the polarizations were measured are different; the observations of Martin (1983) are made at shorter bluer wavelengths, so if the polarization mechanism is wavelength dependent, or the unpolarized diluting flux is greater at bluer wavelengths, then the measurements would be expected to be different. The other possibility for this discrepancy is that the polarization is different either because of intrinsic variations or that the measurements

could have been centred on different places in the nucleus, which would lead to different polarization measurements. To check on this, the centre of the simulated aperture was shifted by a couple of pixels in different directions, and this can lead to a change in polarization level by up to 0.5%, which would bring the measurements into agreement within the error estimates. However this seems quite contrived, so it seems far more likely that the measured difference is real and demonstrates wavelength dependence with a lower polarization percentage level in the blue.

Figure 5.59 gives a map with polarized intensity plotted as greyscale. The vertical gap in coverage and visible banding effects are due to problems with the alignment and normalisation of the data sets. These normalisation problems have not seriously reduced the overall polarization data quality though, as can be seen by the good pattern alignment even in the affected areas. The location of the peak total nuclear intensity is shown by the cross (the peak polarized intensity is measured to be within 1 pixel north of this). The polarized flux is highest in the nucleus, but since the total intensity is also highest there, the resulting degree of polarization is not greatest in the nucleus. A high polarized flux is seen along the inner edge of the western spiral arm, corresponding to the maximum degree of polarization, and in the eastern interarm region (at the beginning of the eastern arm) an increase in polarized flux is seen. Also notable is the small region of high polarized flux in the bright spot in the north west spiral arm, which has a polarization orientation perpendicular to the spiral arm alignment, and also perpendicular to the polarization in the corresponding R-band map. Figures 5.51 and 5.53 give traces along the spiral arm and interarm regions respectively.

5.4.6 Results: R-band

R-band maps of the galaxy are presented in figure 5.47, where the polarization vectors are averaged over 8.4″ squares, and in figure 5.48, averaged over 6 arcsecond squares, both plotted at 65% confidence levels. These show that the highest significant levels of polarization over the main galaxy are in west inter-arm region. The level of polarization is in this region is around 1.5% to 2% and the orientation approximately follows the spiral arms. There are also a few polarization vectors in the east inter-arm region, close to the gap in coverage, which suggestively appear to follow the spiral structure of the east inter-arm region in figure 5.48, however the data gap at this point means it is not possible to see what is happening. In the north west, north east and south west regions just outside the bright spiral arms, the polarization vectors are also orientated broadly parallel to the spiral arms and with levels of the order 1.5% to 3%. On the preliminary maps, the entire south of the image below the west spiral arm was contaminated with a

gradient of scattered moonlight, leading to apparent band of vectors aligned north-south. This was successfully corrected for by modelling the sky background using a linear rather than a constant fit. With this in mind, the apparent region of alignment (north-south) of the polarization vectors in the south west of the map over the region of lowest intensity is most likely to be due to residual scattered moonlight effects, and not a real feature.

The central region of NGC 1566 is shown in figures 5.49 and 5.50. The polarization data in figure 5.49 is averaged over 6 arcsecond squares plotted at 65% confidence levels, and in figure 5.50 over 3.6 arcsecond squares also plotted with confidence levels of 65%. The presence of intrinsic nuclear polarization is signalled by the very central polarization vectors showing an increase in polarization level and a different polarization angle when compared to the surrounding ones. Aperture polarimetry measurements of the nucleus are presented in table 5.13, and they show the nuclear polarization over a 3 arcsecond diameter to be approximately 3.6% at 51°, which is a high optical polarization for a Seyfert nucleus.

Figures 5.52 and 5.54 present maps showing a trace of the polarization along the spiral arm regions and inner inter-arm regions. The polarization vectors of the inter-arm regions are seen to follow the spiral configuration well except for the southernmost inter-arm region. The polarization vectors along the bright spiral arms have a general tendency to be aligned parallel to the spiral structure, however it is a weaker trend than that shown by the inter-arm vectors.

Figure 5.60 gives a map of polarized intensity as greyscale overlaid with polarization vectors, which shows high levels of polarized flux in the nuclear region (the location of the peak total nuclear intensity is indicated by the cross). High levels of polarized flux are also seen in a small patch approximately 50 arcseconds west of the nucleus corresponding to a bright spot on the western spiral arm, and also there is polarized flux associated the bright knots in the north west of the western arm.

5.4.7 Results: H_α band

The H_α maps here unfortunately have very limited sky coverage, and the signal levels were low in spite of multiple exposures, and the red continuum has not been subtracted. The total intensity maps in figure 5.55 and 5.56 show complex localised regions of emission in the two main spiral arms, which correspond well with the H_α intensity image of Ehle *et al.* (1996) [71]. Figures 5.57 and 5.58 give traces of polarization vectors along the spiral arm and the inter-arm regions respectively, where the polarization data is averaged over simulated 4 arcsecond apertures.

Table 5.13: V and R band nuclear aperture polarimetry of NGC 1566

Aperture (arcsec)	Aperture (pixels)	Polarization (percent)	Position Angle (degrees)
V-band			
3	2.5	1.47% ± 0.18%	45°± 4°
4	3.3	1.33% ± 0.18%	46°± 4°
5	4.2	1.23% ± 0.17%	48°± 4°
6	5.0	1.04% ± 0.17%	50°± 5°
R-band			
3	2.5	3.63% ± 0.27%	51°± 2°
4	3.3	3.25% ± 0.27%	50°± 2°
5	4.2	2.83% ± 0.27%	50°± 3°
6	5.0	2.61% ± 0.27%	49°± 3°

Table 5.14: Comparison of nuclear polarization measurements of NGC 1566

Aperture (arcsecs)	Range of wavelength (Å)	Polarization (percent)	Position Angle (degrees)	Reference [1]
4	V band	1.33 ± 0.18	46 ± 4	F99
4	R band	3.25 ± 0.27	50 ± 2	F99
4	3800 - 5600[2]	0.6 ± 0.24	52.6 ± 11.6	M83

[1]References: F99 = this thesis, Felton (1999), M83 = Martin (1983)
[2]Blue-green Corning 4-96 filter

Both east and west inter-arm region shows polarization levels of about 3%, oriented approximately parallel to the spiral arms, similar to that seen in the R and V band images, but with additional coverage of the eastern inter-arm region. Around the bright spots in the east spiral arm, both on the inside and outside of the arm, the polarization vectors again run parallel to the spiral configuration as seen in the west inter-arm region. In the bright spots themselves however, the polarization is much lower, and not preferentially aligned along the spiral pattern. At the beginning of each of the spiral arms, there is a tendency for the polarization to be aligned perpendicular to the pitch of the spiral arm, which is not seen in the other bands (although they only cover the start of the eastern spiral arm). Because of the potential moonlight contamination, and the low signal levels in these H_α observations, care was taken to ensure a representative sky subtraction was performed, but unlike in the R-band maps, there was no significant difference made to the polarization pattern between using a constant sky subtraction model or a linear one.

5.4.8 Results: Discussion

Radio-optical polarization correspondence

There is a striking correspondence between the V-band and R-band optical polarization maps presented here and the radio polarization maps of this galaxy (at wavelengths of 6 cm and 13 cm) produced by Ehle *et al.* (1996) [71], of which the 6 cm map is reproduced here in chapter 3, figure 3.1, page 65. Their radio maps show that the bulk of the radio polarization is located between the main spiral arms at 6 cm, and at the inner edge of the eastern spiral arm at 13 cm. The maximum polarizations in these regions are up to 30% polarized at 6 cm, and up to 5% at 13 cm, although the average is 7% at 6cm and much lower at 13 cm. This radio polarization is due to synchrotron emission, so the measured polarization vectors should trace out the magnetic field in the galaxy. The radio polarization measured in the north west region of the galaxy is spatially well-matched by the optical polarization measured in this study, with approximately the same angles of polarization (*i.e.* aligned with the spiral configuration), although the optical polarization levels (about 1-2%) are much lower than the radio levels. This alignment is strong evidence for the optical polarization being produced by dichroic extinction by dust particles aligned in the spiral magnetic field traced out by the radio synchrotron measurements, and which is also traced out by the optical polarization as described in section 3.2.3.

The high radio polarization in the south eastern spiral arm and inter-arm region is not spatially matched by correspondingly high optical polarization, which is not significantly above the noise levels in the arm. Unfortunately the gap in coverage occurs over the south eastern inter-arm region preventing comparison. Further west of the gap, around 40″–60″ south of the nucleus, the V-band optical polarization is significantly above the noise level to a degree of 1.5% and aligned with the radio polarization. In the same region of the R-band image however, the polarization is not aligned in this manner, which may be partly due to the contamination by scattered moonlight, and its subsequent incomplete subtraction.

Wavelength dependence in the polarization of the host galaxy

There is a strong wavelength dependence found in the optical polarization pattern observed over the galaxy of NGC 1566. In the R-band images, the polarization levels are generally higher, and over some regions there is a large shift in polarization angles compared to those in the V-band. If there are different competing mechanisms producing polarization, namely scattering and dichroic extinction, then it is possible that a flip of

90°in polarization position angle can occur with a change in wavelength as the different processes come to dominate.

Wavelength dependence of the polarization of the nucleus

The polarization of the nucleus over an aperture of 3 arcseconds is measured to be 3.6% at 51° in R-band, and 1.5% at 45° in V-band. A further measurement by Martin (1983) [148] at bluer wavelengths (a filter covering 3800-5600Å) gives a polarization measurement of 0.6% at 52°. This rise in polarization level towards longer wavelengths may be because the diluting unpolarized flux from the host galaxy is less at these wavelengths, so that the polarized nuclear emission constitutes a larger fraction of the observed flux. Further support for this explanation comes from the measurements shown in table 5.13, which shows that increasing the aperture size for the nuclear polarization measurement leads to a fall in polarization level, which would be consistent with greater dilution by stellar flux.

Polarisation around the bright spots in the spiral arms

In the limited H_α images, the bright spots have a much lower polarization than in the immediate surrounding region, and the polarization is not preferentially aligned along the spiral pattern. This decrease in polarization could be due to the polarizing dust grains losing their alignment, which would support the theory of magnetic field tangling in star-forming regions (Sukumar & Allen 1989 [223] and Beck *et al.* 1991 [25]), *i.e.* the field is tangled or disordered on scales around or smaller than the polarization resolution (around 6 arcseconds or 500 pc). This should also show up in radio polarization measurements. Alternatively it could be due to scattering rather than dichroic extinction becoming the dominant polarization mechanism. Inspection of subtle changes in the polarization angle around these bright spots hints at traces of centro-symmetry, which points towards polarization by scattering, (field tangling would lead to lower polarization levels either at the same position angle or at random angles if the alignment is completely lost). The signal-to-noise levels are low in these regions however, so it is difficult to tell which possibility is actually the case.

Comparison to the spiral galaxy NGC 6946

The polarization properties of the host galaxy NGC 1566 may be compared to those of NGC 6946, an extensively studied type Scd spiral galaxy inclined at about 30°(Rogstad

& Shostak 1973 [194]), which has H_{II} regions but does not host a Seyfert nucleus. Linear polarization at radio wavelengths from synchrotron radiation reveals a spiral magnetic field in NGC 6946 (*e.g.* Ehle & Beck 1993 [70]) that is strongest in the inter-arm regions (Beck 1996 [26]), but seems to disappear in the actual spiral arms, due to either field tangling or dust destruction in the star-forming regions. Optical polarization measurements by Fendt *et al.* (1998) [76] (over 400-750 nm) show a spiral pattern along much of the optical arms and eastern and western inter-arm regions corresponding to the radio polarization. Since the radio vectors trace out the spiral magnetic field, this radio-optical polarization correspondence is evidence of dichroic extinction.

The optical polarization maps by Fendt *et al.* (1998) [76] show an anomalous region (extending out to 3 arcminutes) of well aligned polarization structure just south of the outer spiral arm with almost constant polarization angle and degree (2-3%) and attribute this to some kind of magnetic cloud (*i.e.* a region of enhanced magnetic field or alignment, but without an increase of mass density because there is no local increase in extinction). Since this is very similar to the feature found on the R-band maps in this study, which has been demonstrated to be due to contamination by moonlight, their anomalous feature might, in spite of their sky modelling procedures, also be due to problems in correctly subtracting the scattered sky background light due to uneven moonlight contamination.

Spectrophotometry of the nuclear region of NGC 1566 by Roy & Walsh (1986) [196] reveals a much higher visual extinction ($A_B = 2.0$) than the Galactic extinction expected in this region ($A_B \approx 0.66$ by Sandage & Tammann 1981 [197]). This suggests that there is a large amount of extinction *i.e.* dust associated with the galaxy NGC 1566 itself. The nuclear region of NGC 6946 shows a circular polarization pattern characteristic of scattering from dust. In the nuclear region of NGC 1566 however, there is not an obvious alignment pattern, which perhaps could be to competing polarization mechanisms from the circumnuclear regions.

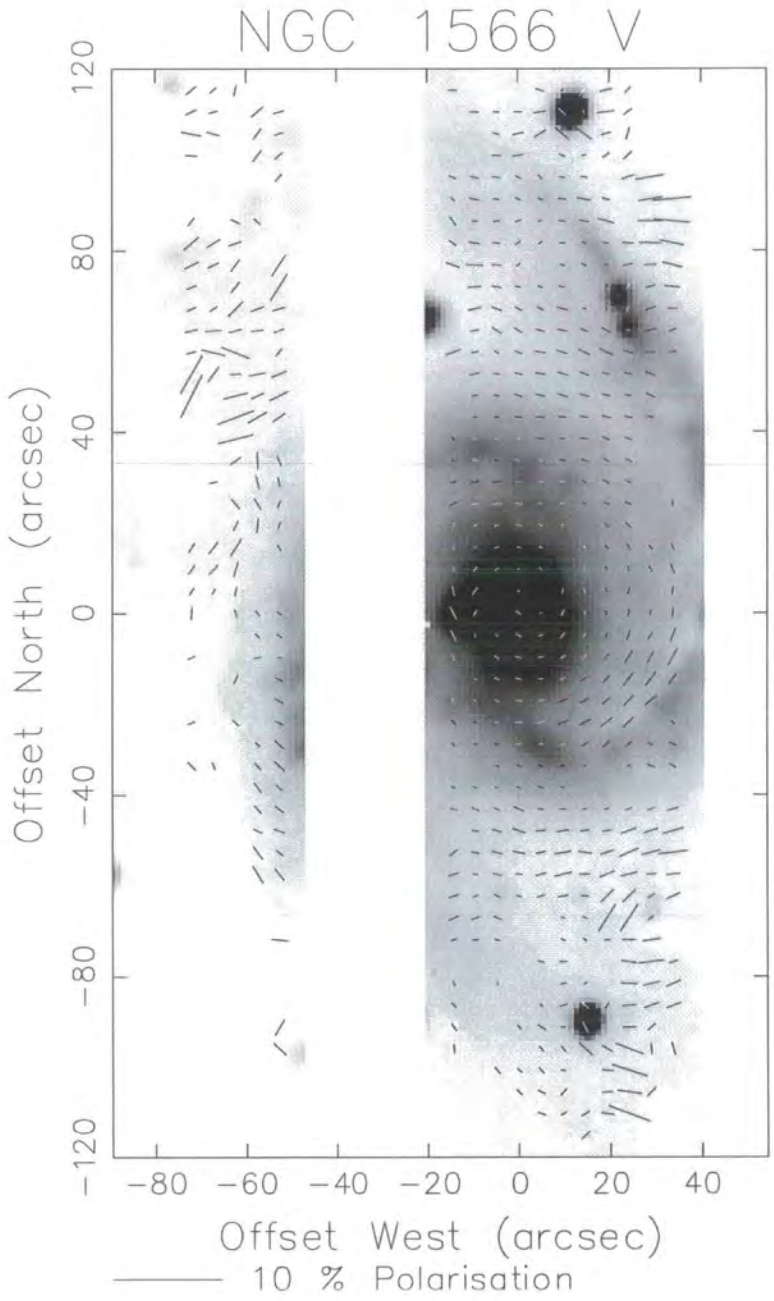

Figure 5.43: V-band greyscale total intensity image of NGC 1566, overlaid with polarization vectors plotted at 65% confidence levels

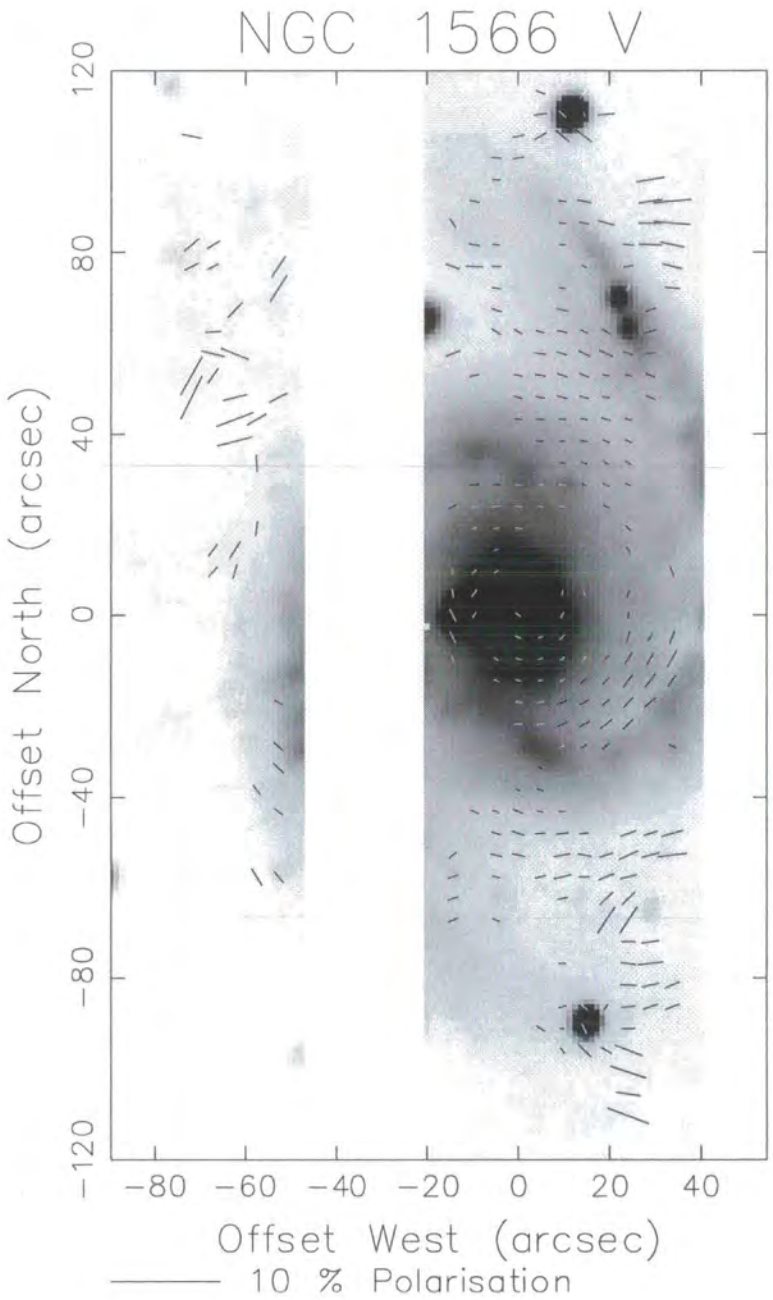

Figure 5.44: V-band greyscale total intensity of NGC 1566, overlaid with polarization vectors plotted at 95% confidence levels

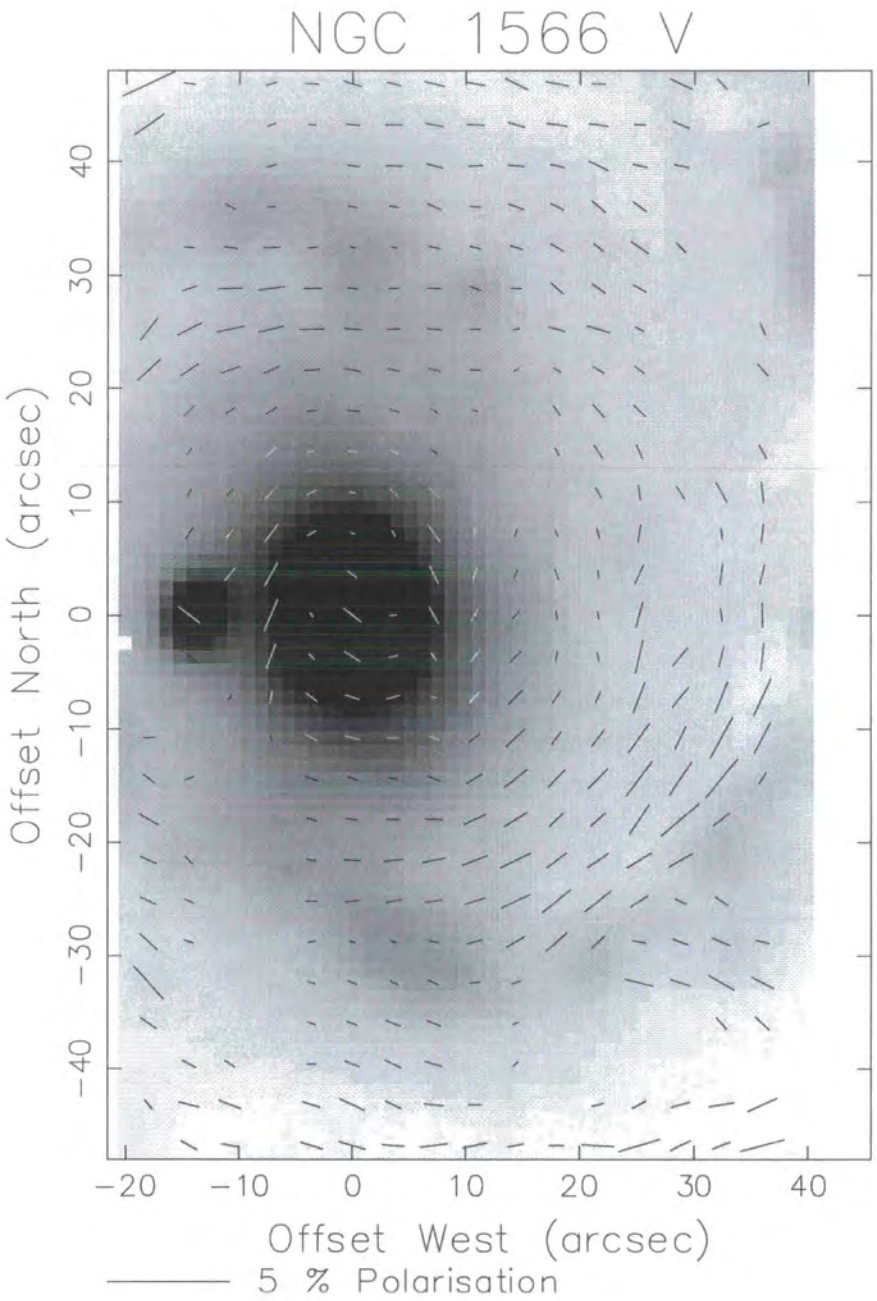

Figure 5.45: V-band greyscale total intensity image of the central region of NGC 1566, overlaid with polarization vectors plotted at 65% confidence levels

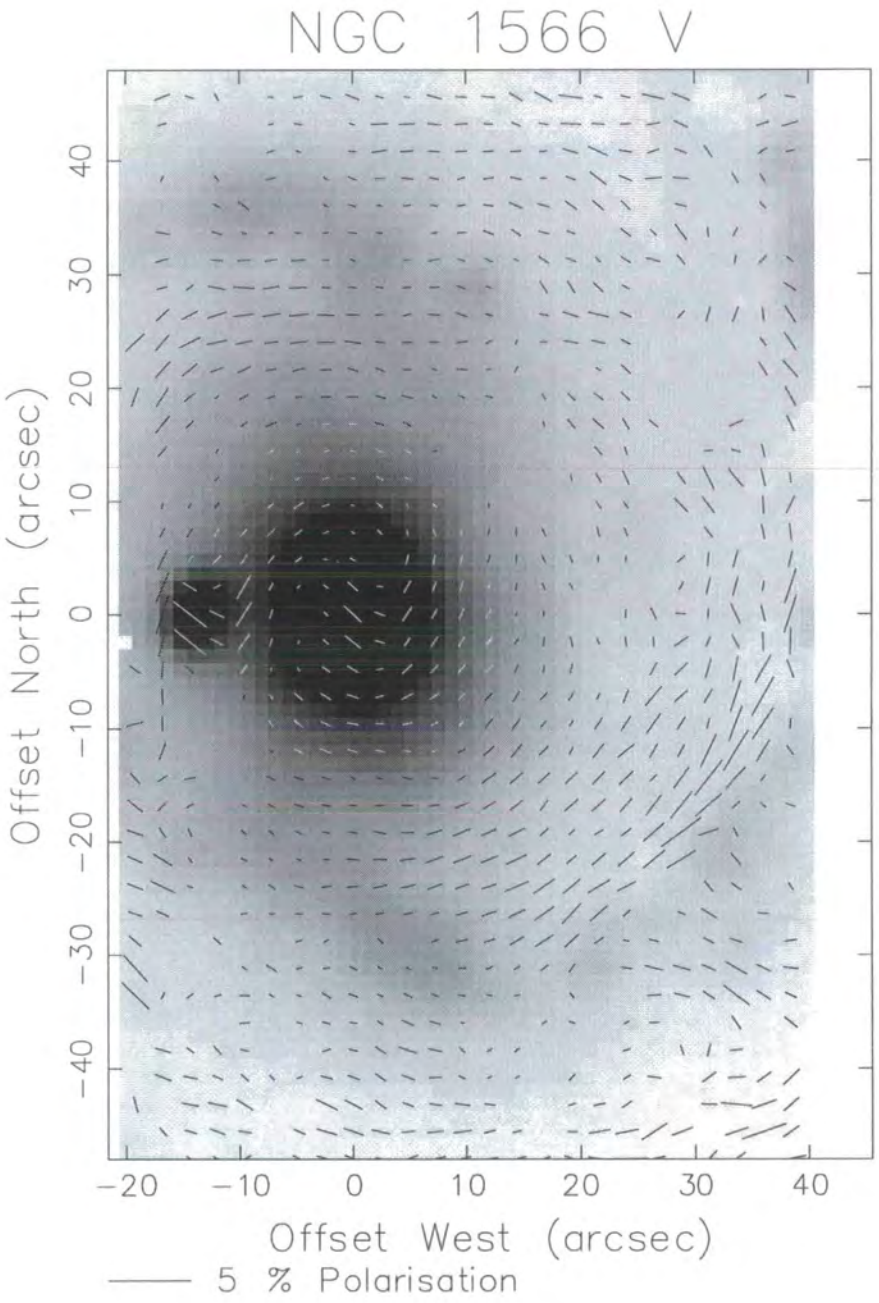

Figure 5.46: V-band greyscale total intensity image of the central region of NGC 1566, overlaid with polarization vectors plotted at 65% confidence levels

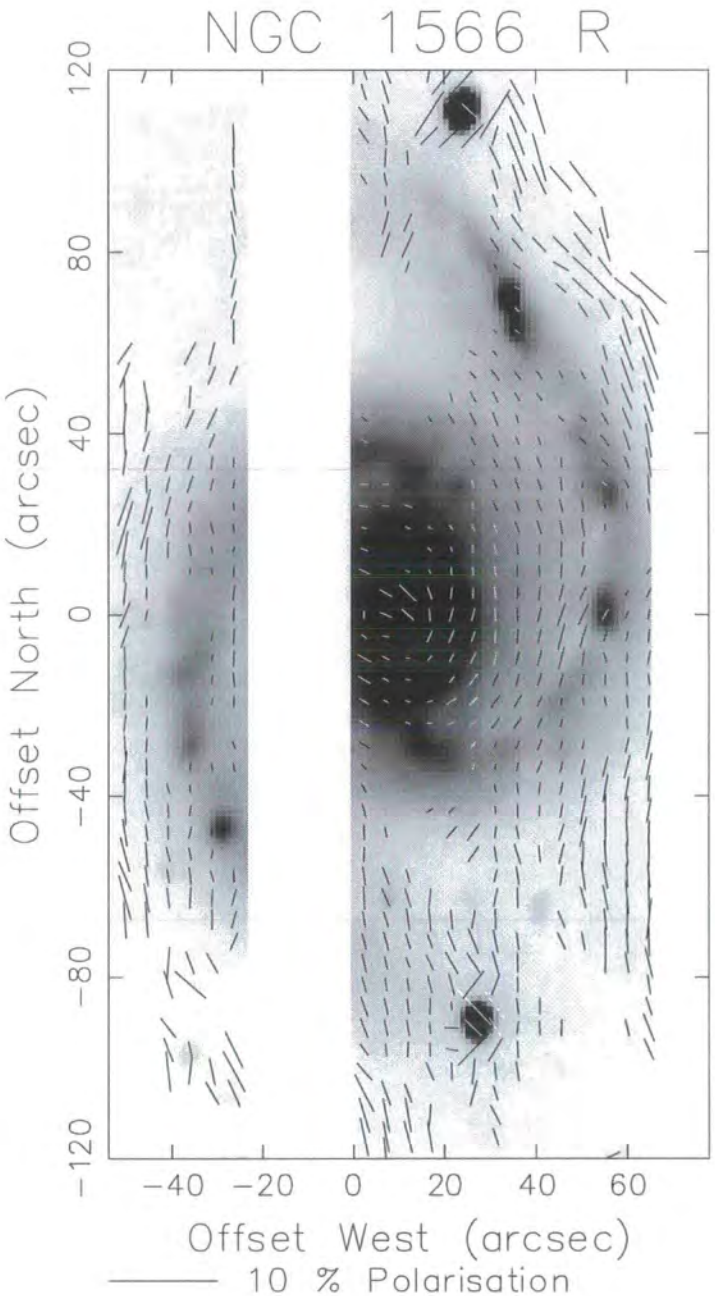

Figure 5.47: R-band greyscale total intensity image of NGC 1566, overlaid with polarization vectors plotted at 65% confidence levels

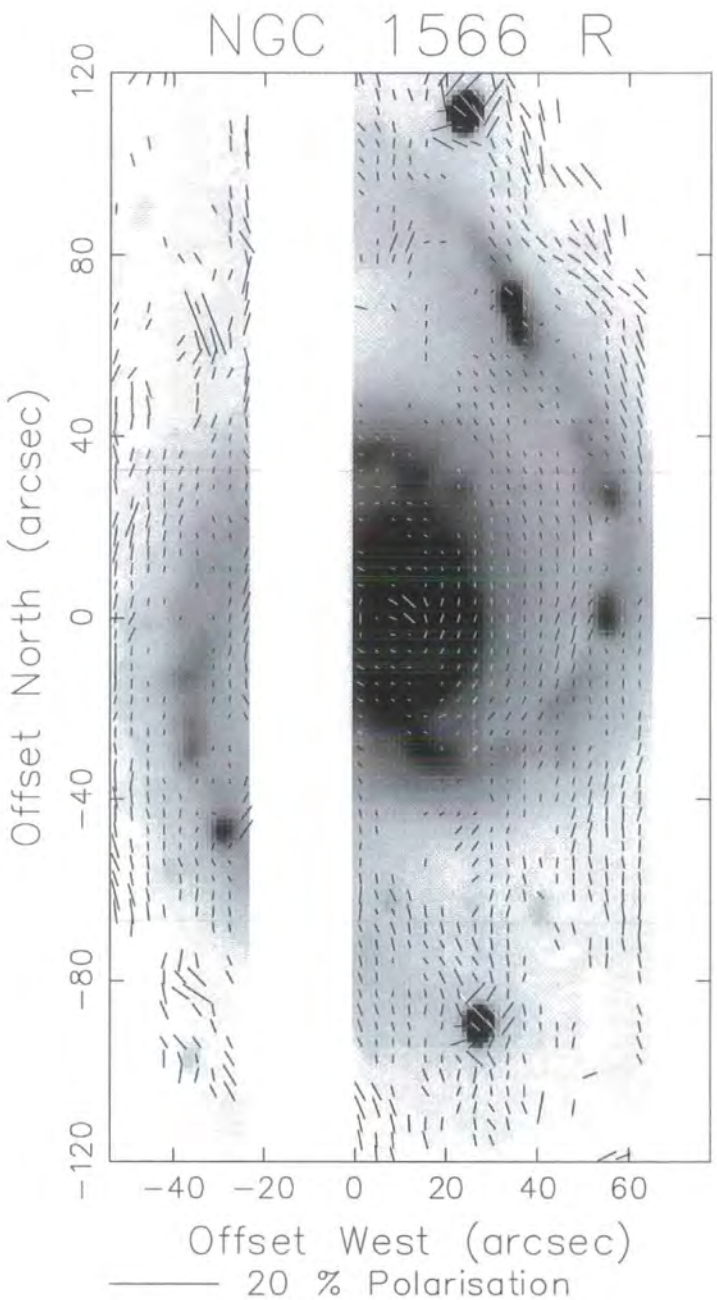

Figure 5.48: R-band greyscale total intensity image of NGC 1566, overlaid with polarization vectors plotted at 95% confidence levels

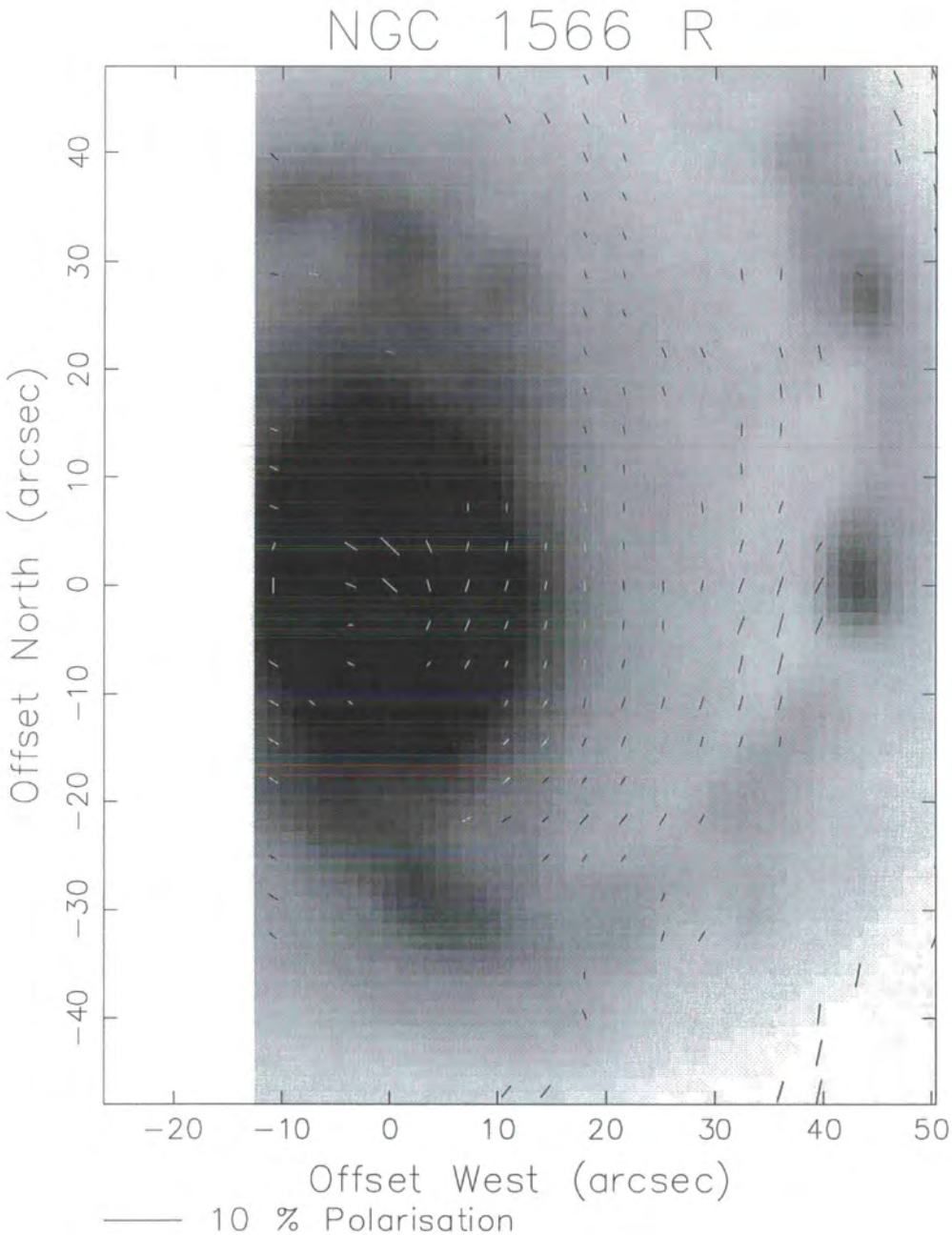

Figure 5.49: R-band greyscale total intensity image of the nucleus of NGC 1566, overlaid with polarization vectors plotted at 65% confidence levels

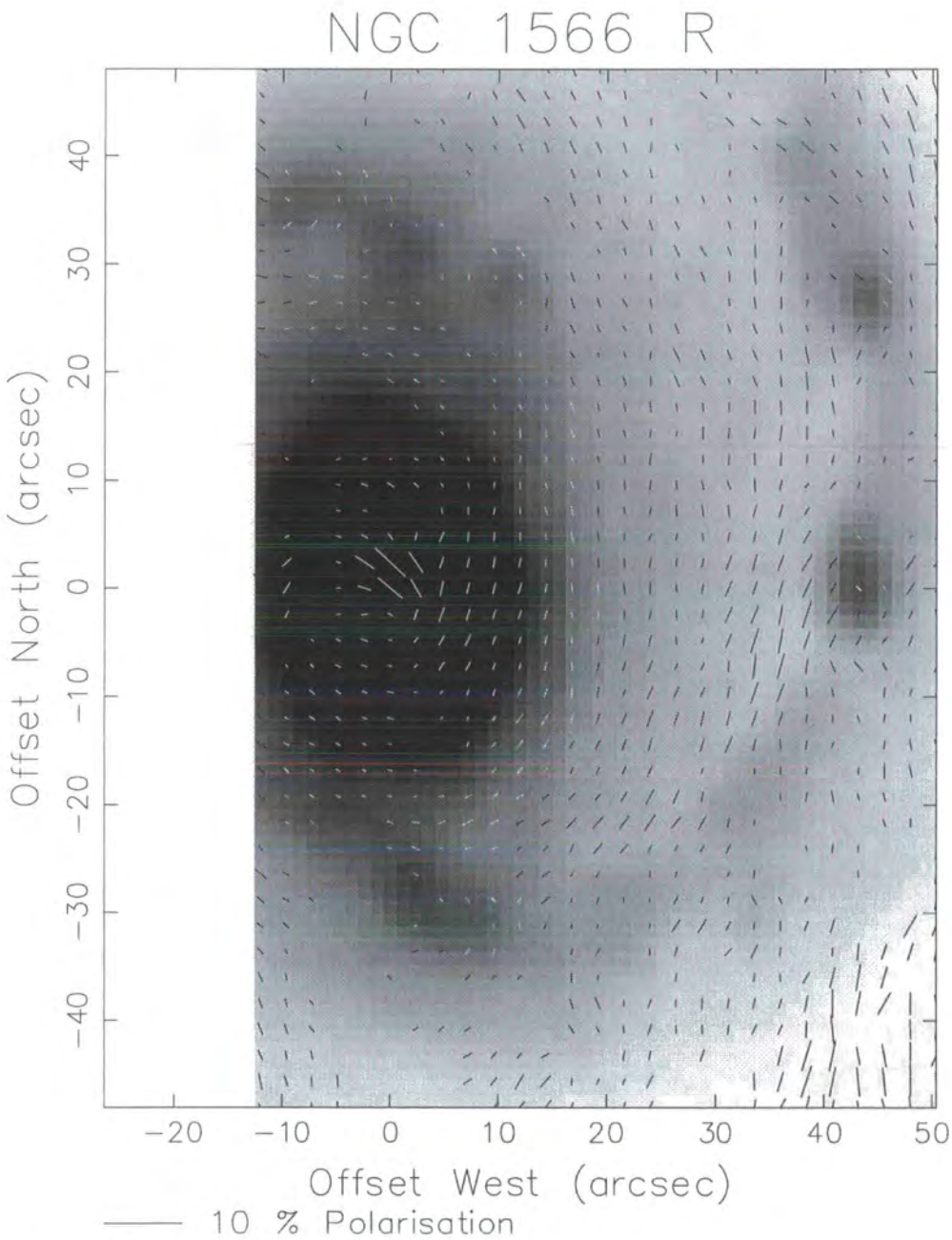

Figure 5.50: R-band greyscale total intensity image of the nucleus of NGC 1566, overlaid with polarization vectors plotted at 65% confidence levels

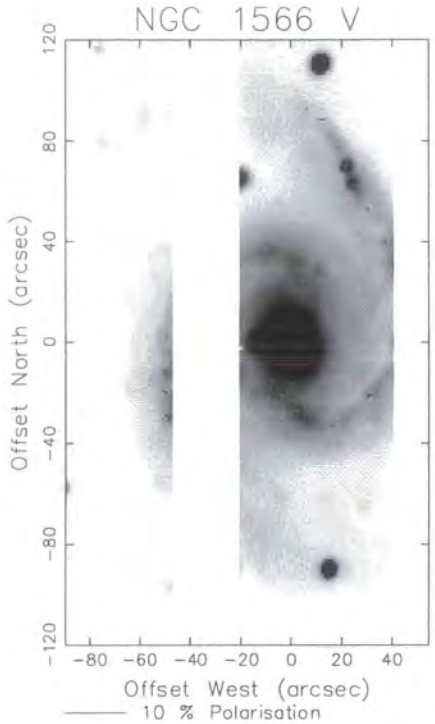

Figure 5.51: V-band greyscale total intensity image with vectors tracing the spiral arm polarization

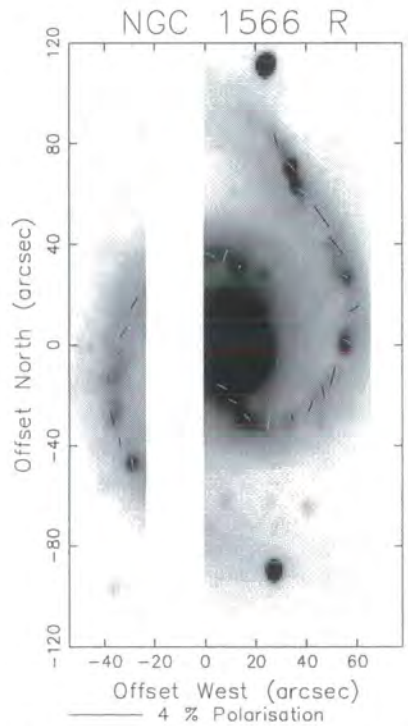

Figure 5.52: R-band greyscale total intensity image with vectors tracing the spiral arm polarization

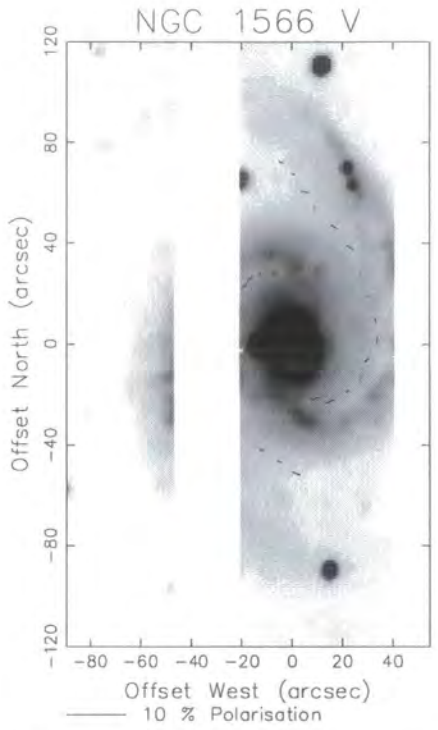

Figure 5.53: V-band greyscale total intensity image with vectors tracing the inter-spiral arm polarization of NGC 1566

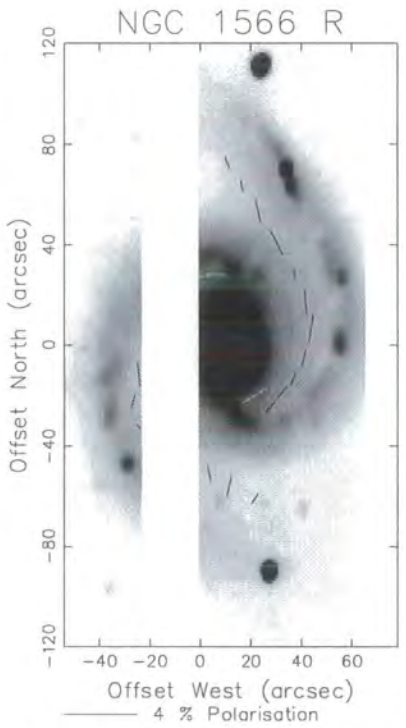

Figure 5.54: R-band greyscale total intensity image with vectors tracing the inter-spiral arm polarization of NGC 1566

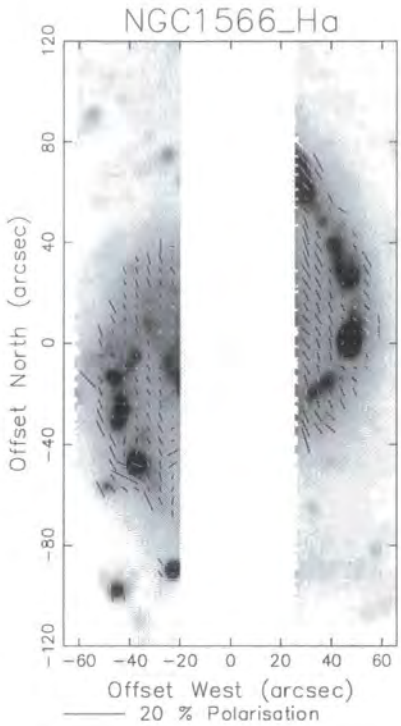

Figure 5.55: H_α greyscale total intensity image of NGC 1566, overlaid with polarization vectors plotted at 65% confidence levels

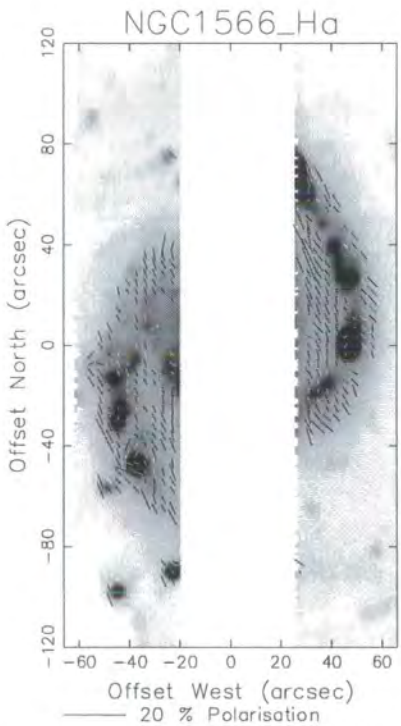

Figure 5.56: H_α greyscale total intensity image of NGC 1566, overlaid with polarization vectors plotted at 95% confidence levels

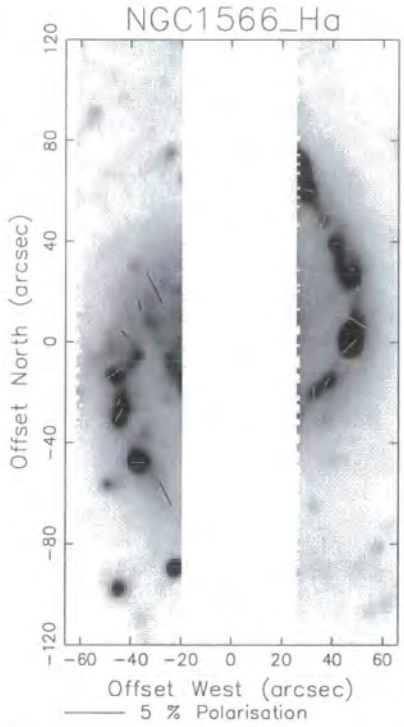

Figure 5.57: H_α greyscale total intensity image with polarization vectors tracing the spiral arm polarization of NGC 1566

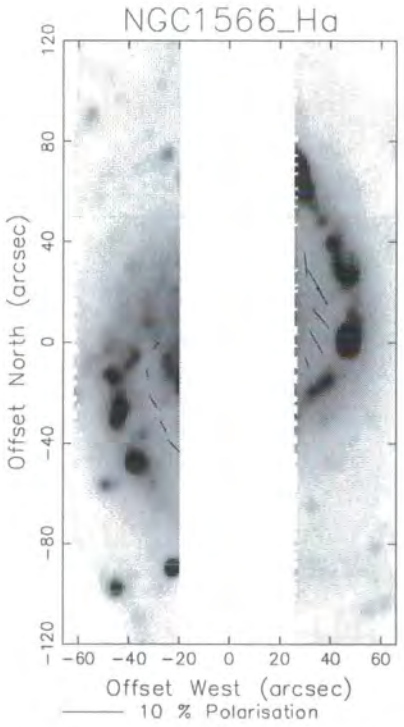

Figure 5.58: H_α greyscale total intensity image with polarization vectors tracing the inter-spiral arm polarization trace of NGC 1566

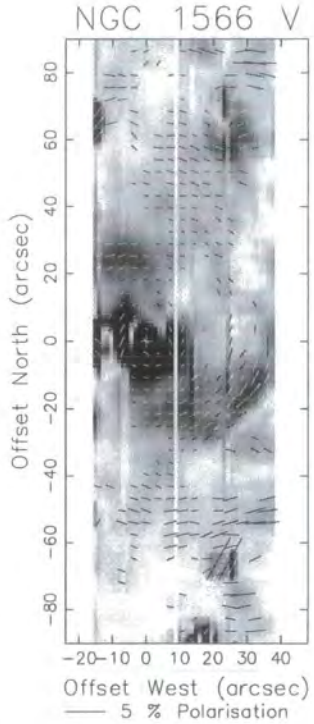

Figure 5.59: V-band polarized intensity greyscale image of NGC 1566, vectors plotted at 95% confidence levels

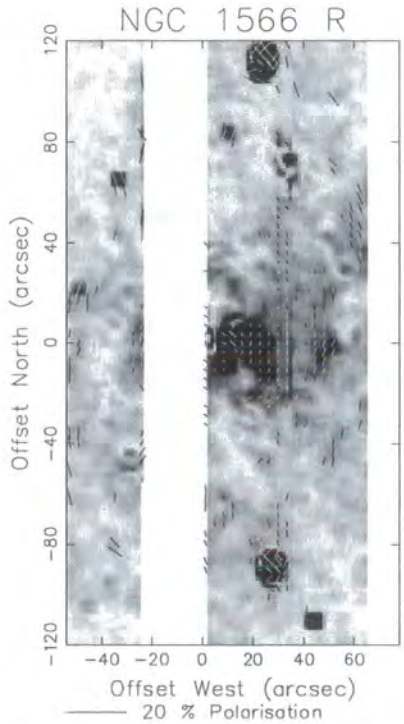

Figure 5.60: R-band polarized intensity greyscale image of NGC 1566, vectors plotted at 95% confidence levels

Chapter 6

Edge-on Seyfert galaxies

6.1 Introduction

This chapter presents the results of polarimetric observations carried out on four nearly edge-on Seyfert galaxies, together with a review of other observations at different wavelengths and modelling studies that have been published about these Seyfert nuclei and their host galaxies. Comparisons are made between previous polarization measurements and other observations to those of this current study and attempts are made to link these observations with predictions from theoretical models and are discussed in the final chapter.

6.2 Markarian 3

6.2.1 Introduction

Markarian 3 is a type 2 Seyfert galaxy at a distance of 55 Mpc away (assuming H_0=75 km s^{-1} Mpc). In 1977, it was classified as type SB0 by Adams (1977) [1], but more recent work (Jenkins 1981 [114] and Wagner 1987 [251]) suggests the host may be an elliptical galaxy with a small edge-on disc of differentially rotating gas and stars lying perpendicular to the minor axis of the galaxy, extending out to 16 arcseconds from the centre. This would be unusual since elliptical galaxies usually host more powerful radio nuclei than Seyfert nuclei.

The outer optical isophotes on DSS[1] images are almost circular, although Thompson & Martin (1988) [228] calculate a position angle of 15° for the brighter isophotes, and Wagner (1987) [251] finds a position angle of approximately 20° for the major axis in V, R, and I images. Mkn 3 appears to be an isolated galaxy, *i.e.* there are no close companions.

Radio observations by Nagar (1999b) [166] show a triple structure extending over 2″ at 3.6 cm, and to a lesser extent at 20 cm. Higher resolution maps at 5 GHz (6 cm) by Kukula *et al.* (1993) [132] show a highly collimated bipolar radio jet of about 2″ (about 600 pc) in length and less than 50 milli-arcseconds across. The jet extends along a position angle of 84°, with a slight S-shape and several bright spots, ending in a hotspot on the western side. At 18 cm, Kukula *et al.* (1999) [73] found a similar structure, but with more contrast between the bright knots and the diffuse surrounding emission. The radio peak is offset south of the optical nucleus by 200 milli-arcseconds. WSRT[2] images at 6 cm by Baum (1993) [24] show residual larger-scale radio emission that becomes apparent after a model of the nuclear emission is subtracted. This is a halo structure, including two peaks separated by 4″ along a position angle of 36°, with a maximum extent of 5.5″.

Emission-line HST images by Capetti *et al.* (1995) [39] shows ionized gas emission in a spiral shape extending over 2″, with the brightest part corresponding spatially to the radio morphology shown by Kukula *et al.* (1993) [132]. The optical emission lines are blue asymmetric, indicating absorption by dust surrounding the NLR clouds. Capetti *et al.* (1995) also find a more diffuse extended emission region around the compact spiral, a large-scale 7.5″ diffuse biconical structure extended along a position angle of 114°, with a continuity of morphology between the spiral and the diffuse emission. This diffuse emission is also mapped by Schmitt (1996) [206] and Pogge & de Robertis (1993) [187]. Higher resolution imaging of the central 2″ of the narrow-line region by Capetti *et al.* (1998) [38] shows strong evidence of interactions between the radio-outflow and the ambient gas. These are attributed to jet-induced shocks heating and compressing the gas, forming a hot cocoon, which then expands and compresses the surrounding gas to cause the observed narrow-line emission.

Optical colour maps by Kotilainen (1997) [127] show a blue extension approximately parallel to the extended radio and narrow-line emission. It is composed of two blue maxima elongated at position angle 95°. The west maxima is 1.3″ from the nucleus, and in the east, the blue feature extends out to 4.6″ curving away from the nucleus, and shows a similar curvature to that seen in the emission-line and radio observations. This blue structure is in agreement with the location of the UV (blue) components found by

[1]Digitized Sky Survey, of the Space Telescope Science Institute
[2]Westerbork Synthesis Radio Telescope

Pogge & De Robertis (1993) [187] in their UV/red colour map. They also find a diffuse blue component with a biconical structure extending out to 5″ either side of the nucleus with position angle of 114°. These blue extensions are thought to be due to scattering of nuclear light by extranuclear 'mirrors'. The colours are measured over a 2 arcsecond aperture.

Tran (1995) [230] made spectropolarimetric measurements of Mkn 3, finding a clear BLR in polarized light (< 1 pc in size), confirming that found in previous spectro-polarimetry studies by Miller & Goodrich (1990) [160]. After correction for ISP (estimated to be ≈ 1.2% at 132°), he found the position angle (168°) of the polarized broad lines to be the same as the polarized adjacent continua (and perpendicular to the radio axis), suggesting a common geometric scattering geometry for them both, with electrons as the main scatterers.

BeppoSAX observations by Bassani *et al.* (1999a) [22] show Mkn 3 to be a source of X-rays with evidence for both a heavily absorbed component and an unabsorbed reflected component, dominated by the reflected component, on the borderline between being Compton thin or thick, with an absorbing column density of $N_H \approx 13 \times 10^{23}$ cm^{-2}. Cappi *et al.* (1999) [41] combined BeppoSAX data with previous X-ray observations to show that variations between the absorbed component and unabsorbed reflected component indicate a reprocessing region of diameter ≥ 2 pc, which can be identified as an (edge-on) obscuring torus. The heavily absorbed component would be the radiation transmitted through the rim of the torus, and the reflected component that which is reflected from the inner surface of the torus, in order to fit in with unified schemes. This dusty torus model is also consistent with the finding by Edelson (1986) [68] that near infra-red emission of Mkn 3 has a dust-dominated steep spectrum. Figure 6.2 gives a diagram showing visually the different emission regions and axes of the various observations for easier comparison. It also shows the angle of polarization of the nuclear optical polarization measured in this study.

6.2.2 Observational notes

Mkn 3 was observed on the 19th of January 1991 with the 4 m William Herschel Telescope (WHT) in La Palma, the Canary Islands. The Cassegrain focus with focal ratio of 11 was used, and observations were taken using a broad band V filter. For this configuration, the scale of the sky on the CCD detector of the Durham Imaging Polarimeter was 0.39 arcseconds per CCD pixel, covering a total field of approximately 3.6 arcminutes by 2.7 arcminutes. At the estimated distance of 54 Mpc, assuming $H_0 = 75$ km s^{-1} Mpc^{-1}, 1

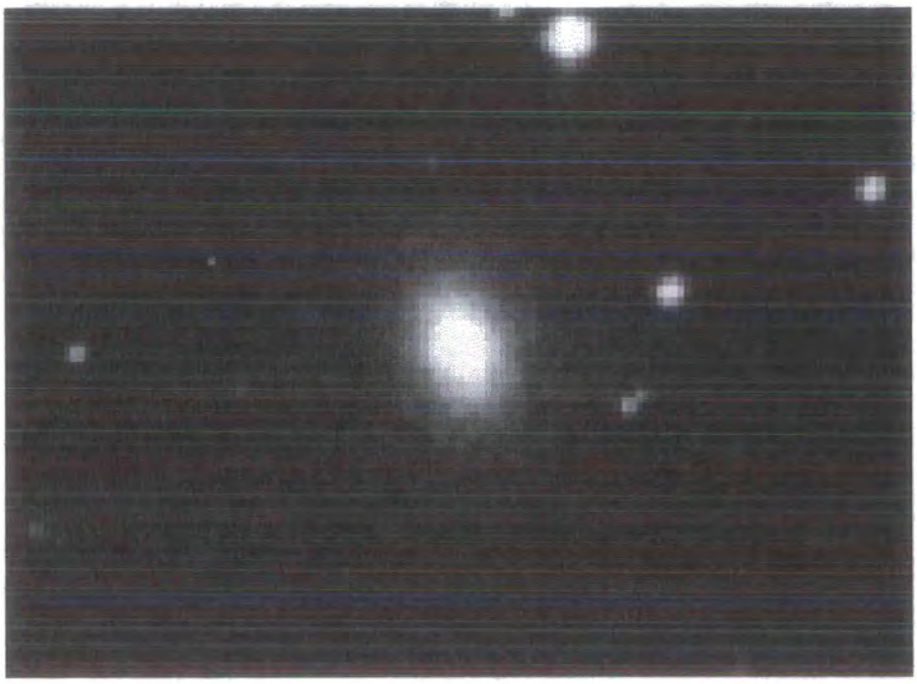

Figure 6.1: DSS intensity image of Mkn 3, field of 4' x 3'

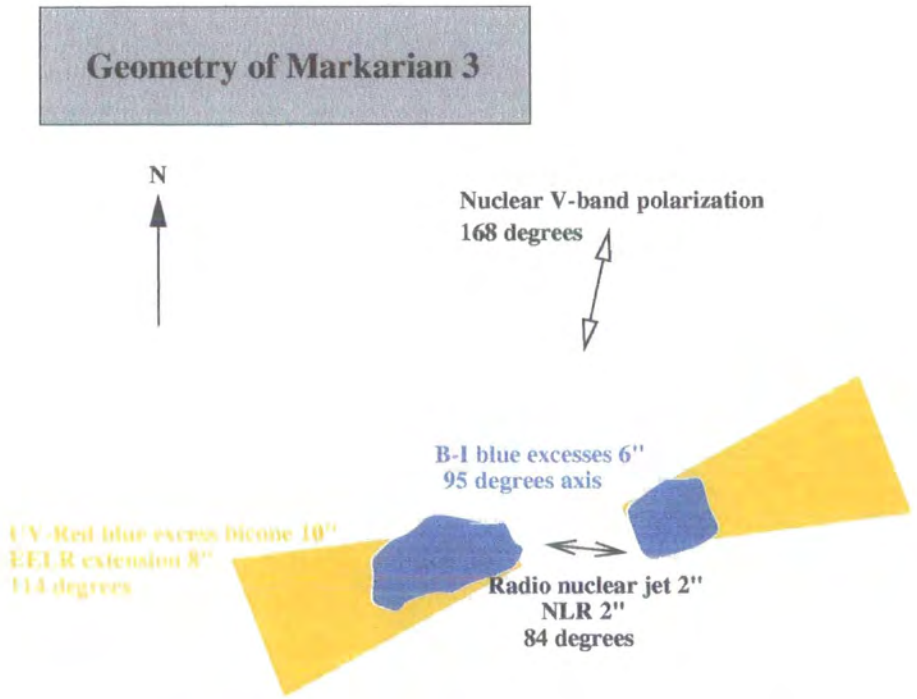

Figure 6.2: Diagram of the axes of observations of Mkn 3

arcsecond corresponds to approximately 260 pc. A DSS image of Mkn 3 is given in figure 6.1, which shows the total extent of the field that was mapped by the polarimeter.

Data were taken at one position only since most of the galaxy fitted on to one grid space on the detector. Four CCD frames, each of 200 seconds, were taken of the object, together with suitable flatfield frames. The telescope was slightly defocussed and, due to a lack of stars in the field, the accuracy of the alignment of the exposures was limited. The seeing on this night was calculated to be approximately 2.0″ arcseconds using star images from previous observations taken on that night, because there were not enough suitable stars in the field of the Mkn 3 observations to measure seeing in those frames. The moon was 0.14 illuminated during the observations, which means that the night sky would be slightly polarized (the maximum polarization occurs at full moon and at 90 degrees from the moon). The moon was around 99° away from the Mkn 3 during the observations, which implies that there could be some moonlight contamination. A linear sky surface model was used for sky subtraction, as it was found experimentally to give a better fit to the sky polarization than a constant one, probably due to some moonlight polarization contamination.

6.2.3 Image details

Figures 6.3 to 6.10 present V-band images of Mkn 3, north to the top, east to the left. The scale is in arcseconds, centred on the peak nuclear intensity of the image. Except where otherwise stated, the greyscale is of total intensity. The intensity contours of the maps are plotted logarithmically. The polarization vectors were calculated in a similar manner to those in the previous chapter, with square bin sizes of 5 by 5 pixels separated by 3 pixels in figures 6.3, 6.4, 6.7 – 6.10, and 3 by 3 pixels separated by steps of 2 pixels in figures 6.5 and 6.6. The polarization vectors are plotted either with signal-to-noise confidence levels of 65% or 95% or a minimum polarized intensity cut, as appropriate.

Figures 6.7 and 6.8 present polarized intensity greyscale maps, uncorrected and corrected for ISP respectively, with darker shades representing higher polarized intensity or polarization. Figures 6.9 and 6.10 are maps of polarization level, uncorrected and corrected for ISP respectively, darker shades representing a higher polarization percentage.

6.2.4 Interstellar polarization

The galactic co-ordinates ($l = 143°$,$b = 23°$) show that the galactic latitude is quite low, so interstellar polarization due to dust in the galactic plane of our galaxy may be expected to be significant. Indeed the galactic extinction value of E_{B-V} of 0.25 in table 4.6 indicated that there is likely to be an ISP level of at least around 0.75%. The interstellar polarization values used are those calculated by Schmidt & Miller (1985) [203] from measuring the polarization of two very faint field stars within $3'$ of the line of sight. For white light this was measured to be 1.17% ± 0.2% at 132°± 5°. They also measure the mean polarization of the forbidden emission lines to have a polarization of 1.0% ± 0.1% at 134°± 3°, a similar value, which implies they are polarized only by the ISP component, so 1.1% at 134° is therefore a reasonable ISP estimate for emission around 5500 Å, and the value that has been adopted for the ISP corrections performed on the maps of Mkn 3 in this thesis.

Attempts were made to measure the polarizations of stars in the field of Mkn 3 in the data observed for this thesis, in order to make an independent ISP estimate, but, as can be seen from the DSS image in figure 6.1, there are very few stars in the field. Unfortunately all of these few stars were either not in the field of the polarimeter (which is of alternate strips) or located too close to the grid edges of the polarimetry frames and were thus affected by stray light, so none were suitable for taking polarization measurements.

6.2.5 Results: V-band

The polarization maps of Mkn 3 in figures 6.3 and 6.5 show a strong general tendency for the polarization to be broadly aligned, almost uniformly polarized to the level of around 2% with position angle ≈ 135° across the most of the observed portion of the galaxy. This large-ranging effect is a classical manifestation of a significant level of ISP. Only in the south east and north west regions does this pattern break down. The levels of polarization drop rapidly going south-east from the nucleus, as the polarization angle changes by 90° to end up at around 45° beyond $3''$ from the nucleus. In the south-east away from the nucleus, the polarization pattern show some signs of centro-symmetry centred on the nucleus.

Results of nuclear aperture polarimetry performed over a range of simulated apertures are presented in table 6.1. The figures in brackets are the expected errors, calculated according to the error model described in section 4.4.4. The decrease in polarization with increasing aperture size is to be expected, as there is more diluting unpolarized light from

Table 6.1: V-band nuclear aperture polarimetry of Mkn 3 (uncorrected)

Aperture (arcsec)	Aperture (pixels)	Polarization (percent)	Position Angle (degrees)
2	5.1	1.60 ± 0.28	156 ± 6
2.5	6.4	1.53 ± 0.28	154 ± 6
3	7.7	1.51 ± 0.27	152 ± 6
4	10.3	1.47 ± 0.27	150 ± 6
5	12.8	1.41 ± 0.27	148 ± 6
6	15.4	1.35 ± 0.27	146 ± 6

the host galaxy allowed in as the aperture increases. The measurements show that at the nucleus, the level of polarization is $\approx$ 1.5% at a polarization angle of 150° over a 4″ aperture and accord well with the measurements of previous observations by various researchers, which are presented in table 6.2.

The map of polarized intensity in figure 6.7 shows a region of high polarized flux at the nucleus extended along a position angle of approximately 37°, with no regions of significantly high polarized intensity elsewhere. The polarization level map in figure 6.9 shows two regions of decreased polarization level south east and north west of the optical nucleus, which is marked by a cross. Possible reasons for this decrease in polarization are discussed in the next section after the maps have been corrected for ISP, where this effect is also still found.

Table 6.2: Comparison of nuclear polarimetry of Mkn 3 (uncorrected)

Range of wavelength (Ångstroms)	Aperture or slit width (arcsec)	Polarization level (percent)	Polarization angle (degrees)	Reference[1]
4600-7400[2]	2.4	1.52	145.0	T95
3250-5400[2]	2.4	1.27	146.5	T95
3315-4400[2]	2.4	2.14	159.2	T95
5100-6200[2]	2.4	1.75	147.0	T95
3200-6300[2]	2	1.50 ± 0.04	144 ± 0.8	K94
3200-6300[2]	2	1.75 ± 0.03	146 ± 0.5	K94
4189-6909[2]		1.57	148.3	MG90
3246-6425[2]		1.50	145.1	MG90
near 5000[2]	2.8	2.1 ± 0.2	147 ± 3	SM85
3800-5600[3]	4	2.00 ± 0.12	142.8 ± 1.6	M83
3800-5600[3]	4	1.82 ± 0.11	144.8 ± 1.6	M83
3800-5600[3]	4	1.31 ± 0.16	148.8 ± 3.5	M83

[1]References: T95 = Tran (1995), MG90 = Miller & Goodrich (1990), SM85 = Schmidt & Miller (1985), K94 = Kay (1994), M83 = Martin (1983)
[2]Spectropolarimetry
[3]Survey using a blue-green Corning 4-96 filter (3800-5600 Å), with a 4 arcsecond aperture

6.2.6 Results: V-band after correction for ISP

The low galactic latitude of Mkn 3, together with the fact that the uncorrected polarization maps show features which are typical effects of ISP, demonstrate the importance of applying an appropriate ISP correction for this galaxy. Using an ISP value of 1.1% at 134° estimated from the values obtained by Schmidt & Miller (!985) [203], the ISP corrected maps in figures 6.4 and 6.6 show a much clearer centro-symmetric pattern beyond a radius of about 4″ from the nucleus. This pattern would be expected from the polarization due to scattering from the central source in a galaxy, and indicates that the ISP correction applied is a good approximation, one which at least partially removes the ISP effects.

The pattern in the nucleus is curious. The polarization in the inner 3″ east-west along the nucleus is orientated at around 0°, but beyond this the polarization angle becomes perpendicular to this at around 90° for about 1″-1.5″ on both sides, then becomes closer to 0° again to fit in with the centro-symmetric arrangement of vectors at 4″ from the nucleus. There appears to be a north-south polarization feature through the nucleus extending over 4″ in length and 2″ in width, where the polarization vectors are all aligned around 0°. This region is approximately where there is an edge-on disc of gas and stars, extending out to 16″, Wagner (1987) [251], and this direction is also perpendicular to the radio jet (which is at 84°), and therefore where, according to the unified scheme, a small-scale dusty torus is expected in the nucleus oriented perpendicular to the radio jet. It would be interesting to see whether there is a large-scale red feature that corresponds well to the extent of this polarization feature, because such a red feature would indicate the presence of dust, *i.e.* dust in the centre of the stellar disk, which could be causing the polarization. This would be interesting because such a large scale dust feature would be at the same orientation as the postulated small-scale nuclear dusty torus and they might be associated, *e.g.* the dusty disk feeding the torus. The polarization angles are aligned parallel to the edge-on stellar disk in the central regions, which is similar to the pattern seen in other galaxies *e.g.* IC 4329A (Wolstencroft *et al.* 1995) where there is significant polarization parallel to the dust lane of the galaxy disk due to dichroic absorption, indicating a similar process in Mkn 3. The absorbing column calculated for the central nuclear emission however is so high that the optical emission from the accretion disk could not be seen directly, only through scattering from the dust or electrons surrounding the nuclear region.

Aperture polarimetry of the nuclear regions over apertures of 2″ to 6″ is presented in table 6.3. These corrected position angles of around 172° are accurately perpendicular to the position angle of the radio structure (84°), fitting the trend for the optical polarization angles of Seyfert 2 galaxies (Brindle *et al.* 1990 [36]). Previous published measurements of the nuclear polarization are given in table 6.4. The corrected polarizations of this

thesis agree well with the measurements of Schmidt & Miller (1985) [203], but are not in agreement with Kay (1994) [119], who calculated the level of polarization to increase after ISP correction, which seems strange because same value of ISP correction is used in all three cases, although the wavelength ranges for which Kay quotes the polarization with and without ISP correction are different, so it could be because of wavelength dependence of the light, although such a large difference due to this seems unlikely. In the cases where the different researchers have corrected for dilution as well as ISP, the large differences in their results can be expected because they use different galaxy templates for starlight subtraction, different dilution fractions, assume different amounts of reddening, and calculate values over different wavelength ranges.

The map of polarized intensity in figure 6.8 shows a definite change in morphology after correction for ISP. The central polarized emission is still elongated, but along a position angle of approximately 0° (north-south) rather than along 37°. Also notable is the apparent elongated ring of very low polarized intensity encircling the nucleus, of radius $\approx 3''$- $4''$, beyond which there are significant polarized levels again with vectors aligned in a centro-symmetric pattern. This could be interpreted as delineating the boundary where the central dominant polarization mechanism loses its dominance and cancels out with the (centro-symmetric) scattering mechanism which becomes dominant at the larger radii. Alternatively there could be less dust/scatterers in these regions, and hence less scattering. This depolarized ring is much more apparent in the map of polarization level in figure 6.10 (the cross marks the location of the peak total intensity).

There are significantly high levels of polarized flux in a patch$\approx 3''$- $5''$to the south-east along a position angle of $\approx 115°$ from the nucleus. Since there is a blue structure observed by Kotilainen (1997) and Pogge & de Robertis (1993) west of the nucleus, extending to $4.5''$ or $5.5''$ along position angle 114°(see section 6.2.1), and which is believed to be from scattered nuclear light, it seems plausible that the increase in polarized flux in this region is due to this scattered light, polarized by scattering. The position angle of the polarization in this region is consistent with scattering from the central nuclear source. There is a diffuse extended biconical emission-line region in this direction, along position angle 114° extending to about $8''$(Capetti *et al.* 1995, which is also discussed in section 6.2.1), indicating radiation from the nucleus, so this observed polarization is most probably scattered nuclear continuum. In the polarized intensity map in figure 6.7 there are also hints of a enhanced level of polarized flux in a tentatively halo shape around the nucleus at a radius of about 5 or $6''$.

The distinct differences between the polarization patterns and polarized flux distribution before and after the ISP correction demonstrate the importance of the ISP correction, and therefore consideration should be given to the accuracy of the applied correction, so

Table 6.3: V-band nuclear aperture polarimetry of Mkn 3 (ISP corrected)

Aperture (arcsec)	Aperture (pixels)	Polarization (percent)	Position Angle (degrees)
2	5.1	1.2 ± 0.28	175 ± 6
2.5	6.4	1.1 ± 0.28	174 ± 6
3	7.7	1.0 ± 0.27	173 ± 6
4	10.3	0.9 ± 0.27	171 ± 6
5	12.8	0.8 ± 0.27	170 ± 6
6	15.4	0.7 ± 0.27	169 ± 6

it is particularly unfortunate that the data in this thesis did not allow an independent calculation of ISP, something which is important for further study, as it could be applied to the data collected for this thesis in addition to new data.

Schmidt & Miller (1985) [203] and Tran (1995) [231] note that the polarizations of the permitted and the forbidden lines have different values. The permitted lines share the polarization of the continuum, but that of the forbidden lines is reduced and at a different polarization angle, which they assume to be due purely to ISP. However, considering that Mkn 3 has an almost edge-on stellar disk, there is also the possibility of polarization in the host galaxy itself, *e.g.* dichroic extinction in a dusty galaxy disk, in addition to the ISP effect from our galaxy, for example this is found to be the case of IC 4329A (Wolstencroft *et al.* 1995 [266]). If this is in operation, then all the nuclear spectral lines will be affected by this polarization in addition to the ISP. The ISP can be determined by independently sampling suitable Galactic stars and can then be corrected for, but this would leave unchanged any host galaxy dust-lane polarization effects in the observations, as well as any intrinsic Seyfert nuclear polarization. From the observations of this thesis, it is not possible to tell how much of the nuclear polarization is intrinsic to the small-scale Seyfert nucleus and how much to the dust lane in the host galaxy.

Multi-waveband measurements by Tran (1995) [231] show the wavelength dependence of the nuclear polarization, which rises steeply in the blue, from 1.8% in the red to 7.0% in the blue. Unfortunately the observations in this thesis were only made in the V-band, so it is not possible to investigate the wavelength dependence of the polarization in the different parts of galaxy, which could be used for example to confirm whether the polarization along the stellar disk across the galaxy is due to dichroic absorption by its characteristic wavelength dependence.

Table 6.4: Comparison of nuclear polarimetry of Mkn 3 (ISP corrected)

Range of wavelength (Ångstroms)	Aperture or slit width (arcsec)	Polarization level (percent)	Polarization angle (degrees)	Reference[1]
near 5000	2.8	1.1 ± 0.2	170 ± 5	SM85
5100-6200[2]	2.4	0.9	167	T95
5100-6200[2]	?	?	166.5	MG90
4150-4650[2]	2	2.2 ± 0.11	164.3 ± 1.5	K94
5100-6200[2]	2.4	7.0*	167	T95
5100-6200[2]	?	1.25**	167	MG90
4150-4650[2]	2	3.86*** ± 0.21	164.1 ± 1.5	K94

[1]References: F99 = this thesis (1999), SM85 = Schmidt & Miller (1985), K94 = Kay (1994), MG90 = Miller & Goodrich (1990), T95 = Tran (1995)
[2]Spectropolarimetry averaged over wavelength range
*Corrected for Galactic reddening E_{B-V}=0.22, galaxy dilution fraction of 0.88 and ISP
**Corrected for Galactic reddening E_{B-V}=0.45?, galaxy dilution fraction of 0.45 and ISP
***Corrected for Galactic reddening E_{B-V}=0.11, galaxy dilution fraction of 0.42 and ISP
? Information not available

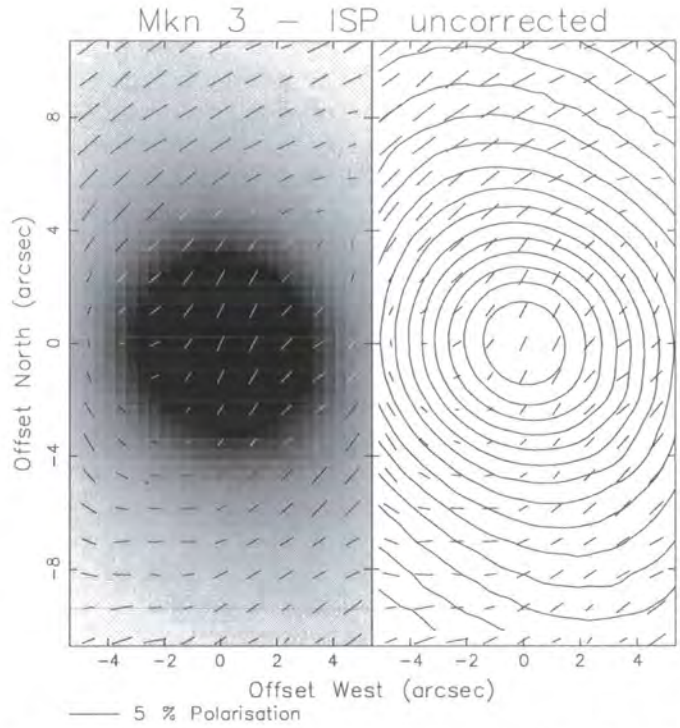

Figure 6.3: V-band total intensity and polarization images of Mkn 3, uncorrected for ISP, polarization vectors 5x5 bins, step size 3 pixels

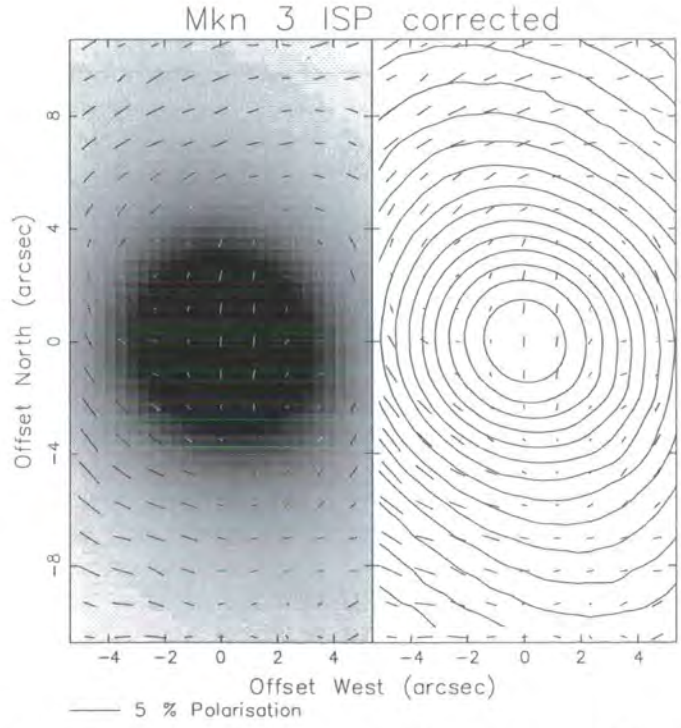

Figure 6.4: V-band total intensity and polarization images of Mkn 3, corrected for ISP, polarization vectors 5x5 bins, step size 3 pixels

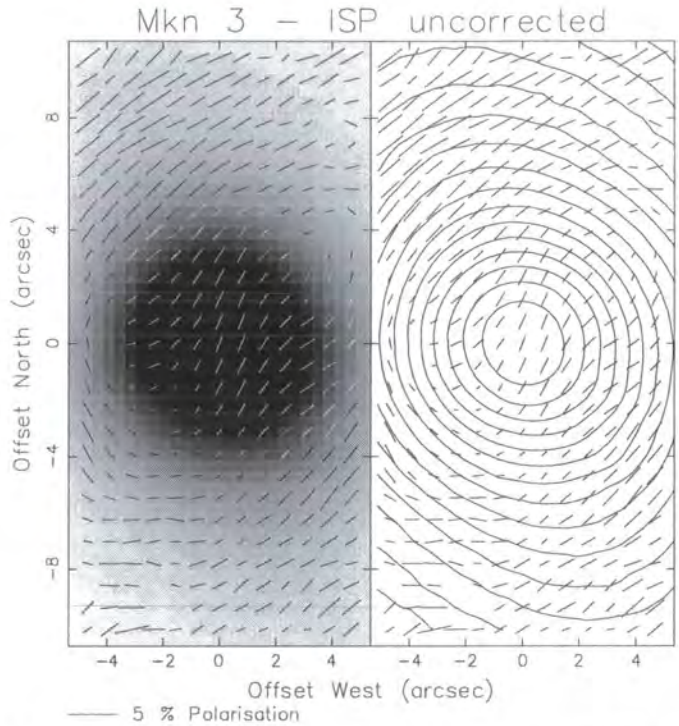

Figure 6.5: V-band total intensity and polarization images of Mkn 3, uncorrected for ISP, polarization vectors 3x3 bins, step size 2 pixels

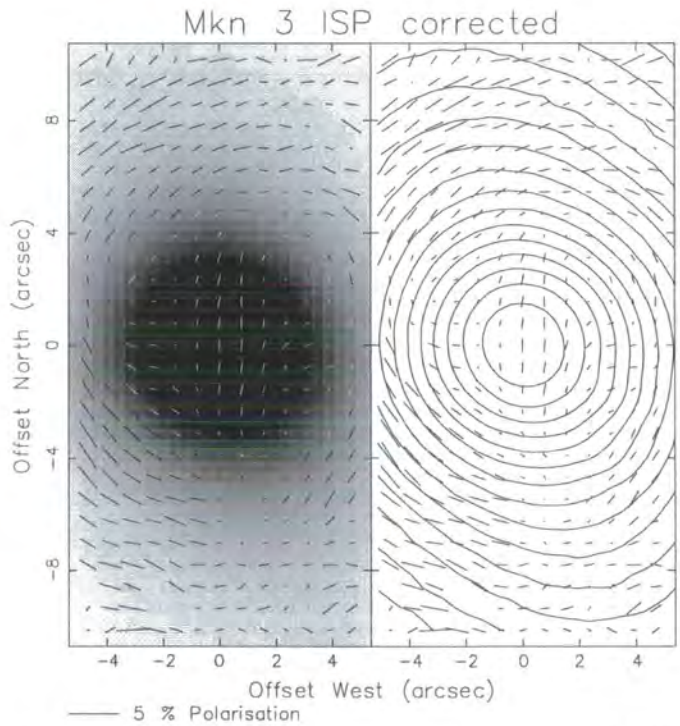

Figure 6.6: V-band total intensity and polarization images of Mkn 3, corrected for ISP, polarization vectors 3x3 bins, step size 2 pixels

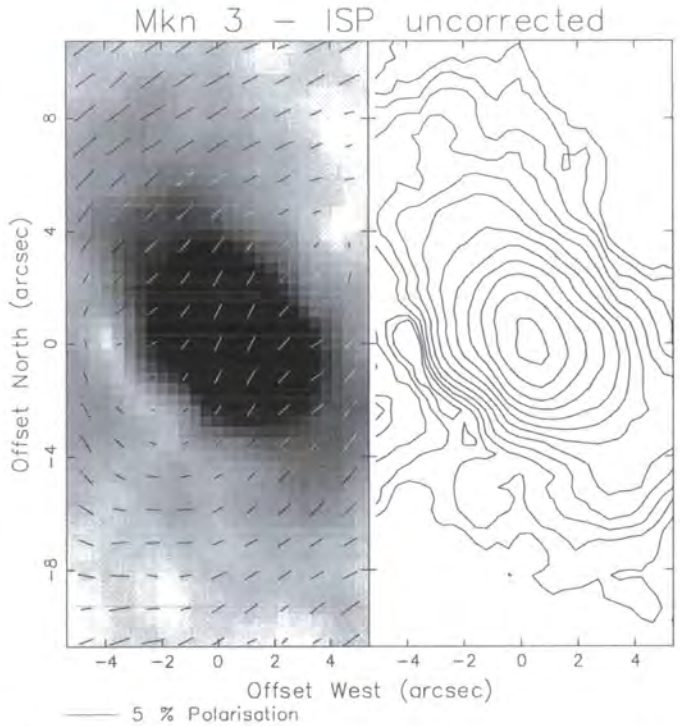

Figure 6.7: V-band polarized intensity image of Mkn 3, uncorrected for ISP, polarization vectors 5x5 bins, step size 3 pixels

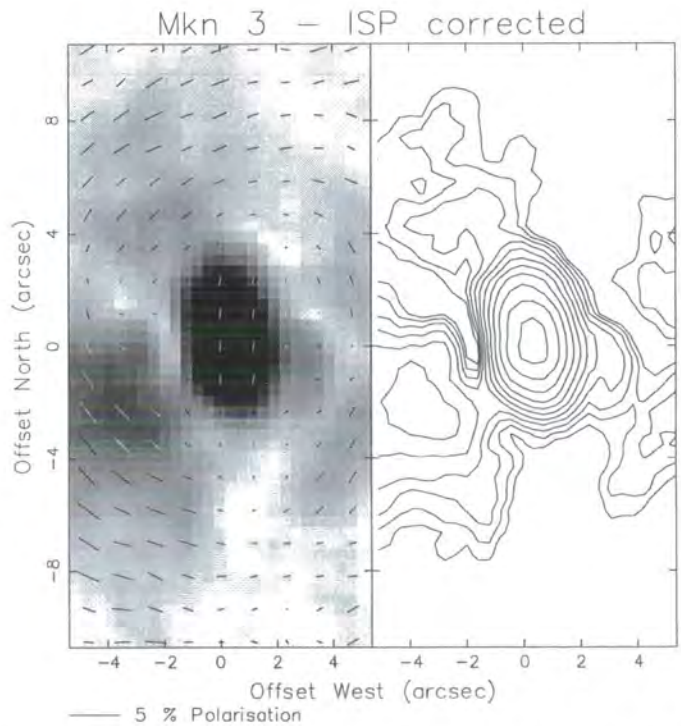

Figure 6.8: V-band polarized intensity image of Mkn 3, corrected for ISP, polarization vectors 5x5 bins, step size 3 pixels

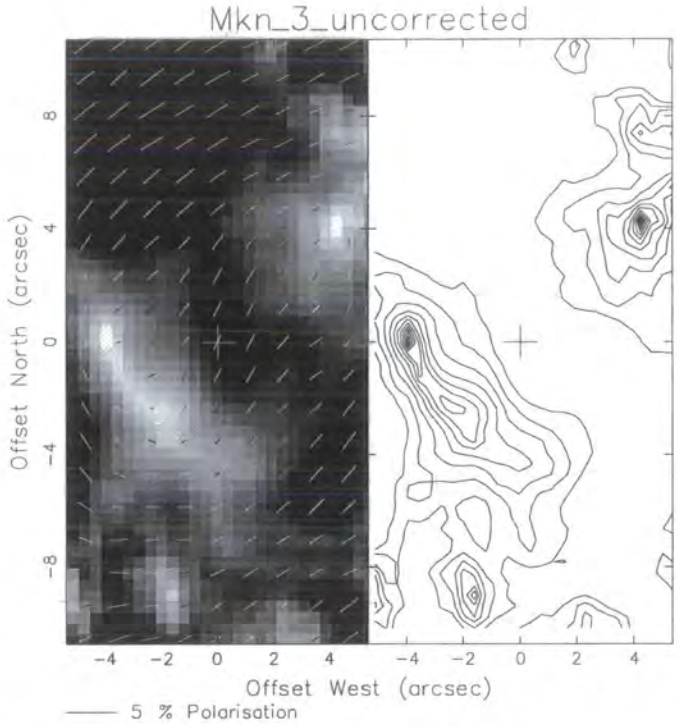

Figure 6.9: V-band polarization level image of Mkn 3, uncorrected for ISP, polarization vectors 5x5 bins, step size 3 pixels

y

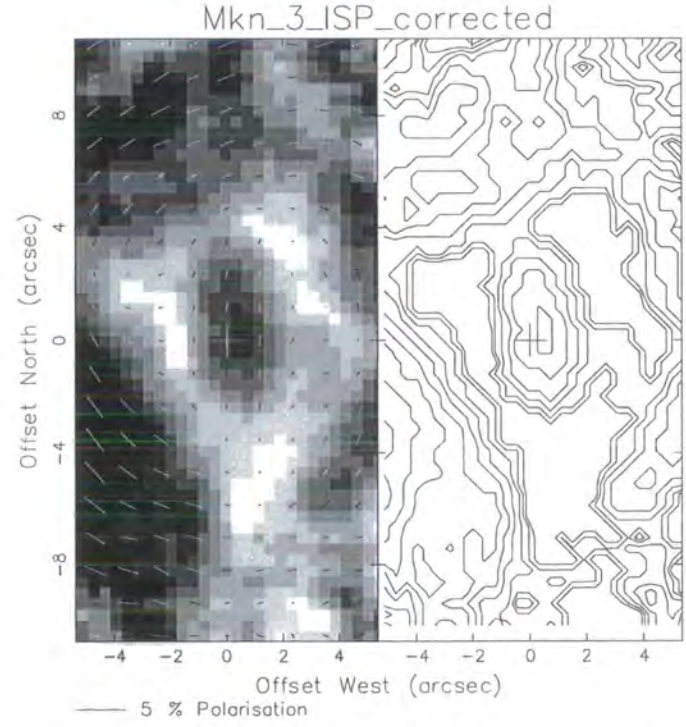

Figure 6.10: V-band polarization level image of Mkn 3, corrected for ISP, polarization vectors 5x5 bins, step size 3 pixels

6.3 Markarian 1376 - NGC 5506

6.3.1 Introduction

Markarian 1376 (also known as NGC 5506) is a southern dusty nearly-edge-on early-type galaxy where the Seyfert 2 nucleus is viewed through the obscuring host galaxy disc. It has a nearby companion, NGC 5507 with a velocity difference of 480 km s^{-1} between them (Dahari 1985 [54]). Although Seyfert 2-like in the optical spectrum, in the infra-red it has broad permitted lines, has a high X-ray luminosity, and emission line ratios which are more usually associated with Seyfert 1s (Maiolino *et al.* 1994 [142]).

Diffuse loop- or bubble-like structures of radio emission extend out from the disk to 30″ from the nucleus along the minor axis at position angle 140°, resolving into a compact nuclear component plus diffuse halo. Minor axis nuclear outflows are detected in both optical and radio images by Colbert *et al.* (1996) [49] [48] which may fuelled by either by a Seyfert driven jet entraining and heating ambient gas as it flows outward, or by star formation driven winds. Such a region of star formation in the central few hundred pc of the nucleus is detected by Maiolino *et al.* (1994) [142], but the star formation rate is not as high as in a starburst galaxies.

The emission line profiles are complex and Wilson *et al.* (1985) [263] fitted the observed velocity field to one consisting of normal rotation in a plane with a major axis close to the east-west direction plus a second expansion component out of the galaxy plane (which is also found by Maiolino *et al.* 1994). This is confirmed by $H_\alpha + [N_{II}]$ emission-line imaging by Colbert *et al.* (1996) [49] showing emission along the minor axis, extending out to $\approx 5''$ north and south from nuclear region, with a width of about 7″ to 8″, highly indicative of a minor axis outflow.

Both the narrow and broad IR emission lines are heavily reddened (Veilleux *et al.* 1997 [249]), but this is to be expected as dust in the edge-on host galaxy must be obscuring observations of the central source. Their measurements suggest that an unreddened source dominates the optical line emission, but the infra-red line emission is produced in a stronger reddened source. There is tentative detection of a broad component to the H_β line by Blanco (1990) [33] suggesting an obscured Seyfert 1 BLR in nucleus, but Veilleux *et al.* (1997) [249] argue that there are highly reddened wings, but that they are not representative of a Seyfert 1 type BLR.

Markarian 1376 has Seyfert 1 type X-ray emission (Mushotzky 1982 [164]), rapid X-ray variability of timescales as short as an hour (Konig & Timmer 1997 [125], a soft X-ray

excess, and a Fe K_α line. Recent RXTE[3] results (Weaver 1998 [254]) detect characteristic Compton reflection, and relativistically broadened Fe $K\alpha$ emission lines, consistent with viewing a relativistic accretion disk at approximately 40°, supporting the idea that much of the reprocessing in Seyfert 1 nuclei occurs in a central accretion disk. Wang *et al.* (1999) [252] explain the extended (kpc scale) soft X-ray excess by either thermal emission from a very low abundance material or by scattered flux from the primary power-law emission plus a small amount of thermal emission, *i.e.* a partially obscured source (Stanga *et al.* 1993 [220]). Spatially, the soft X-ray emission at least partly comes from an extended kpc scale region, elongated along 150°approximately along the minor axis (Colbert *et al.* 1996 [49]), which is not consistent with a Seyfert model where the 2 types are due only to partial covering of the central source, but requires the central continuum to illuminate and interact with the surroundings, and the authors favour a scattering dominated model with relatively cold scatterers (kT << 1 keV), which is consistent with the torus model unification scheme. They suggest that the intermediate inclinations found for narrow-line X-ray galaxies are consistent with the accretion disk plane being aligned with the outer absorbing torus.

6.3.2 Observational details

Mkn 1376 was observed on the 4 m Anglo Australian telescope (AAT) with a focal ratio of 15 on the night of 21 March 1994, using a broad band V filter. For this configuration, the scale of the sky on the CCD detector was 0.31 arcseconds per pixel, covering a total field of 2.9 arcminutes by 2.1 arcminutes. At the estimated distance of 25 Mpc, assuming $H_0 = 75$ km s^{-1} Mpc^{-1}, 1 arcsecond corresponds to approximately 120 pc. A DSS image of Mkn 1376 is given in figure 6.11, which shows the total field that was mapped by the polarimeter.

Data were taken at one position only due to time constraints, and consequently only the central regions of the galaxy were imaged. Four CCD frames each of 600 seconds exposure, and four frames each of 30 seconds exposure for the nucleus, together with suitable flatfield frames were taken. The seeing for these observations was calculated to be 2.0 arcseconds using star images from other observations on that night (since there were no suitable stars in the field, as can be seen in figure 6.11). The moon was down during the observations.

[3]Rossi X-ray Timing Explorer

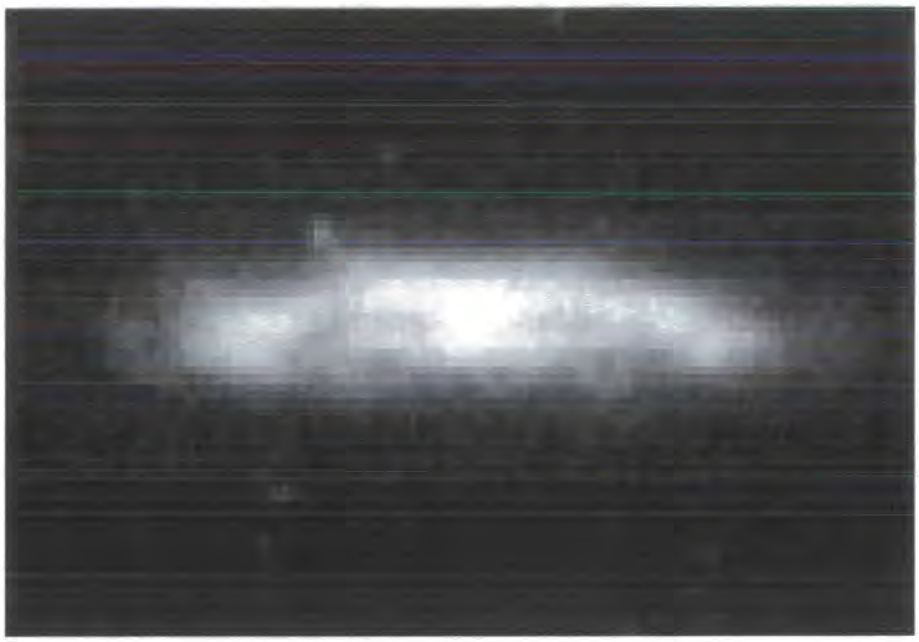

Figure 6.11: DSS intensity image of Mkn 1376, field of 3' by 2'

6.3.3 Image details

Figures 6.12 to 6.17 present broad V-band images of Mkn 1376. The scale is in arcseconds, centred on the peak nuclear intensity of the image. The greyscale intensity is reversed, *i.e.* black representing the highest intensity. The contours of the maps are plotted in levels of magnitudes. The polarization vectors were calculated by binning the polarization data in either squares of 5 pixels by 5 pixels centred on the selected pixel, plotting the average polarization over this area, then moving on 3 pixels to select the central pixel for the next polarization vector to be calculated, or squares of 3 by 3 pixels and moving on by 2 pixels. The polarization vectors are plotted with signal-to-noise confidence levels of 65% in all maps.

Figures 6.15 and 6.16 present a polarized intensity greyscale map and a percentage polarization greyscale map respectively (both corrected for interstellar polarization), with darker shades representing higher polarized intensity or polarization.

6.3.4 Interstellar polarization

The galactic co-ordinates (l=339°,b=54°) suggest the ISP effect should be small. Kay (1994) [119] measures the polarization of two near field stars (HD 123235 and HD 124701) and calculates an average of 0.48% ± 0.09% at 84.1°± 5.3°to be representative of ISP. Unfortunately there were no stars in the field of the observations for this thesis which

were suitable for measuring the polarization of, therefore it was not possible to arrive at an independent estimate of ISP. The value measured by Kay therefore is used for the ISP corrections applied to Mkn 1376 in this thesis.

6.3.5 Results: V-band

The V-band filter map shows both a wide band of polarization across the nucleus and central regions of the galaxy, and traces of a centro- symmetric scattering pattern centred about the nucleus. The band of polarization across the nucleus has a position angle of approximately 90°, *i.e.* parallel to the apparent dust lane, suggesting dichroic extinction as the polarization mechanism (Scarrott 1996 [199]). It is particularly strong in the southern half the galaxy, which, as can be seen from the contour maps, is the most heavily obscured part of the dust lane.

The nuclear polarization is approximately 3.0% at 81°, approximately the same position angle as the aligned band suggesting that it too is being seen through the dust lane. Aperture polarimetry of the nucleus was performed and the results are given in table 6.5. These show a reduction in polarization level with an increase of aperture size, to be expected due to greater starlight dilution. These measurements agree closely with most previous nuclear polarization measurements, which are presented in table 6.6.

Unfortunately only half the field of view was observed as the gaps on the map show, so primarily only the centre of the galaxy was mapped. There are some coherent polarization measurements towards the edges of the dust lane, on the two outer data strips. These polarizations have position angles perpendicular to the dust lane, a pattern which has been observed in other edge-on galaxies (section 3.2.4). Also there are some polarization vectors towards the edges of the galaxy, which are orientated in a pattern similar to a centro-symmetric pattern, implying scattering in the host galaxy on a large scale.

Table 6.5: V-band nuclear aperture polarimetry of Mkn 1376 (uncorrected)

Aperture (arcsec)	Aperture (pixels)	Polarization (percent)	Position angle (degrees)
2	6.5	3.17 ± 0.28	81 ± 3
2.5	8.1	3.03 ± 0.28	81 ± 3
3	9.7	2.90 ± 0.28	81 ± 3
4	12.9	2.66 ± 0.29	81 ± 3
5	16.1	2.43 ± 0.29	82 ± 3
6	19.4	2.21 ± 0.30	82 ± 4

Table 6.6: Comparison of nuclear polarization measurements of Mkn 1376 (uncorrected)

Band name	Range of wavelength (Ångstroms)	Aperture or slit width (arcsec)	Polarization level (percent)	Polarization angle (degrees)	Reference[1]
-	4600-6200[3]	1.7	2.5 ± 0.35	79 ± 2.0	Y96
-	3800-5600[3]	4	3.10 ± 0.16	84.3 ± 1.5	M83
-	3200-6200[3]	2	2.60 ± 0.41	72.8 ± 4.5	K94
V	5000-5900[2]	6	2.35±0.26	80±3	BH90
RI	5700-8800[2]	6	2.13±0.39	76±5	BH90
I	7300-8800[2]	6	3.10±0.31	70±3	BH90
J	10900-13700[2]	6	2.07±0.24	70±3	BH90
H	15100-17900[2]	6	2.44±0.13	72±2	BH90
K2	19700-23900[2]	6	2.76±0.46	69±5	BH90

[1]References: Y96 = Young *et al.* (1996), BH90 = Brindle & Hough (1990), M83 = Martin (1983)
[2]Broad band observations
[3]Spectropolarimetry

6.3.6 Results: V-band after ISP correction

The value of ISP applied, 0.48% at 84°, is small compared with the general levels of polarization in the central parts of the galaxy. Therefore it would be expected that there should not be a great deal of difference to the polarization pattern after subtracting the ISP estimate, and indeed when comparing the wide-field figures 6.12 and 6.13, it can be verified that there is very little difference in polarization pattern.

The maps showing the nucleus in more detail, figures 6.14 and 6.15 show that the ISP correction has not altered the details. The contour map is better than the greyscale map for showing more clearly the position of the dust lane, which absorbs the light from the centre of the galaxy. The centro-symmetry can be seen most clearly in the northern half, while the southern half of the centre is mostly of uniform polarization, suggesting the nuclear dust lane is thicker here, *i.e.* the southern half is inclined away, therefore the light has to travel through more of the dusty galaxy disc, thus suffering more dichroic absorption. Aperture polarimetry was performed on the nucleus, and the ISP corrected results are presented in table 6.7. The ISP correction has the effect of reducing the polarization level in the nucleus. There are no previous published results corrected for ISP to compare the measurements to.

Figures 6.16 and 6.17 show maps of polarized intensity. These show an elongation north and south from the nucleus, extending out to 4 or 5 arcseconds each way, and are spatially coincident with the extended emission line region found by Colbert *et al.* (1996) [49], which indicates a nuclear outflow as explained in section 6.3.1.

The multi-wavelength nuclear polarization measurements of Brindle & Hough (1990) [36], [35] show a rotation in polarization angle between the V and I bands; at V band the polarization is approximately aligned with the galaxy optical axis, and at I band aligned more with the radio axis. They suggest this is due to a dominant non-thermal or electron scattering component in the infra-red, but that there is an interstellar component associated with the galaxy dust lane dominating in the visible band. The evidence in the V band maps in this thesis indicates the presence of dichroic polarization associated with the galaxy dust lane in the visible by the strongly aligned band of vectors across the dust lane. To test the prediction of Brindle (*et al.* 1990), further imaging polarimetric observations in I and R wavebands are required to detect this electron scattered component and its spatial extension.

In addition to the observations made on the AAT, there were also some old observations from the 1m WISE telescope in Israel taken in 1986. The data was reduced and new polarization maps were made to produce a lower resolution wide-field view of the galaxy.

Table 6.7: V-band nuclear aperture polarimetry of Mkn 1376 (ISP corrected)

Aperture (arcsec)	Aperture (pixels)	Polarization (percent)	Position Angle (degrees)
2	6.5	2.77 ± 0.28	80 ± (±)
2.5	8.1	2.63 ± 0.28	80 ± (±)
3	9.7	2.50 ± 0.28	80.5 ± (±)
4	12.9	2.23 ± 0.29	81 ± (±)
5	16.1	2.00 ± 0.29	81 ± (±)
6	19.4	1.77 ± 0.30	81 ± (±)

These showed that the band of aligned polarization extends to nearly 20 arcseconds from the nucleus, following the dust lane, and starts off parallel to the dust lane in the centre, but becomes perpendicular towards the extremities, common to a number of other edge-on galaxies. The nuclear polarization was in close agreement with the measurement taken on the AAT. However the quality of the maps made with this old data was poor, so they are not presented here in this thesis.

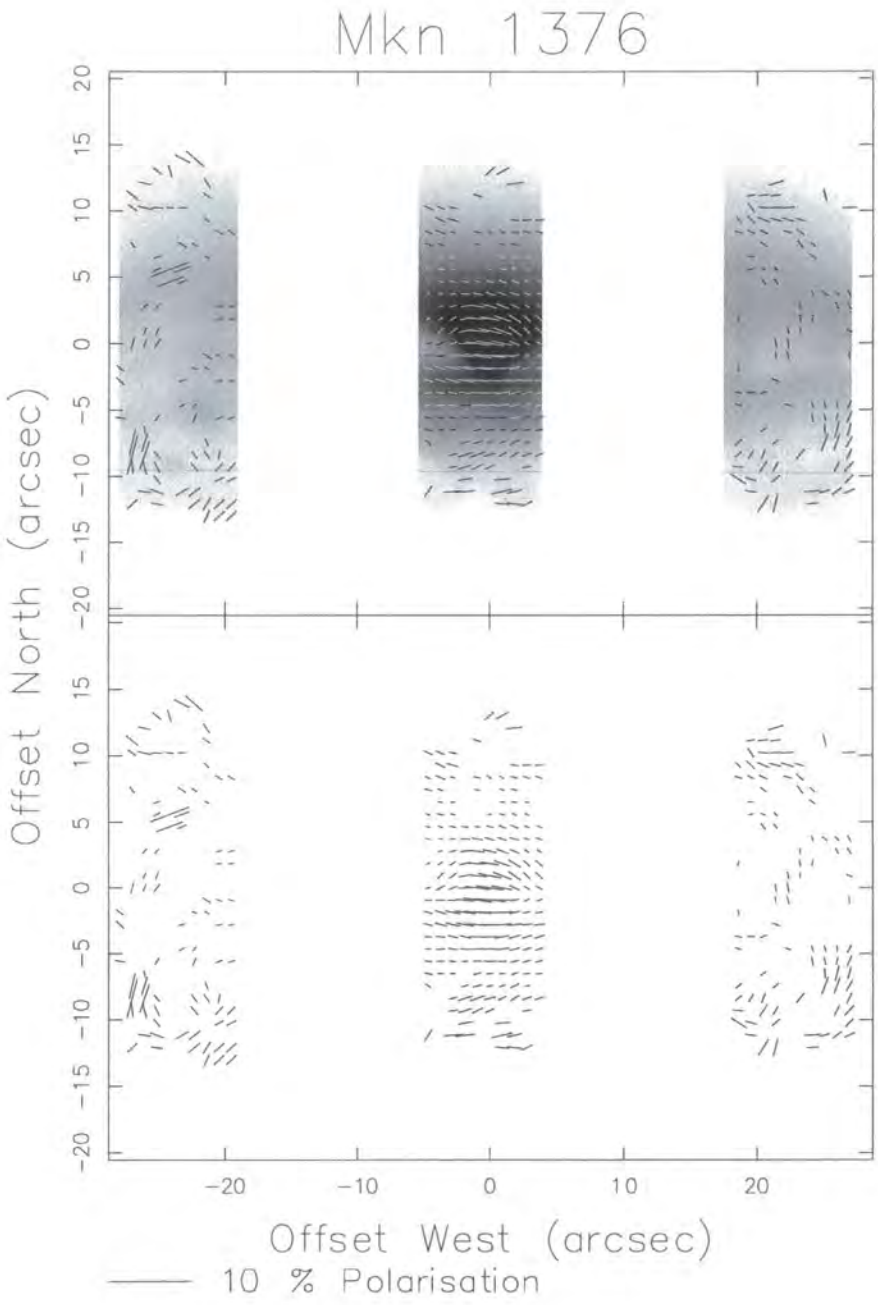

Figure 6.12: V-band greyscale total intensity and polarization wide-field images of Mkn 1376 - ISP uncorrected, polarization vectors 5x5 bins, step size 3 pixels

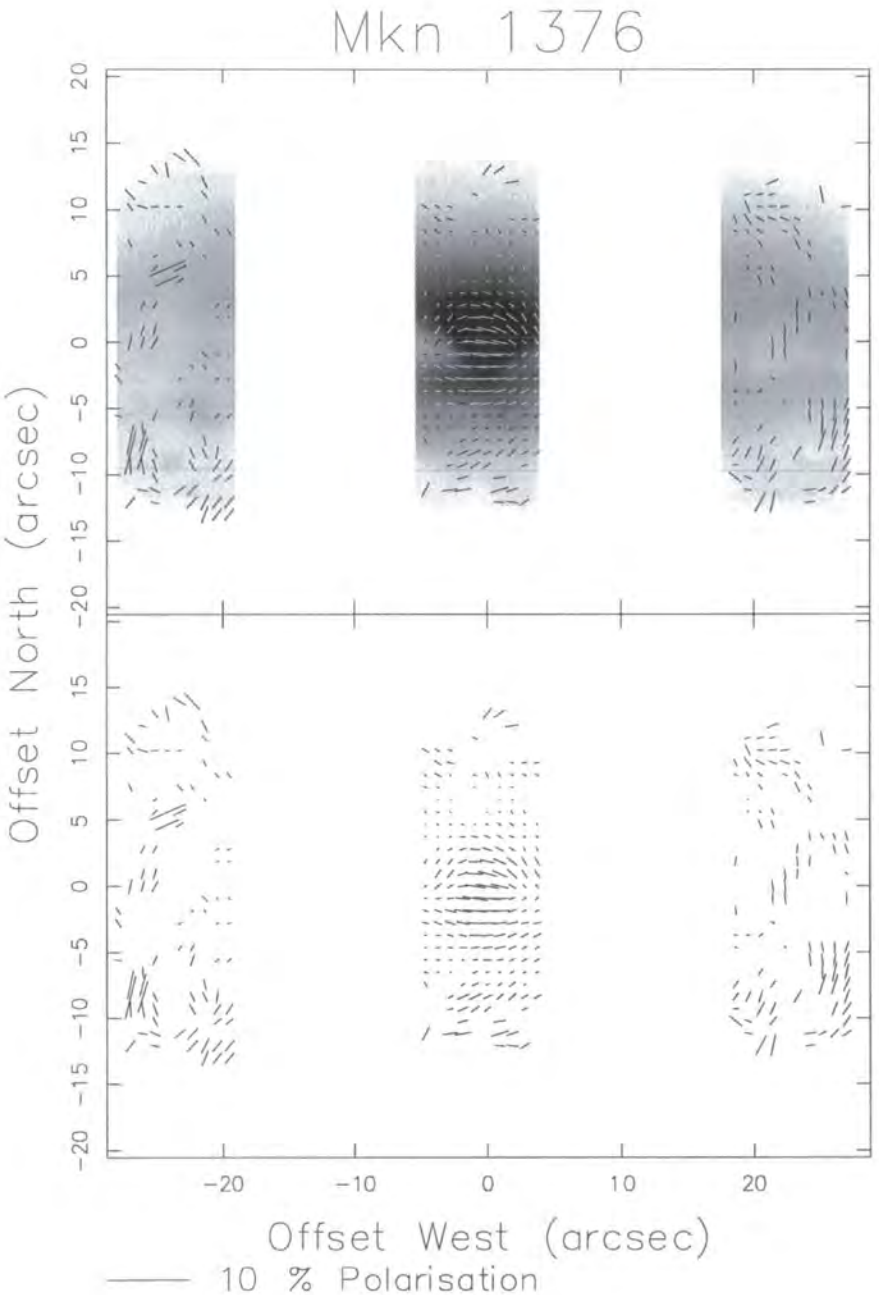

Figure 6.13: V-band greyscale total intensity and polarization wide-field images of Mkn 1376 - ISP corrected, polarization vectors 5x5 bins, step size 3 pixels

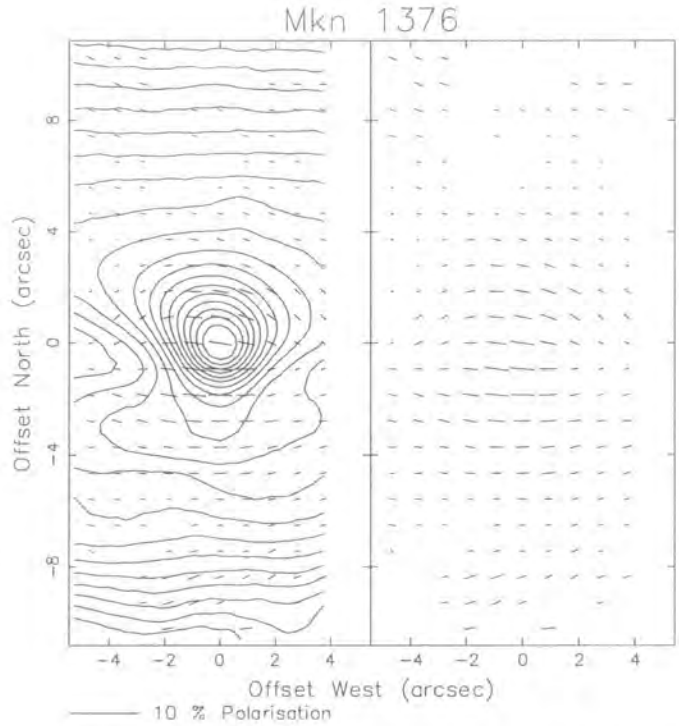

Figure 6.14: V-band contour total intensity and polarization image of the nucleus of Mkn 1376 - ISP uncorrected, polarization vectors 5x5 bins, step size 3 pixels

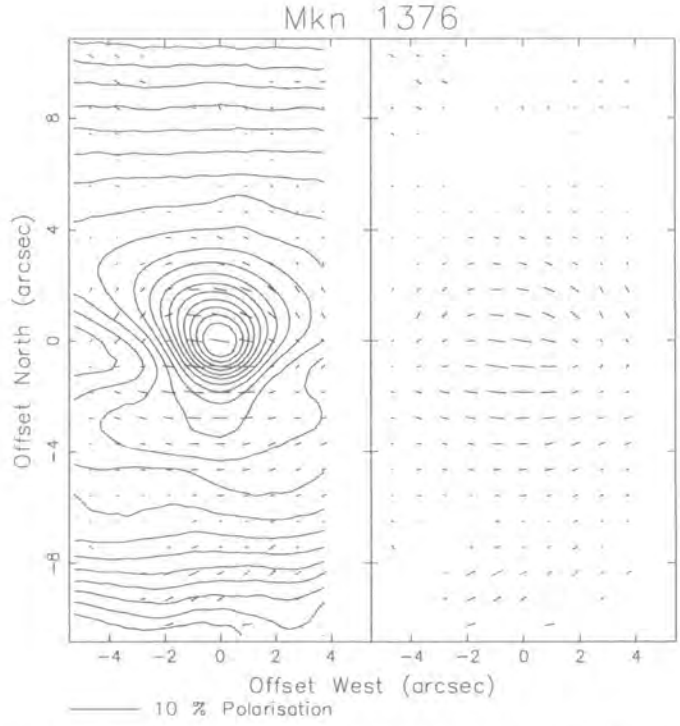

Figure 6.15: V-band contour total intensity and polarization image of the nucleus of Mkn 1376 - ISP corrected, polarization vectors 5x5 bins, step size 3 pixels

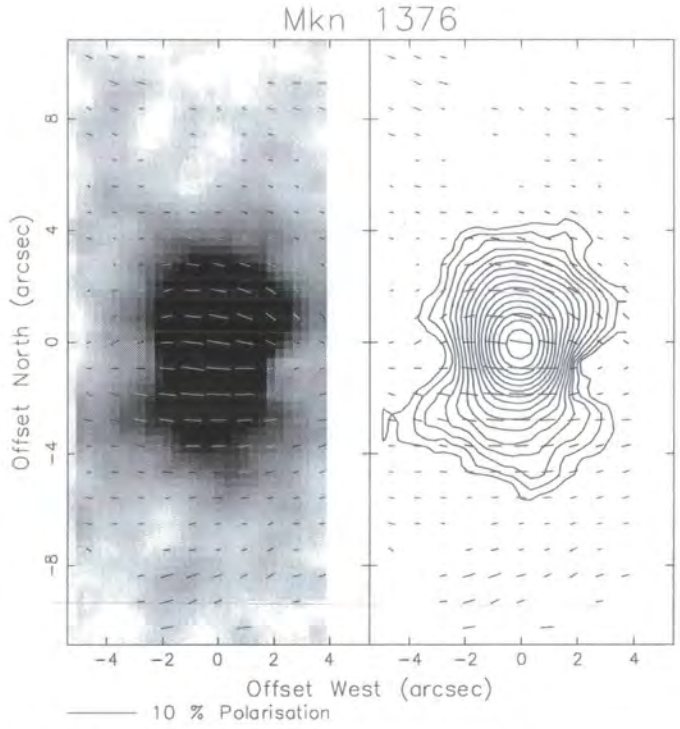

Figure 6.16: V-band polarized intensity greyscale and contour images of the nucleus of Mkn 1376 - ISP uncorrected, polarization vectors 5x5 bins, step size 3 pixels

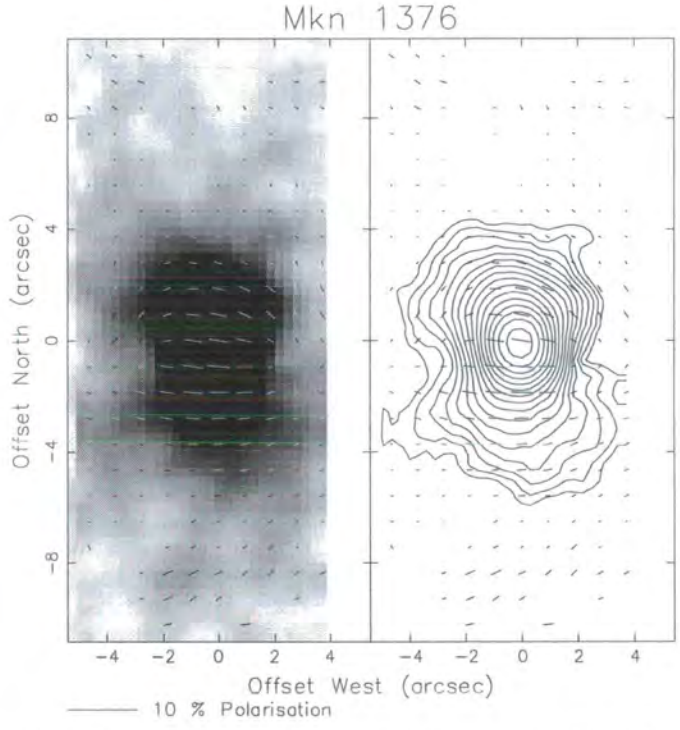

Figure 6.17: V-band polarized intensity greyscale and contour images of the nucleus of Mkn 1376 - ISP corrected, polarization vectors 5x5 bins, step size 3 pixels

6.4 NGC 2992

6.4.1 Introduction

NGC 2992 is a nearly edge-on Sa type galaxy crossed by a dust lane, and is interacting with the galaxy NGC 2993 three arcminutes to the south-east, connected by a tidal tail. It is highly inclined at 70° (Morphological Catalog of Galaxies, Vorontsov-Velyaminov, 1962-1974), and the disk of NGC 2992 is generally assumed to be oriented with the north-west edge closest to the observer (Allen *et al.* 1998 [3]). Its spectrum is well studied at all wavelengths leading to its classification as a narrow-line X-ray galaxy. It has a Seyfert 1.9 nucleus obscured by a dust lane, although it is also classified as a Seyfert 2, since the broad component detections are tentative.

The radio emission consists of several compact nuclear radio sources Condon *et al.* (1982) [52] and Unger *et al.* (1986) [248], a figure of eight loop at 6 cm centred on the nucleus along approximately position angle 160° out to 2″ north and south (Wehrle & Morris 1988 [257]), and diffuse emission around the galaxy (Ulvestad & Wilson 1989) [245] to an extent of 9.1″ at 20 cm (at the 10% flux contour), and at 6 cm the diffuse emission extends further out to 20″– 30″ in nearly all directions (Colbert *et al.* 1996 [48]). Hummel *et al.* (1983) [111] show 20cm emission extended also over about 2 arcseconds along a position angle of 100°.

Infra-red observations by Chapman *et al.* (1999) [43] trace the spiral structure of the galaxy, and find a loop of IR emission embedded in the radio loop described above. This is interpreted as being due to both outflow from the nucleus, and star formation in the galaxy disk. Infra-red spectroscopy shows broad lines typical of Seyfert 1 spectra. Reddening in the BLR gives E_{B-V} as 2.1, Schmitt (1997) [207].

The nuclear optical spectrum shows typical Seyfert 2 characteristics except possibly a weak broad H_α component Veron *et al.* (1980) [177]. Ionized O_{III} emission is detected over 42″ along position angle 197° by Durret & Bergeron (1988) [65]. $[O_{III}]$ and H_α gas kinematics are modelled by Marquez *et al.* (1998) [146] as circular rotation round a disk of major axis 30° and inclination 70° plus a constant radial outflow perpendicular to the disk plane, which is also supported by Brinks *et al.* (1999) [37]. Reddening in the narrow-line region is significant and was calculated to be $E_{B-V} = 0.84$ by Durret & Bergeron (1988), with values somewhat greater towards the north east.

Colbert (1996) [49] finds a dust lane separating the line emission that immediately surrounds the nucleus from the bright emission line region. This extended line emission

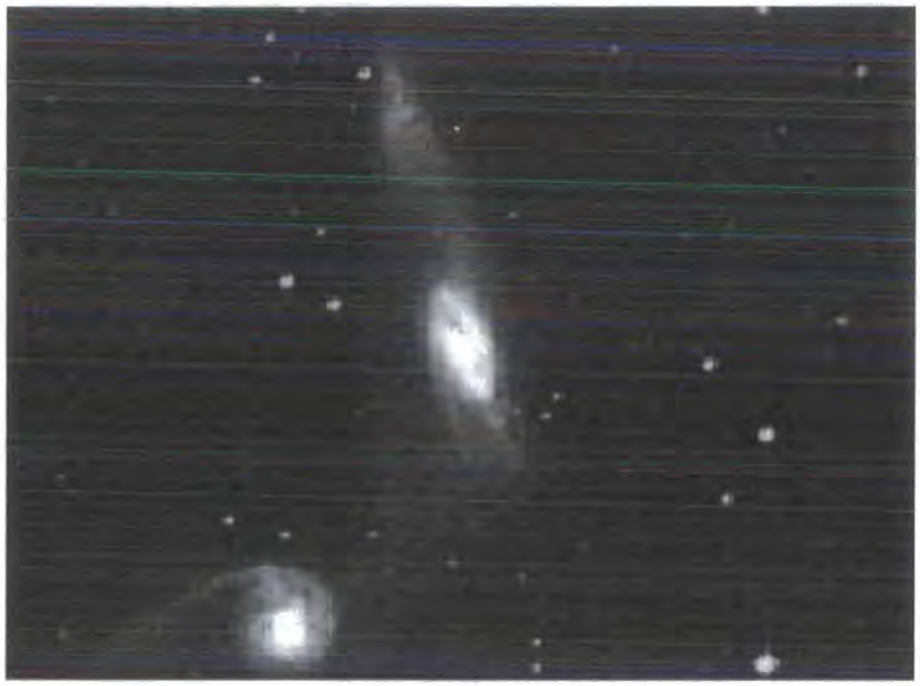

Figure 6.18: DSS intensity image of NGC 2992 (centre) and NGC 2993 (left), field of 11' x 8'

extends from 5″ to 15″ to the north-west in the direction of the minor axis at approximately position angle 120°, and there are ionized filaments as far out as 30 arcseconds, but they do not correspond to the radio loop structure. Spectroscopic measurements by Tsvetanov, Dopita & Allen (1995) [234] show outflowing gas extending several kpc out from the galaxy disk. The radio and ionized emission morphology suggest a powerful galactic outflow, presumably a starburst driven superwind. H_I clouds detected by absorption are seen to be falling in towards the nucleus, possibly fuelling the AGN (Brinks 1999 [37]).

Ultra-violet imaging to investigate star formation by Fanelli & Collins (1997) [75] showed only diffuse patchy emission with no nuclear bright spot, presumably due to obscuration by the large amounts of dust in the edge-on galaxy disk.

The X-ray spectrum of NGC 2992 has a significant absorbing column (Weaver *et al.* 1996 [253]), and the flux is variable on a timescale of a few days to months (Barr & Mushotzky 1982 [19]) and has been interpreted as due to a central source partially covered by patchy absorbers. ROSAT images by Colbert *et al.* (1998) [47] shows soft X-ray emission extending to 1′ elongated along position angle 100°, approximately co-incident with the radio structure along the minor axis, suggesting the emission is due to outflow nuclear gas. Figure 6.19 gives a diagram showing visually the different emission regions and axes of the various observations for easier comparison. It also shows the angle of polarization of the nuclear optical polarization measured in this study.

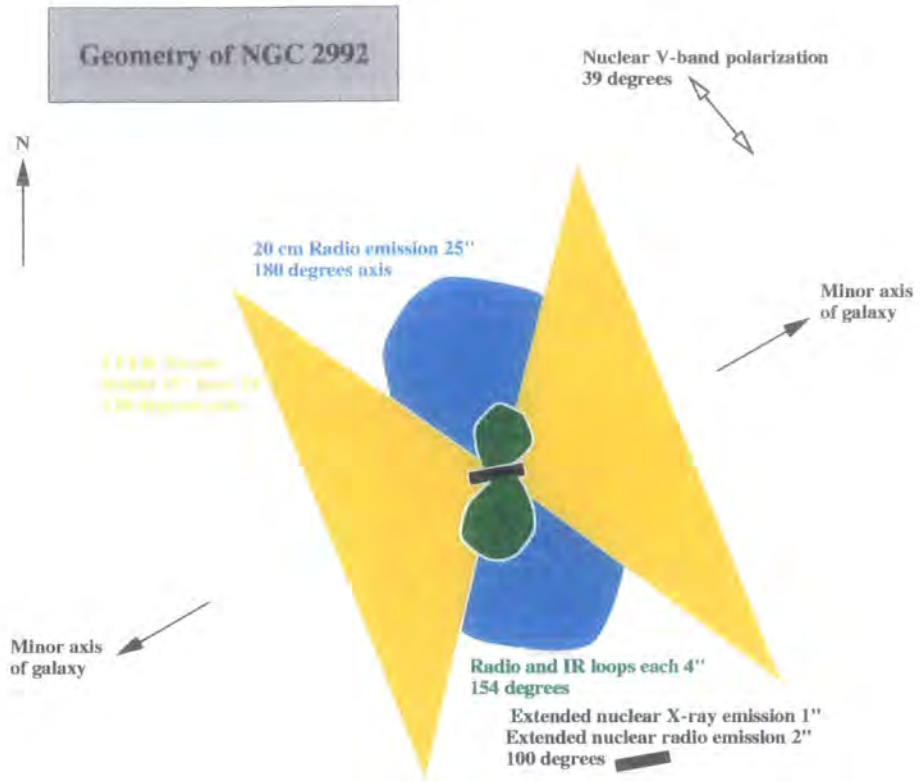

Figure 6.19: Diagram of the axes of observations of NGC 2992

6.4.2 Observational details

NGC 2992 was observed on the 1 m Jacobius Kapteyn telescope (JKT) with a focal ratio of 15, using a broad band V filter on the 30th January 1995 and an I filter on the 31st January 1995. Additional data were taken at the Cassegrain focus (focal ratio 15) of the SAAO 1 m telescope in February 1997 using a broad band V filter. For both these configurations the scale of the sky on the CCD detector was 1.2 arcseconds per pixel, covering a total field of about 11 arcminutes by 8 arcminutes. At the estimated distance of 42 Mpc, assuming $H_0 = 75$ km s^{-1} Mpc^{-1}, 1 arcsecond corresponds to approximately 200 pc. A DSS image of NGC 2992 is given in figure 6.18, which shows the total field that was mapped by the polarimeter.

For the JKT observations, data were taken at 3 positions to allow complete coverage for both the V-band and I-band data, giving a total of twelve 900 second exposures, plus flatfield frames. The I-band data were badly affected by scattered light entering the telescope, but careful sky subtraction, using a second degree polynomial sky model fit was successful in removing this. For the V-band data, a linear sky model fit was sufficiently representative. The seeing for the JKT V-band observations was calculated to be approximately 2.1 pixels *i.e.* 2.5 arcseconds, and for the I-band observations 2.8

arcseconds, using star images from the field on that night. The moon was down for both nights.

For the SAAO observations data were taken at one position around the nucleus for the SAAO observations. Four CCD frames each of 900 seconds of the object were taken, together with suitable flatfield frames (a further few frames were in fact taken, but were severely clouded, with the cloud then preventing further observations that night). For the SAAO observations the seeing was 2.7 arcseconds. The moon was up and 0.59 illuminated, and about 84° from the target, which should therefore cause significant sky polarization, necessitating careful sky subtraction.

6.4.3 Image details

Figures 6.20 to 6.22 present broad V-band and I-band images of NGC 2992. The scale is in arcseconds, centred on the peak nuclear intensity of the image. In figure 6.20 a wide field image is given, showing NGC 2992 in relation to its companion, NGC 2993 in the south-east. Figures 6.21,6.23,6.24 - 6.28 give dual maps of NGC 2992, the left-hand side is a greyscale total intensity image, right-hand side a contour total intensity image, both with polarization vectors plotted at 65%. The greyscale intensity is reversed, *i.e.* black representing the highest intensity. The contours of the maps are plotted in levels of magnitudes. The polarization vectors were calculated by binning the polarization data in either squares of 5 pixels by 5 pixels centred on the selected pixel, plotting the average polarization over this area, then moving on 3 pixels to select the central pixel for the next polarization vector to be calculated, or squares of 3 by 3 pixels and moving on by 2 pixels. The polarization vectors are plotted with signal-to-noise confidence levels of 65%. Figures 6.26 to 6.28 give maps of NGC 2993, the companion galaxy interacting with NGC 2992, which was fortuitously mostly within the image field observed for NGC 2992.

6.4.4 Interstellar polarization

The galactic co-ordinates (l=143°,b=23°) show that the galactic latitude is low, so interstellar polarization contamination might be expected to be significant. Kay (1994) [119] may have applied a correction but does not state the values used.

Efforts were therefore made to search for ISP effects in the images from this thesis, and to calculate any ISP. This was done by measuring the polarization of stars in the V-band image field, *i.e.* very close to the line of sight and, assuming them to be intrinsically

unpolarized, and polarized only by passage though the our Galaxy's foreground dust, looking for a general trend that would be representative of the ISP in this region. To adequately sample the ISP, distant stars are required in order that their light passes through most of the dust in our Galaxy, but as I did not have the distances to the stars available, I excluded the brightest few on the rough assumption that they were likely to be closest, and therefore would sample the ISP least well. The obvious problem here however, is that the fainter the star, the more uncertain the polarization measurements. After measuring the polarizations of five sufficiently bright stars, the brightest had negligible polarization, and for two out of the four remaining there was agreement of a polarization of about 1.2% at 167°, with a third star having a polarization comparable to this within its large error estimates.

A supplementary method by which it might be possible to see the effects of any ISP presents itself by the fact that, in addition to the Seyfert galaxy NGC 2992, the companion Sa galaxy, NGC 2993 was also imaged for this thesis. The polarization pattern in the image of NGC 2993 in figure 6.26, is seen to have obvious centro-symmetry, as would be expected from scattering from a bright central source. Since the polarization levels are of the order of 2%, then any ISP of this level would severely distort this pattern. Therefore any ISP is expected to be below about 1%. More importantly the polarization pattern of this companion galaxy can be used to check on ISP estimates. From polarizations of nearby stars, an estimate of 1.1% at 170°was obtained as explained in the paragraph above. When this value of ISP correction was applied to the images however, the centro-symmetry of the polarization pattern in NGC 2993 was strongly distorted, and although it is possible that NGC 2993 is intrinsically polarized object.

Therefore it can be concluded that the ISP value is most likely very much smaller than this value of 1.2% (at 167°), and it is not possible to determine a representative value from the data in this thesis. Hence all the maps presented for NGC 2992 and NGC 2993 in this thesis are uncorrected for ISP. Furthermore, it can be noted that for NGC 2992, fortunately most of the polarizations measured are sufficiently high ($\approx$ 3%) that the demonstrably small ISP effect will be largely unimportant in the maps presented. At the longer wavelengths of I band, the Serkowski law of the wavelength dependence of polarization in this galaxy demonstrates the ISP effects will be even smaller.

6.4.5 Results: V-band

In the V-band maps, (figures 6.20-6.22), this galaxy shows a polarization of approximately 3% in and around the nucleus. This polarization is at a position angle of approximately

40° and extends as a wide band across the central parts of the galaxy towards the south-east, extending to about 10 arcsecs wide south-east of the nucleus, and 25″ long along the major axis of the galaxy, implying polarization by dichroic extinction. Figure 6.28 gives a V-band map from the SAAO observations, for comparison of the polarization vectors. This shows very good agreement, both for NGC 2992 and NGC 2993, demonstrating the reliability of the observations by the polarimeter, and the constancy of the polarization.

In figure 6.22, which shows the polarization data binned at higher resolution, it can be seen that outside the central band of aligned polarization following the major axis, particularly in the western side of the galaxy, beyond 5″from the nucleus, the polarization pattern shows signs of being more centro-symmetric centred around the V-band nuclear peak, suggesting scattering by dust from the nuclear and circumnuclear radiation. The linearly aligned polarization pattern in the central band suggests alignment by the dust grains in the magnetic field of the galaxy, since the polarization vectors seem to also follow the spiral arms. Any intrinsic Seyfert nuclear polarization is swamped by the polarization from the foreground dust lane in the host galaxy, which can be clearly seen total intensity contour maps. Goodrich (1992)[87] detects polarization of the narrow $[O_{III}]$ lines indicating polarization of the NLR radiation by dust transmission.

The polarization pattern around the nucleus seen in figures 6.21 and 6.22 shows an increase in polarization level at the centre of the nucleus, as expected with less dilution of the polarized component in the centre. Aperture polarimetry of the nucleus is given in table 6.8 at different sized apertures, and table 6.9 lists previously published values compared to the measurements of this thesis.

6.4.6 Results: I-band

The polarization in the nuclear region is significant at about 2.5%, slightly lower than in the V-band, and with the same polarization angle, as can be seen comparing figures 6.23 and 6.21. In the south-east region of the galaxy, the polarization vectors show a consistent trend to an alignment angle of about 52°, rather than along the angle of the major axis of the galaxy (about 38°) as is seen in the V-band vectors.

Infra-red observations by Colbert *et al.* (1996) [48] show an emission line region extending up to 15 arcseconds to the north-west along the minor axis, with some ionized filaments up to 30 arcseconds. Radio observations show radio structure extending out to 2 arcseconds to the north-west. These observations are strong evidence of a powerful galactic outflow in this north-west region.

Table 6.8: Multi-band nuclear aperture polarimetry of NGC 2992

Aperture (arcsec)	Aperture (pixels)	Polarization (percent)	Position Angle (degrees)
I-band (JKT)			
2.5	2.1	2.68 ± 0.25	38 ± 3
3	2.5	2.61 ± 0.23	38 ± 3
4	3.3	2.31 ± 0.22	41 ± 3
5	4.2	2.25 ± 0.22	43 ± 3
6	5.0	2.02 ± 0.22	40 ± 3
V-band (JKT)			
2.5	2.1	3.28 ± 0.39	39 ± 3
3	2.5	3.25 ± 0.36	39 ± 3
4	3.3	3.11 ± 0.33	39 ± 3
5	4.2	2.84 ± 0.32	39 ± 3
6	5.0	2.68 ± 0.31	38 ± 3

The multi-wavelength nuclear polarization measurements of Brindle & Hough (1990) [36], [35] show a strong wavelength dependence, fitted to a Serkowski-type law with $P_{max} = 3.1\% \pm 0.3\%$ at $\lambda_{max} = 0.51\mu\text{m} \pm 0.07\ \mu\text{m}$. The continuum polarization is nearly aligned with the dust lane axis.

Table 6.9: Comparison of nuclear polarization measurements of NGC 2992

Band name	Range of wavelength (Å)	Aperture (arcsec)	Polarization (percent)	Position Angle (degrees)	Reference[1]
BV	3800-5600[2]	4	3.32± 0.18	33.3±1.6	M83
B	3800-4900[3]	6	3.34± 0.34	39±3	BH90
V	5000-5900[3]	6	3.16± 0.26	36±3	BH90
R	5700-7100[3]	6	2.40± 0.21	38±3	BH90
J	10900-13700[3]	6	1.27± 0.11	36±3	BH90
H	15100-17900[3]	6	1.18± 0.11	38±3	BH90
-	3200-6200[4]	2	3.11± 0.10	36.1±0.9	K94
-	4150-4650[4]	2	2.62± 0.40*	47.7±4.1	K94
-	4150-4650[4]	2	15.9± 2.70**	35.2±3.9	K94

[1]References: M83 = Martin (1983), BH90 = Brindle & Hough (1990), K94 = Kay (1994)
[2]Broad band survey using a blue-green Corning 4-96 filter (3800-5600 Å)
[3]Broad band survey, FWHM as stated
[4]Spectropolarimetry
*Corrected for ISP
**Corrected for ISP, Galactic reddening, and galaxy dilution fraction of 0.84

Table 6.10: Multi-band nuclear aperture polarimetry of NGC 2993

Aperture (arcsec)	Aperture (pixels)	Polarization (percent)	Position Angle (degrees)
I-band (JKT)			
2.5	2.1	0.2 ± 0.4	52 ± 45
3	2.5	0.2 ± 0.4	54 ± 45
4	3.3	0.2 ± 0.3	56 ± 45
5	4.2	0.3 ± 0.3	66 ± 33
6	5.0	0.3 ± 0.3	72 ± 28
V-band (JKT)			
2.5	2.1	1.22 ± 0.38	45 ± 9
3	2.5	1.20 ± 0.35	45 ± 8
4	3.3	1.16 ± 0.32	46 ± 8
5	4.2	1.11 ± 0.31	44 ± 8
6	5.0	1.06 ± 0.30	43 ± 8

6.4.7 Results: NGC 2993

Figures 6.26-6.27 give maps of NGC 2993, the companion galaxy to NGC 2992. In the V-band map, the polarization vectors show obvious signs of centro-symmetry, as would be expected for scattering from a central source. The nuclear polarizations are of the order 1.1% and results of aperture polarimetry of the nucleus are presented in table 6.10. In I-band, the polarization of the nucleus is very low and is indistinguishable from being unpolarized within the noise estimates.

In the I-band map there are some apparently high polarizations around the galaxy at the lower intensity levels. However these vectors are mostly due to noise and the apparent alignment of some is most probably due to residual effects of the scattered light (and hence polarization) contamination which was obvious on the preliminary total and polarized intensity maps. Although largely this was successfully removed, some regions of low total intensity are still likely to be affected.

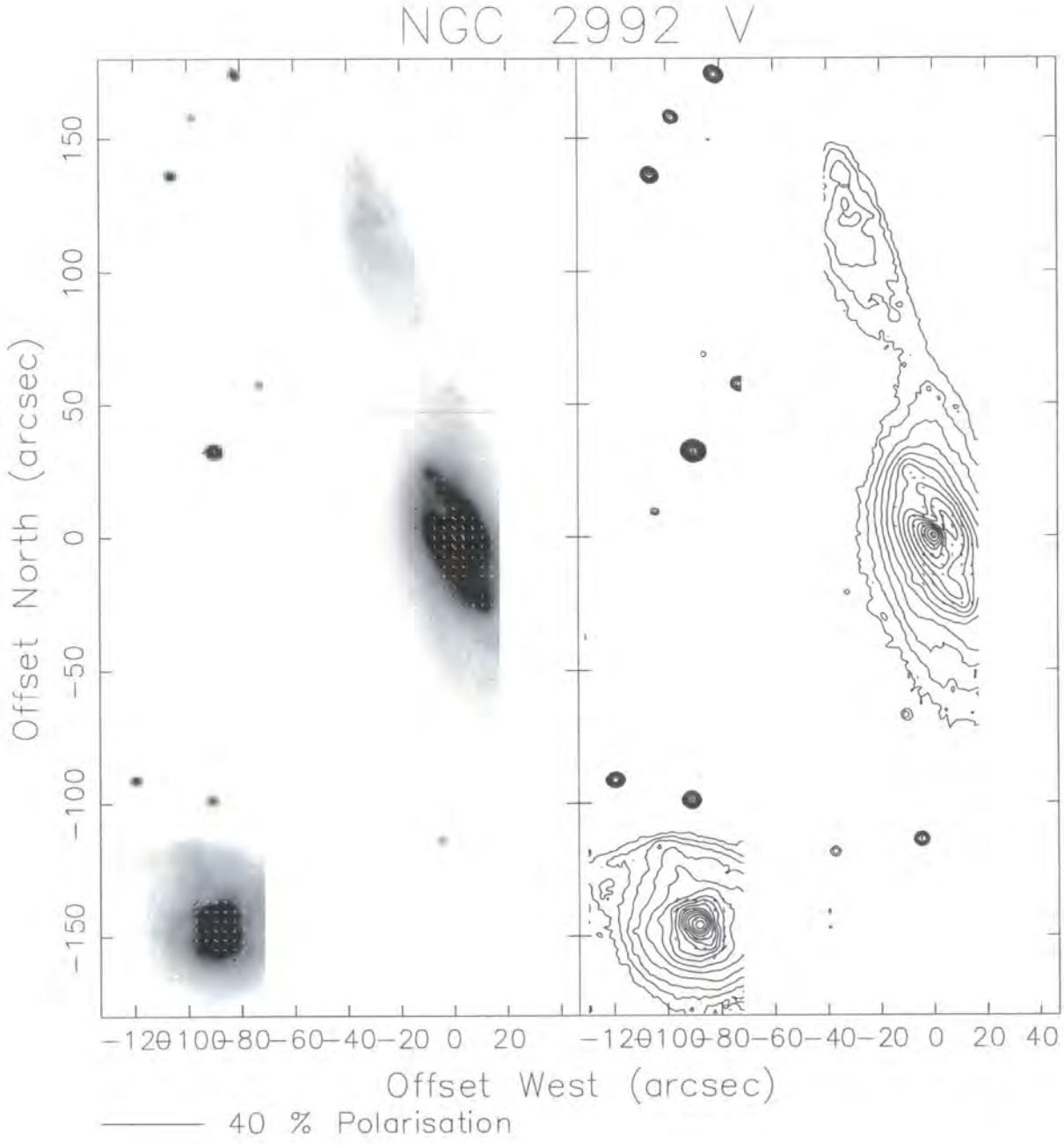

Figure 6.20: V-band wide-field greyscale and contour intensity and polarization image of NGC 2992, polarization vectors 5x5 bins, step size 3 pixels

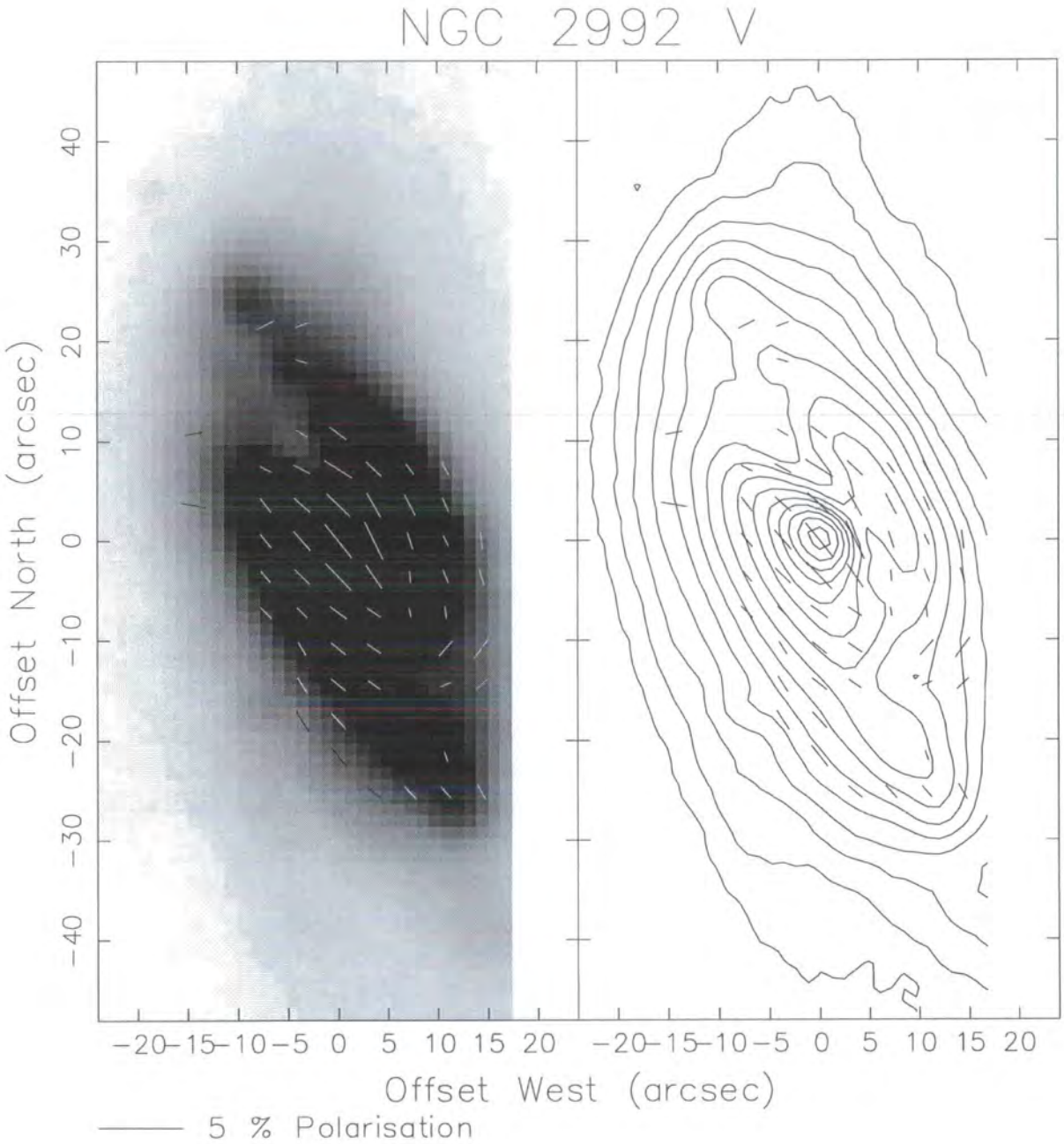

Figure 6.21: V-band greyscale and contour intensity and polarization image of NGC 2992, polarization vectors 5x5 bins, step size 3 pixels

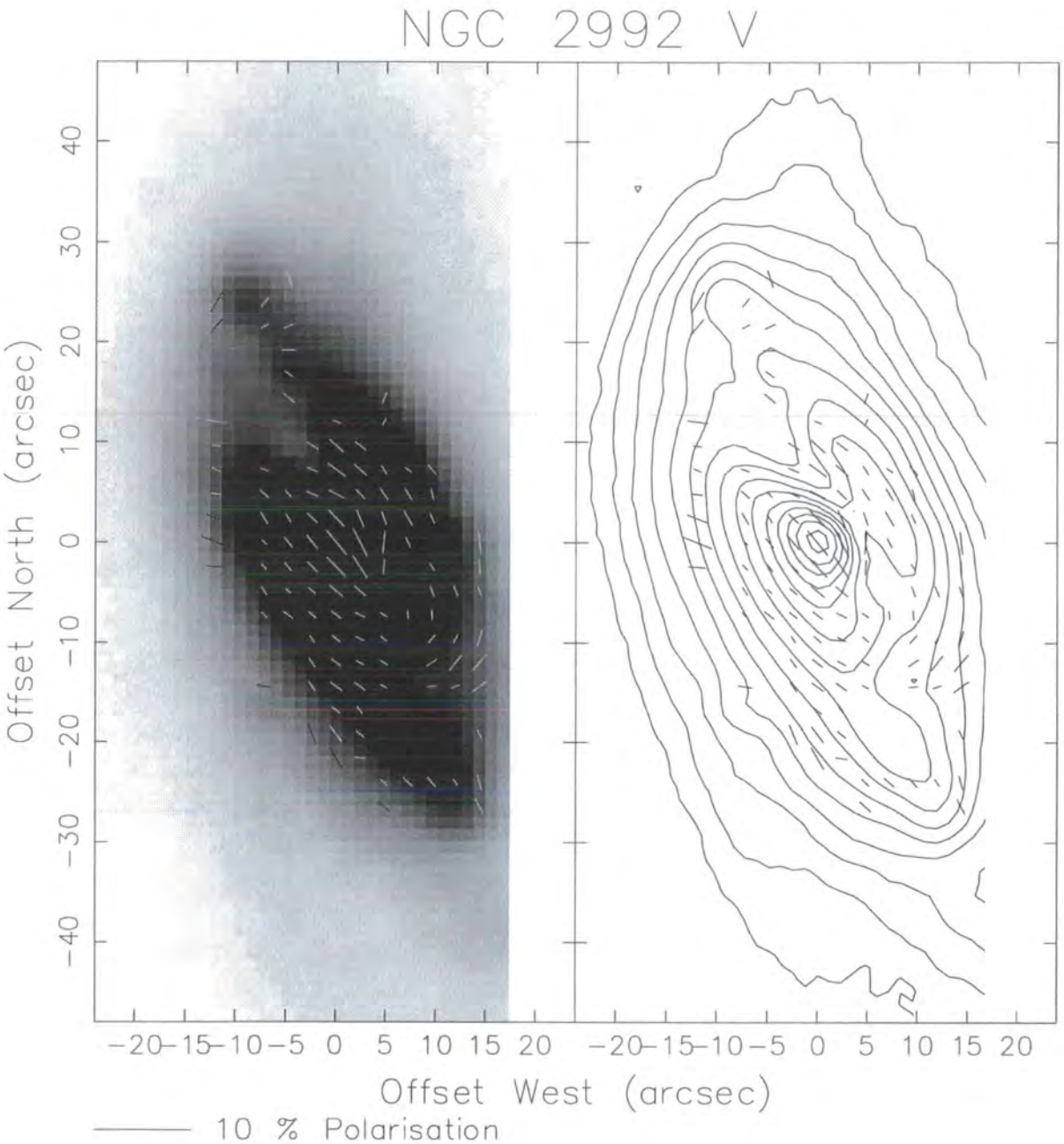

Figure 6.22: V-band greyscale and contour intensity and polarization image of NGC 2992, polarization vectors 3x3 bins, step size 2 pixels

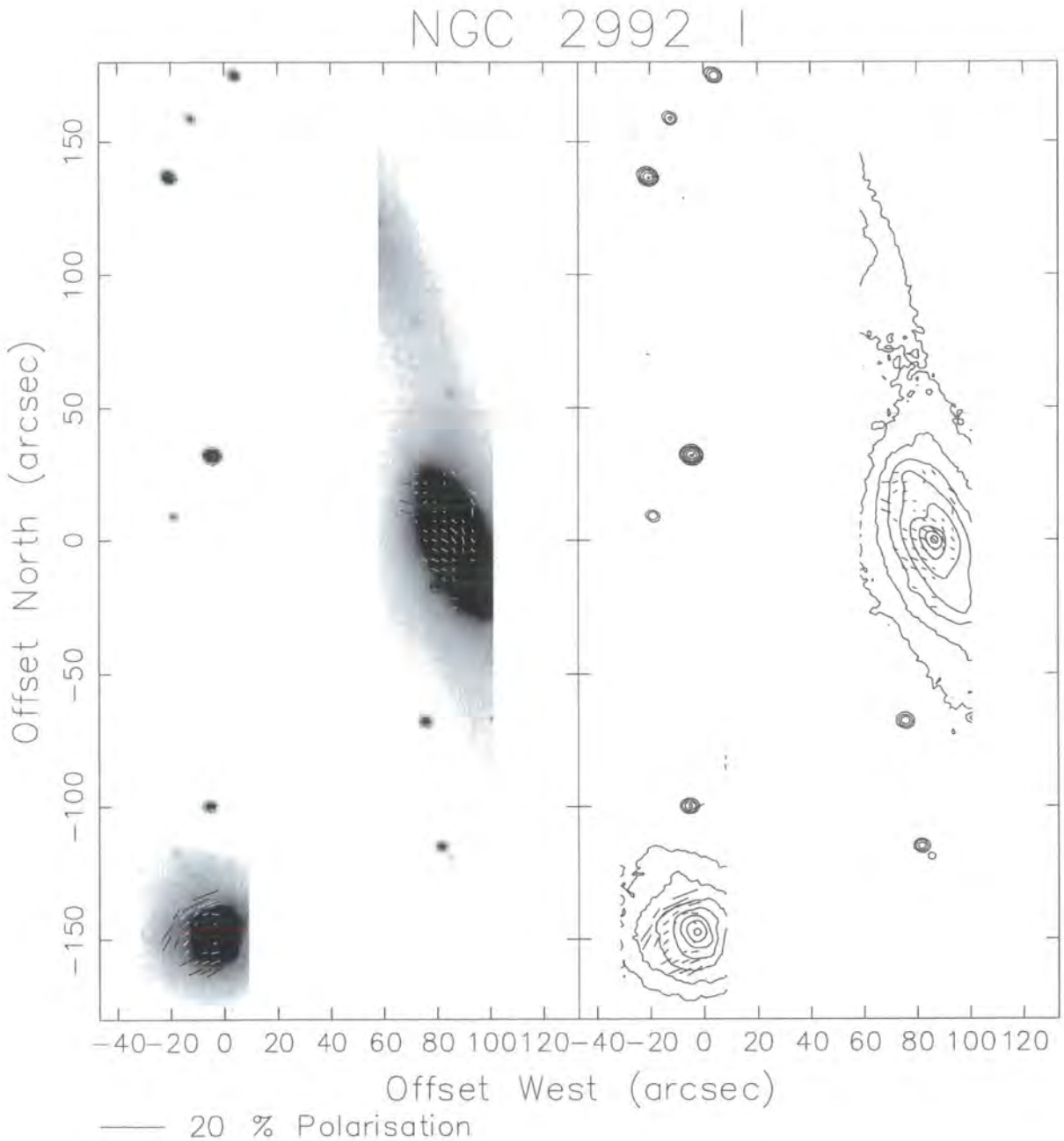

Figure 6.23: I-band wide-field greyscale and contour intensity and polarization image of NGC 2992, polarization vectors 5x5 bins, step size 3 pixels

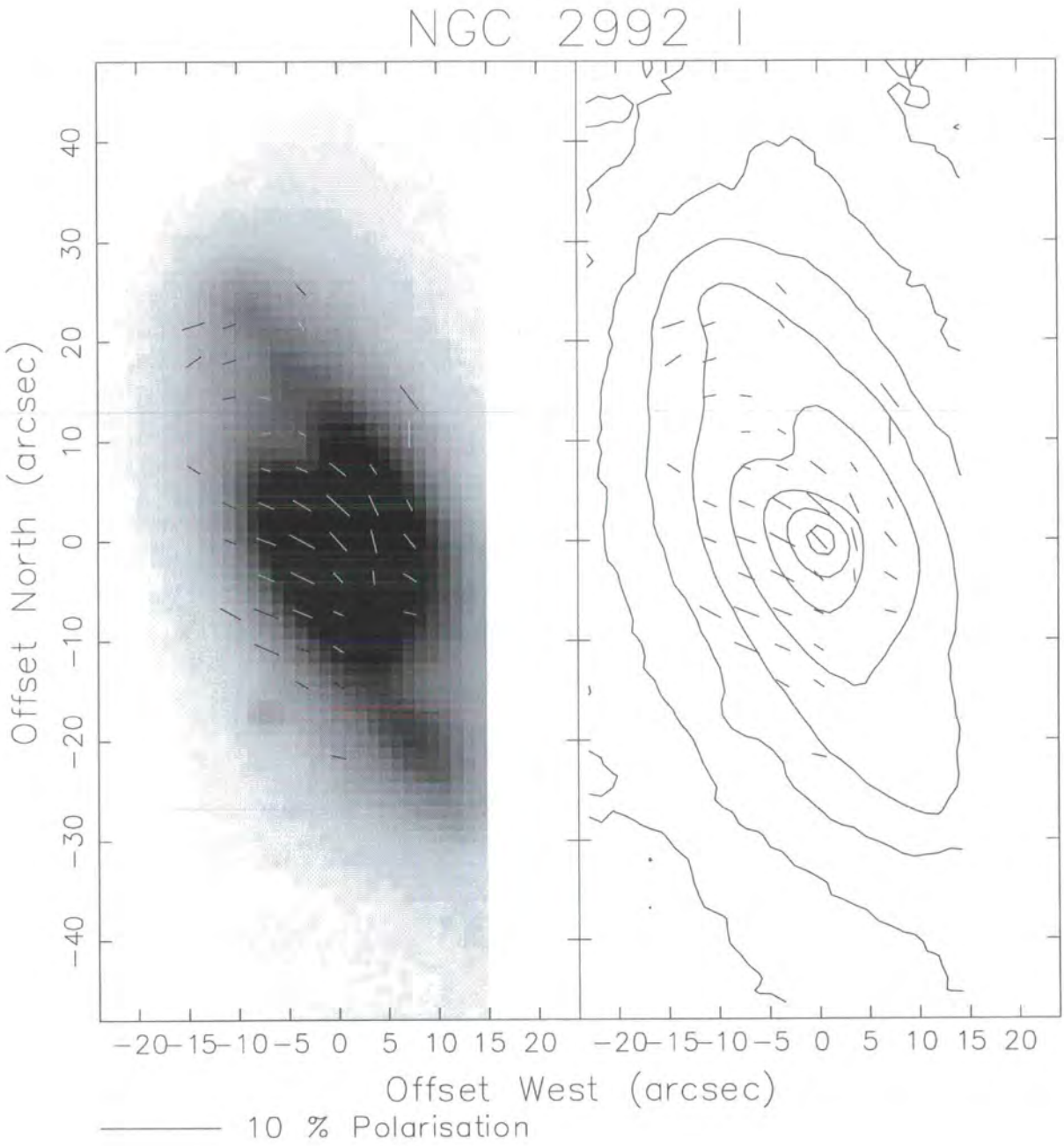

Figure 6.24: I-band greyscale and contour intensity and polarization image of NGC 2992, polarization vectors 5x5 bins, step size 3 pixels

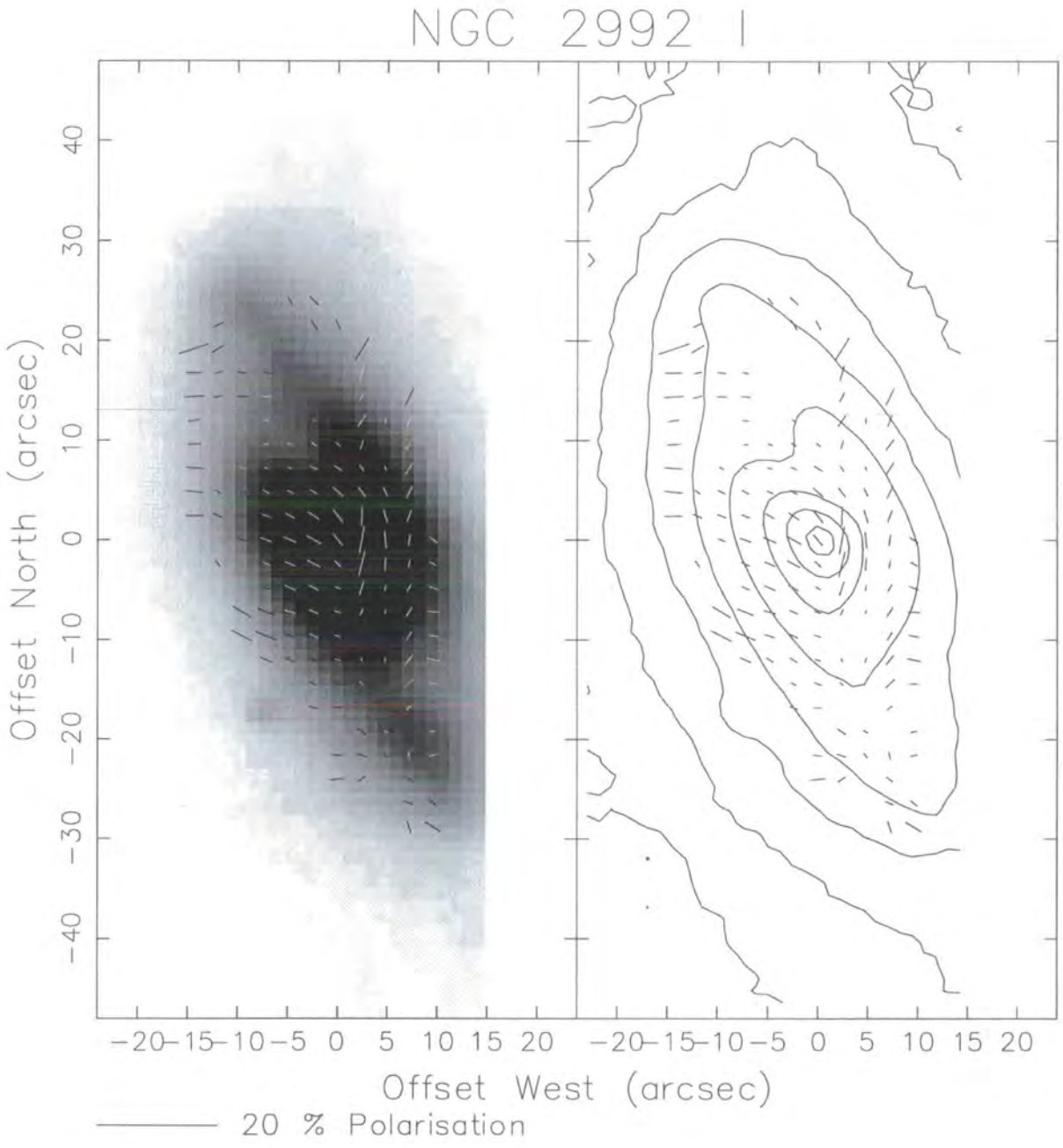

Figure 6.25: I-band greyscale and contour intensity and polarization image of NGC 2992, polarization vectors 3x3 bins, step size 2 pixels

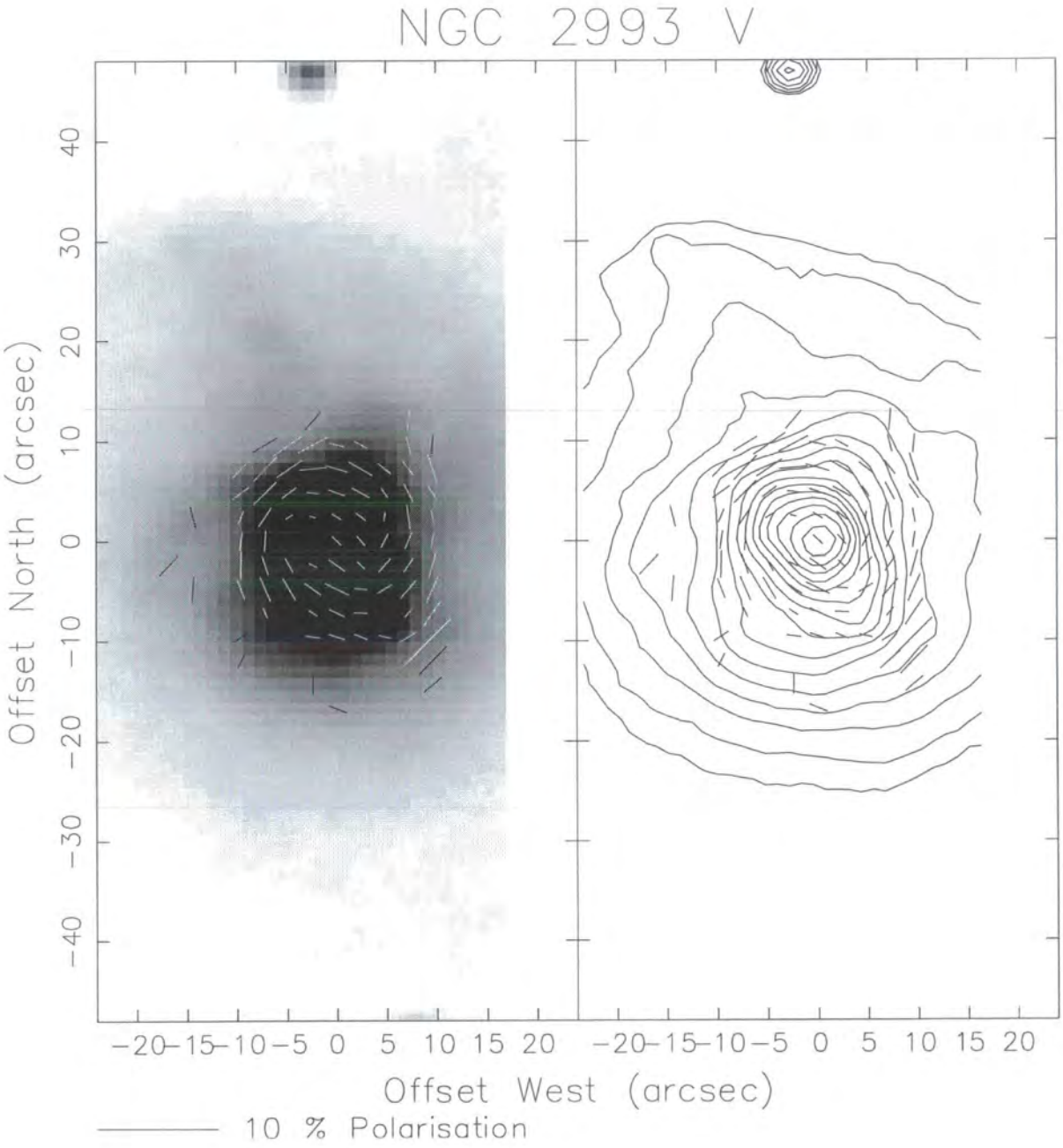

Figure 6.26: V-band greyscale and contour intensity and polarization image of NGC 2993, polarization vectors 3x3 bins, step size 2 pixels

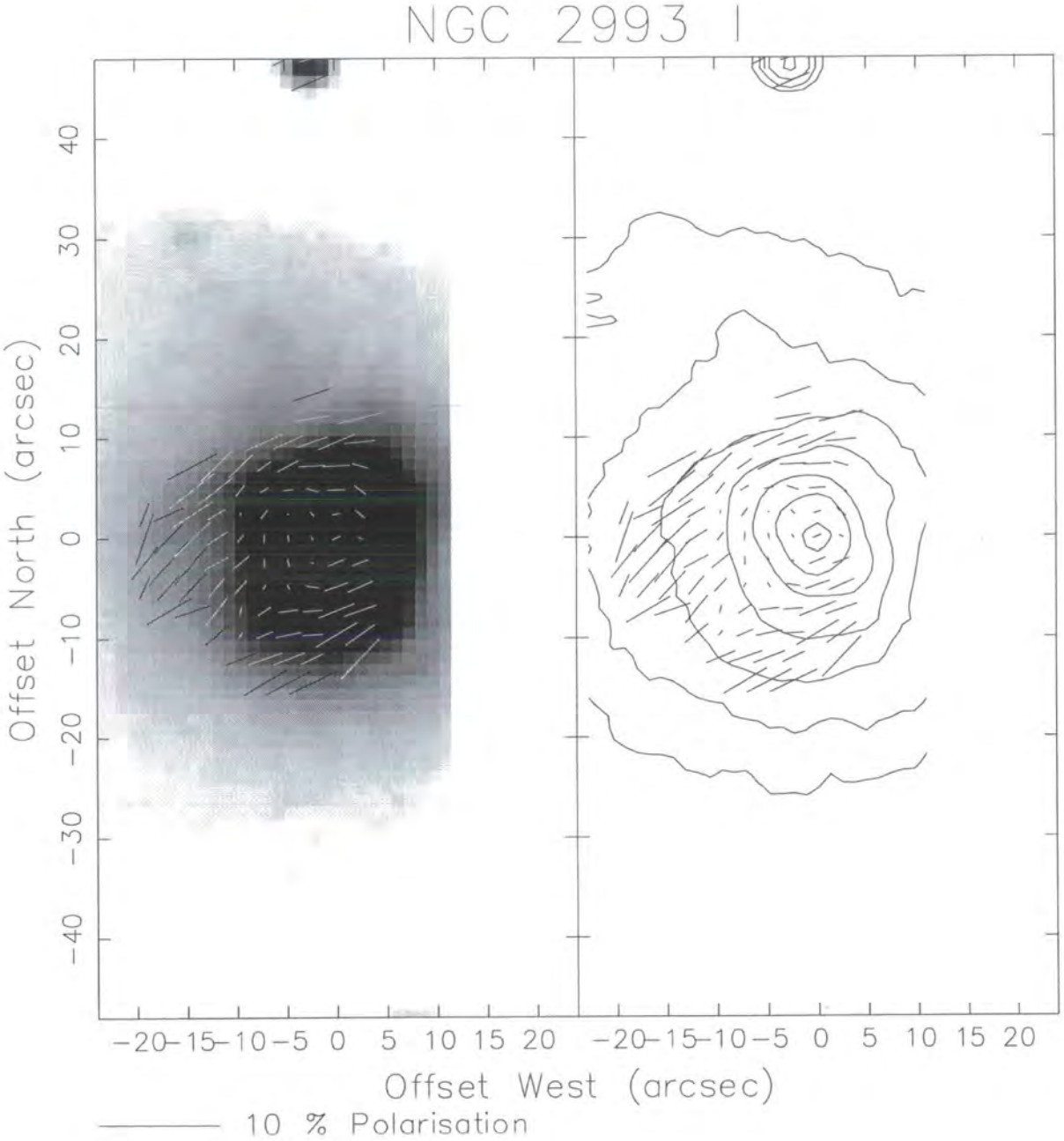

Figure 6.27: I-band greyscale and contour intensity and polarization image of NGC 2993, polarization vectors 3x3 bins, step size 2 pixels

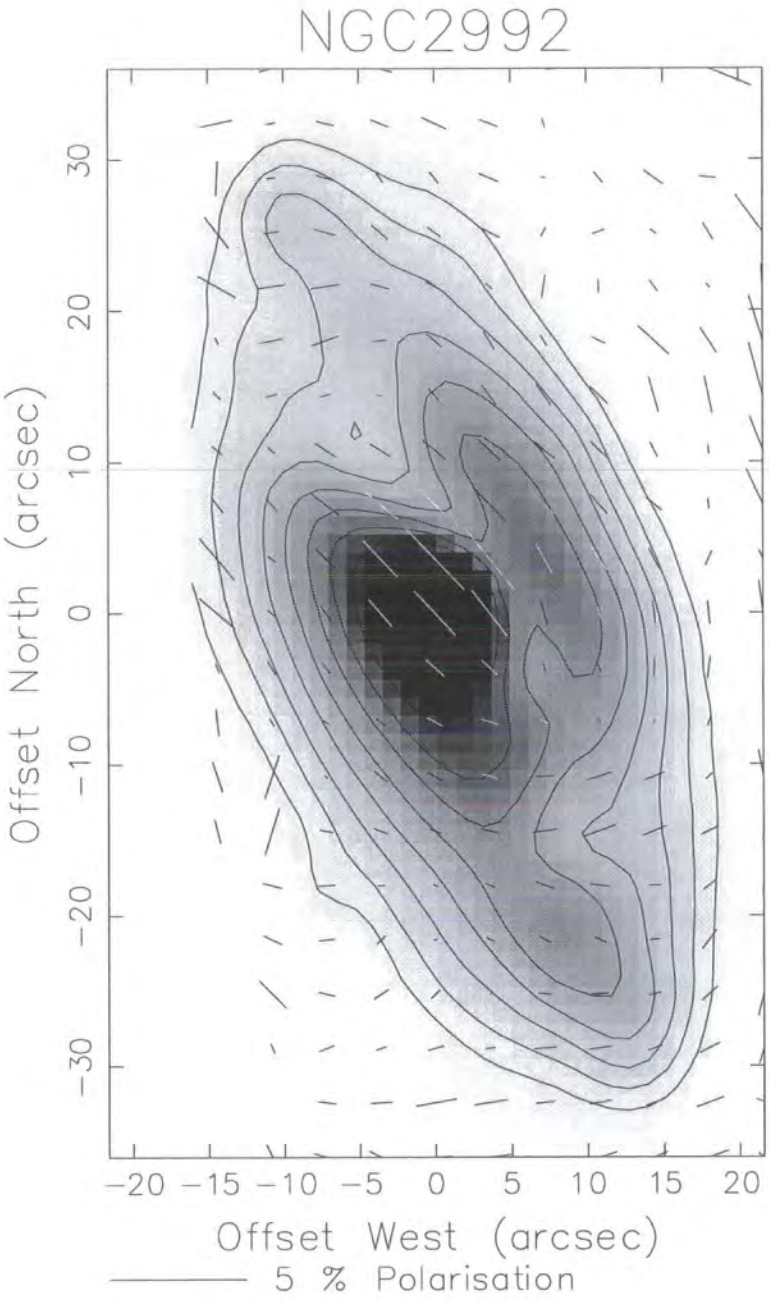

Figure 6.28: V-band greyscale and contour intensity and polarization image of NGC 2992 from SAAO observations, polarization vectors 5x5 bins, step size 3 pixels

6.5 NGC 3079

6.5.1 Introduction

NGC 3079 is an amorphous almost edge-on powerful starburst galaxy classified as SBc, with both Seyfert 2 and LINER characteristics in its nucleus (Ho 1997 [108]). It has an abnormally high concentration of CO gas in the centre (Sofue *et al.* 1992 [219]), and extensive radio emission, high emission-line velocities, a jet-like outflow along the minor axis (at approximately 80°) and X-ray activity show it is a violently active galaxy. It is dominated by the central starburst in its nucleus, but some contribution from an AGN has been detected. The large-scale emission features of flows of excited gas are evidence of a powerful 'superwind' from the nucleus, most probably energetic starburst activity. It has a companion satellite galaxy, NGC 3073, a dwarf spiral, which is being affected by the superwind outflow from NGC 3079.

Israel & Van der Werp (1998) [113] image the nucleus in J, H, and K bands, and the range of colours shows contributions from both direct and scattered stellar light and emission from hot dust and extinction gradients in the central few kiloparsecs. The central $1''$ is heavily extinguished, with a peak total extinction of $A_V \approx 6$ mag. The galaxy shows large amounts of dust irregularly distributed through its disk, a number of dust lanes, and a large reddening towards its nucleus. Garcia *et al.* (1998) [79] find its infra-red spectral energy distribution can be fitted by a three component model at temperatures of 21, 41 and 151 K, with the lowest temperature component being the most intense. The highest temperature component is thought to be from dust close to the AGN, the middle component from dust heated in the star-forming region, and the lowest temperature component due to the general galactic interstellar radiation field.

X-ray observations by Pietsch *et al.* (1998) [184] show extended emission co-incident with the optical super bubble seen on optical images, plus a component consisting of three point-like sources from the inner disk of the galaxy, and also from the halo. The X-ray luminosity is ten times higher than starburst galaxies of similar luminosity and this can be used to argue for the presence of an AGN to contribute this excess X-ray luminosity.

6.5.2 Observational notes

NGC 3079 was observed on the 27th of May 1990 with the 1 m JKT in La Palma, the Canary Islands. The Cassegrain focus with focal ratio of 15 was used, and observations

Figure 6.29: DSS intensity image of NGC 3079

were taken using a broad band V filter. For this configuration, the scale of the sky on the CCD detector of the Durham Imaging Polarimeter was 1.2 arcseconds per CCD pixel, covering a total field of approximately 11 arcminutes by 8 arcminutes. At the estimated distance of 16 Mpc, assuming $H_0 = 75$ km s^{-1} Mpc^{-1}, 1 arcsecond corresponds to approximately 78 pc. A DSS image of NGC 3079 is given in figure 6.29, which shows the total field that was mapped by the polarimeter.

Data were taken at three positions, however the third set had problems with very poor seeing of 4″, whereas the other two sets had seeing of 2″. The polarization data is therefore presented only for the two data sets with good seeing, as the third dataset was of insufficient quality to be useful. Twelve CCD frames each of 600 seconds of the object were used, together with suitable flatfield frames. The moon was down during the observations. The initial data reduction processes for this galaxy were performed by S.M. Scarrott, the subsequent refinement, some re-reduction and the plotting was done by the author of this thesis. There were problems with aligning and normalising the data sets because there were hardly any stars in the overlap regions between the frames, and because of the difference in seeing. Careful localised sky subtraction was performed for each telescope position, which improved the polarization maps, but the difficulties in alignment and normalisation are still visible as a vertical band in the maps, which was not possible to correct.

6.5.3 Image details

Figures 6.30 to 6.32 present broad V-band images of NGC 3079. The scale is in arcseconds, centred on the peak nuclear intensity of the image. The greyscale intensity is reversed, *i.e.* black representing the highest intensity. The contours of the maps are plotted in levels of magnitudes. The polarization vectors were calculated by binning the polarization data in either squares of 7 pixels by 7 pixels centred on the selected pixel, plotting the average polarization over this area, then moving on 5 pixels to select the central pixel for the next polarization vector to be calculated, or squares of 5 by 5 pixels and moving on by 3 pixels, or 3 by 3 pixels moving on by 2 pixels. The polarization vectors are plotted with signal-to-noise confidence levels of 65% or 95%. Figure 6.33 gives a greyscale and a contour map of polarized intensity, with the darker shades representing higher polarized intensity.

6.5.4 Interstellar polarization

The galactic co-ordinates (l=158°,b=48°) show that the galactic latitude is quite high, out of the plane, so interstellar polarization contamination would be expected to be small. The polarizations of the stars in the field of NGC 3079 in these observations were measured, but unfortunately the most suitable stars were in the frames with very poor variable seeing (4-5 arcseconds), so the reliability of these measurements is questionable. Out of measurements of four stars, all gave completely different, low polarizations (less than 0.6%), hence it was not possible to determine whether there is a significant ISP contribution or not. Attempts were also made to measure the polarization of stars with the other data sets with good seeing, but the stars in the field were too faint for meaningful polarization data to be calculated.

6.5.5 Results: V-band

Figures 6.30 and 6.31 present a wide field view of NGC 3079, figure 6.32 presents the central regions. There is a general alignment of polarization vectors parallel to the major dust lane in the central regions indicating preferential extinction, and the vectors become more nearly perpendicular at about 40″ north and south of the centre. This is typical of galaxies with dust lanes, the feature is very similar to that seen in the polarization maps of NGC 2992 presented in the previous section.

The polarization vector patterns, seen best in the right-hand map of figure 6.31, clearly

Table 6.11: V-band nuclear aperture polarimetry of NGC 3079 (uncorrected)

Aperture (arcsec)	Aperture (pixels)	Polarization %	Position Angle
2	1.7	1.4% ± 0.6%	6°± 13°
2.5	2.1	1.4% ± 0.6%	6°± 12°
3	2.5	1.3% ± 0.5%	6°± 11°
4	3.3	1.3% ± 0.4%	5°± 10°
5	4.0	1.2% ± 0.4%	3°± 9°
6	4.7	1.2% ± 0.4%	1°± 9°

shows signs of centro-symmetry about several localized points in the galaxy, as well as around the extended nuclear area out to about 30″ north and south of the centre. The localised patterns are most probably due to clusters of bright stars, *i.e.* star-forming regions, located deep in the dust of the disk of the host galaxy, so that the dust scatters and polarizes their light into a centro-symmetric pattern.

The region containing the major axis outflow, along a position angle of approximately 80°east of the nucleus, unfortunately is close to the edge of the sky coverage in the data, so it is not possible to image the whole region well. The region close to the nucleus is polarized parallel to the dust lane, and due east for about 10-15 arcseconds the polarization is lower but still parallel to the dust lane. The polarized intensity flux map in figure 6.33 shows the main polarized flux emission to be extended over the nucleus, extending north west, south west and also due east out to 10 arcseconds.

Aperture polarimetry of the nucleus is given in table 6.11, which shows that the nucleus is polarized at a level of 1.3% at 6° over a 3″ diameter aperture. This is a fairly low polarization, typical of many Seyfert nuclei, however the light in the nuclear region is polarised by the dust lane of the galaxy, and any contribution made by a Seyfert nucleus cannot be distinguished. A map of polarized flux intensity was also made, given in figure 6.33, which shows the highest polarized flux in the galaxy to be in the central few arcseconds, coincident with the peak total intensity, and also elevated levels in a few of the bright spots in the galaxy, presumably bright star-forming regions. The polarization characteristics of the nuclear region are dominated by dust in the host galaxy rather than the Seyfert nucleus. The nuclear polarization is parallel to the polarization of the central dust lane and approximately of the same level, so it is not possible to tell whether the Seyfert nucleus is intrinsically polarized or not, but if it is it cannot be a highly polarized and large component, otherwise the central polarization vector would be noticeably different to the surrounding ones.

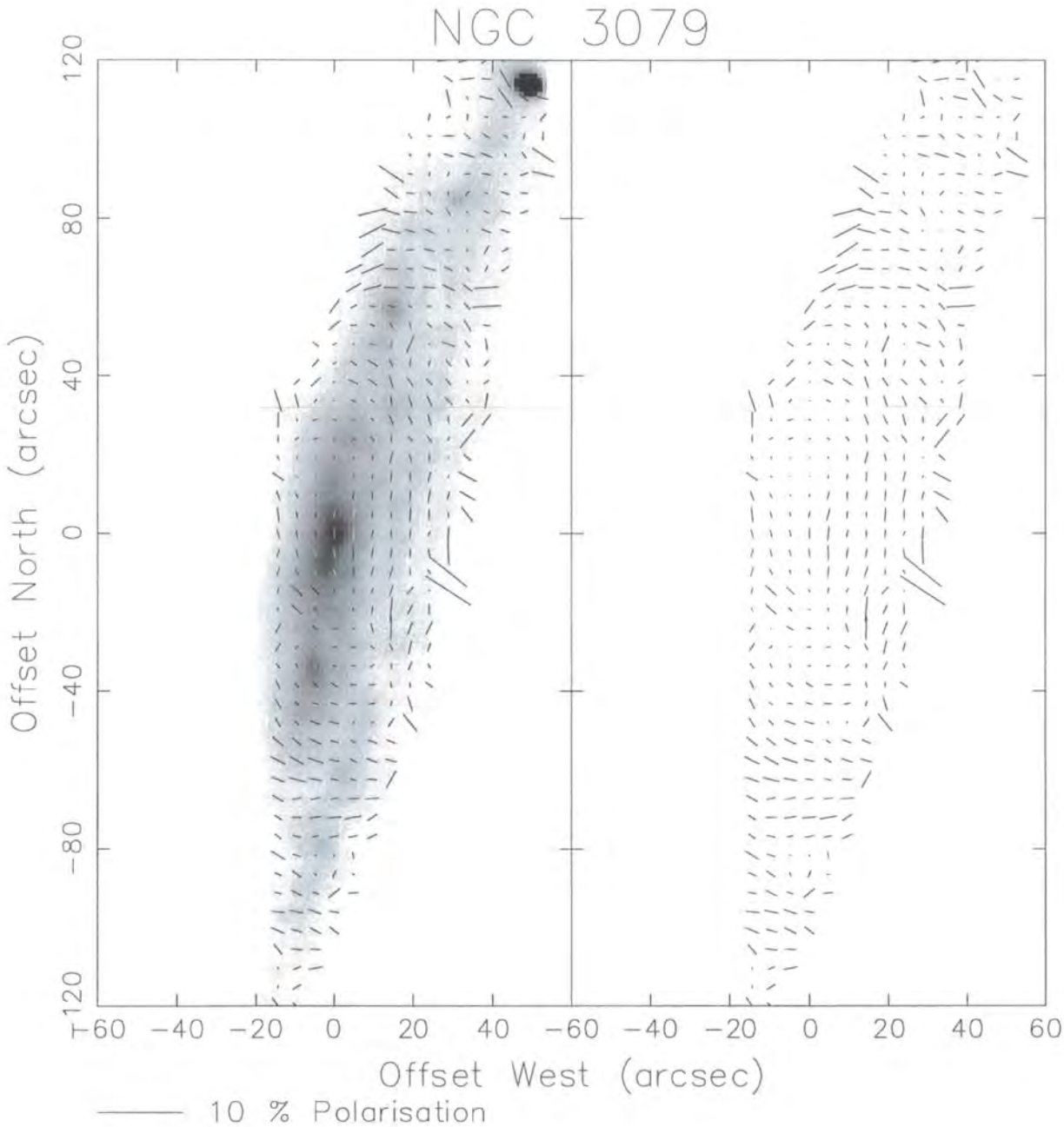

Figure 6.30: V-band greyscale total intensity and polarization images of NGC 3079, polarization vectors 7x7 bins, step size 5 pixels

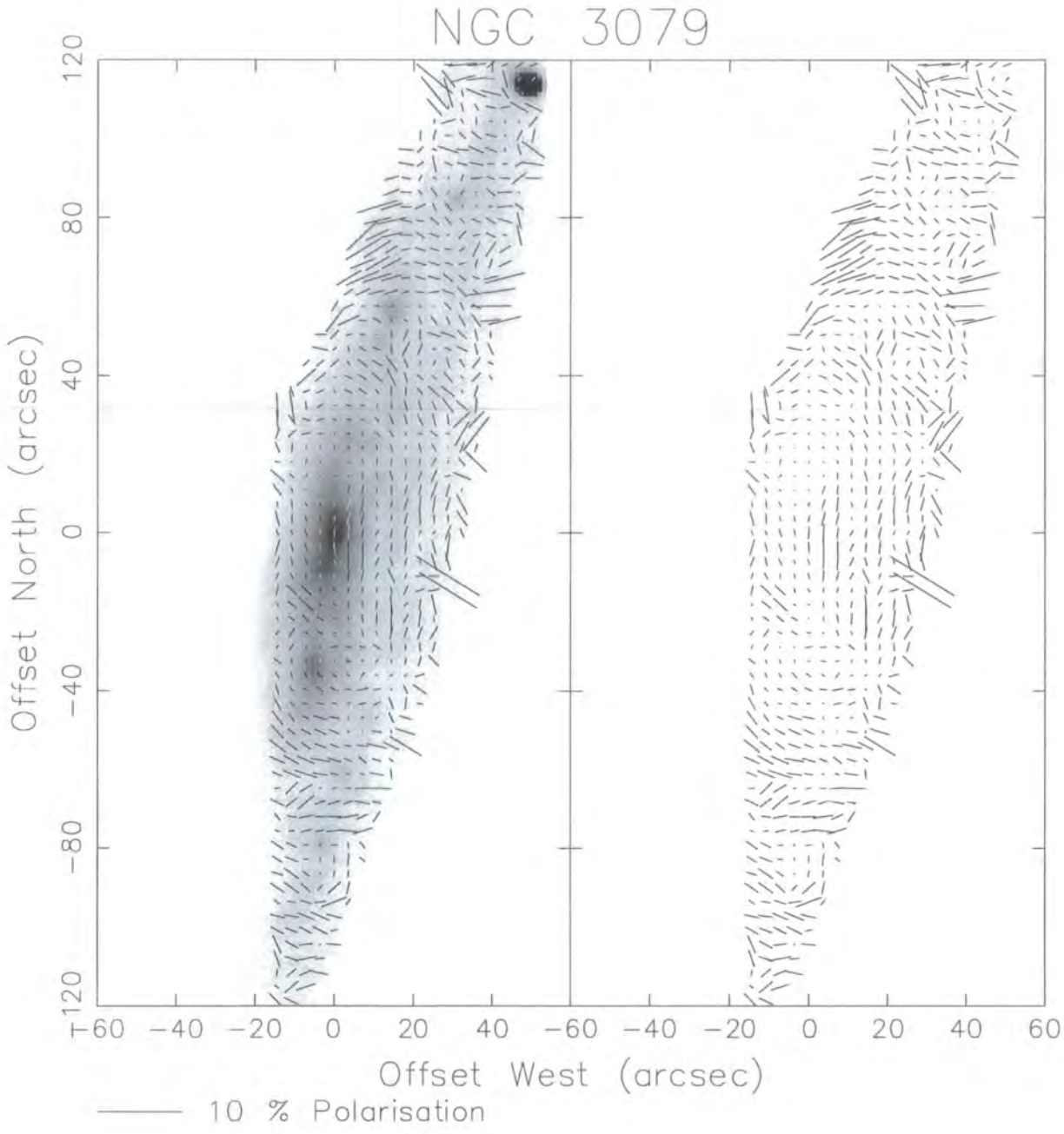

Figure 6.31: V-band greyscale total intensity and polarization image of NGC 3079, polarization vectors 5x5 bins, step size 3 pixels

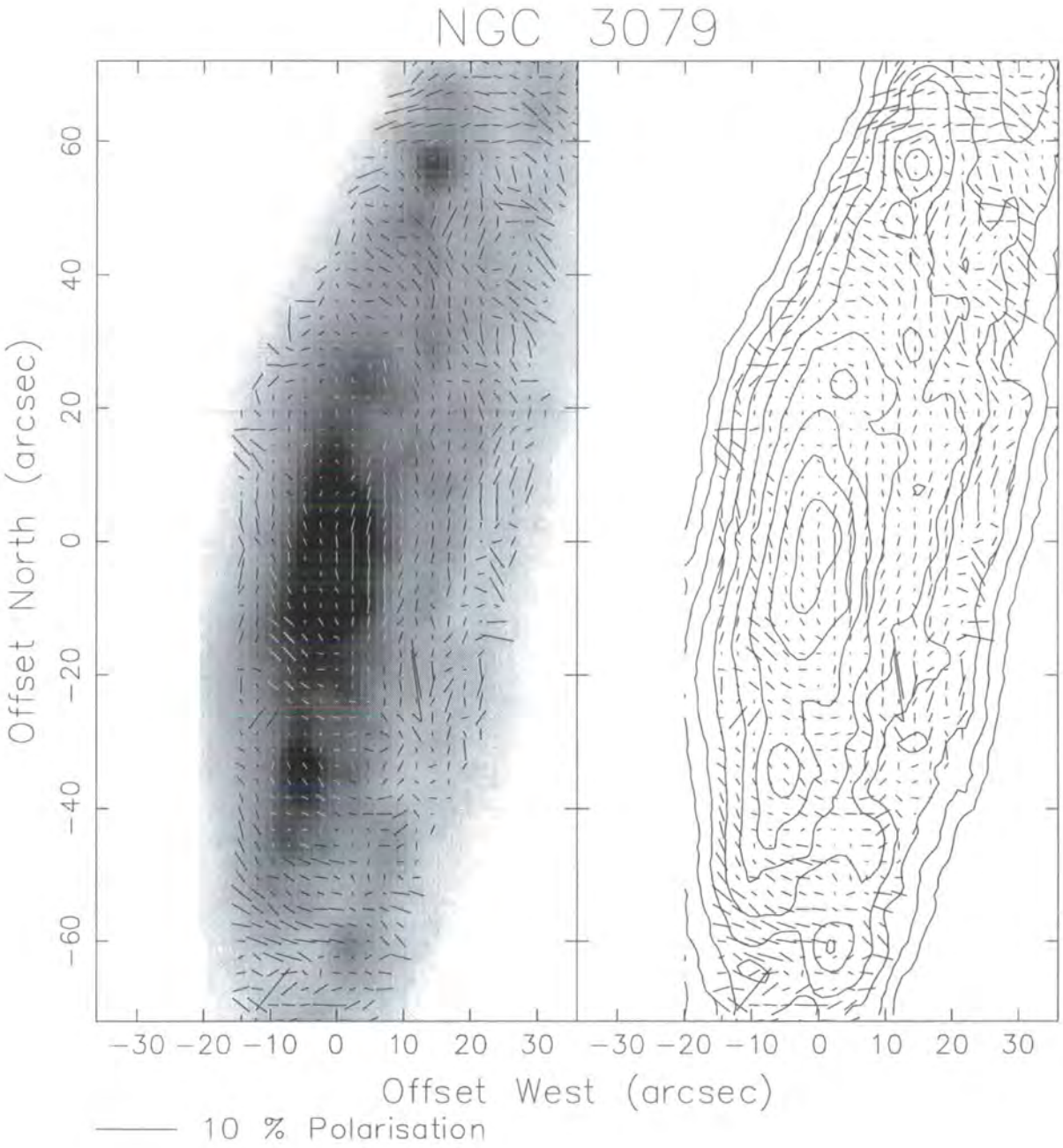

Figure 6.32: V-band greyscale and contour total intensity and polarization image of the nucleus of NGC 3079, polarization vectors 3x3 bins, step size 2 pixels

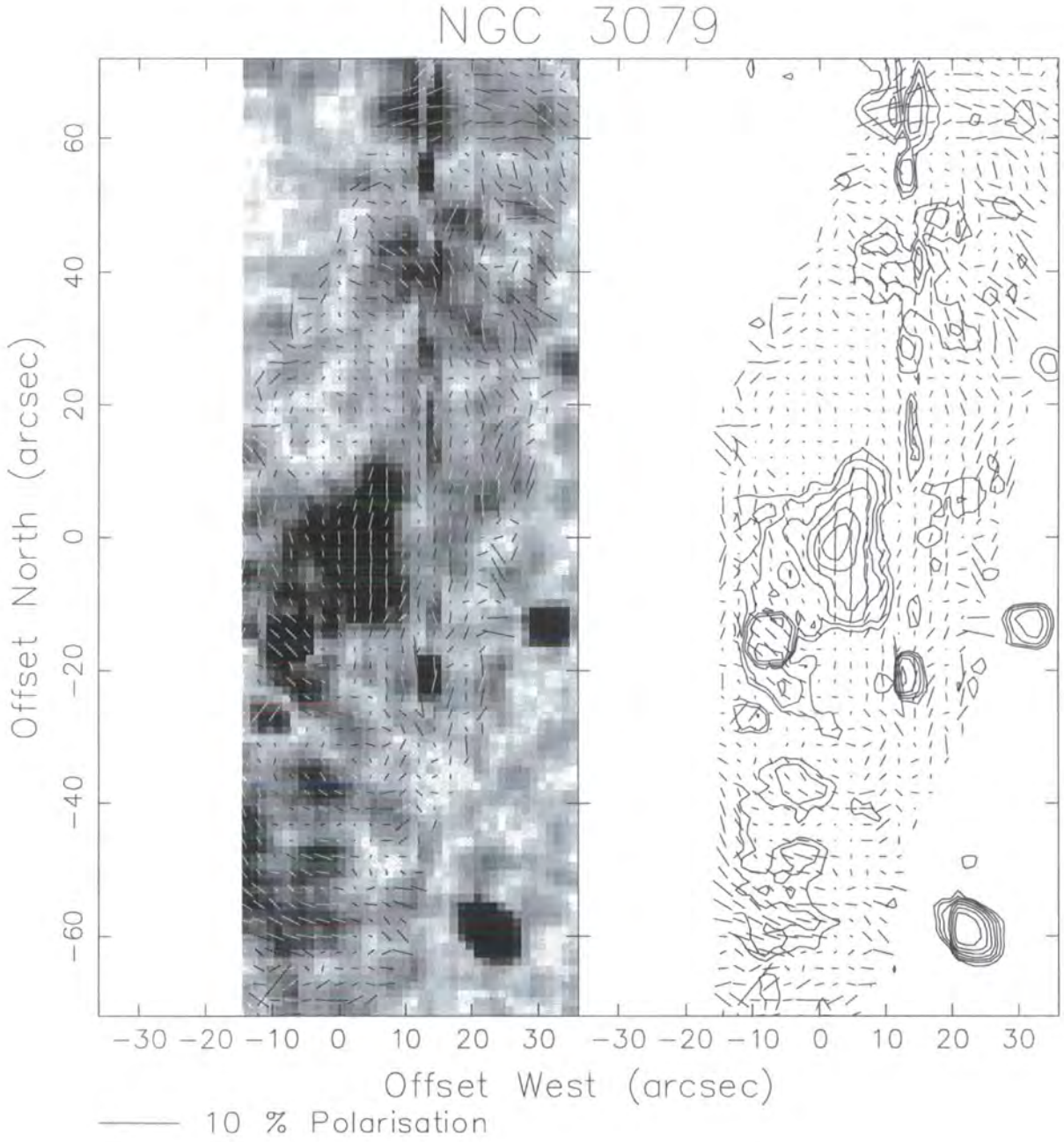

Figure 6.33: V-band greyscale and contour polarized intensity image of the nucleus of NGC 3079, polarization vectors 3x3 bins, step size 2 pixels

Chapter 7

Summary and conclusions

In the previous two chapters, imaging polarimetric maps at visible wavebands of three face-on and four edge-on nearby Seyfert galaxies were presented and discussed. The resolution of these images, in most cases, allows some investigation of the polarization phenomena in the circumnuclear and nuclear Seyfert regions as well as the polarization processes occurring over the host galaxy on a larger scale. When summarising the results, the properties of the Seyfert-host galaxy dominance in polarized light are seen to form a progression in the observed images. Markarian 348 and 573, in the observations of this thesis, all have relatively faint small host galaxies, whereas NGC 2992, NGC 5506 all have larger, brighter, well-imaged host galaxies, and NGC 3079 is completely dominated by its powerful starburst nucleus.

In this chapter, the observational results are summarised and discussed briefly with previous studies of other Seyferts and their host galaxies. They are discussed in the context of what support they can provide in terms of the unified scheme for Seyfert galaxies, and also how they compare in relation to published results of qualitative and quantitative numerical modelling of polarization processes, both in the spiral host galaxies and their Seyfert nuclei. Then, in conclusion, the limitations of the scope of the present thesis are considered, and suggestions are made with respect to possible future observations and analysis that would be either complementary to, or would build upon or extend this study.

7.1 Modelling of the Seyfert nuclear polarization

7.1.1 The Unified scheme Seyfert model

To summarize, the standard unified scheme of AGN consists of a compact featureless continuum source from an accretion disk system and compact broad-line emission region, surrounded by a geometrically and optically thick torus, then by a somewhat more extended narrow-line region along the polar axis of the torus. An observer's line of sight along the polar regions of the torus therefore sees emission directly from all the different regions, giving a Seyfert 1 appearance, whereas a line of sight through the torus means that the direct broad-line and optical-UV continuum emission are obscured, giving a Seyfert 2 appearance. This is shown in schematically in figure 1.3 in chapter 1.

Warm dusty material around the NLR can also scatter the otherwise hidden optical-UV continuum and broad-line emission into the line of sight of Seyfert 2 views, and thus this broad-line and continuum emission be may be seen in polarized light. Only some Seyferts however, show polarized broad-lines, and these have been noted to be Seyferts with significantly bluer colours (Heisler, Lumsden & Bailey 1997) [103]. This has been interpreted as an effect of the scattering material (which scatters the nuclear continuum and broad-lines into view), having only a small spatial extent, so that at high inclinations, this scattering region as well as the BLR is obscured. Therefore, the only Seyferts 2s that would have scattered broad lines, would be those that are inclined just slightly beyond the half-opening angle of the torus, *i.e.* intermediate in orientation.

7.1.2 Numerical modelling of polarization features

The first models of optical polarization from Seyferts were of polarization by electron atmospheres of the accretion disk. The simplest case of a geometrically thin disk with electron scattering atmosphere, in the form of an infinite slab by Chandreskhar (1960) predicted polarization levels of up to 11.7% edge-on (with the vectors aligned in the plane of the slab), which were much higher than the levels actually observed, for more face-on viewing the polarization level is much lower. Subsequent more realistic models, *e.g.* thick disks, wedge shaped disks, electron and dust scattering, predicted lower levels of a few percent polarization for most inclinations. Laor, Netzer & Piran (1990) [135] calculated that the opacity (due to photoelectric absorption) of a thin accretion disk significantly reduces the maximum expected polarization for lower frequencies of radiation, and general relativistic effects reduce the polarization of higher frequency radiation. This reduction

of the maximum polarization up to a few percent at even edge-one orientations is more consistent with the polarization observations.

In 1991, Miller, Goodrich & Mathews [158] modelled the polarization using scattering by a cloud of warm electrons in a cone geometry, and applied this modelling to the parameters of the archetypal Seyfert 2, NGC 1068. The polarization of the scattered optical continuum and broad-line source radiation was perpendicular to the axis of the torus and the ionization cone as seen in observations of NGC 1068.

Considering both the IR as well as optical spectrum for a typical Seyfert one, Young *et al.* (1995) [271] modelled the scattering of a typical Seyfert 1 radiation spectra in a Seyfert 2 model geometry of the kind applicable to NGC 1068. As well as electron scattering from a scattering cone, they found that an additional polarization component is required in the near-IR to produce the observed features. This component is modelled by dichroic absorption of the near-IR radiation by dust grains aligned in the Seyfert torus, and is successful in modelling the polarization properties of Seyfert 2 nuclei. The measured polarizations of Seyfert 2 scattered BLRs and central continuum sources generally support this model since they are usually aligned perpendicular to the ionization cone axis and torus axis, as predicted.

This scattering model of Young predicts that as the object is viewed more pole-on *i.e.* more type 1, then the polarization will be reduced, but it will still be aligned perpendicular to the ionization cone axis. However, studies of Seyfert 1s show that the polarizations of the BLR and central continua tend to be parallel rather than perpendicular to the ionization cone or radio axis, Antonucci (1984) [11], Brindle *et al.* (1990) [36], (as in type 2 Seyferts). To account for this, Goodrich & Miller (1994) proposed a qualitative model of scattering in an optically thin disk which reproduces this flip in polarization angle, however when applied numerically to actual geometries, the simple optically thin models can predict very high polarization $\leq$50% levels, which are certainly not observed. For Seyfert 2s the disk is optically thick.

An alternative model was developed by Kartje (1995) [117], who calculated the polarization of the continuum by multiple scattering in a stratified-density disk-driven wind with electron and dust scattering, and dichroic absorption. This model reproduced the observed features, including this change of alignment, and predicted polarizations of the order of $\leq$ 30% for tori and $\leq$ 20% which are closer to the intrinsic polarizations of Seyferts that are calculated by correcting the measured polarizations for dilution by the surrounding nuclear stellar flux, in recent studies including this thesis. A schematic diagram of these two models of Kartje for different line-of sights, is given in figure 7.1.

Young (2000) [270] also further developed the scattering model of Young (1995) [271],

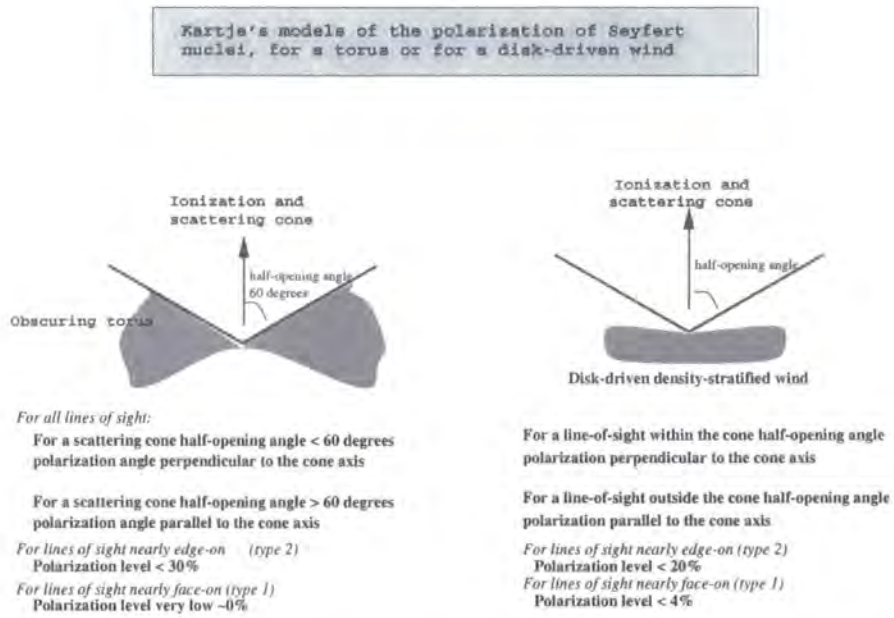

Figure 7.1: Model of expected Seyfert 1 features for the torus and wind models of Kartje (1995)

including 3 main components in the model, an extended scattering cone with bulk motion, the dusty molecular torus (where scattering and dichroic absorption can take place) and a compact scattering region (to allow for polarization variability observed in some Seyfert 1s), creating a model valid for both Seyfert 1s and Seyfert 2s. This model was then successfully applied to the Seyfert 1.2, Markarian 509, including accommodating the variable polarization. Since scattering regions are apparently detected in several Seyferts in the observations of this thesis, it would be interesting to apply this scattering model of Young (2000) to the geometry of these objects, with the geometrical information on the scattering regions detected to compare the levels and patterns of polarization that would be modelled from this. A schematic diagram of this model is given in figure 7.2 with a description of the components. If the host galaxy is face-on, it shouldn't affect the polarization, however edge-on galaxies can contribute a component of polarization parallel to the major axis by dichroic transmission.

Building on earlier work with thin disc single scattering modelling by Martin (1985) [66], more advanced polarization modelling of AGN radiation using a Monte-Carlo radiative approach for both electron and dust scattering (Thomson, Rayleigh and Lie scattering) was performed by Wolf & Henning (1999) [265], who include both point-like and extended sources, single and multiple scattering. They found it can explain the observed wavelength dependence on the polarization where the AGN radiation has dust scattering in optically thin cones, where the extra electrons enhances the polarization level, and the torus geometry and density also affect the polarization level.

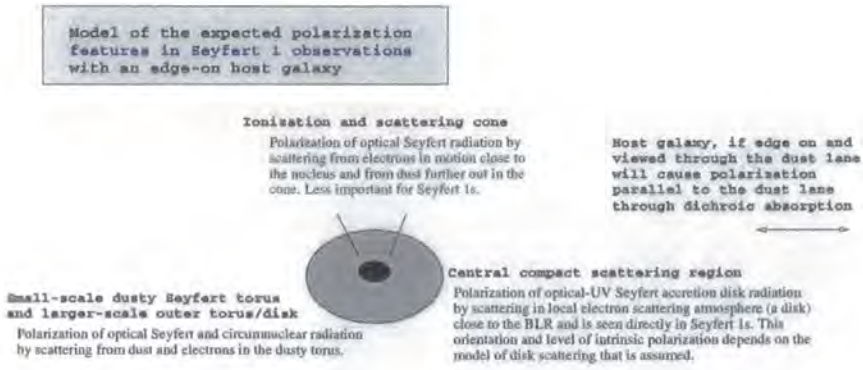

Figure 7.2: Model of expected Seyfert 1 features with host galaxy

7.2 Modelling of the host galaxy polarization

In spiral galaxies, Monte-Carlo models by Bianchi (1996) [29] give scattering polarization levels in spiral galaxies of a few percent, with a centro-symmetric pattern for face-on viewing, and vectors perpendicular to the major axis of the galaxy for higher inclinations. Dichroic polarization gives levels of a few percent with the vectors aligned parallel to the magnetic field direction projected onto the plane of the sky, Jones *et al.* (1992) [115], *i.e.* a spiral pattern for spiral galaxies. The results of the spiral galaxies in this thesis support these basic findings as regards large-scale overall polarization pattern levels and orientation of polarization, in particular the spiral pattern and dust lane features, however the detailed polarization structure they exhibit is not reproduced in these simple models, because for example, there are bright star forming knots in the spiral arms with localised null points and centro-symmetry from scattering, and minor scale outflows outside of the disk, perhaps the origin of some polarization by scattering, for which provision is not included in the models. Also for example NGC 3079 is a powerful starburst galaxy with a very disturbed morphology, so it would be expected that the polarization patterns for a normal spiral galaxy be disturbed.

Scattering calculations by Bianchi *et al.* (1996) [29] suggest that polarization measurements may help determine the orientation of a galaxy with respect to the sky plane. For a galaxy inclined at 20° (similar to that of NGC 1566 at 27°) with a bulge luminosity half of the total luminosity, where the dominant polarization mechanism is scattering from interstellar dust in the Mie limit. Bianchi *et al.* (1996) [29] calculate that the polarization along the minor axis will differ by a factor of two between the near and far sides (as has been done for NGC 6946 by Fendt 1998). For NGC 1566, if there is scattering it will be present in the central regions illuminated by the nucleus. Therefore the average polarization along the minor axis (taken to be at position angle 131°, Pence *et al.* 1990 [179]) was measured either side of the galaxy. For the V-band measurements of NGC

1566, polarization levels in the south-east range from 1 to 3 times larger than those in the north-west, an average of 1.5 times as large, calculated from 625 pixels on each side along the minor axis and averaged over six different positions within the 30 arcseconds from the nucleus. This suggests that the south-east is the side of the galaxy further away from us, which is in accordance with the kinematic studies of Pence *et al.* (1990), and demonstrates an additional use of polarization data for a disk galaxy.

7.3 Previous studies of other Seyfert nuclei

Large surveys have shown Seyferts to generally have very low optical polarizations of less than 1%, Martin *et al.* (1983) [148], Brindle (1990) [36], Kay (1994) [119] and Grupe (1998) [91]. These studies have shown that in both types there is a tendency for the polarization vector to be aligned with the major axis or dust lane of the host galaxy. This would be expected due to dichroic polarization in the disk and dust lane of the host galaxy, which would align the polarization parallel to the dust-lane or major axis, and is independent of any Seyfert nucleus characteristic. The optical polarization of the Seyfert 2s generally tends to be perpendicular to the nuclear radio and or high-excitation emission-line axis, whereas in Seyfert 1s, it is more likely to be aligned parallel to the radio and emission-line axis, Antonucci (1984), Brindle *et al.* (1990).

An analysis of a large survey of Seyferts with colour maps by Mulchaey *et al.* (1996) [163], finds that 40% of Seyfert galaxies of all inclinations (but almost exclusively Seyfert 2s) show a red excess around the nucleus, consistent with reddening by approximately 100 parsec scale red tori or disks. Size indications of the Seyfert nucleus torus are more on the scale of a few parsecs, so these red excess features map out a torus or disk on a slightly larger scale than the actual Seyfert torus, however, an outer torus or disk aligned and associated with the smaller Seyfert nuclear torus is suggested as a plausible explanation. This red feature may be polarized due to dichroic transmission of some of the near-IR radiation through the magnetic alignment of dust grains in the larger scale dusty torus or disk and through the obscuring torus in Seyferts. They also find extended blue features in some Seyfert 2 galaxies, which were attributed to either scattered nuclear light or shocks in the ionized gas. Diagrams of this model of Seyfert 2 nuclei are given in figures 7.3 (a face-on host galaxy would not be expected to contribute a polarization component, so the Seyfert polarization should be unaffected), and 7.4 (with an edge-on host galaxy aligned with its minor axis parallel to that of the ionization and radio cones), and 7.5 (with an edge-on galaxy not aligned with the torus). The diagrams show these features visually, in terms of their expected qualitative polarization properties and in

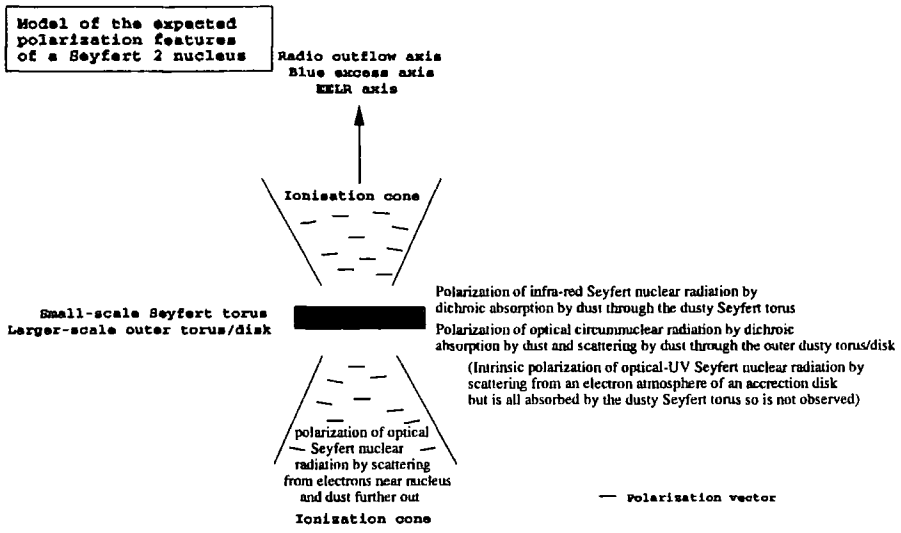

Figure 7.3: Model of expected Seyfert 2 features for the Unified scheme with a face-on host galaxy

relation to the host galaxy for the case of edge-on hosts. In face-on hosts, unless there is a great deal of dust and scattering and star-formation activity, normally the host galaxy shouldn't affect the polarization measurements of the nucleus, *e.g.* there may be a large scale spiral polarization pattern, but not in reaching in as far as the nucleus. Therefore, in addition to the much larger scale polarization patterns produced in the host galaxy, the galaxies mapped for this thesis were examined for evidence of polarization that could be due to these processes, *i.e.* the nuclear Seyfert light polarized by scattering from the circumnuclear environment corresponding to blue regions. The nuclei of the host galaxies in all cases can dilute the observed Seyfert polarization if they have a strong nuclear (unpolarized) flux.

In NGC 1068, a well-studied Seyfert 2 galaxy, the existence of dusty regions scattering nuclear light by a cone of electron-scatterers is observed by Miller & Goodrich & Mathews (1991) [158]. Spectro-polarimetry studies by Inglis *et al.* (1995) [112] around the ionization cone of NGC 1068 show that the polarized broad lines are visible only within or just outside the ionization cone, showing their view is obscured by presumably a nuclear torus perpendicular to the cone. The scattering in the nuclear region is primarily electron scattering, but further out in the cone, dust scattering also become significant. Extensions of length 20 parsecs along the expected orientation of the Seyfert torus in the near-IR images by Rouan *et al.* (1998) [195] also support the interpretation of a Seyfert torus and larger-scale torus or disk perpendicular to the radio and emission-line axes.

Spectro-polarimetry of NGC 4258 by Barth *et al.* (1999) [20], where there is known to be an edge-on rotating disk of molecular gas surrounding the Seyfert torus, reveals strongly polarized narrow emission lines from a barely resolved core, from 1% to 13% oriented

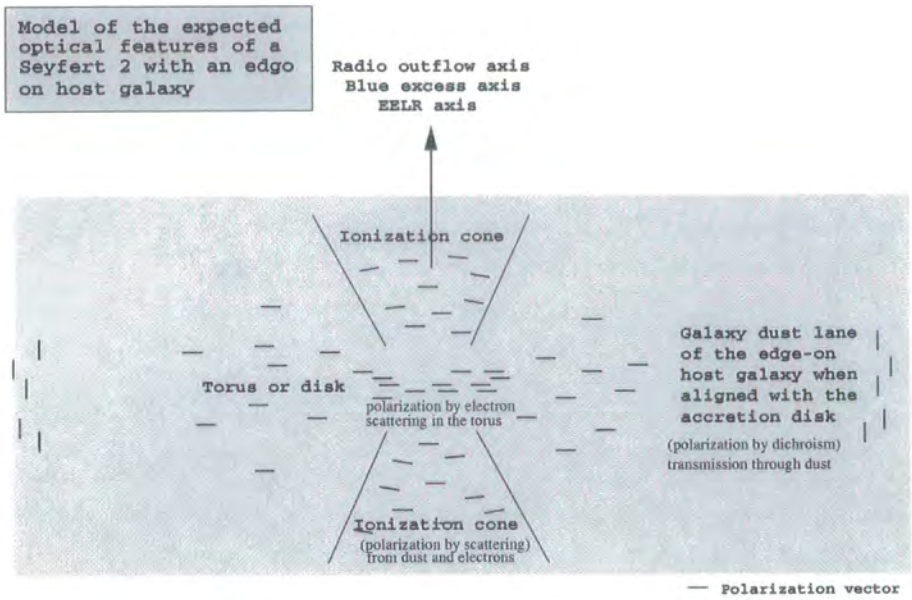

Figure 7.4: Model of expected Seyfert 2 features with edge-on host galaxy aligned with the Seyfert torus

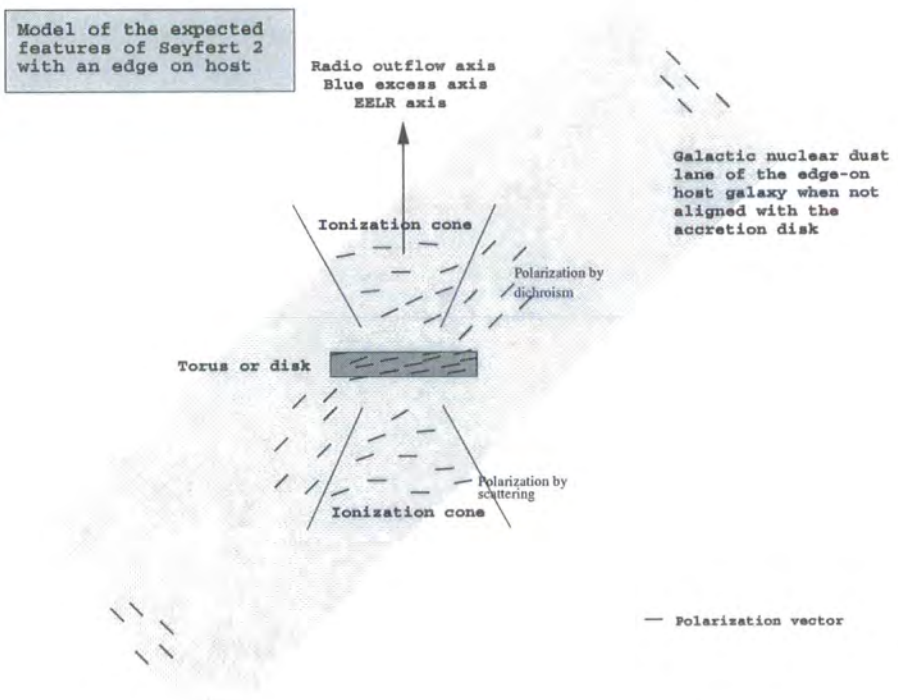

Figure 7.5: Model of expected Seyfert 2 features with edge-on host galaxy not aligned with the Seyfert torus

parallel to the projected plane of the molecular disk. The most likely explanation of this polarization is a obscuring torus or disk which is strongly stratified in density surrounding the NLR.

HST imaging polarimetry of NGC 5728 by Capetti *et al.* (1996) [40] shows evidence of polarization through dichroic transmission through dust grains in the kiloparsec scale bar and the inner bar with the angle of polarization parallel with the bars, but after subtraction of this dichroic contribution, a centro-symmetric pattern indicated the hidden nucleus. The extended polarized flux follows the emission line cones, but covers a larger extent with a wider opening cone. This implies that either there is a transition region in the torus which blocks the ionizing flux, but allows through at least some UV, or that the line emitting material does not fill all the region illuminated by the ionizing flux from the nucleus.

7.4 Summary of the observations

In the observed set of Seyfert galaxies, there are three comparatively 'strong' Seyfert 2 sources, *i.e.* where the host galaxy is fairly small or low power so that the Seyfert nuclear polarization is not completely dominated by the host galaxy output. Of these, Markarian 348 and 573 are in face-on host galaxies, and Markarian 3 also is in a small host galaxy, but the galaxy is edge-on, so there is more contamination of the nuclear polarization as it passes through the width of the edge-on galaxy. All three nuclei have a BLR visible only in polarized light (although only tentatively detected for Markarian 573). They are all fairly similar in terms of magnitude and distance away, with Markarian 348 being somewhat smaller, even after their distance is taken into account. They are about three to four times further away than the group of galaxies with the prominent hosts.

The next two galaxies, NGC 2992 and NGC 5506 are intermediate in dominance, and harbour either a Seyfert 2 or 1.9 nucleus - the classification is ambiguous, and both nuclei also contain star-forming activity, but not to levels found in starbursting galaxies. In the last two galaxies, the galaxy totally dominates any possible Seyfert polarization. NGC 3079 harbours a Seyfert 2 nucleus, NGC 1566 has a Seyfert 1 or 1.9 nucleus. NGC 3079 is much larger, brighter and closer than the other galaxies and is a very powerful starburst galaxy. NGC 1566 also has star-forming activity, but not to levels found in starbursting galaxies. They are also well resolved as galaxies for these observations, thus are good candidates for investigating the polarization features of the galaxies. The differences in the parameters such as distance and size have implications when comparing the results

between different galaxies and their Seyfert nuclei, although as a group together they are fairly similar in terms of distance away.

7.4.1 Markarian 573 (Face-on host galaxy)

Markarian 573 hosts a Seyfert 2 with tentatively detected polarized broad-lines, and like Markarian 348, it also has evidence to support the Seyfert model of a dusty torus and outflow. It has alignment of the nuclear emission-line region with the nuclear radio-optical jet along an axis approximately 125° to 140° , and a biconical ionization emission structure along position angle 120° aligned with extended nuclear radio emission and an H_α bar signalling a nuclear outflow. This is perpendicular to a parsec scale red excess structure across the nucleus at 45°, which has been attributed to the Seyfert dusty torus. The polarization observations support this by the angle of the nuclear polarization (after ISP correction) being at 45°, which is parallel to the observed red excess structure, indicating scattered nuclear light.

There is also blue excess along the emission-line axis implying scattered nuclear light from the bicone. The polarization observations support this by showing clear higher polarized flux and higher polarization in the regions that spatially correspond to the blue excesses, which are extended along the emission-line axis. This is further supported by the wavelength dependence of the polarization observations. At B-band the images show an enhanced polarization in these regions, *i.e.* the blue light is contributing most of the polarization, and whereas the R-band images do not show any significant polarization near the nucleus. Figures 7.6 and 7.7 show the polarization map with the diagram of the emission regions to show the correspondence between the features and the polarization patterns and alignments.

7.4.2 Markarian 348 (Face-on host galaxy)

Markarian 348 hosts a Seyfert 2 nucleus with scattered broad lines visible in polarized emission. It has clear alignment of the nuclear radio, optical line emission, nuclear radio jet and extended emission line structures along an axis approximately 165° to 170°, which is approximately perpendicular to the nuclear IR elongation of 2 and 5 arcseconds along an axis of 90°, attributed to emission from host galaxy dust from a large scale torus and stellar flux. The optical polarization in the central few arcseconds of the nucleus measured in this thesis, after correction for ISP, has a position angle of approximately 83° (or 75° depending on which ISP value is used). This is well aligned parallel to the IR elongation

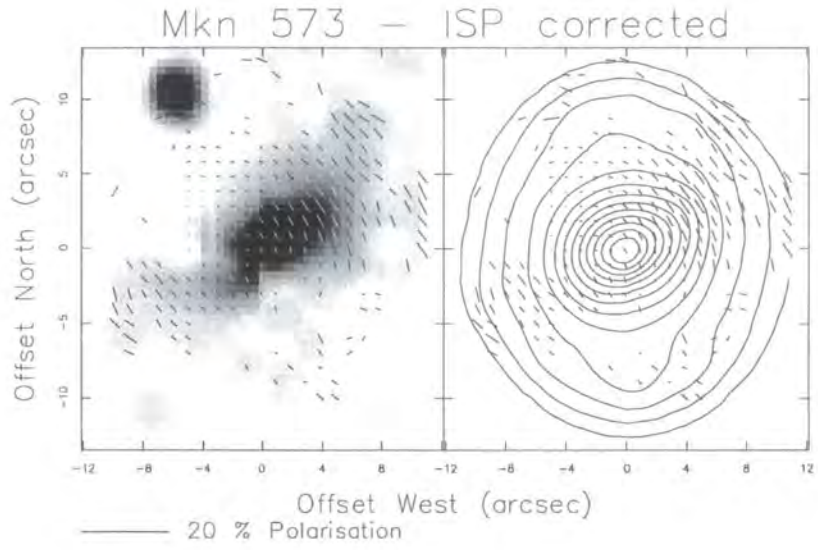

Figure 7.6: V-band greyscale polarized intensity image and total intensity contour image of Mkn 573, overlaid with polarization vectors with a polarized intensity cutoff, corrected for ISP of 0.6% at 110°

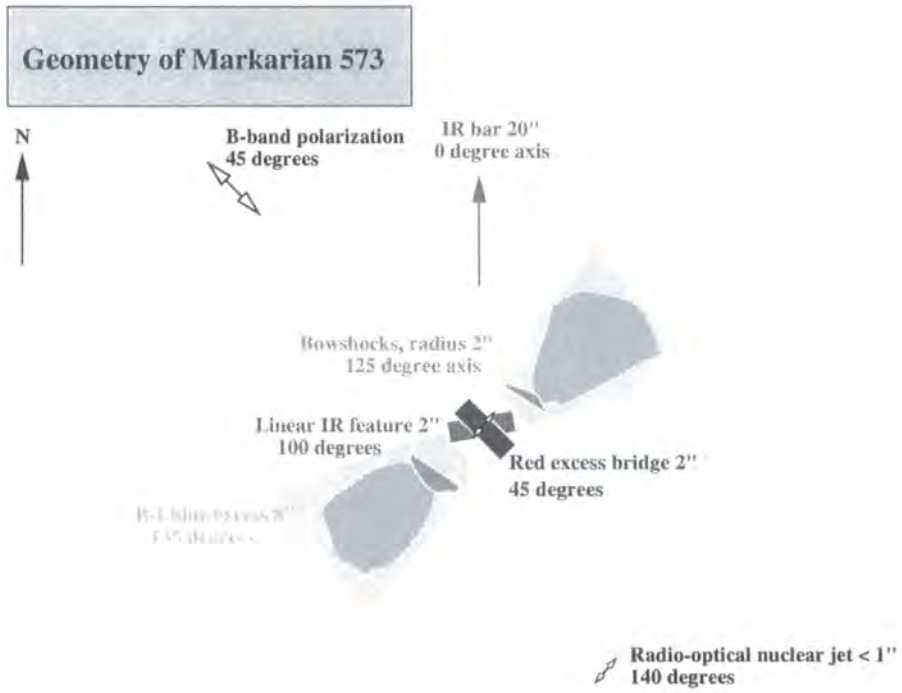

Figure 7.7: Diagram of the axes of observations of Mkn 573

and perpendicular to the nuclear radio and emission-line axes. This supports the Seyfert model of a dusty torus situated perpendicular to a biconical nuclear outflow and NLR, where the IR feature is identified as the dusty torus with a parallel polarization, and the nuclear outflow is traced by the radio and extended NLR emission. It is further supported by the observation of blue excess seen in the colour maps of Mulchaey *et al.* (1996) which corresponds to the southern excitation cone. However, why there is only one blue excess and not also one at the northern excitation peak is not clear. For comparison, in the well-studied Seyfert 2, NGC 1068, the nuclear radiation is scattered in the ionization cones by electrons to the level of 10% or 16% in the UV, Antonucci, Hurt & Miller (1994) [10] with the polarization perpendicular to the radio emission axis.

The polarized intensity map of the nucleus in figure 7.8 shows an elongation in emission along approximately a position angle of 170°, which also traces the outflow axis of the nucleus shown in figure 7.9. Outside of the central 3 arcsecond diameter of the nucleus, the polarization pattern in the galaxy is approximately centro-symmetric. The blue ring around the nucleus with diameter of 3 arcseconds which has been attributed to scattered light by Kotilainen & Ward (1997) [127] is not seen in the V-band maps of this thesis.

7.4.3 Markarian 3 (Edge-on host galaxy)

Markarian 3 hosts a Seyfert 2 nucleus with a BLR visible in polarized light indicating an obscured Seyfert 1 nucleus. Previous observations show that it has an interesting nuclear region featuring a radio jet, a nuclear emission line region, biconical ionized line emission and blue excess structures. After correction for ISP, the V-band nuclear polarization is measured (through a 2″aperture) to have a polarization angle of 175°, which is accurately perpendicular to the position angle of the radio and emission-line structures at around approximately 84° to 95°. This fits in with the general observed trend for Seyfert 2 galaxies, and supports the Seyfert models where the Seyfert nuclear polarization is from the electron or dust scattering perpendicular to the projected plane.

There is clear correspondence between regions of polarized flux *e.g.* in the south east of the galaxy and regions of blue excess measured by Kotilainen *et al.* (1997) [127], indicating that this is scattered Seyfert nuclear continuum light, at least partly from the Seyfert nucleus. A B-band polarization map of the region would be useful to confirm this feature, to see whether the level of polarization rises in this waveband whether the polarization features correspond well to the blue features found by Kotilainen (1997).

There is a striking polarization feature in both the polarized intensity map and the polarization level vectors extending north-south, about 4 arcseconds that appears to correspond

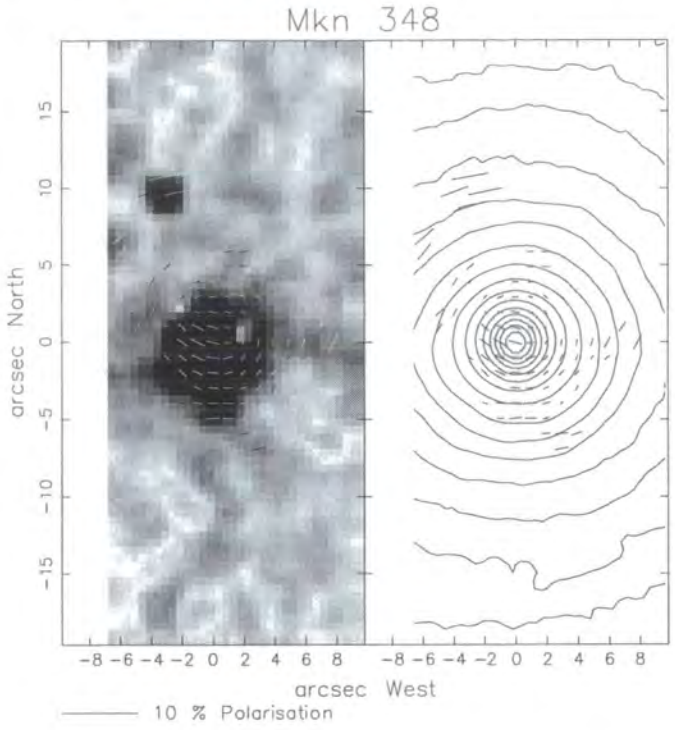

Figure 7.8: V-band polarized intensity greyscale and total contour images of Mkn 348, overlaid with polarization vectors binned with square size 3 and step size 2, corrected for ISP_{Tran1}

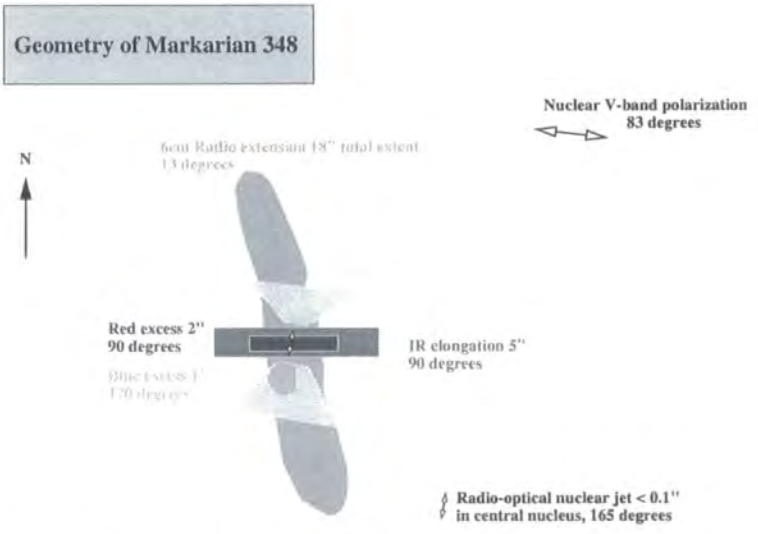

Figure 7.9: Diagram of the axes of observations of Mkn 348

to where the obscuring torus of the model would be located, but on a slightly larger scale, out to a kiloparsecond, rather than on the scale of 100 parsecs as is often taken as a torus diameter estimate. It is also aligned along the galactic of the edge-on disc of gas and stars, where the angle of polarization of both the nucleus and the extended feature is perpendicular to the radio jet, *i.e.* aligned approximately north-south. It is consistent with the accretion disc and torus system being aligned with the larger scale extended stellar disc, as found in some other Seyfert galaxies. Unfortunately, although the polarization pattern in the images was shown to be very sensitive to the ISP correction, it was not actually possible to calculate a ISP from the observations taken for this thesis. The correspondence of the polarization features with the various different emission regions of the galaxy is shown by the figures 7.10 and 7.11, which are placed together for easier comparison.

7.4.4 Markarian 1376 (Edge-on host galaxy)

Markarian 1376 (NGC 5506) hosts a Seyfert 2 nucleus which is seen through the dust lane of the edge-on galaxy, although some of its Seyfert nuclear emission parameters are more like those of Seyfert 1s, so that in some literature it is classed as a Seyfert 1.9. After ISP correction, the main polarization feature seen in the maps of this thesis, is the polarization along the centre of the dust lane and major axis, with the polarization angle aligned parallel to the dust lane near the centre. Towards the edges of the galaxy however, the vectors become aligned perpendicular to the major axis. This is classical polarization behaviour for edge-on dust lane galaxies showing the dust-lane dominating the polarization by dichroic extinction. Further out, there are clear signs of a centro-symmetric pattern around the nucleus which has been superimposed upon the aligned band of polarization along the dust lane.

The nuclear polarization is at approximately the same angle as the polarization along the dust lane of the galaxy, so it appears that the nuclear polarization measurement is dominated by the dust lane polarization, so that any possible different contribution to the polarization due to the Seyfert continuum is not significant enough to be seen. The nuclear polarization is shown in figure 7.13, together with the DSS total intensity map of the whole galaxy in figure 7.12 clearly showing the dust lane.

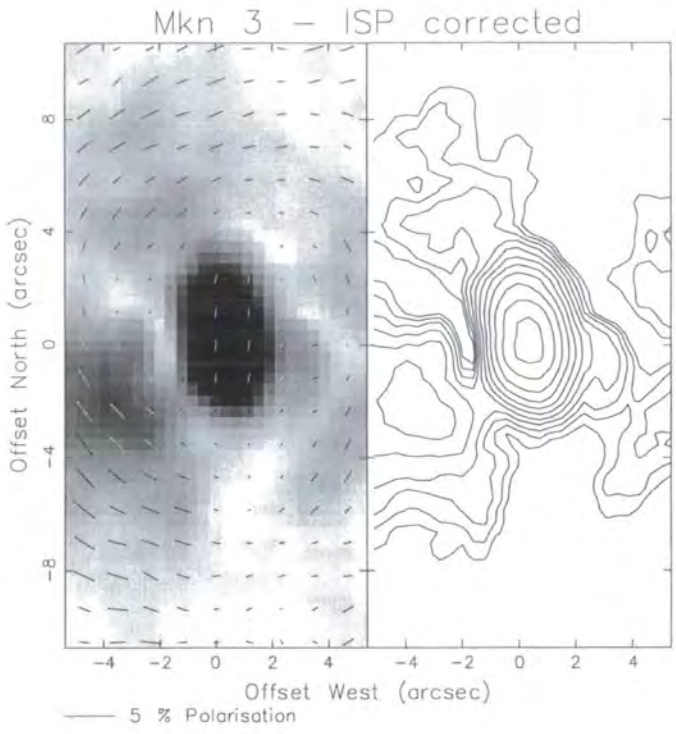

Figure 7.10: V-band greyscale polarized intensity image and polarized intensity contour image of Mkn 3, overlaid with polarization vectors with a polarized intensity cutoff, corrected for ISP

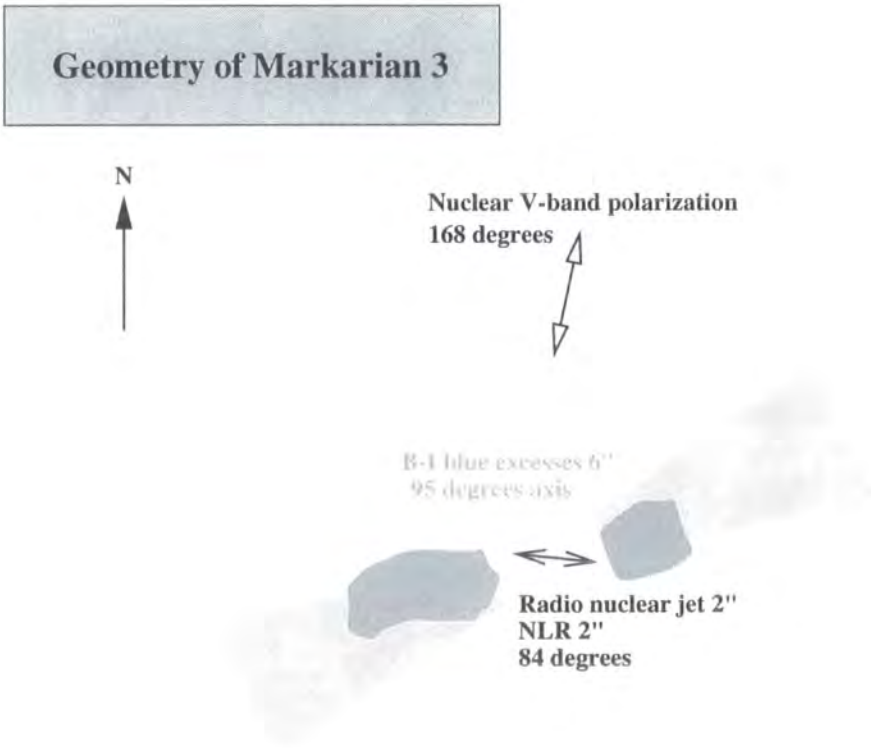

Figure 7.11: Diagram of the axes of observations of Mkn 3

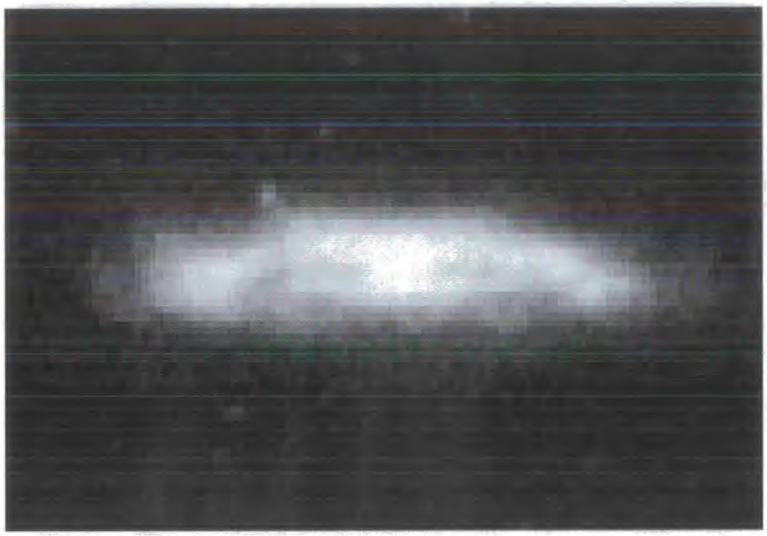

Figure 7.12: DSS intensity image of Mkn 1376, field of 3' by 2'

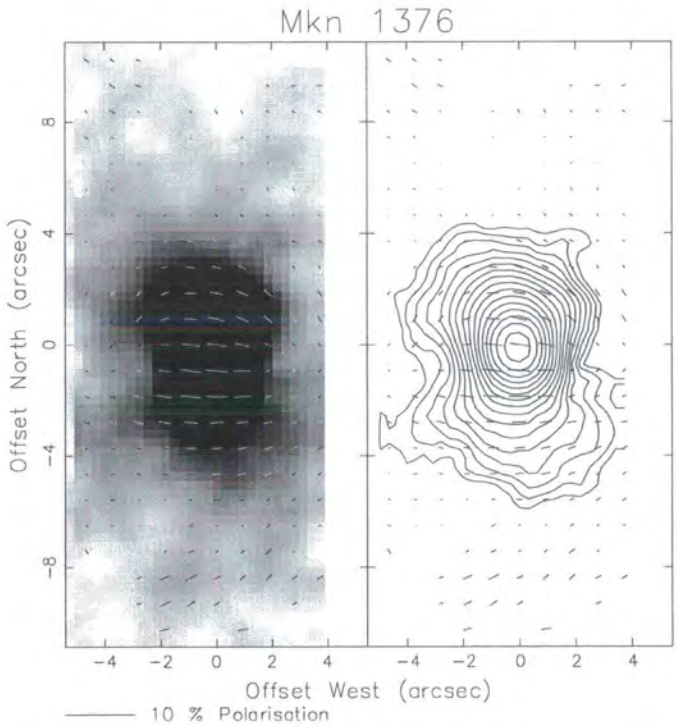

Figure 7.13: V-band polarized intensity greyscale and contour images of the nucleus of Mkn 1376 - ISP corrected, polarization vectors 5x5 bins, step size 3 pixels

7.4.5 NGC 2992 (Edge-on host galaxy)

The edge-on galaxy NGC 2992 hosts a Seyfert 2 or in some observations, a Seyfert 1.9 nucleus. It has a nuclear outflow along the minor axis at 120° traced by an extended emission-line region, and there is a also radio and IR loop, though not co-spatial with the emission-line region. The nuclear polarization is relatively high at 3% at 40°, and the uniformity of the alignment of the polarization vectors with the dust lane shows dichroic absorption through the dust lane of the galaxy. The orientation of the vectors is at 40°, which is approximately perpendicular to the minor axis emission-line region and nuclear outflow. A map of the polarized intensity is given in figure 7.15 compared with the diagram of the radiation regions in figure 7.14. The polarized intensity is mostly from the centre, but there is a slight enhancement in the western ionization cone area.

The polarization pattern in general over the galaxy shows two main components, the first from centro-symmetric scattering from the nuclear source and the second from the edge-on dust lane of the host galaxy. Although the nuclear polarization angle is the same as that of the dust lane, the level of polarization is enhanced, which could suggest either intrinsic Seyfert nuclear polarization (from electron scattering in the atmosphere of the accretion disk) aligned in approximately the same direction as the dust lane (possible if as a Seyfert 1.9 some of the optical continuum is directly visible), or some of the optical continuum viewed through a line-of-sight which just about passes through the edge of the obscuring torus (polarized by scattering by dust in the torus). However, since the enhancement in polarization is more extended over the central nuclear regions it is more likely that this is because there is a greater quantity of dust causing dichroic extinction in the very central nuclear region in general.

7.4.6 NGC 3079 (Edge-on host galaxy)

NGC 3079 hosts a Seyfert 2 nucleus and has a powerful starburst nucleus. The host galaxy is the main influence in the polarization patterns observed in the images. The nuclear polarization is of the level 1.3% and the central nuclear region does not show obvious additional polarization other than that due to dichroic absorption by the dust lane in the galaxy, at least to the resolution of the image.

Over the larger scale of the galaxy, the polarization vectors clearly show localised centro-symmetric scattering from point sources hidden deep in the dusty disk of the host galaxy, which must be star-forming regions with high amounts of dust to scatter the stellar light. NGC 253 is another starburst galaxy, of similar size with similar features, but does not

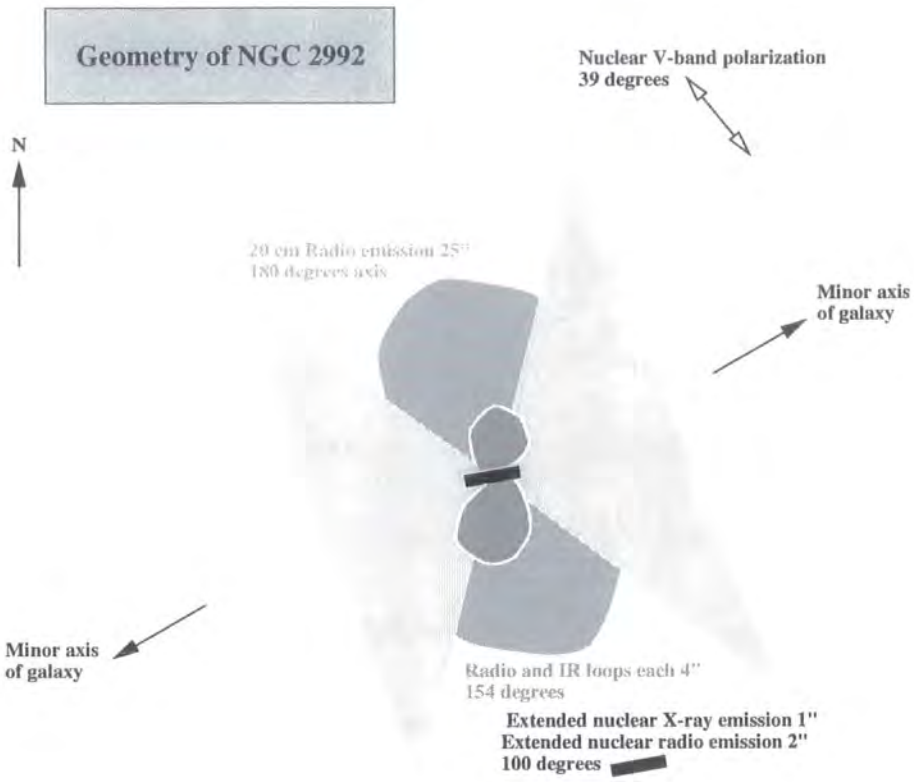

Figure 7.14: Diagram of the axes of observations of NGC 2992

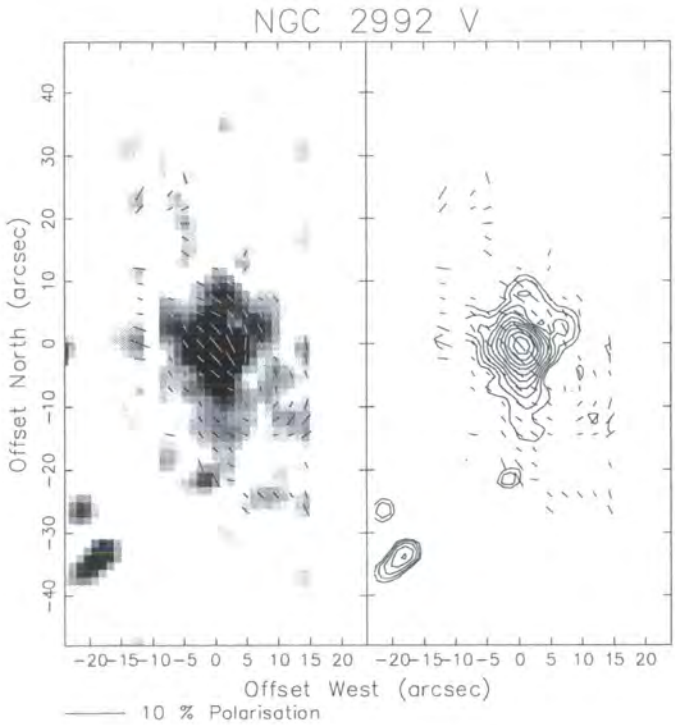

Figure 7.15: V-band contour and greyscale polarized intensity images of the nucleus of NGC 2992, polarization vectors 3x3 bins, step size 2 pixels

host a Seyfert nucleus. This has a high optical nuclear polarization in the optical bands (5% at V-band) following a Serkowski law indicating dichroic extinction in the dust-lane of the galaxy. Radio polarization of the measurements reveal a galactic plane parallel magnetic field. Similarly, the nuclear polarization of NGC 3079 appears to be dominated by the dust-lane of the galaxy.

7.4.7 NGC 1566 (Face-on host galaxy)

NGC 1566 hosts a Seyfert 1 or 1.9 nucleus. The clear spiral arm features of this face-on host galaxy dominate the appearance and the arms can be traced in as close as 1 arcsecond from the nucleus in HST images. The nuclear regions of this galaxy, do not show either an obvious centro-symmetric or linearly aligned polarization pattern that would be expected from scattering of the light from the unresolved nucleus. The percentage polarization level is low, although there is an enhancement in polarization in the very centre, which could indicate a polarized AGN contribution. The nuclear polarization angle of 45° at V-band, 51° at R-band, is about 30° to 36° away from the major axis of the optical stellar bar, which is at 15°. The nuclear polarization level increases significantly in the R-band, over double that in the V-band images, which could be the intrinsically polarized AGN continuum showing through because there is less dilution from the host galaxy nuclear flux at red wavelengths.

The larger scale polarization pattern across the galaxy shows a clear spiral galactic structure in the V- and R-band maps presented here. Here, the polarization vectors clearly trace out the spiral arm pattern, and notably correspond very well to the radio polarization detected by Ehle *et al.* (1996) [71], which also traces out the spiral arms. The optical polarization pattern is also very similar to that observed in spiral galaxy NGC 6946 by Fendt *et al.* (1998) [76]. The very limited cover H_α images demonstrate some polarization due to scattering around some bright knots in the spiral arms.

7.5 Conclusions from observations

Previous studies show that the nuclear polarizations of Seyfert 2s are generally perpendicular to the radio jet axis; this is also true of the three Seyfert 2s, Markarian 3, 348, and 573 discussed here. The nuclear polarization (at V-band) is more or less aligned perpendicularly to the radio, the ionized line emission and the also blue excess that have

been observed close to the nucleus. The axes of the ionization cone, radio and blue excess indicate the outflow of the Seyfert nuclear radiation. The orientation of the V-band polarization is consistent with the polarization that would be expected from electron scattering models of the Seyfert continuum into the line of sight, as discussed in section 7.1 on modelling studies of Seyfert polarization. The orientation of this polarization is also consistent, with dichroic transmission though the dusty torus, but the optical depth is sufficient such that the optical continuum could not be transmitted directly, so this is not causing the observed optical polarization. At infra-red wavelengths though this would become possible through transmission, so it would be interesting to investigate the IR polarizations along these regions.

Evidence for polarization due to scattered light extending along the radio and ionization emission-line cone axis is seen in Markarian 573, and more tentatively in Markarian 3 and 348, as well as clear evidence of centro-symmetric scattering further out of the nucleus in these galaxies. Markarian 573 shows the strongest polarization evidence for a biconical nuclear outflow where the scattering of the nuclear light indicated by the enhanced polarization is found to be spatially coincident with the most blue areas on previously made colour maps. These cones of polarization were detected at both B- and V-bands but not in R-band, further confirming that this polarization is due mainly to blue light. In fact, it is important that to know that this blue excess is polarized, because a blue excess could be due to processes other than scattering, such as star formation - many young bluer stars, so the polarization is further evidence for scattering. However this does not help distinguish whether the scattering agent is electrons or dust because the B-waveband is where scattering occurs most efficiently for the typical sizes of dust grains expected to reside in the circumnuclear area, and although electron scattering is wavelength independent, there is less diluting flux from the host galaxy in the blue region, so that the polarization level would also be greater in the blue.

The faint spiral arms found in H_α images of Markarian 348 are not visible at the resolution of the observations of this thesis, thus it is not possible to see whether the polarization vectors trace out the field. Neither was it possible to detect the faint large-scale spiral structure seen in the blue DSS image in the V-band observations of this thesis. Markarian 573 has faint large-scale spiral arms seen in H_α observations, but these are not visible on the V-, R- or B-band images, because the signal in these regions is too low for meaningful polarization measurements, so again it is not possible to see whether a spiral magnetic field is traced out by the polarization vectors over the galaxy. Markarian 3, being an S0 type galaxy, didn't have a visible spiral structure to investigate.

The differences in distance and size are small between these three galaxies. When comparing the nuclear polarizations, to have approximately the same area covered by the

aperture for comparing the nuclear polarization, there would be a difference of no more than 1 arcsecond in the diameter when using a 3 arcsecond diameter for one, so the nuclear polarizations can be compared more or less directly. For a 2 arcsecond aperture, the polarization levels range from 0.8% to 1.7% (Markarian 573), and only the polarization of 1.7% of Markarian 573 is higher than the average polarization of Seyferts - most Seyferts are polarized to the level of 1%. For Markarian 3 and 348 the polarization is also subject to uncertainty due to the ISP correction, which is significant since the ISP component is of a comparable level at these polarization levels. Since these three galaxies are further away than the other galaxies, the aperture size over which the polarization is measured is important when comparing them, table 7.2 lists the polarization levels at different aperture sizes for each of the galaxies, the aperture was chosen to partially take into account the different distances at which the galaxies are located, with a smaller aperture quoted for the further away galaxies to try to include less dilution from the circumnuclear regions. The nuclear polarizations of the of Seyferts with less prominent host galaxies generally have a lower levels than the group with more prominent host galaxies especially those with edge-on host galaxies, which probably have higher levels of polarization due to strong dichroic extinction in the galaxy dust-lane regions.

The other Seyferts with more prominent host galaxies are at different distances, hence different resolutions, have different sizes and are of different types. These parameters, (type, distance, angular size and magnitude) are presented in table 7.1 for comparison. NGC 3079 is the closest, with NGC 2992 and NGC 5506 being approximately twice as far away, and NGC 1566 being in between at about 30% further away as NGC 3079. This group is about 3 times closer than the group of Seyferts with less prominent hosts as discussed in the previous section and the polarizations are given of all the galaxies observed in table 7.2.

Three of the nuclei with more prominent hosts are ambiguous in Seyfert classification, Mkn 1376 and NGC 2992 are either Seyfert 1.9 or 2, and in the case of NGC 1566, Seyfert 1 or 1.9, and only NGC 3079 always appears to be clearly a Seyfert 2. Previous studies show that the nuclear polarizations of Seyfert 2s are generally perpendicular to the radio jet axis, whereas Seyfert 1s in general have optical polarization tending to be parallel to the optical axis of the galaxy. In Markarian 1376, which hosts a Seyfert 1.9 or 2, the polarization angle is aligned with the galaxy major axis (within 9°), but the other two Seyfert 1.9 have intermediate orientations, it is also nearly perpendicular to the narrow emission line regions, *i.e.* more consistent with the Seyfert 2 polarization trend. NGC 1566, with a Seyfert 1 (or 1.9) nucleus, has a nuclear polarization oriented 35° away from the major axis of the bar of the galaxy, *i.e.* intermediate rather than parallel. The radio emission follows its spiral arms, and so no nuclear radio outflow axis has been identified in previous observations for comparison of orientation. Accretion disc models predict

Table 7.1: Parameters of observed galaxies

Name	Galaxy Type[1]	Seyfert Type[3]	Distance[1,2] Mpc	Relative distance	Mag.	Diameters[1] arcmin
Mrk 3	S0	2+	54	3.6	14.0	1.8x1.6
Mrk 348	SA(s)0/a	2+	61	4	13.9	1.1x1.1
Mrk 573	(R)SAB(rs)0	2+?	69	4.6	13.7	1.3x1.3
Mrk 1376	Sa pec sp	2 (1.9)	25	1.7	13.4	2.8x0.9
NGC 1566	SAB(rs)bc	1 (1.9)	20	1.3	10.3	8.3x6.6
NGC 2992	Sa pec	2 (1.9)	31	2	13.1	3.5x1.1
NGC 3079	SB(S)c LINER starburst	2	15	1	11.5	7.9x1.4

[1]Data taken from NASA/IPAC Extragalactic Database (NED)
[2]calculated using H_0=75 km s^{-1} Mpc
[3]+ indicates presence of optical broad lines in polarized flux, +? tentative detection of optical broad lines in polarized flux, (1.9) classified as Seyfert 1.9 in some observations

negligible polarization from the Seyfert nucleus when face-on *i.e.* type 1, so that as a Seyfert 1 then NGC 1566 would not be expected to have intrinsic Seyfert polarization. NGC 2992 has the polarization angle oriented 33° away from the major axis. NGC 3079, the Seyfert 2, has the polarization angle oriented 21° from the major axis, which doesn't fit in with the model for Seyfert 2s. This implies the nuclear radiation measured is overwhelmingly from the nuclear star formation rather then any Seyfert activity, and the polarization is dominated by dichroic extinction by the edge-on dust lane and indeed is dominated over all the regions observed here by the powerful starburst nucleus of the host galaxy.

7.6 Conclusions for further work

The observations of these nearby Seyfert galaxies provided the opportunity to measure both intrinsic Seyfert nuclear polarizations and to map out large-scale polarization features in the host galaxies such as dust lanes and spiral arms; in particular the images of NGC 1566 showed polarization vectors clearly tracing the spiral structure, in striking correspondence with published radio polarization maps. However in the case of edge-on host galaxies and powerful star bursting activities, the Seyfert nuclear features could not be distinguished against other polarization sources. The Seyferts in face-on galaxies and also Markarian 3 allowed the possibility of mapping polarization features in the nucleus, including scattered light from the Seyfert nucleus and possibly medium-scale dusty disks

Table 7.2: Parameters of nuclear regions of observed galaxies

Name	Seyfert Type[1]	Major axis[2]	Radio axis[2]	IR axis[2]	NLR axis[2]	EELR axis[2]	Blue axis[2]	Aper. diam[3]	Polzn % angle[4]
Mrk 3	2+	20	84	-	84	114	95	2″	1.2% 175°
Mrk 348	2+	170	165	90	155	170	170	2″	1.7% 83°
Mrk 573	2+?	-	125	100	125	125	135	2″	0.8% 42°
Mrk 1376	2(1.9)	90	140	-	180	180	-	4″	2.0% 81°
NGC 1566	1(1.9)	15	-	-	-	-	-	5″	1.2% 48°
NGC 2992	2(1.9)	6	160	160	4	-	96	3″	3.3% 39°
NGC 2992			180						
NGC 3079	2	165	75	-	-	-	-	6″	1.2% 1°

[1]+ indicates presence of optical broad lines in polarized flux, +? tentative detection of optical broad lines in polarized flux, (1.9) classified as Seyfert 1.9 in some observations
[2]Position angle for axes of nuclear features, in degrees from north, taken from references given in chapters 5 and 6 in the section for each object
[3]Aperture diameter in arcseconds that was used for polarization measurements
[4]Data taken from observations of this thesis

surrounding the torus surrounding the central Seyfert source, observations which support the unified scheme for Seyferts. The multi-wavelength polarization observations allowed identification of scattering regions and dichroism through the wavelength dependence.

7.6.1 Limitations of the observations

The main problems of observing and distinguishing the host galaxy and Seyfert polarization features were the contribution in the nucleus of the host galaxies, especially strong star formation and obscuring dust lanes, and also of seeing-limited resolution and the resolution of the observations, because a high resolution and small aperture is required to minimise the galaxy nuclear starlight contamination and dilution of the central Seyfert emission, Similarly, the reliability of observations of the polarization features in the nuclear regions that may correspond to dusty tori or electron scattering regions is also limited by the resolution of the current data and by the seeing. Small aperture polarimetry was required to compare values to previous spectro-polarimetric measurements of the nuclei, but this was limited by the seeing conditions during the observations of this thesis.

The importance of ISP corrections and their determination for low latitude, low polarization sources is clearly demonstrated in Markarian 348 and Markarian 3 where the polarization patterns are strongly influenced by ISP, however since it was not possible

to obtain independent ISP estimates for Markarian 3, the validity of the ISP corrections applied remain questionable, The use of nearby galaxies or stars to independently check the ISP corrections from other observations is demonstrated with the measurements of the polarization of galaxies as ISP probes in the field of Markarian 348 and NGC 2992.

7.6.2 Further work

This thesis employed polarimetry to map out optical polarization features of dichroically absorbed or scattered (and hence polarized) nuclear light in Seyfert galaxies and to investigate the connections between the Seyfert nuclei and their host galaxy features, but the results from aperture polarimetry have shown the need to use narrower apertures for less dilution for the Seyfert nuclear polarizations, and certainly higher resolution, since the scale of these features even in the nearest galaxies observed are near the limit of resolution. The importance of multi-band measurements is demonstrated to allow more certain identification of polarization features as characteristic of scattering or dichroic polarization mechanisms, and therefore possibly to distinguish between intrinsic Seyfert polarization and polarization in the host galaxy. To supplement these observations, these objects imaged in this thesis should be observed at the different optical wavebands, preferably at higher resolution, and also care taken to ensure suitable observations are taken to allow an estimate if ISP to be calculated, particularly where ISP is known to be significant. A set of higher resolution images, particularly of the nuclear regions would also further the investigation of the Seyfert nucleus - host galaxy features.

As a complement to the observations of this thesis, it would be important to perform modelling of Seyfert plus spiral galaxy polarization components, with varying contributions of each component and varying their relative orientations, calculating the resulting polarization pattern at different resolutions, and to compare the theoretical polarization predictions of the model with the actual results of the observations of this thesis.

A further 6 Seyfert galaxies have been imaged by the Durham polarimeter and reduced, as included on the list of objects in tables 4.6 and 4.7 and observation log in table 4.3. These however, are further away and poorly resolved, therefore not much polarization information can be gleaned from the Seyfert nucleus, so the maps of these have not been included here. Nearly all of the bright nearby Seyferts suitable for imaging by the current Durham polarimeter with the 1 metre telescopes have now been imaged, so in order to extend the program of investigating the polarization of Seyferts and their host galaxies by observing fainter further away Seyfert galaxies, it is necessary to use the polarimeter with telescopes with higher resolution, light-gathering power and with sufficient integration time.

Bibliography

[1] T.F. Adams. *ApJS*, 33(19), 1977.

[2] E. Agol, O. Blaes, and C. Ionescu-Zanetti. *MNRAS*, 293(1), 1998.

[3] M.G. Allen, M.A. Dopita, Z.I. Tsvetanov, and R.S. Sutherland. *ApJ*, 511(686), 1999.

[4] D. Alloin, D. Pelat, M. Phillips, and M. Whittle. Recent spectral variations in the active nucleus of NGC 1566. *ApJ*, 288:205–220, January 1985.

[5] A. Alonso-Herrero, C. Simpson, M.J. Ward, and A.S. Wilson. *ApJ*, 495(196), 1998.

[6] A. Alonso-Herrero, M.J. Ward, and J.K. Kotilainen. *MNRAS*, 288(977), 1997.

[7] P. Alton. *A polarimetry study of starburst galaxies.* University of Durham, 1996.

[8] J. R. P. Angel, H. S. Stockman, N. J. Woolf, E. A. Beaver, and P. G. Martin. *ApJ*, 206L(5), 1976.

[9] R. Antonucci. *ARAA*, 31(473), 1993.

[10] R. Antonucci, T. Hurt, and J. Miller. HST ultraviolet spectropolarimetry of NGC 1068. *ApJ*, 430:210–217, July 1994.

[11] R. R. J. Antonucci. Optical spectropolarimetry of radio galaxies. *ApJ*, 278:499–520, March 1984.

[12] R. R. J. Antonucci and J. S. Miller. *ApJ*, 297(621), 1985.

[13] F.D. Arago. *Astronomie Populaire.* Paris, 1856.

[14] I. Aretxaga, B. Joguet, D. Kunth, J. Melnick, and R.J. Terlevich. *ApJ*, 519(L123), 1999.

[15] H. Awaki, K. Koyama, H. Inoue, and J. P. Halpern. *PASP*, 43(195), 1991.

[16] D.J. Axon and R.S. Ellis. *MNRAS*, 177(499), 1976.

[17] J. A. Baldwin, A. S. Wilson, and M. Whittle. *ApJ*, 319(84), 1987.

[18] T. Baribaud, D. Alloin, I. Galss, and D. Pelat. *A & A*, 256(375), 1992.

[19] P. Barr and R. F. Mushotzky. Limits of X-ray variability in active galactic nuclei. *Nature*, 320:421–423, April 1986.

[20] A. J. Barth, H. D. Tran, M. S. Brotherton, A. V. Filippenko, L. C. Ho, W. van Breugel, R. Antonucci, and R. W. Goodrich. Polarized Narrow-Line Emission from the Nucleus of NGC 4258. *AJ*, 118:1609–1617, October 1999.

[21] P.D. Barthel. *ApJ*, 336(606), 1989.

[22] L. Bassani, M. Cappi, G. Malaguti, G. G. C. Palumbo, A. Dadina, M.; Comastri, P. di Cocco, G.; Blanco, A. dal Fiume, D.; Fabian, G. Frontera, F.; Ghisellini, M. Grandi, P.; Guainazzi, T. Haardt, F.; Maccacaro, G. Maiolino, R.; Matt, A. Piro, L.; Santangelo, and N Trifoglio, M.; Zhang. BeppoSAX Observations of Bright Seyfert 2 Galaxies: Measuring the Intrinsic Continuum Emission. *MmSAI*, 70(65), 1999.

[23] L. Bassani, M. Dadina, R. Maiolino, M. Salvati, G. Risaliti, R. della Ceca, G. Matt, and G. Zamorani. *ApJS*, 121(473), 1999.

[24] S.A. Baum, C.P. O'Dea, D. Dallacassa, A.G. De Bruyn, and A. Pedlar. *ApJ*, 419(553), 1993.

[25] R. Beck. *A & A*, 251(15), 1991.

[26] R. Beck and P. Hoernes. *Nature*, 379(47), 1996.

[27] A. M. Beloborodov. Polarization Change Due to Fast Winds from Accretion Disks. *ApJL*, 496:L105, April 1998.

[28] Berriman. *ApJ*, 345(713), 1989.

[29] S. Bianchi, A. Ferrara, and Giovanardi C. *ApJ*, 465(127), 1996.

[30] G. Bica. *A & A*, 195(76), 1998.

[31] W. Bickell and W. Bailey. *AJP*, 53(468), 1985.

[32] D.S. Birney. *Modern Astronomy*. 1974.

[33] P. R. Blanco, M. J. Ward, and G. S. Wright. *MNRAS*, 242:4P–8P, 1990.

[34] C.J. Bonatto and M.G. Pastoriza. *ApJ*, 486(132), 1997.

[35] C. Brindle, J.H. Hough, J.A. Bailey, D.J. Axon, M.J. Ward, W.B. Sparks, and I.S. Mclean. *MNRAS*, 244(604), 1990.

[36] C. Brindle, J.H. Hough, J.A. Bailey, D.J. Axon, M.J. Ward, W.B. Sparks, and I.S. Mclean. *MNRAS*, 244(577), 1990.

[37] E. Brinks, P. A. Duc, V. Springel, and B. Pichardo. Inflows and Outflows in Interacting Systems: The NGC 2992/3 Test Case. In *American Astronomical Society Meeting*, volume 194, page 4908, May 1999.

[38] A. Capetti, D. J. Axon, F. D. Macchetto, A. Marconi, and C. Winge. The Origin of the Narrow-Line Region of Markarian 3: an Overpressured Jet Cocoon. *ApJ*, 516:187–194, May 1999.

[39] A. Capetti, D.J. Axon, F. Macchetto, W.B. Sparks, and A. Boksenberg. *ApJ*, 448(600), 1995.

[40] A. Capetti, D.J. Axon, F. Macchetto, W.B. Sparks, and A. Boksenberg. *ApJ*, 469(554), 1996.

[41] M. Cappi, L. Bassani, A. Comastri, M. Guianazzi, T. Maccacaro, et al. BeppoSAX observations of Mkn 3: Piercing through the torus of a Seyfert 2 galaxy. *A & A*, 344:857–867, 1999.

[42] S. Chandrasekhar. *Plasma physics.* 1960.

[43] S.C. Chapman, L.M. Simon, A. Alonso-Herrero, and . Falcke, H. *MNRAS*, in press(in press), 1999.

[44] R. A. Chevalier and A. W. Clegg. Wind from a starburst galaxy nucleus. *Nature*, 317:44, 1985.

[45] R.D. Cohen. *ApJ*, 273(489), 1983.

[46] E. J. M. Colbert, S. Baum, C. O'Dea, and S. Veilleux. Soft X-ray Emission from Large-Scale Galactic Outflows in Seyfert Galaxies. In *American Astronomical Society Meeting*, volume 191, page 13009, December 1997.

[47] E. J. M. Colbert, S. A. Baum, C. P. O'Dea, and S. Veilleux. Large-Scale Outflows in Edge-on Seyfert Galaxies. III. Kiloparsec-Scale Soft X-Ray Emission. *ApJ*, 496:786, March 1998.

[48] E.J.M. Colbert, S.A. Baum, J.F. Gallimore, C.P. O'Dea, and J.A. Christensen. *ApJ*, 467(551), 1996.

[49] E.J.M. Colbert, S.A. Baum, J.F. Gallimore, C.P. O'Dea, M.D. Lehnert, Z.I. Tsvetanov, J.S. Mulchaey, and S. Caganoff. *ApJS*, 105(75), 1996.

[50] S. Collin-Souffrin, B. Czerny, A.-M Dumont, and P.T. Zycki. *A & A*, 314(393), 1995.

[51] S. Collin-Souffrin, M. Joly, S. Dumant, and D. Turcan. *A & A*, 83(190), 1980.

[52] J. J. Condon, M. A. Condon, G. Gisler, and J. J. Puschell. Strong radio sources in bright spiral galaxies. II - Rapid star formation and galaxy-galaxy interactions. *ApJ*, 252:102–124, January 1982.

[53] O. Dahari. *AJ*, 89(966), 1984.

[54] O. Dahari. *AJ*, 90(1772), 1985.

[55] L.Jnr Davis and J.L. Greenstein. *ApJ*, 114(206), 1951.

[56] M.M. De Robertis, K Hayhoe, and H.K.C. Yee. *ApJS*, 115(163), 1998.

[57] M.M. De Robertis, H.K.C. Yee, and K. Hayhoe. *ApJ*, 496(93), 1998.

[58] G. de Valcouleurs. *ApJ*, 181(31), 1973.

[59] M. R. Deshpande and U. C. Joshi. Evidence for nonthermal radiation from the nuclei of Seyfert galaxies. *Bulletin of the Astronomical Society of India*, 21:455–456, September 1993.

[60] L.M. Dougherty and A. Dollfus. F D Arago's polarimeter and his original observation of extraterrestrial polarisation in 1811. *J. BR. Astron. Assoc.*, 99(183), 1989.

[61] B.T. Draine. *Polarimetry of the Interstellar Medium.* ASP Conference Proceedings), 1997.

[62] D. Dultzin-Hacyan, Y. Krongold, I. Fuentes-Guridi, and P. Marziani. The Close Environment of Seyfert Galaxies and Its Implication for Unification Models. *ApJL*, 513:L111–L114, March 1999.

[63] D. Dultzin-Hacyan and C. Ruano. *A & A*, 305(719), 1996.

[64] M. Dumke, M. Krause, R. Wielebinski, and U. Klein. *A & A*, 302(619), 1995.

[65] F. Durret and J. Bergeron. Long slit spectroscopy of emission line galaxies. I - The sample. *A & AS*, 75:273–297, October 1988.

[66] L.E. Dyson, editor. *Active Galactic Nuclei.* Manchester University Press, 1985.

[67] R. A. Edelson, M. A. Malkan, and G. H. Rieke. Broad-band properties of the cfa seyfert galaxies. ii - infrared to millimeter properties. *ApJ*, 321:233–250, October 1987.

[68] R.A. Edelson and M.A. Malkan. *ApJ*, 308(59), 1986.

[69] A. Efstathiou, A. McCall, and J. H. Hough. Polarization due to dichroic absorption and emission by aligned grains in dusty discs. *MNRAS*, 285:102–110, February 1997.

[70] M. Ehle and R. Beck. *A & A*, 273(45), 1993.

[71] M. Ehle, R. Beck, R.F. Haynes, A. Vogler, W. Pietsch, M. Elmouttie, and S. Ryder. *A & A*, 306(73), 1996.

[72] M. Eracleous, A.P. Koratkar, L.C. Ho, and C. Leitherer, editors. *The Physics of LINERs in View of Recent Observations*, chapter 1. ASP Conference Series. San Francisco:ASP, 1996.

[73] Kukula *et al.* . *ApJ*, 518(117), 1999.

[74] H. Falcke, A. S. Wilson, and C. Simpson. HST and VLA Observations of Seyfert 2 Galaxies: The Relationship between Radio Ejecta and the Narrow-Line Region. *ApJ*, 502:199, July 1998.

[75] M.N. Fanelli, N. Collins, R.C. Bohlin, S.G. Neff, R.W. Connell, M.S. Roberts, A.M. Smith, and T.P. Stencher. *AJ*, 114(575), 1997.

[76] C. Fendt, R. Beck, and N. Neininger. *A & A*, 335(123), 1998.

[77] P. Ferruit, A. S. Wilson, H. Falcke, C. Simpson, E. Pécontal, and F. Durret. The extended emission-line region of the Seyfert galaxy Mrk 573. *MNRAS*, 309:1–25, October 1999.

[78] T. Fuentes-Williams and J.T. Stocke. *AJ*, 96(1235), 1988.

[79] A.M.P. Garcia, J.M.R. Espinosa, and A.E.S. Rey. *ApJ*, 500(685), 1998.

[80] M. L. Garcia Vargas, A. I. Diaz, R. Terlevich, and E. Terlevich. A simple population synthesis model for the continuum of the Seyfert type-2 galaxy Mk 348. *ApSS*, 157:125–130, July 1989.

[81] G. Giuricin, D. Fadda, and M. Mezzetti. Compact Radio Cores and Nuclear Activity in Seyfert Galaxies. *ApJ*, 468:475, September 1996.

[82] D. Gondek and more. *MNRAS*, 282(646), 1996.

[83] D. Gonzalez, M.P. Rosa, C. Tadhunter, J.M. Vilchez, and J. Rodriguez-Esopinosa. *ApJS*, 108(155), 1997.

[84] R. M. Gonzalez-Delgado and E. Perez. Star formation and AGN. *ApSS*, 205:127–134, July 1993.

[85] D. Gonzlez, Rosa M., T. Heckman, C. Leitherer, G. Meurer, J. Krolik, A. S. Wilson, A. Kinney, and A. Koratkar. *ApJ*, 505(174), 1998.

[86] R.W. Goodrich. *ApJ*, 342(224), 1989.

[87] R.W. Goodrich. *ApJ*, 399(50), 1992.

[88] R.W. Goodrich and J.S. Miller. *ApJ*, 434(82), 1994.

[89] V. Gorjian. *ApJ*, 450(L51), 1995.

[90] J. M. Greenberg. Physics and astrophysics of interstellar dust. In *Infrared Astronomy: Proceedings of the Advanced Study Institute*, pages 51–95, 1978.

[91] D. Grupe, B.J. Wills, D. Wills, and K. Beuermann. *A & A*, 333(827), 1998.

[92] Q.S. Gu, J.H. Huang, and L. Ji. Enhanced Star Formation in Seyfert 2 Galaxies. *Ap & SS*, 260(389), 1999.

[93] Q.S. Gu, J.H. Huang, H.J. Su, and Z.H. Shang. *A & A*, 319(92), 1997.

[94] J.A. Hackwell and F. Schweizer. *ApJ*, 265(643), 1983.

[95] J.S. Hall. *Science*, 109(165), 1949.

[96] J.P. Halpern, M. Eracleous, and K. Forster. *ApJ*, 501(103), 1998.

[97] J.I. Harnett. *MNRAS*, 210(13), 1984.

[98] B. Harrison, A. Pedlar, S. W. Unger, P. Burgess, D. A. Graham, and E. Preuss. The parsec-scale structure of the radio nucleus of NGC 4151. *MNRAS*, 218:775–784, February 1986.

[99] S. A. Hawley and M. M. Phillips. Spectrophotometry of H II regions and the nucleus of NGC 1566. *ApJ*, 235:783–785, February 1980.

[100] E. Hecht. *Optics, Second edition.* Addison-Wesley Publishing Company, 1987.

[101] T. M. Heckman, R. Sancisi, B. Balick, and III Sullivan, W. T. High-resolution mapping of the giant H I envelope of the Seyfert galaxy Mkn 348. *MNRAS*, 199:425–433, May 1982.

[102] T.M. Heckman, M.D. Lehnert, and L. Armus. *A & A*, 89(355), 1993.

[103] C.A. Heisler, S.L. Lumsden, and J.A. Bailey. *Nature*, 385(700), 1997.

[104] C.A. Heisler and J.P. Vader. *AJ*, 110(87), 1995.

[105] T. L. Hill, C. A. Heisler, R. Sutherland, and R. W. Hunstead. Starburst or Seyfert? Using Near-Infrared Spectroscopy to Measure the Activity in Composite Galaxies. *AJ*, 117:111–125, January 1999.

[106] W. A. Hiltner. INTERSTELLAR POLARIZATION IN M 31. *ApJ*, 128:9, July 1958.

[107] W.A. Hiltner. *Science*, 109(471), 1949.

[108] L.C. Ho, A.V. Filippenko, W.L.W. Sargent, and C.Y. Peng. *ApJS*, 112(391), 1997.

[109] S. Huard. *Polarization of Light.* John Wiley & Sons, 1997.

[110] P.A. Hughes, editor. *Beams and Jets in Astrophysics*, chapter 1. Cambridge Astrophysics Series. Cambridge University Press, 1991.

[111] E. Hummel, J. van Gorkom, and C. Kotanyi. *ApJ*, 267(L5), 1983.

[112] M. D. Inglis, S. Young, J. H. Hough, T. Gledhill, D. J. Axon, J. A. Bailey, and M. J. Ward. Spatially resolved spectropolarimetry of the galaxy NGC 1068. *MNRAS*, 275:398–416, July 1995.

[113] F.P. Israel, P.P. Van der Werp, T.G. Hawarden, and C. Aspin. *A & A*, 336(433), 1998.

[114] C. R. Jenkins. What is markarian 3. *MNRAS*, 197:1049–1053, December 1981.

[115] T.J. Jones, D. Klebe, and J.. Dickey. *ApJ*, 389(602), 1992.

[116] M. Jura. Large-scale magnetic fields in spiral galaxies. *ApJ*, 258:59–63, July 1982.

[117] J.F. Kartje. *ApJ*, 452(565), 1995.

[118] L. E. Kay and E. C. Moran. A Hidden Broad-Line Region in the Weak Seyfert 2 Galaxy NGC 788. *PASP*, 110:1003–1006, September 1998.

[119] L.E. Kay. *ApJ*, 430(196), 1994.

[120] K.I. Kellerman, R. Sramek, M. Schmidt, D.B. Shaffer, and R. Green. *AJ*, 98(1195), 1989.

[121] E. Y. Khachikian and D. W. Weedman. An atlas of Seyfert galaxies. *ApJ*, 192:581–589, September 1974.

[122] M. Kishimoto. The Location of the Nucleus of NGC 1068 and the Three-dimensional Structure of Its Nuclear Region. *ApJ*, 518:676–692, June 1999.

[123] W. Kollatschny and K. J. Fricke. The group environment of Seyfert galaxies. *A & A*, 219:34–52, July 1989.

[124] S. Komossa and Janek M. *Testing NLSy1 scenarios with photoionization models*, volume 320 of *Astronomische Nachrichten*. 1996.

[125] M. Konig and J. Timmer. Analyzing X-ray variability by linear state space models. *A & AS*, 124:589–596, September 1997.

[126] A. Koratkar, R. Antonucci, R. Goodrich, and A. Storrs. Below the Lyman Edge: Ultraviolet Polarimetry of Quasars. *ApJ*, 503:599, August 1998.

[127] J.K. Kotilainen and M.J. Ward. *A&AS*, 121(77), 1997.

[128] S.B. Kraemer, D.M. Crenshaw, A.V. Filippenko, and B.M. Peterson. *ApJ*, 499(719), 1998.

[129] G.A. kriss, G.F. Hartig, L. Armus, W.P. Blair, S. Caganoff, and L. Dressel. *ApJ*, 377(L13), 1991.

[130] J. H. Krolik, K. Horne, T. R. Kallman, M. A. Malkan, R. A. Edelson, and G. A. Kriss. Ultraviolet variability of NGC 5548 - Dynamics of the continuum production region and geometry of the broad-line region. *ApJ*, 371:541–562, April 1991.

[131] P.P. Kronberg. *Rep. Prog. Phys.*, 57(325), 1994.

[132] M. J. Kukula, T. Ghosh, A. Pedlar, R. T. Schilizzi, G. K. Miley, A. G. De Bruyn, and D. J. Saikia. HIGH-RESOLUTION RADIO OBSERVATIONS OF MARKARIAN:3. *MNRAS*, 264:893, October 1993.

[133] Lang. *Astrophysical Formulae*. Springer-Verlag, 1980.

[134] A. Laor and H. Netzer. *MNRAS*, 238(897), 1989.

[135] A. Laor, H. Netzer, and T. Piran. *MNRAS*, 242(569), 1990.

[136] A. Lazarian and B. T. Draine. Disorientation of suprathermally rotating grains and the grain alignment problem. *ApJ*, 487:248, September 1997.

[137] F. Lin, C.C. & Shu. *ApJ*, 140(646), 1964.

[138] S. L. Lumsden, T. J. T. Moore, C. Smith, T. Fujiyoshi, J. Bland-Hawthorn, and M. J. Ward. Near- and mid-infrared imaging polarimetry of NGC 1068. *MNRAS*, 303:209–220, February 1999.

[139] J. W. Mackenty. Seyfert galaxies. I - Morphologies, magnitudes, and disks. *ApJs*, 72:231–244, February 1990.

[140] R. Maiolino, G. Risaliti, and M. Salvati. The effect of bars on the obscuration of active nuclei. *A & A*, 341:L35–L38, January 1999.

[141] R. Maiolino, M. Ruiz, G.H. Rieke, and Papadopoulos P. *ApJ*, 485(552), 1997.

[142] R. Maiolino, R. Stanga, M. Salvati, and J. M. Rodriguez Espinosa. NGC 5506: physics of the extended narrow line region. *A & A*, 290:40–48, October 1994.

[143] G. Malaguti, G.G.C. Palumbo, and M. Cappi. *A & A*, 331(519), 1998.

[144] M.A. Malkan. *Theory of Accretion Disks.* Kluwer Academic Publishers: Dordrecht, 1989.

[145] M.A. Malkan, V. Gorjian, and R. Tam. *ApJS*, 117(25), 1998.

[146] I. Marquez, C. Boisson, F. Durret, and P. Petitjean. A kinematical analysis of NGC 2992. *A & A*, 333:459–465, May 1998.

[147] P. G. Martin, H. S. Stockman, J. R. P. Angel, J. Maza, and E. A. Beaver. Optical polarization of the Seyfert galaxies IC 4329A and MRK 376. *ApJ*, 255:65–69, April 1982.

[148] P.G. Martin, I.B. Thompson, J. Maza, and J.R.P. Angel. *ApJ*, 266(470), 1983.

[149] P. Marziani, J. W. Sulentic, D. Dultzin-Hacyan, M. Calvani, and M. Moles. *ApJS*, 104(37), 1996.

[150] D.S Mathewson and V.L. Ford. *Mem.RAS*, 74(139), 1970.

[151] J.S. Mathis. *ARAA*, 28(37), 1990.

[152] J.S. Mathis. *Rep.Prog. Phys.*, 56(605), 1993.

[153] J.S. Mathis, W. Rumpl, and K.H. Nordsieck. *ApJ*, 217(425), 1977.

[154] J.S. Mathis and G. Whiffen. *ApJ*, 341(808), 1989.

[155] M. Matsumura and M. Seki. *A & A*, 209(8), 1989.

[156] N. I. Merkulova, L. P. Metik, and I. I. Pronik. Simultaneous UBVRI Light Curves of the Seyfert Galaxy NGC 4151 during the Extraordinary Brightening from 1989 to 1996. *AJ*, 117:2177–2184, May 1999.

[157] G. Mie. *Ann. Phys.*, 25(377), 1994.

[158] J. S. Miller, R. W. Goodrich, and W. G. Mathews. Multidirectional views of the active nucleus of NGC 1068. *ApJ*, 378:47–64, September 1991.

[159] J.S. Miller and R.R.J. Antonucci. *ApJ*, 271(L7), 1983.

[160] J.S. Miller and R.W. Goodrich. *ApJ*, 355(456), 1990.

[161] A.F.M. Moorwood and E. Olivia. *ApJ*, 429(602), 1994.

[162] J.S. Mulchaey, A.S. Wilson, and Z. Tsvetanov. *ApJS*, 102(309), 1996.

[163] J.S. Mulchaey, A.S. Wilson, and Z. Tsvetanov. *ApJ*, 467(197), 1996.

[164] R. F. Mushotzky. The X-ray spectrum and time variability of narrow emission line galaxies. *ApJ*, 256:92–102, May 1982.

[165] N.M. Nagar and A.S. Wilson. The Relative Orientation of Nuclear Accretion and Galaxy Stellar Disks in Seyfert Galaxies. *ApJ*, 516(97), 1999.

[166] N.M. Nagar, A.S. Wilson, J.S. Mulchaey, and J.F. Gallimore. Radio Structures of Seyfert Galaxies. VIII. A Distance- and Magnitude-Limited Sample of Early-Type Galaxies. *ApJS*, 120(209), 1999.

[167] S. G. Neff and A. G. De Bruyn. The compact radio core of Mkn 348 - Evidence for directed outflow in a type 2 Seyfert galaxy. *A & A*, 128:318–324, December 1983.

[168] C. Norman and N. Scoville. *ApJ*, 332(124), 1988.

[169] R. Ogley. *MERLIN mapping of the radio-loud quasar 3C345 at a frequency of 408 MHz.* University of Manchester, 1995.

[170] J.B. Oke and T.R. Lauer. *ApJ*, 230(360), 1979.

[171] E. Oliva, L. Origlia, J.K. Kotilainen, and A.F.M. Moorwood. *A & A*, 301(55), 1995.

[172] D. E. Osterbrock. Physical state of the emission-line region. *PhySSCR*, 17:285–292, March 1978.

[173] D. E. Osterbrock. *Astrophysics of gaseous nebulae and active galactic nuclei, publisher = Research supported by the University of California, John Simon Guggenheim Memorial Foundation, University of Minnesota, et al. Mill Valley, CA, University Science Books, 1989, 422 p.* 1989.

[174] D.E. Osterbrock. *ApJ*, 249(462), 1981.

[175] D.E. Osterbrock. Active galactic nuclei. *Rep. Prog. Phys.*, 54(579), 1991.

[176] D.E. Osterbrock and R.W. Pogge. *ApJ*, 297(166), 1988.

[177] Veron P., P.O. Lindblad, E.J. Zuiderwijk, M.P. Veron, and G. Adam. *A & A*, 87(245), 1980.

[178] A. Pedlar, S. W. Unger, and J. E. Dyson. Radio Seyferts and the forbidden-line region. *MNRAS*, 214:463–473, June 1985.

[179] W.D. Pence, K. Taylor, and P. Atherton. *ApJ*, 357(415), 1990.

[180] G. C. Perola and L. Piro. X-ray reprocessing and UV continuum in AGN: The case of NGC 4151. *AAP*, 281:7, January 1994.

[181] B.M. Peterson. *An introduction to active galactic nuclei*, chapter 1. Cambridge University Press, 1997.

[182] B.M. Peterson, I. Wanders, R. Bertram, J.F. Hunley, R.W. Pogge, and R.M. Wagner. *ApJ*, 501(82), 1998.

[183] P. O. Petrucci, A. Chelli, G. Henri, I. Cruz-Gonzaacute;lez, L. Salas, and R. Mujica. Search for optical microvariability in a large sample of Seyfert I galaxies. *A & A*, 342:687–703, February 1999.

[184] W. Pietsch, G. Trinchieri, and A. Vogler. NGC 3079: X-ray emission from the nuclear super-bubble and halo. *A & A*, 340:351–370, December 1998.

[185] Pogge and Eskridge. *AJ*, 106(1405), 1993.

[186] R. W. Pogge. Shocking Outflows in Seyfert Galaxies: an Imaging Perspective. In *ASP Conf. Ser. 113: IAU Colloq. 159: Emission Lines in Active Galaxies: New Methods and Techniques*, page 378, 1997.

[187] R.W. Pogge and M.M. De Robertis. *ApJ*, 404(563), 1993.

[188] R.W. Pogge and M.M. Robertis. *ApJ*, 451(585), 1995.

[189] A. C. Quillen, A. Alonso-Herrero, M. J. Rieke, C. McDonald, H. Falcke, and G. H. Rieke. Dust Lanes Causing Structure in the Extended Narrow-Line Region of Early-Type Seyfert Galaxies. *ApJ*, 525:685–690, November 1999.

[190] P. Rafanelli, M. Violato, and A.. Baruffolo. *AJ*, 109(1546), 1995.

[191] M.W. Regan and J.S. Mulchaey. *AJ*, In press(In press), 1999.

[192] W. G. Roberge. An adiabatic approximation for grain alignment theory. *MNRAS*, 291:345–352, October 1997.

[193] W. G. Roberge, T. A. Degraff, and J. E. Flaherty. The Langevin Equation and Its Application to Grain Alignment in Molecular Clouds. *ApJ*, 418:287, November 1993.

[194] D.H. Rogstad and G.S. Shostak. *A & A*, 22(111), 1998.

[195] D. Rouan, F. Rigaut, D. Alloin, R. Doyon, O. Lai, D. Crampton, E. Gendron, and R. Arsenault. Near-IR images of the torus and micro-spiral structure in NGC 1068 using adaptive optics. *A & A*, 339(687), 1998.

[196] J. Roy and J.R. Walsh. *MNRAS*, 223(39), 1986.

[197] A. Sandage and G.A. Tammann. *A revised Shapley-Ames Catalog of bright galaxies.* Washington: Carnegie Institution, 1981, Preliminary version, 1981.

[198] S.M. Scarrott. *Vistas in Astronomy*, 34(163), 1991.

[199] S.M. Scarrott. *QJR*, 37(297), 1996.

[200] S.M. Scarrott, C.D. Rolph, R.D. Wolstencroft, and C.N. Tadhunter. *MNRAS*, 249(16), 1991.

[201] S.M. Scarrott, R.F. Warren-Smith, W.S. Pallister, D.J. Axon, and R.G. Bingham. *MNRAS*, 204(1163), 1983.

[202] S.M. Scarrott, R.F Warren-Smith, and R.F Warren-Smith. *MNRAS*, 224(299), 1991.

[203] H.R. Schmidt and Miller. J.S. *ApJ*, 290(517), 1985.

[204] M. Schmidt and R.F. Green. *ApJ*, 269(352), 1983.

[205] H.R. Schmitt. *ApJ*, 506(647), 1998.

[206] H.R. Schmitt and A.L. Kinney. *ApJ*, 463(498), 1996.

[207] H.R. Schmitt, A.L. Kinney, T. Storchi-Bergmann, and R. Antonucci. *ApJ*, 477(623), 1997.

[208] K. Serkowski, D.S. Mathewson, and V.L. Ford. *ApJ*, 197(261), 1975.

[209] C.K. Seyfert. *ApJ*, 97(28), 1943.

[210] G. Shields. A Brief History of Active Galactic Nuclei . *PASP*, 111(661), 1999.

[211] R.A. Simcoe, K.K. McLeod, and J. Schachter. *AAS*, 187(5004), 1995.

[212] R.A. Simcoe, K.K. McLeod, J. Schachter, and M. Elvis. *ApJ*, 489(615), 1997.

[213] S. M. Simkin, H. J. Su, and M. P. Schwarz. Nearby Seyfert galaxies. *ApJ*, 237:404–413, April 1980.

[214] S. M. Simkin, H. J. Su, J. Van Gorkom, and J. Hibbard. Markarian 348 - A tidally disturbed Seyfert galaxy. *Science*, 235:1367–1370, March 1987.

[215] C. Simpson, J.S. Mulchaey, A.S. Wilson, M.J. Ward, and A. Alonso-Herrero. An Ionization Cone and Dusty Disk in Markarian 348: The Obscuring Torus Revealed? *ApJ*, 457L(19), 1996.

[216] D.A. Smith and C. Done. *MNRAS*, 280(355), 1996.

[217] H. A. Smith, C. J. Lada, Jr. Thronson, H. A., W. Glaccum, D. A. Harper, R. F. Loewenstein, and J. Smith. Far-infrared observations of the type 1 Seyfert galaxy NGC 4051. *ApJ*, 274:571–576, November 1983.

[218] P.S. Smith, G.D. Schmidt, R.G. Allen, and D.C. Hines. *ApJ*, 488(202), 1997.

[219] Y. Sofue and J.A. Irwin. *PASJ*, 44(3531), 1992.

[220] R. Stanga, R. Maiolino, and Rodriguez Espinosa. J.M. *NASA ARC*, 1(319), 1993.

[221] S.A. Stephens. *AJ*, 97(10), 1989.

[222] T. Storchi-Bergmann, R. C. Fernandes, and H. R. Schmitt. The Nature of the Optical Light in Seyfert 2 Galaxies with Polarized Continua. *ApJ*, 501:94, July 1998.

[223] S. Sukumar and R.J. Allen. *Nature*, 340(537), 1996.

[224] W.-H. Sun and M.A. Malkan. *ApJ*, 346(68), 1989.

[225] Y. Taniguchi. *ApJ*, In press, 1999.

[226] R. Terlevich and J. Melnick. The relation between variability and star formation in Seyfert nuclei. In *Starbursts and Galaxy Evolution*, pages 393–400, 1987.

[227] I.B. Thompson, J.D. Landstreet, H.S. Stockman, J.R.P Angel, and E.A. Beaver. *MNRAS*, 192(53), 1980.

[228] I.B. Thompson and P.G. Martin. *ApJ*, 330(121), 1988.

[229] J.E. Tohline and D.E. Osterbrocke. *ApJ*, 210(L117), 1976.

[230] H. Tran. *ApJ*, 440(565), 1995.

[231] H. Tran. *ApJ*, 440(578), 1995.

[232] H. Tran. *ApJ*, 440(597), 1995.

[233] C. A. Tremonti, A. Uomoto, R. R. J. Antonucci, Z. I. Tsvetanov, H. C. Ford, and G. A. Kriss. Discovery of the Hidden Seyfert 1 Nucleus in Markarian 463. In *American Astronomical Society Meeting*, volume 189, page 1105, December 1996.

[234] Tsvetanov, Dopita, and Allen. *BAAS*, 27(871), 1995.

[235] Z. Tsvetanov, R. Morganti, R. A. E. Fosbury, M. G. Allen, and J. Gallimore. Radio Continuum and Emission Line Morphologies of Southern Seyfert Galaxies. In *Looking Deep in the Southern Sky, Proceedings of the ESO/Australia Workshop. Held at Sydney, Australia, 10-12 December 1997. Edited by Raffaella Morganti and Warrick J. Couch. Springer-Verlag, 1999., p.248*, page 248, 1999.

[236] Z. Tsvetanov and J.R. Walsh. *ApJ*, 386(485), 1992.

[237] T. J. Turner, I. M. George, K. Nandra, and R. F. Mushotzky. *ApJS*, 113(23), 1997.

[238] T. J. Turner, I. M. George, K. Nandra, and D. Turcan. On X-Ray Variability in Seyfert Galaxies. *ApJ*, 524:667–673, October 1999.

[239] M.-H Ulrich and K. Horne. *MNRAS*, 283(748), 1996.

[240] M.-H *et al.* Ulrich. *MNRAS*, 206(221), 1996.

[241] J. S. Ulvestad, A. L. Roy, E. J. M. Colbert, and A. S. Wilson. A Subparsec Radio Jet or Disk in NGC 4151. *ApJ*, 496:196, March 1998.

[242] J. S. Ulvestad and A. S. Wilson. Radio structures of Seyfert galaxies. V - A flux-limited sample of Markarian galaxies. *ApJ*, 278:544–557, March 1984.

[243] J. S. Ulvestad, J. M. Wrobel, A. L. Roy, A. S. Wilson, H. Falcke, T. Krichbaum, G. Bower, and A. Zensus. Sub-relativistic, Sub-parsec Radio Jets in Two Seyfert Galaxies. In *AAS*, volume 193, page 9003, December 1998.

[244] J.S. Ulvestad, R.J. Antonucci, and R.W. Goodrich. *AJ*, 109(81), 1995.

[245] J.S. Ulvestad and Wilson. *ApJ*, 343(659), 1989.

[246] Unger. *MNRAS*, 209(15), 1984.

[247] S. W. Unger, A. Pedlar, D. J. Axon, M. Whittle, E. J. A. Meurs, and M. J. Ward. The extended narrow-line region in radio Seyferts - Evidence for a collimated nuclear UV field? *MNRAS*, 228:671–679, October 1987.

[248] S. W. Unger, A. Pedlar, R. V. Booler, and B. A. Harrison. Compact radio components in Seyfert galaxies. *MNRAS*, 219:387–402, March 1986.

[249] S. Veilleux, R.W. Goodrich, and G.J. Hill. *ApJ*, 477(631), 1997.

[250] S. M. Viegas-Aldrovandi and M. Contini. A guideline to the interpretation of the narrow emission-line spectra of active galactic nuclei. *ApJ*, 339:689–699, April 1989.

[251] Wagner. *A & A*, 185(77), 1987.

[252] T. Wang, T. Mihara, C. Otani, M. Matsuoka, and H. Awaki. Broadband X-Ray Observations of the Narrow-Line X-Ray Galaxy NGC 5506. *ApJ*, 515:567–575, April 1999.

[253] K. A. Weaver, J. Nousek, T. Yaqoob, R. F. Mushotzky, F. Makino, and C. Otani. X-Ray Reprocessing by a Molecular Torus in the Seyfert 1.9 Galaxy NGC 2992. *ApJ*, 458:160, February 1996.

[254] K.A. Weaver. *AAS*, 192(3202), 1998.

[255] K.A. Weaver and C.S. Reynolds. *ApJ*, 503(39), 1998.

[256] W. Webb, M. Malkan, G. Schmidt, and C. Impey. *ApJ*, 419(494), 1993.

[257] A. E. Wehrle and M. Morris. Radio and H-alpha images of the 'figure-8' radio nucleus of the interacting Seyfert galaxy NGC 2992. *AJ*, 95:1689–1694, June 1988.

[258] D. C. B. Whittet, P. G. Martin, J. H. Hough, M. F. Rouse, J. A. Bailey, and D. J. Axon. Systematic variations in the wavelength dependence of interstellar linear polarization. *ApJ*, 386:562–577, February 1992.

[259] M. Whittle. *ApJS*, 79(49), 1992.

[260] R. Wielebinski and F. Krause. *AARA*, 4(449), 1993.

[261] B. A. Wilking, M. J. Lebofsky, and G. H. Rieke. The wavelength dependence of interstellar linear polarization - Stars with extreme values of lambda/max/. *AJ*, 87:695–697, April 1982.

[262] B.J. Wills and D.C. Hines. Mass Ejection from Active Galactic Nuclei. volume 128 of *ASP Conference Series*, page 99, 1999.

[263] A. S. Wilson, J. A. Baldwin, and J. S. Ulvestad. Kinematics and ionization of extended ionized gas in active galaxies. I - The X-ray luminous galaxies NGC 2110, NGC 5506, and MCG -5-23-16. *ApJ*, 291:627–654, April 1985.

[264] A. S. Wilson and Z. I. Tsvetanov. Ionization cones and radio ejecta in active galaxies. *AJ*, 107:1227–1234, April 1994.

[265] S. Wolf and T.H. Henning. *A & A*, 341(675), 1999.

[266] R.D Wolstencroft, C.J. Done, S.M. Scarrott, and R.M.J. Scarrott. *MNRAS*, 276(460), 1995.

[267] L. Woltjer. *Active Galactic Nuclei*, chapter 1. Springer-Verlag:Berlin, 1990.

[268] K. Wood. *ApJ*, 477(L25), 1997.

[269] K. Wood and T.J. Jones. *AJ*, 114(1405), 1997.

[270] S. Young. A generic scattering model for AGN. *MNRAS*, 312:567–578, March 2000.

[271] S. Young, J. H. Hough, D. J. Axon, J. A. Bailey, and M. J. Ward. Near-IR spectropolarimetry and modelling of NGC 1068. *MNRAS*, 272:513–527, February 1995.

[272] S. Young, J.H. Hough, A. Efstathiou, B.J. Wills, J.A. Bailey, M.J. Ward, and D.J. Axon. *MNRAS*, 281(1206), 1996.

[273] A.A. Zdziarski, W.N. Johnson, C. Done, D. Smith, and K. McNaron-Brown. *MNRAS*, 438(63), 1995.

Acknowledgements

There are many people I would like to thank for helping me complete this thesis. I would like to thank the Heads of the physics department, Brian Tanner and Mike Pennington, my supervisor Mike Scarrott, and PPARC for allowing me the opportunity and means to do a PhD in Astronomy. The basis of this thesis is of course the observations, so many thanks go to my fellow observers Steve Bowlzer, Dave Stockdale (especially for keeping the polarimeter running), Steve Lishman, Ray Wolstencroft and the other people who observed the rest of data that I have used in this thesis, in particular Mike Scarrott, Steve, Paul Booth, and Paul Alton. Thanks to my supervisor, Mike Scarrott for his help. I'd really like to thank Christine Done for reading and commenting on my thesis chapters and being generally very encouraging, supportive and interested in my thesis. Also many thanks to Peter Draper for commenting on my maps and for coming in specially at the weekend to boot up the servers after the power cuts. Anche molte grazie a Alessandro Bressan at the Observatory of the University of Padova for his help in arranging for and allowing me to use the Observatory facilities to finish writing up my thesis.

Grazie mille mille a Michael for the vast amounts of time spent proof-reading, being very supportive, very patient, and for co-ordinating all the printing, bureaucracy and handing in of my thesis while I was many miles away in Italy or somewhere else, thanks so so much. Spassebar Dan for all sorting out all those weird invisible problems with the LaTeX script, for all the proof-reading, organization and checking of references and all of your enduring support and always encouraging emails from all over the world. Thanks also Gavin and Aya for going to the Science Museum library to get that elusive reference paper for me.

I have really really appreciated all the support of all my friends, from all different places, who have all been been very supportive and encouraging, whether by phone, letter or in person, as well as all those emails at odd hours in the morning when the writing up was getting very difficult. In particular thanks to Dan, Michael, Gavin, Robert, Karima, Charlotte, those in the astronomy department, those in Palatine house e molte grazie a Paolo e Carlos per la pizza mezzanotte al osservatorio (senza mozzarella!) and Eeny Meeny for always smiling.

And, in particular, a really huge thank-you to all my family at home, to Mum, Dad, Grandad, Nicola, Jo and Chris for all their love, support, patience and encouragement, always being ready to listen, always doing everything they can and more to help, and always putting up with me rushing around here, there and everywhere, helping me to do all the too many things in too short a time, despite me somehow never actually managing to stay at home for more than too few days at a time although missing them all very much.

This research has made use of NASA's Astrophysics Data System Abstract Service, and also the NASA/IPAC Extragalactic Database (NED) which is operated by the Jet Propulsion Laboratory, California Institute of Technology, under contract with the National Aeronautics and Space Administration.

The author also made use of the Astrophysics e-Print archive at http://xxx.lanl.gov/. This archive is based upon activities supported by the U.S. National Science Foundation under Agreement No. 9413208 (1 Mar 1995 thru 28 Feb 2000) with the Los Alamos National Laboratory, and by the U.S. Department of Energy in collaboration with local support.

The Digitized Sky Survey was produced at the Space Telescope Science Institute under U.S. Government grant NAG W-2166. The images of these surveys are based on photographic data obtained using the Oschin Schmidt Telescope on Palomar Mountain and the UK Schmidt Telescope. The plates were processed into the present compressed digital form with the permission of these institutions.

The National Geographic Society - Palomar Observatory Sky Atlas (POSS-I) was made by the California Institute of Technology with grants from the National Geographic Society.

The Second Palomar Observatory Sky Survey (POSS-II) was made by the California Institute of Technology with funds from the National Science Foundation, the National Geographic Society, the Sloan Foundation, the Samuel Oschin Foundation, and the Eastman Kodak Corporation.

The Oschin Schmidt Telescope is operated by the California Institute of Technology and Palomar Observatory.

The UK Schmidt Telescope was operated by the Royal Observatory Edinburgh, with funding from the UK Science and Engineering Research Council (later the UK Particle Physics and Astronomy Research Council), until 1988 June, and thereafter by the Anglo-Australian Observatory. The blue plates of the southern Sky Atlas and its Equatorial Extension (together known as the SERC-J), as well as the Equatorial Red (ER), and the Second Epoch [red] Survey (SES) were all taken with the UK Schmidt.